

PHOTOELECTROCHEMICAL AND ELECTROCHEMICAL BIOMOLECULAR DETECTION

INTEGRATED BIORECOGNITION AND DUAL-SIGNAL TRANSDUCTION STRATEGIES FOR  
OLIGONUCLEOTIDE-BASED BIOMOLECULAR DETECTION IN COMPLEX MEDIA

BY  
AMANDA VICTORIOUS  
B.A.Sc (UNIVERSITY OF WATERLOO)

A Thesis Submitted to the School of Graduate Studies in  
Partial Fulfillment of the Requirements for the Degree  
Doctor of Philosophy in Biomedical Engineering  
McMaster University © Copyright by Amanda Victorious, February 2022

McMaster University, Doctor of Philosophy (2022) Hamilton, Ontario (Biomedical Engineering)

TITLE: Integrated Biorecognition and Dual-Signal Transduction Strategies for Oligonucleotide-Based Biomolecular Detection in Complex Media

AUTHOR: Amanda Victorious, B.A.Sc., Nanotechnology Engineering (University of Waterloo)

SUPERVISOR: Leyla Soleymani, Associate Professor, Department of Engineering Physics, McMaster University

NUMBER OF PAGES: 205

## **Lay Abstract**

To address critical limitations in the field of point-of-care molecular diagnostics, it is vital to develop new tools integrating bio-recognition systems with programmable photoelectrochemical and electrochemical signal transduction that enables the design of more effective biosensors. In photoelectrochemical (PEC) systems, plasmonic materials such as gold nanoparticles are often featured to either amplify or attenuate signal response. While there is a significant amount of literature regarding the interaction of gold nanoparticles (Au NPs) with semiconductive systems, the exact nature of the interaction between the two particles has not yet been fully mapped out. In this thesis, we examine various degrees of freedom—including surface coverage density and separation distance—that influence the design of effective photoelectrochemical systems. The understanding gained is further harnessed to design dual-signal photoelectrochemical systems featuring titanium dioxide (TiO<sub>2</sub>) photoelectrodes and Au linked dynamic deoxyribonucleic acid (DNA) motifs to enable predictive modulation in response to target identification. An electrochemical (EC) analogue featuring structure switching DNA motifs and redox tagged barcodes was also developed. The resultant PEC and EC biosensing assays were critically examined, and their analytical performance was subsequently evaluated in terms of limit-of-detection, sensitivity, and specificity. Ultimately, new classes of bioassays featuring integrated biorecognition and dual-signalling capability for oligonucleotide (i.e., nucleotide sequences and aptamers) based biomolecular detection in urine and saliva were realized.

## Abstract

PEC bioanalysis represents a unique and dynamically developing methodology that offers an elegant route for sensitive biomolecular detection. Building on the principle of EC analysis, PEC biosensors harness the unique properties of optically active species to enhance analytical performance. Owing to the current based outputs evolved in both PEC and EC bioanalysis, they can be miniaturized and potentially integrated with handheld and portable analyzers, making them uniquely positioned as tools to build effective POC diagnostics.

The commercialization of PEC technology for building POC diagnostics, however, heavily depends on enhancing the stability of the photoelectrodes upon repeated use, lowering the limit-of-detection (LOD) of the PEC biosensor used, enhancing the efficiency of signal transduction and the ability of the device to detect minute amounts of biomolecular target in complex biological matrices. In order to address these constraints, we first developed a new solution-based strategy integrating inorganic semiconductive species ( $\text{TiO}_2$ ) in an organic framework to construct photoelectrodes with enhanced signal baselines and adequate stability for the cyclic measurements required in biosensing.

These transducers were subsequently used to investigate the interaction mechanisms (wavelength dependency, coverage density dependency and spatial dependency) between plasmonic NPs (Au) and the photoelectrodes ( $\text{TiO}_2$ )—chosen as model materials—with the goal of enabling predictive dual-signal modulation and enhanced limit-of-detection in PEC biosensors. The understanding gained was used to design a dual-signal PEC transduction strategy—operated at a single excitation wavelength and on a single electrode—to detect nucleic acid sequences in urine without direct target labeling, target amplification or target enrichment. Here, Au NP terminated biobarcode served as dynamic signal amplifiers that enabled a low limit-of-detection (5 fM), a wide linear range (1 fM – 100 pM), and the ability to discern between single and double base-mismatched nucleic acid sequences. In parallel, we also detail the development of an EC biosensor featuring dynamic DNA motifs, capable of reagentless, sensitive and specific detection of N-PEDv (nucleocapsid protein of porcine epidemic diarrhea virus)—a protein target with emerging global significance—in both buffer (LOD  $\sim 1.08 \mu\text{g mL}^{-1}$ ) and urine (LOD  $\sim 1.09 \mu\text{g mL}^{-1}$ )

Ultimately, this work presents innovations in material architecture and programmable dual-signal transduction that enhance the performance metrics of biosensors; thus, presenting the potential to design POC molecular diagnostics of the future.

## **Acknowledgements**

First and foremost, I would like to thank my supervisor Dr. Leyla Soleymani for her guidance, support and encouragement for the past two years. Without her motivation, insight, insistence on tackling challenges head-on and knowledge, I would not have achieved all that I have at the culmination of my graduate studies.

I would additionally like to thank my supervisory committee members, Dr. Igor Zhitomirsky and Dr. Tohid Didar for always providing me with insightful feedback and opportunities to grow while continuing to inspire me on my PhD journey.

A special thanks to my mentor, research partner and good friend—Dr. Sudip Saha. You have taught me to relentlessly ask questions, inspired me to think in new ways and always weed out the positives in trying situations.

To my peers in the lab, I thank you for your numerous collaborations, engaging and unique personalities and the nurturing environment you have helped foster at the Soleymani Lab. The times we have spent together, inside, and outside of the lab, will be some of my most cherished memories. I feel lucky to have had the opportunity to work alongside such brilliant minds. A special shoutout to Richa, Sarah, Noor, Rod, Julia, Devon, and Colleen for all the giggles, silly conversations, and shenanigans; you made Hamilton feel like home.

Mom, Dad and Allen, thank you for always believing in me and pushing me to be the best I can. And most importantly, for never letting me give up, even when a PhD seemed like an incredibly daunting task. And Brad, my partner in crime, I thank you for always having my back, being the rock to my chaos and always being ready to take on an adventure. To the Reitzel clan, I thank you for your honesty, games, laughter, and verbal tussles; you keep things exciting.

To my close friends, Clarisa, Karina, Lucy, Kezia, thank you for the constant chats and cheers.

Finally, I would like to acknowledge the Natural Sciences and Engineering Research Council of Canada (NSERC), and McMaster University for their financial support.

## Table of Contents

Lay Abstract.....	iii
Abstract.....	iv
Acknowledgements.....	v
Table of Contents.....	vi
List of Figures.....	ix
List of Tables.....	xviii
List of Abbreviations.....	xix
Declaration of Academic Achievement.....	xx
Chapter 1: Introduction.....	1
1.1 Point-of-care Biosensors – Overview and Technical Challenges.....	1
1.2 Biosensor Architecture.....	4
1.2.1 Bioreceptors in Disease Diagnostics.....	4
1.2.2 Classification of Biosensors by Transduction Methods.....	6
1.2.2.1 Piezoelectric Biosensors.....	6
1.2.2.2 Magnetic Biosensors.....	7
1.2.2.3 Optical Biosensors.....	7
1.2.2.4 Electrochemical Biosensors.....	7
1.2.2.5 Photoelectrochemical Biosensors - Exploiting Light for Better Diagnostics.....	8
1.3 Motivation – Signalling Strategies to Enhance Analytical Performance in Biological Matrices.....	11
1.4 Research Objectives.....	14
1.5 Thesis Overview.....	15
Chapter 2: Overview of Photoactive species and PEC transduction.....	17
2.1 Abstract.....	18
2.2 Introduction.....	18
2.3 Construction of a photoelectrochemical cell.....	19
2.4 Photoactive species for PEC biosensors.....	20
2.4.1 Inorganic Semiconductors.....	20
2.4.2 Organic Semiconductors.....	22
2.4.3 Hybrid semiconductors.....	23
2.5 Transduction mechanism.....	26
2.5.1 Introduction of photoactive species.....	27
2.5.2 Generation of electron/hole donors.....	30
2.5.3 Steric-hindrance based assay.....	32
2.5.4 In situ induction of light.....	35
2.5.5 Resonance energy transfer.....	36
2.6 Challenges and Future Perspectives.....	40

Chapter 3: Engineering a robust three-dimensional transducer for signal-off PEC biosensing (Objective 1)	42
3.1 Abstract	42
3.2 Introduction	42
3.3 Materials and Methods	42
3.4 Results and Discussion	42
3.5 Conclusions	42
3.6 Acknowledgements	42
3.6 Supplementary Information	42
Chapter 4: Examining Au coverage density to design signal-on PEC TiO <sub>2</sub> architectures for biosensing (Objectives 2, 3)	42
4.1 Abstract	44
4.2 Introduction	44
4.3 Materials and Methods	45
4.4 Results and Discussion	47
4.5 Conclusions	53
4.6 Acknowledgements	54
4.7 Supplementary Information	54
Chapter 5: Investigating spatial dependency in TiO <sub>2</sub> /Au NP systems for differential PEC biosensing (Objectives 2, 4, 5)	57
5.1 Abstract	59
5.2 Introduction	59
5.3 Materials and Methods	60
5.4 Results and Discussion	62
5.5 Conclusions	70
5.6 Acknowledgements	71
5.7 Supplementary Information	71
Chapter 6: Dynamic DNA barcodes - A differential strategy for single-electrode PEC nucleic acid detection in urine (Objectives 5, 6)	83
6.1 Abstract	85
6.2 Introduction	85
6.3 Methods and Materials	86
6.4 Results and Discussion	89
6.5 Conclusion	95
6.6 Acknowledgements	95
6.7 Supplementary Information	95
Chapter 7: Dynamic DNA barcodes - A reagentless strategy for dual-electrode EC protein detection in saliva (Objective 6)	100
7.1 Abstract	101
7.2 Introduction	101
7.3 Methods and Materials	102
7.4 Results and Discussion	105
7.5 Conclusion	114
7.6 Acknowledgement	115

7.7 Supplementary Information .....	115
Chapter 8: Conclusion.....	121
8.1 Thesis Summary.....	121
8.2 Thesis Conclusions .....	122
8.3 Contributions to the Field .....	123
8.5 Future Work.....	126
8.6 Final Remarks .....	129
References.....	130

## List of Figures

Figure 1.1 Components of a biosensor.....	4
Figure 1.2 Illustration of target recognition in nucleic acid biosensors.....	6
Figure 1.3 Illustration of a typical 3-electrode PEC cell setup for biosensing.....	9
Figure 1.4 N-type semiconductor interface (a) before and (b) after immersion into redox electrolyte in an PEC cell setup upon illumination in the presence of a counter metal electrode .....	10
Figure 1.5 P-type semiconductor interface (a) before and (b) after immersion into redox electrolyte in an PEC cell setup upon illumination and in the presence of a counter metal electrode. ....	11
Figure 2.1 Schematic representation of the building blocks of a PEC biosensing system: the PEC cell, photoactive materials, and various signal transduction architectures. ....	19
Figure 2.2 Operation of n-type semiconductor (left) and p-type semiconductor (right) in a PEC cell. Electron donors (D) in the redox couple are oxidized by the photoactive species, thereby resulting in the loss of an electron which is then relayed to the collector (underlying conductive substrate), thus yielding an anodic current. Alternatively, electron acceptors (A) in the redox couple gain an electron from the photoactive species following their reduction upon light illumination, subsequently giving rise to a cathodic current. $E_g$ , $E_f$ , WE, RE, CE represent band gap energy, fermi energy, working electrode, reference electrode and counter electrode respectively.....	21
Figure 2.3 Principles of signal transduction in PEC biosensors a) Introduction of photoactive species b) Generation of electron/hole donors c) Use of steric hinderance d) In situ induction of light e) Resonance energy transfer. ....	27
Figure 2.4 Introduction of QDs as Photoactive species: a) Schematic Diagrams of PEC Biosensor for miRNA-141 detection using DSN enzyme-assisted target cycling amplification strategy and DNA TET-CdTe QDs-MB complex (Reprinted from <sup>232</sup> with permission from American Chemical Society); b) Schematic illustration of the PEC detection of miRNA-21 by bringing photoactive N-doped carbon dots following hybridization of the target RNA (Reprinted from <sup>340</sup> with permission from American Chemical Society); c) Schematic representation of ultrasensitive insulin detection based on CdTe QD labels brought into proximity of CdS/TiO <sub>2</sub> /ITO electrode upon affinity-based binding of CdTe QD labeled insulin target (Reprinted from <sup>312</sup> with permission from American Chemical Society); d) Schematic representation of the detection of miRNA-155 based on NPC-ZnO labelled target. Here, NPC-ZnO performs the role of electron scavenger, thus generating a signal-on response (Reprinted from <sup>341</sup> with permission American Chemical Society). ....	29
Figure 2.5 Introduction of photoactive species: a) Schematic representation of two potentiometrically resolvable protein detection assays for PSA and human interleukin-6 involving the affinity-based binding of CS-AgI tagged IL-6 and CS-AgI tagged PSA (Reprinted from <sup>334</sup> with permission from American Chemical Society); b) Liposomal PEC bioanalysis using photocathode and AgI/Ag; Reproduced with permission from (Reprinted from <sup>342</sup> with permission from American Chemical Society). ....	30
Figure 2.6 In situ generation of electron/hole donors : a) Incorporation of dual enzyme tags for multiplexed cardiac troponin I (cTnI) and C-reactive protein (CRP) detection (Reprinted from <sup>346</sup> with permission from American Chemical Society); b) Schematic illustration of near infrared to ultraviolet light-mediated photoelectrochemical aptasensing for cancer biomarker detection and mechanism of signal generation in NaYF <sub>4</sub> :Yb,Tm@TiO <sub>2</sub> photoactive electrode (Reprinted from <sup>316</sup> with permission from American Chemical Society). ....	31

Figure 2.7 Steric-hindrance based biosensing: a) Detection of apoptotic cells by  $\text{TiO}_2/\text{EG}/\text{ZnIn}_2\text{S}_4$  electrodes (Reprinted from <sup>355</sup> with permission from American Chemical Society); (b) Use of Au NPs in conjunction with a semiconductor ( $\text{MoS}_2$ ) to achieve higher photoresponse (Reprinted from <sup>350</sup> with permission from The Royal Society of Chemistry); (c) Detection of N glycan on  $\text{ZnO}_2/\text{CdTe}/\text{GMSNs}$  electrode modified with GQD@conA (Reprinted from <sup>356</sup> with permission from American Chemical Society); (d) Two-channel approach for detecting AFB1 (Reprinted from <sup>328</sup> with permission from American Chemical Society).... 34

Figure 2.8 In situ generation of light. a) PSA detection by coupling  $\text{H}_2\text{O}_2$  – triggered peroxyoxalate self-illuminated system with an external capacitor on the photoanode and digital multimeter as readout device (Reprinted from <sup>365</sup> with permission from American Chemical Society); (b) Schematic of the photocurrent generation mechanism in the modified paper sample zone of the Au-PWE under a CL light source (Reprinted from <sup>366</sup> with permission from Royal Society of Chemistry)..... 35

Figure 2.9 Resonance energy transfer based photoelectrochemical biosensors: a) Energy transfer between CdS QDs and Ag NPs upon the ALP induced Ag deposition on Au NPs (Reprinted from 376 with permission from American Chemical Society); (b)Tata binding protein bends the double-stranded DNA structure and brings CdS QD and Au NPs closer (Reprinted from 378 with permission from American Chemical Society); (c) Schematic illustration of the signal-off sandwich type immunoassay was developed by using CuS nanocrystals as photocurrent quencher for early detection of CEA (Reprinted from 379 with permission from American Chemical Society); (d) Thrombin detection using a PEC aptasensing platform based on exciton energy transfer between CdSeTe alloyed quantum dots and  $\text{SiO}_2@\text{Au}$  nanocomposites. In this approach, RET significantly reduces the photocurrent, which is then quickly restored following the target’s competitive binding and subsequent release of the metal NP tagged capture probe (Reprinted from 380 with permission from The Royal Society of Chemistry). ..... 37

Figure 3.1 Chemical characterization of P25- $\text{TiO}_2$  modified with different ligands. a) Chemical structures of (i) catecholic bonding of DHB to P25- $\text{TiO}_2$ , (ii) bonding between chitosan and P25- $\text{TiO}_2$  and (iii) catecholic bonding between DHB-CHIT and P25- $\text{TiO}_2$ . b) FTIR spectra of as-received (i) DHB and (ii) CHIT powders. FTIR spectra of P25- $\text{TiO}_2$  modified with (iii) CHIT, (iv) DHB and (v) DHB-CHIT..... 42

Figure 3.2 Structural, optical, and photoelectrochemical characterization of films created from unmodified and functionalized P25- $\text{TiO}_2$  nanoparticles. a) Schematics of i) unmodified P25- $\text{TiO}_2$ , ii) DHBA-modified P25- $\text{TiO}_2$ , iii) chitosan-modified P25- $\text{TiO}_2$ , and iv) DHBA-chitosan-modified P25- $\text{TiO}_2$ . Images demonstrating scanning electron micrographs (b), UV/Visible absorbance (c), and IPCE (d) of films created from P25- $\text{TiO}_2$  nanoparticles demonstrated in (a). The inset in (d) demonstrates the mechanism of photoelectrochemical oxidation of ascorbic acid (AA) using P25- $\text{TiO}_2$ ..... 42

Figure 3.3 Enhancing the base photocurrent of the P25- $\text{TiO}_2$  electrodes. a) PEC current density measurements for P25- $\text{TiO}_2$  with different surface functionalization and their respective current response (left) and as summarized in bar plots (right). The inset demonstrates the spectrum of the optical excitation source. “D” denotes DHB, and “C” denotes chitosan. b) PEC current density measurements with increasing P25- $\text{TiO}_2$  concentration in a P25- $\text{TiO}_2$ -DHB-CHIT film (left) and as summarized as bar plots (right). Error bars represent one standard deviation and 1-6x concentration refers to 33.3, 66.6, 99.9, 133.2, 166.5, and 199.8  $\text{g L}^{-1}$ , respectively..... 42

Figure 3.4. Photoelectrochemical DNA detection using  $\text{TiO}_2$ -DHB-CHIT electrodes. a) Scanning electron micrograph of  $\text{TiO}_2$ -DHB-CHIT electrodes. b) Schematic demonstration of the bio-functionalization of electrodes with probe DNA, hybridization with complementary target DNA, and photoelectrochemical detection using ascorbic acid as the reporter. c) Photocurrent density of bare, probe-modified, and probe modified electrode hybridized with complementary DNA target (+target). d) The percentage current

decrease measured between probe modified electrodes incubated with matched (complementary) and mismatched target DNA. Error bars represent one standard deviation.....	42
Figure S3.1 Raman spectroscopy of i) unmodified P25-TiO <sub>2</sub> , ii) DHBA-modified P25-TiO <sub>2</sub> , iii) chitosan-modified P25-TiO <sub>2</sub> , and iv) DHBA-chitosan-modified P25-TiO <sub>2</sub> .....	42
Figure S3.2 Bandgap measurements of modified TiO <sub>2</sub> nanoparticles.....	42
Figure S3.3 Stability measurements of electrodes fabricated with increasing P25-TiO <sub>2</sub> concentration in a P25-TiO <sub>2</sub> -DHB-CHIT film. ....	42
Figure S3.4 Photocurrent response following storage in dark condition at 4°C for 7 days. ....	42
Figure 4.1: Development of the TiO <sub>2</sub> -AuNP photoelectrodes. (a) Schematic diagram illustrating the Au NP deposition on P25-TiO <sub>2</sub> films by varying the deposition time from 5 minutes to 45 minutes with SEM image of the TiO <sub>2</sub> electrodes (scale bar represents 200nm); (b) SEM image of the Au NP-deposited P25-TiO <sub>2</sub> electrodes for the deposition times of (i) 5min, (ii) 10min, (iii) 20min, (iv) 45min (scale bar represents 100 nm). The calculated density of Au NPs is shown at the top-right corner of each SEM image. ....	48
Figure 4.2: Photoelectrochemical characterization of the TiO <sub>2</sub> -AuNP photoelectrodes. (a) Absorption spectrum of TiO <sub>2</sub> NPs and Au NPs (b) Representative PEC curves of the photoelectrode obtained using chopped light chronoamperometry at 0 V bias versus Ag/AgCl at excitation wavelength of (i) 397 nm and (ii) 540 nm. (c) Bar plots summarizing the percentage change in photocurrents of the P25-TiO <sub>2</sub> electrodes following the immersion in Au NP solution. Error bars represent one standard deviation, with experiments performed using at least three separate electrodes. ....	49
Figure 4.3: Understanding the mechanisms of photocurrent modulation in the TiO <sub>2</sub> -AuNP photoelectrodes. (a) IPCE spectrum of the photoelectrodes before and after Au NP deposition (inset shows zoomed in spectrum from 500 nm to 600nm). (b) Mott-Schottky (1/C <sup>2</sup> vs. voltage) diagram for the photoelectrodes before and after AuNP deposition.....	50
Figure 4.4: Schematic drawing showing the mechanisms of Au-TiO <sub>2</sub> interaction at UV (a) and visible (b) light excitation. ....	51
Figure 4.5: DNA detection assay built on the interactions between Au and TiO <sub>2</sub> NPs (a) DNA detection assay on baseline TiO <sub>2</sub> electrode. (i) Schematic illustration of the assay design. (ii) Percentage change in PEC current showing signal-on response for UV and visible light excitation. (iii) Representative PEC graphs obtained on the baseline TiO <sub>2</sub> electrode. (b) DNA detection assay on TiO <sub>2</sub> /Au electrode. (i) Schematic demonstration of the assay design. (ii) Percentage change of PEC current for showing signal-off response for UV and signal-on response for visible light excitation. (iii) Representative PEC graphs obtained on the TiO <sub>2</sub> /Au electrodes. Photocurrent measurements were performed at a bias voltage of 0 V vs. Ag/AgCl and 0.1 M PBS with 0.1 M ascorbic acid was used as the supporting electrolyte. Error bars represent one standard deviation from the mean for the PEC measurements performed with at least three separate devices. ....	53
Figure S4.1: TEM image of Au nanoparticles .....	54
Figure S4.2: X-ray diffraction analysis of the photoelectrodes. A and R refer to the anatase and rutile phases, respectively. TiO <sub>2</sub> /Au (40 min) samples were used as an example of hybrid samples. ....	55
Figure S4.3: Nyquist plots for the photoelectrodes at open circuit voltage. The charge transfer resistance (R <sub>ct</sub> ) decreases as the amount of Au NP increases in the electrode. ....	55

Figure 5.1 Differential photoelectrochemical biosensor. (a) Channels are created by depositing 15-mer or 20-mer probe DNA nano-spacers on photoactive TiO<sub>2</sub> substrates. Au NP-labelled 25-mer targets are hybridized onto the two channels. (b) SEM image of the electrode before (i) and after (ii) DNA hybridization with Au NP-labelled DNA target. The insets show the magnified image of the substrate acquired using the backscatter detector, with the red arrow pointing to Au NPs (scale bar in the inset represents 100 nm)..... 63

Figure 5.2 Photoelectrochemical characterization of the two sensing channels (a) IPCE spectrum of the photoactive electrode after probe attachment and after hybridization with Au NP-labelled complementary DNA targets (inset shows the absorption spectrum of AuNPs and TiO<sub>2</sub> NPs and the spectral range of the light source). (b) Representative PEC curves of the photoelectrode obtained using chopped light chronoamperometry at 0 V bias versus Ag/AgCl, before modification, following modification with 15-mer or 20-mer probe, and after hybridization with a 25-mer complementary or non-complementary Au NP-labelled target. The photoelectrodes were illuminated at 395 nm for 20 seconds starting at 20s (light on) and ending at 40 s (light off) with 0.1 M ascorbic acid in 0.1 M phosphate buffered solution used as the supporting electrolyte. The inset schematically demonstrates photoelectrochemical readout. (c) Bar plots summarizing the percentage change in photocurrents following hybridization of 15-mer and 20-mer channels with Au NP-labelled complementary (C) and non-complementary (NC) targets. Error bars represent one standard deviation with experiments performed using at least three separate devices. .... 64

Figure 5.3 The physics of differential signaling in the 15-mer and 20-mer channels. (a) Schematic diagram of the molecular building blocks of the 15-mer and 20-mer channels by considering the dsDNA as a rod-like structure and ssDNA as a flexible string-like structure on a model planar surface. (b) Band diagram and Schottky contact formation at the TiO<sub>2</sub>-Au interface (left). Valence and conduction band energy level for TiO<sub>2</sub> and Fermi energy level for AuNP are drawn with respect to vacuum and NHE (right). Ascorbic acid oxidation potential is depicted here using a dotted red line. For photocharging process, electrons from TiO<sub>2</sub> will transfer to Au NP (i) and in hot electron transfer process, hot electron from Au NP will transfer to TiO<sub>2</sub> (ii) (c) Mott-Schottky (1/C<sup>2</sup> vs. voltage) plots for 15-mer and 20-mer channels, before and after hybridization with the Au NP-labelled 25-mer target..... 67

Figure 5.4: Differential biosensing enabled by DNA nano-spacers. (a) Illustration of the spatially-multiplexed differential biosensor design (top) and the corresponding PEC data for various concentrations of target 25-mer AuNP-labeled DNA on the 20-mer and 15-mer channels (b) Signal change obtained upon incubation with blank and target drops on the 15-mer and 20-mer-channels. The differential signal changes are calculated by adding the magnitude of signal changes obtained from the 15-mer and 20-mer channels. The inset shows the calibration curve for determining the limit-of-detection. Error bars represent one standard deviation, with experiments performed using at least three separate devices. .... 70

Figure S5.1 Biofunctionalization of photoelectrodes with 15-mer and 20-mer ssDNA probes by drop-depositing the target on the electrodes. Green and Red colors are used to emphasize the spatial difference among the target solutions. .... 71

Figure S5.2 Determining the bandgap of the TiO<sub>2</sub> NP films. The intersection of the slope and x-axis determines the bandgap..... 72

Figure S5.3 Irradiance spectrum of the excitation source used in obtaining the PEC measurements ..... 72

Figure S5.4 Difference of the IPCE values obtained before and after target hybridization for the (i) 15-mer and (ii) 20-mer probes..... 73

Figure S5.5: XPS analysis of the 15-mer and 20-mer channels. Both channels showed similar amount of Au..... 73

Figure S5.6: Schematic model depicting the DNA structure used in this work having two separate sections (ssDNA and dsDNA) with different persistence length..... 74

Figure S5.7 Photoelectrochemical comparison between TiO<sub>2</sub> and TiO<sub>2</sub> – Au NP samples. (a) IPCE spectrum of the photoactive electrodes (b) PEC curves of the photoelectrodes obtained using chopped light chronoamperometry. Both measurements were performed at 0 V bias versus Ag/AgCl and the electrolyte used was 0.1 M ascorbic acid in 0.1 M phosphate buffer solution. .... 75

Figure S5.8 Phase diagram of 15-mer and 20-mer channel before and after hybridization obtained from electrochemical impedance spectroscopy (EIS)..... 75

Figure S5.9 Au NPs used in this work imaged using transmission electron microscopy (TEM) showing an average size of 12 nm. .... 76

Figure S5.10: Mott-Schottky plot for the hybridization of un-labelled 25-mer DNA targets on the 15-mer channel. .... 77

Figure S5.11 Schematics illustrating Photocharging process. Under light excitation, conduction band electrons move to Au NPs and improve electron-hole separation. E<sub>c</sub> and E<sub>v</sub> denotes the conduction band and valence band position, respectively. E<sub>F</sub> denotes the fermi-level position. Holes (h<sup>+</sup>) from TiO<sub>2</sub> oxidize ascorbic acid (AA) to produce photocurrent..... 78

Figure S5.12: Bar plot illustrating the percentage change in photocurrents following hybridization of the 20-mer probes with 34-mer Au NP-labelled complementary targets. The error bars represent standard deviation from at least three separate trials..... 79

Figure S5.13 Hybridization experiments with Au NP attached to the proximal end of 25-mer DNA and hybridized with 15-mer and 20-mer probes. (a) Schematic illustration of (i) 15-mer and (ii) 20-mer channels after hybridization with AuNP-labelled target. (b) Photocurrent enhancement for 15-mer and 20-mer channels. .... 80

Figure S5.14: Calibration curves for the (a) 15-mer and (b) 20-mer channels for various concentration of target DNA as tested in figure 4..... 81

Figure S5.15 Stability test of both 15-mer and 20-mer channels over 15 illumination cycles ..... 82

Figure 6.1 The operation of the differential PEC biosensor (a) Schematic illustration depicting the development of the PEC biosensor with the expected change in photocurrent profile depicted at each stage of sensing. A scanning electron micrograph (SEM) demonstrates the photoelectrode surface structure (bottom left). (i) Baseline photoelectrodes are created via solution deposition of TiO<sub>2</sub> NPs onto ITO substrates, yielding an anodic photocurrent upon 405 nm illumination (ii) Bio-functionalized photoelectrodes are created by depositing 15-mer DNA probes on photoactive TiO<sub>2</sub> substrates, yielding a decrease in photocurrent. (iii) 25-mer nucleotide targets are hybridized onto the transducer, resulting in a further decrease in photocurrent. (iv) Introducing SABs gives rise to an amplified photocurrent following hybridization. (b) A depiction of the combination of signals following target and SAB hybridization to yield the differential signal processing scheme used in this study..... 90

Figure 6.2 Photoelectrochemical signal generation on the differential DNA biosensor. (a) Schematics showing the mechanism for photocurrent generation (i) bare TiO<sub>2</sub> electrode (ii) after hybridization with complementary target (iii) after hybridization with SAB (b) Photocurrent measurement after each step of the biosensor operation with 1 pM target in buffer using a 405 nm LED as excitation source at 160 W/m<sup>2</sup>. All photocurrent measurements were performed at 0 V bias vs. Ag/AgCl. using 0.1 M ascorbic acid (AA) in 0.1 M PBS as electrolyte at each step of the biosensor construction. (c) Electrochemical impedance

spectroscopy measurements were performed in dark at open circuit potential vs. Ag/AgCl reference electrode using 2 mM  $[\text{Fe}(\text{CN})_6]^{3-/4-}$  in 0.1 M PBS and 0.1 M KCl as electrolyte. The equivalent circuit based on the shape of the Nyquist diagram is shown in the inset. Charge transfer resistance between the redox couple and the electrode is denoted by  $R_{ct}$ , which can be determined from the diameter of the semicircle.  $R_s$ ,  $Z_w$  and CPE denote the solution resistance, Warburg impedance and constant phase element, respectively. .... 92

Figure 6.3 Limit-of-detection and sensitivity of the differential assay. All photocurrent measurements were performed at 0 V versus Ag/AgCl in 0.1 M ascorbic acid in 0.1 M PBS as electrolyte, illuminated using a 405 nm LED excitation source at 160 W/m<sup>2</sup> (a, c) PEC graphs demonstrate signal responses following target and SAB binding in PBS and urine respectively. (b, d) Jitter plots (i) demonstrating the signal changes obtained from target and SAB binding in buffer and urine respectively, obtained from (a) and (c). Representation of the differential signal (ii) obtained from the data presented in (i). The linear region of the calibration curve of the PBS graph was fitted using the equation  $\Delta I \% = -49 \log_{10}C + 173$  (correlation coefficient of 97.97%) while the equation  $\Delta I \% = -25 \log_{10}C + 106$  (correlation coefficient of 99.84%) was used to fit the urine data. This graph is depicted using a semi-log format, with the x-axis representing the logarithmic concentration ( $\log_{10} M$ ) of the target analyte. .... 94

Figure 6.4 Specificity of the differential assay. (a) Change in PEC current following hybridization with 1 pM of matched, 1-base mismatched, 2-base mismatched, and NC targets and SAB binding measured in 0.1 M PBS with 0.1 M AA. b) Differential and signal-off responses for the target sequences in (a) with \* and \*\*\* representing  $p < 0.05$  and  $p < 0.001$ , respectively. .... 95

Figure S6.1 Chronocoulometric measurement of probe density. Blue dots represent the data obtained by running the scan with 10 mM Tris-buffer and orange dots represent the data obtained by running the scan with 100  $\mu\text{M}$  Hexaamineruthenium (III) chloride in 10 mM Tris-buffer. Corresponding solid lines indicate the linear fit that was used to obtain the y-axis intercept. .... 96

Figure S6.2 EIS measured at different fabrication steps of the differential PEC biosensor. The dots indicate the raw data points, whereas the solid line indicates the fit with the circuit model ..... 96

Figure S6.3 Cyclic voltammetry scan for TiO<sub>2</sub> electrodes before and after modification with ssDNA using 10 mM PBS as electrolyte and 50 mV/s scan rate ..... 97

Figure S6.4 Comparison of photocurrent change in detecting 1 pM DNA targets spiked in buffer (PBS) at 20-minute and 40-minute hybridization times. The error bars indicate one standard deviation from the mean and calculated from at least three measurements performed at 0 V versus Ag/AgCl in 0.1 M ascorbic acid in 0.1 M PBS as electrolyte, illuminated using a 405 nm LED excitation source at 160 W/m<sup>2</sup>. .... 98

Figure S6.5 The limit-of-detection of the signal-off-detection mode in (a) PBS and (b) urine. .... 98

Figure S6.6 Signal changes measured with 1 pM DNA target spiked into human plasma, urine, and buffer. The error bars indicate one standard deviation from the mean, calculated from at least three measurements ..... 99

Figure S6.7 Evaluation of the stability of the PEC biosensor. (a) Photocurrent measurement following the storage of probe modified electrodes for a period spanning 1-7 days. (b) Photocurrent measurement for 15 repeated cycles after probe modification. All photocurrent measurements were performed by applying 0 V vs. Ag/AgCl using 0.1 M ascorbic acid in 0.1 M PBS as electrolyte. .... 99

Figure 7.1 Aptamer selection and characterization. (a) Depiction of the aptamer selection process. The secondary structures of (b) full-length aptamer PEA1 and (c) truncated PEA1-3. (d) Binding curves and resultant affinity values ( $K_d$ , nM) extracted from the aptamers binding to the nucleocapsid protein of PEDv

(N-PEDv). Aptamer PEA1-3 was chosen for subsequent testing. (e) Selectivity tests demonstrating PEA1-3 binding of N-PEDv (target protein) in comparison with the control proteins bovine serum albumin (BSA), thrombin and ribonuclease (RNase). A concentration of 5 nM of each protein was used in this study (BA: bound aptamer; UA: unbound aptamer)..... 107

Figure 7.2 Schematic illustration of the operating principles and the components of the DEE-chem assay. (a) Sample-to-test workflow: liquid samples comprising of N-PEDv are introduced to the DEE-Chip using a dropper. (b) Signal changes: (Left) Prior to sample introduction, a methylene blue (MB) redox peak is exhibited by  $E_1$  while an absence of this peak is exhibited on  $E_2$ . (Right) Following N-PEDv introduction, target induced displacement of the redox barcode on  $E_1$  and subsequent capture on  $E_2$  yields a decrease in the MB peak on  $E_1$  while a signal increase is seen on  $E_2$ . (c) Molecular Operation: (Left) E-aptamers comprised of redox barcodes are immobilized on  $E_1$  while single-stranded DNA (ssDNA) capture probes are anchored on  $E_2$ . (Middle) In the presence of the target protein (N-PEDv), these redox barcodes are released from  $E_1$  and diffuse towards  $E_2$ . (Right) Following diffusion, the redox barcodes are subsequently captured on  $E_2$ , yielding a decrease in the redox peak on  $E_1$  and a signal increase on  $E_2$ . ..... 108

Figure 7.3 Dual electrode electrochemical assay for detecting PEDv nucleocapsid protein. (a) Raw square wave voltammetry (SWV) curves obtained from  $E_1$  and  $E_2$  following incubation with various concentrations of target protein spiked in buffer and incubated on the electrode for 45 min. (b) Calibration plots depicting the associated fold-changes in signals attained on  $E_1$  and  $E_2$  following incubation with target concentration of 10 nM ( $0.6 \mu\text{g mL}^{-1}$ ), 20 nM ( $1.2 \mu\text{g mL}^{-1}$ ), 100 nM ( $5.8 \mu\text{g mL}^{-1}$ ), 250 nM ( $14.5 \mu\text{g mL}^{-1}$ ) and 500 nM ( $29.0 \mu\text{g mL}^{-1}$ ) in buffer. (c) Raw square wave voltammetry (SWV) curves obtained from  $E_1$  and  $E_2$  following incubation with various concentrations of target protein spiked in 30% porcine saliva and incubated on the electrodes for 120 min. (d) Calibration plots depicting the associated fold-changes in signal attained on  $E_1$  and  $E_2$  for target concentrations of 10 nM ( $0.6 \mu\text{g mL}^{-1}$ ), 20 nM ( $1.2 \mu\text{g mL}^{-1}$ ), 100 nM ( $5.8 \mu\text{g mL}^{-1}$ ), 250 nM ( $14.5 \mu\text{g mL}^{-1}$ ) and 500 nM ( $29.0 \mu\text{g mL}^{-1}$ ) in porcine saliva. All electrochemical measurements were performed in a 25 mM phosphate buffer solution containing 25 mM NaCl (25/25 buffer) against a silver/ silver chloride (Ag/AgCl) reference electrode and a platinum (Pt) counter electrode in a potential range of 0 to -0.6 V and a scan rate of  $0.1 \text{ V sec}^{-1}$ . Error bars depict the standard deviation from the mean obtained using three ( $n=3$ ) separate devices per sample..... 109

Figure 7.4. Specificity testing of the DEE-Chip in 30% porcine saliva. (a) Square wave voltammograms representing the fold-changes obtained from a pair of  $E_1$  and  $E_2$  electrodes. Each pair was separately incubated with of 250 nM N-PEDv (target protein), bovine serum albumin (BSA), thrombin and ribonuclease (RNase) spiked in 30% porcine saliva. (b) Jitter-plots comparing the signal responses obtained from  $E_1$  and  $E_2$  in the presence of target (N-PEDv) and control (thrombin, BSA, RNase) proteins. All electrochemical measurements were performed in a 25 mM phosphate buffer solution containing 25 mM NaCl (25/25 buffer) against a silver/ silver chloride (Ag/AgCl) electrode and a platinum (Pt) counter electrode in a potential range of 0 to -0.6 V and a scan rate of  $0.1 \text{ V sec}^{-1}$ . Error bars depict the standard deviation from the mean obtained using three ( $n=3$ ) separate devices per sample..... 111

Figure 7.5 (a) A visual representation of the engineering changes made to the DEE-Chip for reducing assay time. The first case (i) demonstrates the original inter-electrode spacing ' $x=500 \mu\text{m}$ ' between  $E_1$  and  $E_2$ . Scenario (ii) depicts the reduction of this inter-electrode spacing to yield the new inter-electrode distance ' $y=300 \mu\text{m}$ '. Scenario (iii), on the other hand, portrays the use of inter-electrode spacing ' $y$ ' in conjunction with an applied positive potential bias (+0.5 V) across  $E_2$ . (b, c) Plots representing the release (top) and capture kinetics (bottom) observed in each of the three cases depicted in (a). Dotted lines in (c) indicate signal onset; extracted using tangents to the linear segments of the curves. For each group,  $n=3$  independent devices were tested per sample, each incubated with 500 nM of N-PEDv at a sample volume

of 10 $\mu\text{L}$ . The data are presented as mean $\pm$ standard deviation with visual guide-lines depicting the overall trend in each scenario.....	112
Figure 7.6 (a) Illustration of the diagnostic workflow from sample collection to sensor operation. Following sample dilution and heating, the collected porcine saliva sample is added to the DEE-Chip, incubated for 60 mins at room temperature and scanned using a lightweight benchtop potentiostat (Palmsens). Jitter-plots depicting fold-changes measured on (b) $E_1$ and (c) $E_2$ for six clinically-obtained positive (navy) and 6 negative (yellow) porcine saliva samples. Dotted lines indicate the cut-off threshold of the assay as extracted using the ‘Analyse-it’ toolkit in excel. The bars represent the mean of the fold-change extracted from square wave voltammograms on $E_1$ and $E_2$ for a given sample. The error bars represent the standard deviation from the mean obtained using three ( $n=3$ ) separate devices per sample. All square wave voltammograms were obtained using 25 mM phosphate buffer solution containing 25 mM NaCl (25/25 buffer) as the supporting electrolyte against a silver / silver chloride (Ag/AgCl) electrode and a platinum (Pt) counter electrode in a potential range of 0 to - 0.6 V and a scan rate of 0.1 V $\text{sec}^{-1}$ . In addition, $E_2$ electrodes were biased using a bias potential of + 0.5V to reduce the detection window to 60 min.....	114
Figure S7.1. Secondary structures and affinities ( $K_d$ ) of full-length aptamer PEA1 and truncated derivatives (PEA1-1 to PEA1-8).....	117
Figure S7.2 EMSA result of aptamer PEA1-3 binding with N-PEDv protein.....	118
Figure S7.3 Selectivity tests of PEA1-3 binding the target N-PEDv in comparison with Spike (S) and N protein of SARS-CoV-2. 10 nM proteins were used in the tests. ....	118
Figure S7.4 SEM micrographs of the two sensing electrodes (a) $E_1$ and (b) $E_2$ .....	118
Figure S7.5 DEE-chip Validation using three independent chips comprising of $E_1$ and $E_2$ electrodes. (a) (i) Cyclic voltammetry (CV) scans of bare gold electrodes in sulphuric acid post acid cleaning to assess reproducibility and surface area of each $E_1$ and $E_2$ pair on the three chips. (ii) Extracted reduction peak heights (Ah) and the associated electrochemical surface areas calculated using these peak heights for $E_1$ and $E_2$ . (b) CV graphs of $E_1$ and $E_2$ electrodes, before (bare) and after probe deposition and post surface blocking agent deposition (PEG-6000) extracted from three independent chips. Characteristic redox curve for Au in 0.5 M $\text{H}_2\text{SO}_4$ produced from reversible cycling from 0 – 1.6 V against Ag/AgCl at a scan rate of 0.1 V/s.....	119
Figure S7.6 RT-PCR testing results of the clinically acquired swine oral fluid samples. Here samples N1 – F6 pertain to samples labeled positive 1 – positive 6 (in the main manuscript) while samples 1 – 6 refer to samples labelled negative 1 – negative 6, respectively.....	119
Figure S7.7 False-negative sample study. Jitter plots obtained from (a) $E_1$ and (b) $E_2$ incubated with 500 nM N-PEDv spiked in clinically acquired sample ‘positive 4’ (Spiked), unspiked clinically acquired sample ‘positive 4’ (Unspiked) and an unspiked clinically acquired PEDv negative sample (Negative Control). The error bars represent the standard deviation from the mean obtained using three ( $n=3$ ) separate devices per sample. All square wave voltammograms were obtained using 25 mM phosphate buffer solution containing 25 mM NaCl (25/25 buffer) as the supporting electrolyte against a silver / silver chloride (Ag/AgCl) electrode and a platinum (Pt) counter electrode in a potential range of 0 to - 0.6 V and a scan rate of 0.1 V $\text{sec}^{-1}$ . In addition, $E_2$ electrodes were biased using a bias potential of + 0.5 V to reduce the detection window to 60 minutes.....	120
Figure S7.8 Receiver Operator Characteristics (ROC) curve for the clinical diagnosis of PEDv as obtained from the analysis of the signal fold-change on the release electrode (yellow) and the capture electrode (navy)	

for a set of 12 anonymized, clinically sourced swine oral fluid samples. TPF is true-positive fraction. FPF is false-positive fraction..... 120

## List of Tables

Table 2.1 Properties of various photoactive species used in PEC biosensing. RSD represents relative standard deviation, which signifies the reproducibility of the sensor.....	24
Table 2.2 Summary of the recent affinity-based PEC biosensors.....	37
Table S4.1: Charge-transfer resistance ( $R_{ct}$ ), charge carrier density ( $N_d$ ) and flat-band potential ( $V_{FB}$ ) of the electrodes used in this work.....	55
Table S5.1 Flat-band potential ( $V_{fb}$ ) and charge carrier density ( $N_D$ ) for the 15-mer and 20-mer channels .....	78
Table S5.2 Summary of the recent PEC DNA sensor utilizing plasmonic properties of metal NPs .....	81
Table S6.1 Values of the charge transfer resistance ( $R_{ct}$ ), constant phase element (CPE) and $n$ , indicating the constant phase ( $-90^\circ/n$ ) of the CPE for each step of the construction of the differential biosensor extracted from Figure S6.1. ....	97
Table S7.1 DNA oligonucleotides used in this study. ....	115
Table S7.2 DNA sequences in pool 10 ranked by their percentage. <sup>[a]</sup> .....	116

**List of Abbreviations**

Au	Gold
CE	Counter Electrode
CV	Cyclic Voltammetry
CHIT	Chitosan
DEE	Dual Electrode Electrochemical
DHB	Dihydroxy benzaldehyde
DNA	Deoxyribonucleic Acid
EC	Electrochemistry
EIS	Electrochemical Impedance Spectroscopy
HIV	Human Immunodeficiency Virus
IPCE	Incident Photon-to-Current Conversion Efficiency
ITO	Indium-Tin-Oxide
LOD	Limit-of-Detection
MB	Methylene blue
NP	Nanoparticle
PEC	Photoelectrochemical
PIRET	Plasmon-Induced Resonance Energy Transfer
POC	Point-of-Care
PS	Polystyrene
QD	Quantum Dot
RE	Reference Electrode
RNA	Ribonucleic Acid
SAB	Signal Amplification Barcode
SEM	Scanning Electron Microscopy
TAS	Transient Absorption Spectroscopy
TEM	Transmission Electron Microscopy
TiO <sub>2</sub>	Titanium Dioxide
UV	Ultraviolet
WE	Working Electrode
WHO	World Health Organization

## **Declaration of Academic Achievement**

This dissertation was written to fulfill the requirements of the doctoral degree in the department of Biomedical Engineering at McMaster University. The work described was undertaken in the period spanning May 2017 to January 2022.

The majority of experiments detailed in the following document were conducted, conceived, analyzed, and written by the author of this thesis, in consultation with the supervisor Dr. Leyla Soleymani, with the following exceptions:

*Chapter 2:* Dr. Sudip Saha and Dr. Richa Pandey contributed equally towards the writing of the manuscript.

*Chapter 3:* Dr. Amanda Clifford designed and synthesized the P25-TiO<sub>2</sub> NPs, performed FTIR and Raman spectroscopy, and contributed to the co-authorship of the manuscript.

*Chapter 4:* Dr. Saha aided with photoelectrochemical characterization. He also contributed equally to the authorship of the manuscript.

*Chapter 5:* All photocurrent measurements and sample preparation work were performed equally with Dr. Saha. He also contributed equally to the authorship of the manuscript.

*Chapter 6:* All photocurrent measurements and sample preparation work were performed equally with Dr. Saha. He also contributed equally to the authorship of the manuscript.

*Chapter 7:* Dr. Zhang designed and characterized the novel aptamer probe, Dr. Zijie Zhang conducted the gel studies while I designed and conducted all the electrochemical work and the pre-clinical study. This project was co-supervised by Dr. Yingfu Li, Dr. Todd Hoare and Dr. Leyla Soleymani. Dr. Zijie Zhang contributed equally to this authorship, he is the co-first author of this manuscript.

## Chapter 1: Introduction

### *Preface*

This chapter presents an introduction into point-of-care (POC) devices for disease diagnostics, their salient features and an assessment of the current challenges obstructing the development of marketable POC diagnostics. Subsequently, various transduction methods for POC biosensing, along with their advantages and limitations, will then be examined. This chapter will also briefly introduce the basics of photoelectrochemical (PEC) and electrochemical (EC) biosensing; and justify the choice of PEC and EC readout in POC diagnostics. Finally, this chapter will discuss the motivation, objectives and organization of this thesis.

### *1.1 Point-of-care Biosensors – Overview and Technical Challenges*

The United Nations estimates that the number of older persons, i.e., those aged 60 years or over, is expected to more than double by 2050 and to more than triple by 2100.<sup>1</sup> Despite this positive reality, as the prevalence of chronic health conditions increases with age, an increased burden on health care resources and cost of treatment is anticipated with this growth in ageing population. Currently, chronic disease accounts for 71% of all deaths globally; with cardiovascular diseases accounting for most of these deaths, followed by cancer, respiratory diseases and diabetes.<sup>2</sup> Interestingly, while chronic disease remains the leading causes of death in high-income countries, communicable diseases (including respiratory illness, diarrhoeal diseases, malaria, and human immunodeficiency virus/acquired immunodeficiency syndrome (HIV/AIDS)) account for most deaths in low-income countries.<sup>3</sup> Additionally, viral infections in animal populations combined with increasing frequency of close human-animal contact carry global public health risks of sporadic human zoonotic infections and the emergence of novel viral strains with pandemic probability. In the last decade alone, we have witnessed 5 world-wide epidemic diseases with potential animal origins - acute respiratory syndrome (SARS), swine flu, Ebola, Zika, Middle East respiratory syndrome (MERS) and coronavirus disease 2019 (COVID-19).<sup>4</sup> In fact, animals are thought to be the source of more than 70% of all emerging infectious diseases.<sup>5</sup> In addition to chronic illnesses, such communicable infections, pose a significant burden to global economy and public health.

With the increase in aging populations, higher prevalence of chronic and infectious diseases, and push for patient self-advocacy; the demand for accessible, high-quality and efficient healthcare is rising. Early disease detection and diagnosis translates into informed interventions that can have lasting value, making it paramount to improving the quality of life and patient survival outcomes. This is particularly true for diseases such as cancer where early diagnosis, followed by timely therapy, is paramount to secondary cancer prevention and improved survival rates.<sup>6</sup> For instance, for all stages combined, the current five-year survival rate of lung cancer (19.0 %)—the leading cause of cancer deaths—is lower than many other common cancer sites such as prostate (98%), skin (92%), and breast (90%).<sup>7</sup> In contrast to late-stage detection (stage IV; three-year survival ~ 5%), this rate rises to 71% for lung cancer cases detected in stage I.<sup>8</sup>

In addition to early diagnosis, timely monitoring of disease progression in combination with medical intervention is the cornerstone to halting or slowing disease progression; ensuring the efficacy of the treatment plan; and sustaining quality of life in diseases such as chronic kidney disease (CKD)<sup>9,10</sup>, rheumatoid arthritis<sup>11,12</sup> and AIDs/HIV<sup>13</sup>. In many high-income countries, patients that progress from CKD to early-stage renal disease (ESRD) represent <0.1% of the total population but account for 1% - 2% of medical-care related spending.<sup>14</sup> In addition to improved clinical outcomes, there is thus a clear-cut economic rationale for inhibiting disease progression.

In general, conventional medical diagnosis and disease monitoring—primarily based on immunology, culture and microscopy, and biochemical screens such as polymerase chain reaction (PCR)— involves patient sample collection and analysis in centralized laboratories.<sup>15</sup> While laboratory-based diagnosis is an essential element of the health-care system, it is often invasive; time consuming (turnaround times

> 24 hours); requires sophisticated infrastructure, equipment, uninterrupted electrical power, expensive reagents (PCR reagents and consumable cost ~ \$12-\$14/specimen), and highly trained personnel (PCR requires ~1-2h of hands-on technician time).<sup>16,17</sup> Furthermore, most low-income, and middle-income countries have under-resourced and fragile health-care systems, in need of structural and policy reform; making laboratory-based diagnosis unamenable to surges in public demand and unreliable for time-sensitive decision making.<sup>18</sup> Unsurprisingly, in many low-income countries, some of the most treatable diseases—such as measles, malaria, polio—and conditions remain health burdens owing to a lack of appropriate diagnostics. Consequently, there is an escalating need for accessible, affordable and advanced point-of-care (POC) diagnostic devices capable of transforming the delivery of care and improving the quality of life, by enhancing the efficiency of preventative diagnosis and facilitating rapid “on-site” detection. Development of ultrasensitive biosensors for monitoring biologically relevant analytes is the key to achieving such POC diagnostics and health monitoring technology.

Biosensors—which combine the sensitivity and specificity of living systems with the processing power of microelectronics—are analytical devices capable of detecting the presence of target biological analytes (i.e., biomolecules, organisms, metabolites, or biostructures) and converting this detection event into a measurable signal using analyte specific sensing elements and transducers.<sup>19</sup> Technological advances in miniaturization, synthetic biology and microfabrication have spurred the translation of such biosensors from specialised laboratories to portable formats closer to the patient at the point-of-care. By providing information at the time and location of care, POC biosensors expedite the sample-to-result time of infectious disease testing (from days to minutes); facilitate early-stage diagnosis; enable early therapeutic intervention and monitoring; allow the containment of disease outbreaks; permit the realization of personalized and precision-based medicine; and empower remote and resource-poor communities through accessible and high-quality disease management capabilities.<sup>15,17,20–22</sup>

Owing to its revolutionary nature, the global biosensors market—valued at USD 22.4 billion in 2020—is expected to expand at a compound annual growth rate (CAGR) of 7.9% from 2021 to 2028.<sup>23</sup> Despite growing investments in the biosensor industry, there are only a limited number of devices with POC capability currently available. The available devices are primarily centered around lateral-flow, immunochromatographic tests for pregnancy, cancer, viral pathogens; wearable EC-systems for continuous glucose, blood gas and metabolite monitoring. This raises the question – what factors currently hinder the successful development and adoption of similar classes of devices beyond the laboratory?

As per the WHO guidelines, an ideal POC biosensor should be affordable, sensitive, specific, user friendly, rapid and robust, equipment free and deliverable to end users.<sup>24–26</sup> Despite the many advantages offered by POC diagnostics, the challenging nature of developing devices embodying all 8 of these hallmarks has limited the number of new devices that enter the consumer market. POC biosensors and the specialized reagents incorporated within these devices are often manufactured as single-use, raising baseline costs.<sup>27</sup> Furthermore, these specialized reagents are often amenable to worldwide shortages, resulting in high-costs, bottlenecks during mass production and limited end-user accessibility during high-demand periods.<sup>28,29</sup> In addition, reagent (both chemical and biological) reliability is a prime factor contributing to the successful implementation of disease diagnostics as functional degradation of products during transport can render them useless while failure during performance in the field can be catastrophic. To minimize environmental effects (i.e., humidity, light and temperature), POC test strips are often transported and stored in sealed foil pouches or desiccant filled amber bottles to ensure stability; thus, driving up auxiliary costs associated with POC diagnostics.<sup>27,30</sup>

Widespread adoption resulting in enhanced consumer demand is pivotal to driving market investment and development of new POC devices. However, new disease diagnostics need to improve clinical decision making to be broadly adopted. While the clinical benefits and logistic need for faster test results than that achievable in the central laboratory is the driving force behind moving any diagnostic technique closer to the patient, rapid POC testing may not mirror the sensitivity offered by gold standard testing in central laboratories. The widely accepted standard threshold for a reliable diagnostic test is a sensitivity  $\geq 80\%$  and specificity  $\geq 90\%$ .<sup>31</sup> Rapid POC diagnostic tests—such as antigen tests for

influenzas, SARS-COV-2, and rotavirus—have notably poor sensitivities, cannot be used for negative-test based elimination and may require confirmatory or supplementary testing with more complex laboratory techniques.<sup>32–34</sup>

An analytical sensitivity of 30% to 40% lower than reverse transcription PCR (RT-PCR; current gold-standard) was noted in a study conducted by Dinnes et al. based on symptomatic and asymptomatic subjects.<sup>35</sup> While their current performance metrics bar their replacement of the gold-standard (biochemical screening and microscopy), on first patient contact, a positive rapid antigen test result helps inform decisions on immediate isolation measures by the identifying individuals with large viral shedding loads; making them indispensable during outbreaks and pandemics in population-dense settings (i.e., residences, places of business and emergency departments) where containment of viral transmission is critical.<sup>36,37</sup> Subtyping of disease strains—such as those pertaining to influenzas—is a public health surveillance measure that is often not commonly available with commercial rapid testing.<sup>34</sup> While subtyping does not affect clinical decision making under normal circumstances; resistance, increased virulence and increased mortality of certain strains may influence therapeutic intervention.

Ultrasensitivity or the ability to detect trace analytes of interest in native biological matrices is yet another requirement of an ideal POC diagnostic device. Clinically relevant levels of cellular and biomolecular analytes are highly dependent on the type of application being pursued. For instance, while detection limits in the sub-picomolar to 100 atto-molar are necessary to screen numerous cancers, neurological disorders, and early-stage infections such as HIV, a nanomolar level of qualification is sufficient for the clinically identifying the presence of TB.<sup>38</sup> For some disease diagnosis samples, while analyte concentrations are expressed at reasonable levels (femtomolar to picomolar levels), biomolecular targets may be outnumbered (by 10<sup>6</sup>-fold) by background species in the native matrix; making ultrasensitive detection, for early disease diagnosis in unprocessed/unenriched clinical specimens, elusive.<sup>38,39</sup>

Quality assurance in the context of sample preparation, test utilization, and POC test performance is yet another challenge faced by institutions seeking to implement these devices for autonomous testing or disease management.<sup>40</sup> A study by Aslan et. al revealed greater imprecision—larger errors and coefficients of variation—stemming from human-error in point-of-care glucose measurement as compared to laboratory glucose analysis despite the use of wider (and far more forgiving) performance limits in the POC assessment of glucose.<sup>41</sup> In addition, most POC devices feature small sample volumes (< 1 mL) to mitigate device complexity and minimize costs.<sup>42</sup> Such sample sizes can often magnify errors in bio-analysis, with minute variations (few microliters) yielding significant discrepancies in the number of target analytes present in the sample specimen; thereby, resulting in inaccurate measurements, larger error margins and irreproducibility<sup>43</sup>. The implementation of automated sample processing (absorbent pads, microfluidics, and cartridges with self-contained reagents) and one-step sample-in-to-result-out formats can minimize human intervention and associated errors.

Commercial market challenges continue to hinder the development of new POC in-vitro diagnostics. While over 100 different POC tests are available in the U.S., not all are widely implemented, including tests for blood-protein based cancer diagnostics. Aside from availability, challenges surrounding acceptance and implementation resulting from lengthy compliance protocols, expensive trials, and rigorous waiver acquisition processes by regulatory agencies often disincentivize their widespread adoption.<sup>44,45</sup> For instance, POC devices often require CLIA (Clinical Laboratory Improvement Amendments) waivers for implementation and are perceived by developers to be a significant hurdle to sustainable business for POC infectious disease diagnostics.<sup>46</sup> In such instances, non-POC tests may offer a more lucrative strategy to diagnostics development, limiting investments into new POC disease biosensors. Furthermore, although CLIA waivers are accessible to doctors' offices and clinics, obtaining a certificate of compliance encompasses requirements that are not attainable for most clinics, further limiting their implementation.

To reiterate, issues related to (1) device and reagent unreliability, stemming from storage conditions and unstable signal outputs; (2) poor sensitivity, in unprocessed/unenriched clinical specimens and small detection volumes; (3) lack of selectivity, such as that required for subtyping; (4) cost and lack of scalability, of auxiliary equipment in non-qualitative formats; and (5) test quality assurance, due to human involvement (lack of automation) in sample collection and test handling as compared to centralized-laboratory testing are some of the main challenges impeding the widespread adoption of POC biosensors. As such, there is a clear need to architect tools for building POC biosensors, capable of addressing these shortfalls, to enable true translation and widespread adoption of such diagnostics.

## 1.2 Biosensor Architecture

Typically, biosensors are comprised of three principal components: (1) the bioreceptor, (2) the transducer, and (3) the signal processing system (Figure 1.1). Principally, bioreceptors such as antibodies, enzymes, nucleic acids and aptamers are used to recognize and interact with the target through analyte-specific reactions, adsorption, or physical/chemical interaction.<sup>47</sup> The transducer—a physicochemical component—then converts bioreceptor-analyte interactions into useful and measurable signals.<sup>48</sup> These transducers are often electronic, optical, piezoelectric, magnetic, EC, or PEC in nature. Irrespective of the transduction format, measured signals are subsequently amplified with respect to the concentration of analyte detected and displayed to the end user via a readout interface (computer, display screen, electronic application).

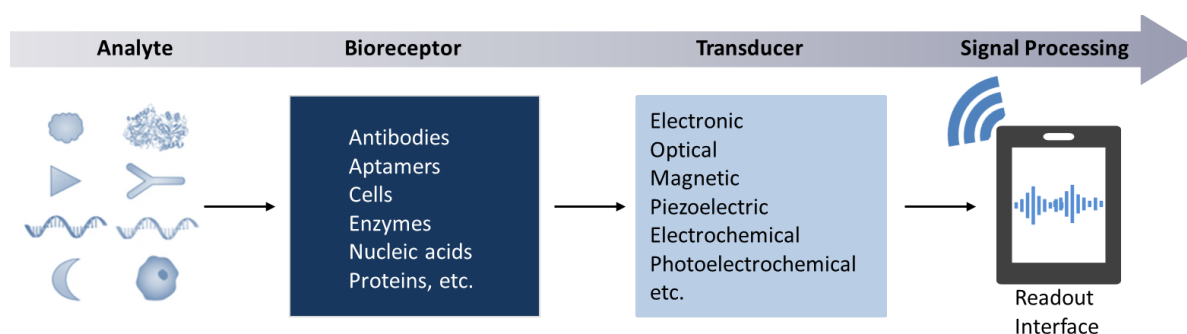


Figure 1.1 Components of a biosensor.

As the components of a biosensor are instrumental to its operation, it is critical to choose bioreceptors and transducers befitting the application. The choice of bioreceptor affects specificity and sensitivity<sup>49,50</sup> while the choice of transducer affects its complexity, portability, miniaturization, and influences signal-to-noise ratio.<sup>51–53</sup> Concurrently, both the bioreceptor and the transduction technique jointly influence the analytical performance of the biosensor.

### 1.2.1 Bioreceptors in Disease Diagnostics

The main purpose of a biorecognition element is to confer the biosensor with target specificity; thus, necessitating selective and potent affinity between the bioreceptor and target analyte. Each of the various classes of biorecognition elements—antibodies, enzymes, nucleic acids and aptamers—possess unique characteristics which advantageously influence or limit biosensor performance. An understanding of these factors is, thus, pivotal to the construction of high-performance disease diagnostics.

Enzymes are large complex macromolecules that serve as biological catalysts capable of capturing bio-analytes and converting them into measurable reaction products (i.e., protons, electrons, light, and heat) that can be integrated with a variety of transduction formats (i.e., optical, EC, thermal).<sup>54</sup> These biological elements utilize binding cavities buried within their 3D structure and resultant hydrogen-bonding, electrostatic interactions, and other noncovalent interactions to achieve analyte specificity.<sup>55</sup> Of all enzymatic biosensors, the EC glucometer is the most widely studied and commercialized. Biosensors relying on enzymatic detection present advantages such as high selectivity; excellent catalytic ability; demonstrated use in quantitative, continuous bio-analyte monitoring (e.g., glucose);

rapid response; broad analyte applicability, high-purity commercial availability and reusability.<sup>56,57</sup> As catalysts, enzymes remain unaltered during catalytic reactions; this preserves the detection (binding) site and its activity following analyte detection, making these recognition elements prime candidates for reusable biosensors.<sup>58</sup> Despite being widely studied; enzymes are limited by cost, immobilization based activity loss, quality control issues and environmental instability.<sup>47,57</sup> To elaborate, environmental susceptibility to pH or temperature variations makes industrial processing, production, and transport difficult<sup>59</sup>; with inappropriate storage and transport conditions yielding biosensor inconsistencies due to compromised enzyme activity<sup>47,60</sup>.

Antibodies are naturally occurring protein structures, typically ~150 kDa in size, that can be identified using biochemical pathways and purified for use in high-affinity applications.<sup>61</sup> These biorecognition moieties are most recognized for their widespread application in immunochromatographic test strips for POC disease detection and health applications (i.e., pathogen testing<sup>62–66</sup>, pregnancy<sup>50</sup>, cardiac biomarkers<sup>67</sup>, etc.). Antibody-based biosensors (or immunoassays) utilize high affinity and specific antibody-antigen interactions, at distal binding domains on their “Y” shaped structure, to identify the presence of target antigens.<sup>47</sup> As such, functionalization of antibodies onto transducing interfaces without altering their specificity kinetic activity remains a crucial step in the fabrication of successful immunosensors.<sup>68</sup> Advantages of antibody-based biosensors include demonstrated POC testing capability, inexpensive construction, rapid response time (<30 mins), wide range of analytical targets, reagentless sensing formats (immunochromatographic assays) and adequate specificity.<sup>15,56</sup> Despite their advantages, factors such as cost of antibody discovery and production (due to animal-based generation, stringent isolation protocol and expensive purification procedures); inability to distinguish between antigens originating from live and dead targets; inadequate sensitivity or qualitative nature of POC formats; difficulty in regeneration for continuous monitoring applications; and requirement for temperature-controlled storage limit their effectivity.<sup>47,56,69</sup>

Nucleic acids are polymeric macromolecules containing repeating monomeric ‘nucleotides’ comprised of a sugar (ribose or 2-deoxyribose), a nucleobase (adenine, thymine, guanine, cytosine or uracil), and phosphoric acid (Figure 1.2).<sup>70</sup> Diagnostics incorporating nucleic acids as the biorecognition element—or molecular diagnostics—rely on affinity-based interaction with target deoxyribonucleic acid (DNA) or ribonucleic acid (RNA) sequences to detect pathogens or assay mutations causing human genetic disorders, and chronic illnesses (i.e., cancer, heart disease, diabetes, etc.).<sup>71</sup> Here, oligonucleotide sequences (probes) capable of hybridizing with specific complementary regions of target DNA (or RNA), through hydrogen bonding between complementary base pairs, confer the system with a high degree of selectivity (Figure 1.2).<sup>72</sup> While nucleic acid biosensors demonstrate versatility in transduction formats, polymerase chain reaction (PCR) based on fluorometric analysis is regarded as the gold standard for the molecular detection and quantification of viral and bacterial pathogens.<sup>73,74</sup> Existing commercial nucleic acid tests involve three primary stages—nucleic acid extraction, amplification, and detection—simultaneously making them exceptionally sensitive (to trace quantities/copies of target sequences), remarkably selective (DNA primers only amplify predefined target sequences), but also more complicated, expensive and time consuming as compared to other POC diagnostics such as immunoassays.<sup>71,75</sup> Furthermore, nucleic acids when used as biorecognition elements pave the way for ultra-sensitive *direct* detection of viruses, bacteria, or fungi. While POC immunoassays are limited by their low limits of detection in the direct sensing of pathogens, substituting these biorecognition elements with nucleic acids capable of targeting RNA molecules present in high copy numbers (100-1000 copies/cell) in these pathogens offers a way to overcome this challenge without necessitating the use of amplification.<sup>71,76</sup> In miniaturization friendly formats such as EC readout, nonspecific electrostatic interactions hinder analyte access to biorecognition elements; thus, increasing background contributions, enhancing signal variation, decreasing analyte specific signals, and ultimately impacting the selectivity and sensitivity of detection.<sup>47,77</sup> In addition, high cost of nucleic acid synthesis; challenges in purification and quality control during production due to the tendency to form aggregates; and pH and temperature susceptibility further limit their widespread use in POC health and disease diagnostics.<sup>56</sup>

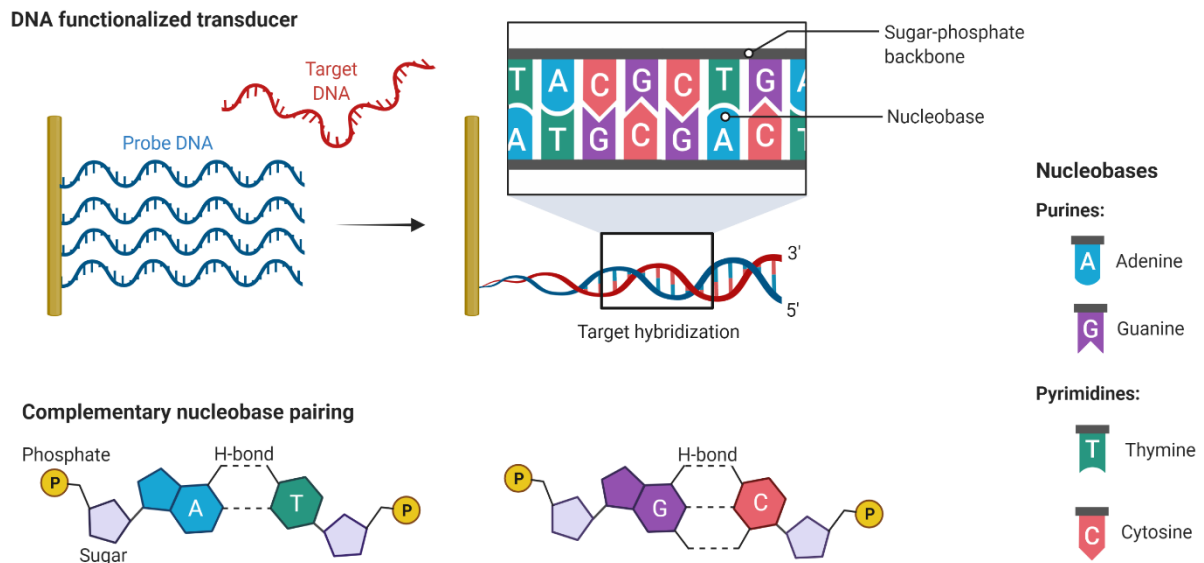


Figure 1.2 Illustration of target recognition in nucleic acid biosensors.

Aptamers are pseudo-natural biorecognition elements, capable of replace antibody function, that have been gaining popularity in the last decade. This class of single-stranded oligonucleotide based biorecognition elements, synthesized via *in vitro* selection methods for specific target binding,<sup>78</sup> offer several key advantages over antibodies for the development of rapid tests, such as small size (~1-2 nm as compared to ~10-15 nm in antibodies), high chemical and thermal stability, facile and precise modification, scalable production, and minimal batch-to-batch variation.<sup>61,79</sup>

The ability to perform bioreceptor functions in conditions far from the physiological norm, makes these moieties especially lucrative in POC diagnostics in low-resource settings; for applications utilizing non-physiological solvent ranges; and in devices boasting temperature aided enhancements to analytical performance (i.e., reduction in operation time, temperature aided kinetic enhancement, etc.) which may be disruptive to protein structures.<sup>56,80</sup> Furthermore, aptamers are capable of directly detecting targets present in complex clinical samples<sup>81,82</sup>, making these recognition elements increasingly popular for rapid diagnostic development. In addition, aptamers are capable of binding and detecting targets in the nanomolar to picomolar range, thereby matching or superseding the sensitivity of antibodies.<sup>80</sup> While lucrative, a notable disadvantage of this biorecognition element is the challenging nature of identifying and developing new aptamer sequences presenting useful binding affinities; thereby, limiting this moiety to a narrow range of available targets.<sup>83,84</sup>

### 1.2.2 Classification of Biosensors by Transduction Methods

To design high-performance disease diagnostics, it is pivotal to recognize the advantages and constraints of the five principal transduction methods used in biosensing – piezoelectric, magnetic, optical, EC and PEC.

#### 1.2.2.1 Piezoelectric Biosensors

Piezoelectric biosensors harness mass changes following bioreceptor-analyte interactions at the transducing surface to elicit measurable analytical signals (i.e., frequency change; transducer deflection).<sup>85,86</sup> Quartz crystal microbalances—thin circular quartz plates with metallic gold electrodes deposited on the opposite sides— have achieved recognition in medical applications due to their simplicity and label-free testing.<sup>86,87</sup> Mass response-type QCM piezoelectric sensors have been successfully employed for laboratory-based virus detection.<sup>85</sup> Advantages of this technique include rapid detection (< 30 minutes), real-time monitoring capability, label-free detection and extraordinary sensitivity with the ability to record sub-nanogram mass changes in high-molecular weight targets.<sup>85,88</sup> However, the remarkable sensitivity of this technique makes it extremely susceptible to environmental

conditions, thus necessitating isolation equipment to mitigate signal-to-noise loss mechanisms such as vibration<sup>89</sup>. Other limitations include (1) lower sensitivity to low-molecular weight analytes (e.g., DNA), (2) brittleness of the piezoelectric element, (3) temperature dependant baseline frequency variation and (4) instability of sensor frequency due uneven stress distribution on the edge of the piezoelectric sensor.<sup>88,90</sup> These limitations make it challenging to translate piezoelectric transduction to POC settings.

### **1.2.2.2 Magnetic Biosensors**

The detection of infectious disease agents using magnetic nanoparticles (MNPs) is a growing field. In general, magnetic biosensors exploit binding affinities between bioreceptor-functionalized (i.e., antibodies, DNA, enzymes etc.) MNPs and the target analyte to enable detection.<sup>91</sup> Magnetic biosensors rely on two different strategies for the detection of pathogens based on MNPs—magnetorelaxation and magnetoresistivity. In magnetorelaxation, MNP binding of target analyte alters the magnetic characteristics (spin relaxation time ( $T_2$ )) of the surrounding water protons through MNP aggregation; this in turn can be quantified by magnetic resonance spectroscopy.<sup>92</sup> Magnetoresistive biosensors, in contrast, employ magnetic nanotags—which disrupt existing magnetic fields and produce electrical signals—to bind captured analytes for quantitative detection.<sup>93</sup> Magnetic biosensors relying on magnetic nanotags are insensitive to matrix effects such as turbidity<sup>94</sup>, making this modality superior to optical transduction formats (i.e., light-based and colorimetric biosensors); are capable of real-time monitoring of the binding kinetics<sup>95</sup>; exhibit reasonable detection times (1-60 minutes)<sup>91</sup> and retain detection sensitivity in physiological matrices (i.e., picomolar to attomolar detection)<sup>91,96</sup>, due to the lack of inherent ferromagnetism in biological samples which in turn reduces background contributions and improves signal-to noise. While the assays can be relatively inexpensive to run (as low as \$3/assay; auxiliary equipment ~ \$4200), the instrumentation needed is not very portable, and are often expensive.<sup>91,97</sup>

### **1.2.2.3 Optical Biosensors**

Optical biosensors focus on the measurement of a change in the optical characteristics (absorption, reflectance, emission, or interferometric pattern) resulting from analyte-bioreceptor interactions at the transducer interface.<sup>98</sup> These biosensors frequently employ mechanisms such as chemiluminescence, absorbance, and fluorescence, surface-enhanced Raman scattering (SERS), plasmon resonance and dispersion spectrometry to measure detection.<sup>99</sup> Applications such as structural studies, fermentation monitoring, receptor-cell interactions, concentration, kinetic, and equilibrium analysis have been reported using this transduction format. Optical diagnostics reliant on colorimetric readout are the most abundant for over-the-counter POC analysis. These devices often incorporate lateral flow formats to measure the absorbance or reflectance using chemo-responsive dyes and change in color that is visible to eye during the interaction with the sensing analyte.<sup>100</sup> Advantages such as non-invasive analysis (saliva, nasal swab), integration with wearable formats, rapid response time (< 30 minutes)<sup>101</sup>, user-friendly format, affordability (<\$12; lateral flow format)<sup>102</sup>, and versatile analytical coverage (HIV<sup>62</sup>, pregnancy<sup>50</sup>, respiratory pathogens<sup>63</sup>, etc.) are expected to foster a growth in the optical biosensor sector by 8.6% from 2021 to 2028.<sup>23</sup> However, these devices are currently limited by (1) environmental effects (i.e., turbidity), in label-free optical detection (e.g., absorbance, fluorescence)<sup>103,104</sup>; (2) insufficient sensitivity and detection limit, with miniaturized and cost-effective formats (e.g., colorimetric lateral flow devices) utilizing qualitative reporting or lacking the sensitivity required to identify trace biochemicals<sup>105</sup> and (3) optical instability<sup>105</sup>, such as photobleaching in fluorescent systems.

### **1.2.2.4 Electrochemical Biosensors**

EC biosensors convert biochemical events—arising from redox reactions at the transducer interface—to electrical signals (voltage, current, impedance, and capacitance) proportional to the concentration of analyte present in a given sample.<sup>106</sup> These biosensors employ three basic transduction strategies for detection: (1) amperometry, (2) potentiometry, and (3) conductimetry.<sup>107</sup> Of these, amperometric and potentiometric techniques are most used in conjunction with EC biosensors. In 2020, EC devices accounted for 70.9% of the biosensor market revenue owing to widespread applications in biochemical and biological analysis and quantification.<sup>23</sup> Enzymatic amperometric glucometers featuring screen-

printed electrodes as test strips and pocket-size potentiostats are the most common commercially available devices and have been widely studied over the last few decades.<sup>108</sup>

Amperometric biosensors measure the current response resulting from the EC oxidation or reduction of electroactive species at a fixed potential.<sup>106</sup> In such systems, electrons are exchanged either directly or indirectly between a biological system and an electrode.<sup>108</sup> As the oxidation (or reduction) potential used for detection is characteristic to the analyte species, this EC technique benefits from enhanced selectivity.<sup>109</sup> Potentiometric biosensors, in contrast, utilize biofunctionalized transducers to convert biorecognition events into measurable potential changes via ion-selective electrodes (ISE) and membranes.<sup>110,111</sup> Conductometric techniques, on the other hand, measure changes in the current (conductivity) of a target analyte bearing solution, under a constant potential difference. As current is inversely related to the solution resistance (current = potential/resistance); biomolecules acting as electrical insulators yield a measurable change in the sampled current.<sup>112</sup> Battery-operated, handheld analyzers integrating a combination of amperometric, conductimetric and/or potentiometric biosensors on a single disposable cartridge, such as the iSTAT<sup>112</sup> (Abbott Point of Care) and epoc<sup>113</sup> (Siemens Healthineers) have demonstrated success in POC clinical analysis of multiple blood-gas electrolytes and metabolites.<sup>114</sup> EC POC monitoring of cardiac biomarkers (e.g., kinase isoenzyme (CK-MB), myoglobin (MYO), cardiac troponin I (cTnI), and plasma N-terminal pro-B-type natriuretic peptide (NT-proBNP)) is also possible using portable, handheld formats as demonstrated using the Cobas (Roche Diagnostics).<sup>115</sup>

EC transduction is quite lucrative for POC analysis. Unlike optical techniques reliant on optical path length (e.g., optical resonators<sup>116</sup>), electrochemistry is a surface technique. As such, it is not strongly reliant on the reaction volume, thereby enabling very small sample volume (<100 uL) bioanalysis.<sup>117</sup> Furthermore, electrodes used for measurement such as working electrodes (typically platinum, gold, or carbon) and reference electrodes (e.g., Ag/AgCl) are easily miniaturized; it is thus commonplace to have dimensions on the order of micrometers<sup>118</sup>, while nanoscale electrodes<sup>119-122</sup> have also been realized. Advancements in micro- and nano-scale fabrication processes have also enabled the miniaturization of auxiliary instrumentation (e.g. potentiostats), enabling individuals to perform in-field measurements using electroanalytical tools as small as a cellphone.<sup>123,124</sup> In addition, these biosensors are capable of ultrasensitive detection, with detection limits as low as sub attomoles reported in the literature for EC immunoassays.<sup>125,126</sup> In fact, EC genosensors based on long-range electron transfer are particularly interesting as they allow single base-mismatch detection at room temperature.<sup>74</sup> EC bioanalysis can also be carried out in colored or turbid samples—such as whole blood, an optically formidable matrix containing fat globules; red blood cells; hemoglobin; and bilirubin—thus, presenting yet another advantage over optical transduction techniques.<sup>109,117</sup> However, this technique is limited by its reliance on applied electric potential to drive reactions, background signals emanating from high applied potentials and matrix effects which compromise detection accuracy (i.e. false-positives).

#### ***1.2.2.5 Photoelectrochemical Biosensors - Exploiting Light for Better Diagnostics***

In PEC systems, electrochemically active species in solution engage in oxidation or reduction reactions at the electrode-electrolyte interface. to generate a measurable current readout upon illumination (Figure 1.3).<sup>127</sup> Generally, a PEC cell consists of an optical excitation source, an EC cell, and an EC reader. The EC cell alone consists of four main components (Figure 1.3): (i) a working electrode (WE) that is often constructed by immobilizing photoactive materials on a conductive substrate, (ii) a counter electrode (CE), (iii) a reference electrode (RE), and (iv) an appropriate electrolyte to generate PEC signals using redox reactions.

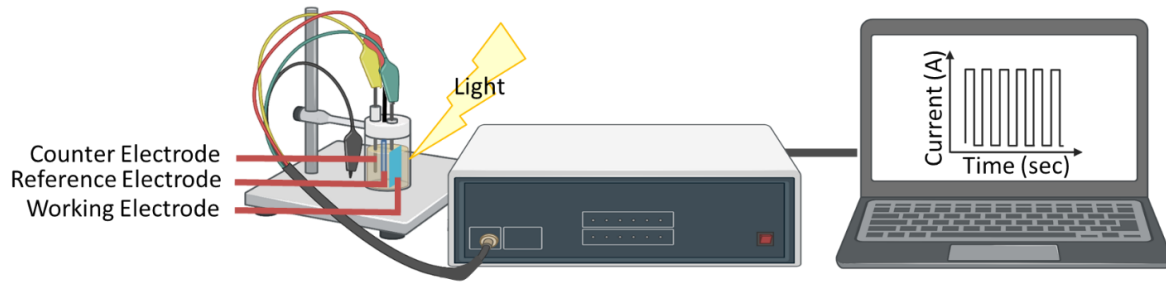
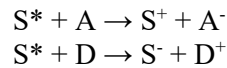


Figure 1.3 Illustration of a typical 3-electrode PEC cell setup for biosensing.

The working electrode is typically fabricated from photoactive materials such as inorganic, organic and hybrid semiconductors.<sup>127</sup> A semiconductor material is characterized by two energy bands, called the valence band (VB) and conduction band (CB), separated by a characteristic band-gap energy ( $E_g$ ). At absolute zero, the lower energy level (VB) is fully occupied while the higher energy (CB) is devoid of any charge carriers and the semiconductor is insulative. In such systems, electrons are excited from the VB to the empty CB upon absorption of photons with energies ( $h\nu$ ) higher than that of their respective band gaps ( $h\nu > E_g$ ).<sup>128</sup> This results in the generation of electron-hole ( $e^-/h^+$ ) pairs that can engage in chemical reactions with the redox couple (R/O) in the electrolyte, if recombination does not occur, where ‘R’ is the reduced species and ‘O’ represents the oxidized species. These photogenerated species, however, are highly prone to recombination. To circumvent this limitation, electron donating (D, hole scavenger) or electron-accepting (A, electron scavenger) species are often used to prevent the recombination of the photogenerated charge carriers prior to their engagement in the desired chemical reaction. The respective reactions of the excited state photoactive material, denoted as ‘S\*’, with the respective ‘D’ and ‘A’ species are as follows<sup>128</sup> :



Additionally, when the semiconductor is in contact with an electrolyte, a junction is formed at the semiconductor-electrolyte interface which determines the electron-hole separation kinetics based on the relative positions of the Fermi level in the semiconductor ( $E_F$ ) and in the electrolyte ( $E_{F, \text{redox}}$ ).<sup>129</sup>  $E_{F, \text{redox}}$  depends on the standard reduction potential ( $U^0$ ), measured against a standard hydrogen electrode (arbitrary zero) of the redox couple, and on the concentrations of O and R species in the electrolyte.<sup>129</sup> In the case of an n-type semiconductor, electrons are the majority carriers. When n-type semiconductors are immersed in an electrolyte containing redox species, where the  $E_{F, \text{redox}}$  lies below that of  $E_F$ , the oxidized species in the solution gain electrons until equilibrium is attained ( $E_F = E_{F, \text{redox}}$ ).<sup>128,129</sup> A depletion layer is subsequently formed, along with band bending due to this transfer of charges (Figure 1.4 a, b). This depletion layer gives rise to an electric field from the bulk of the semiconductor to the interface. Let us consider the case of an n-type semiconductor under light illumination, immersed in a redox electrolyte containing a donor species ‘D’ and in the presence of a metal counter electrode (typical EC cell setup). If  $E_{F, \text{redox}}$  is greater than the photogenerated hole ( $E_{\text{hole}}$ ), oxidation of ‘D’ occurs at the semiconductor surface, electrons are generated through this oxidation and are shuttled from the bulk of the semiconductor to the metal electrode via an external circuit and the associated reduction of oxidized species ‘O’ (present in the redox electrolyte) takes place (Figure 1.4 c).

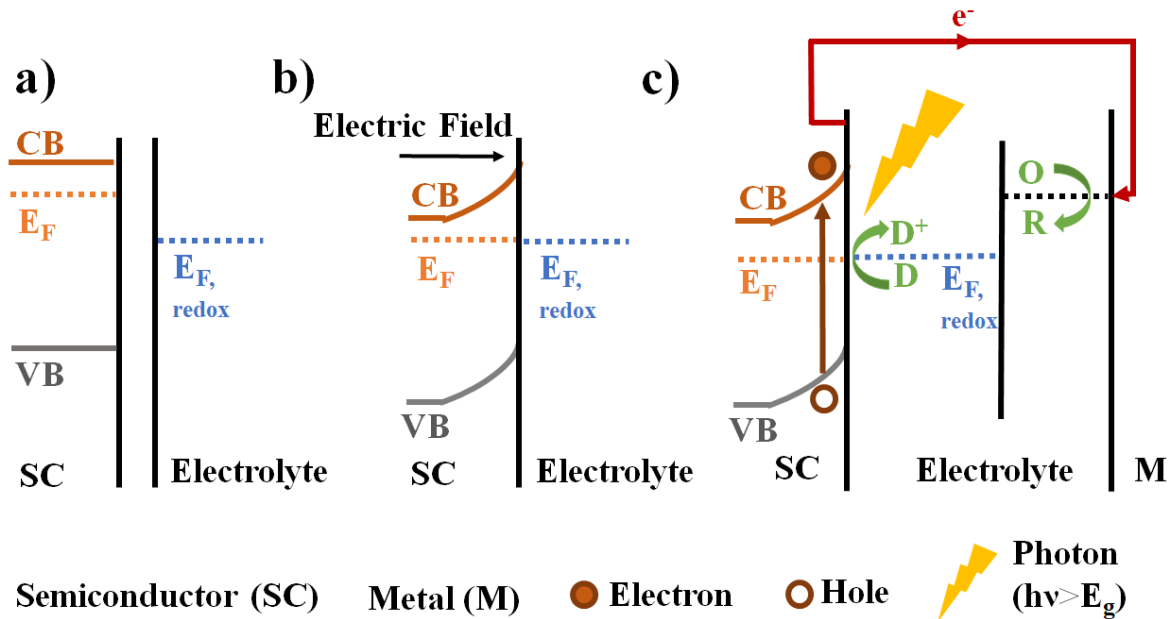
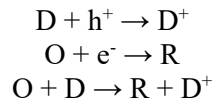


Figure 1.4 N-type semiconductor interface (a) before and (b) after immersion into the redox electrolyte in a PEC cell setup upon light illumination and in the presence of a counter metal electrode.

The equations representing these processes and the resultant overall reaction is as follows:



Subjecting the working electrode (semiconductor) to a potential bias further enhances such reactions, due to an added electric field effect following Fermi level equilibration; this retards the recombination of any photogenerated charges by enhancing the depletion layer.<sup>130</sup> In the case of an illuminated p-type semiconductor in an redox electrolyte with acceptor species ‘A’, a space charge region with an electric field pointing from the surface of the semiconductor to the bulk is generated, electrons move to the semiconductor surface thereby reducing species ‘A’ while oxidizing a reduced form of species ‘R’ at the metal counter electrode (Figure 1.5).

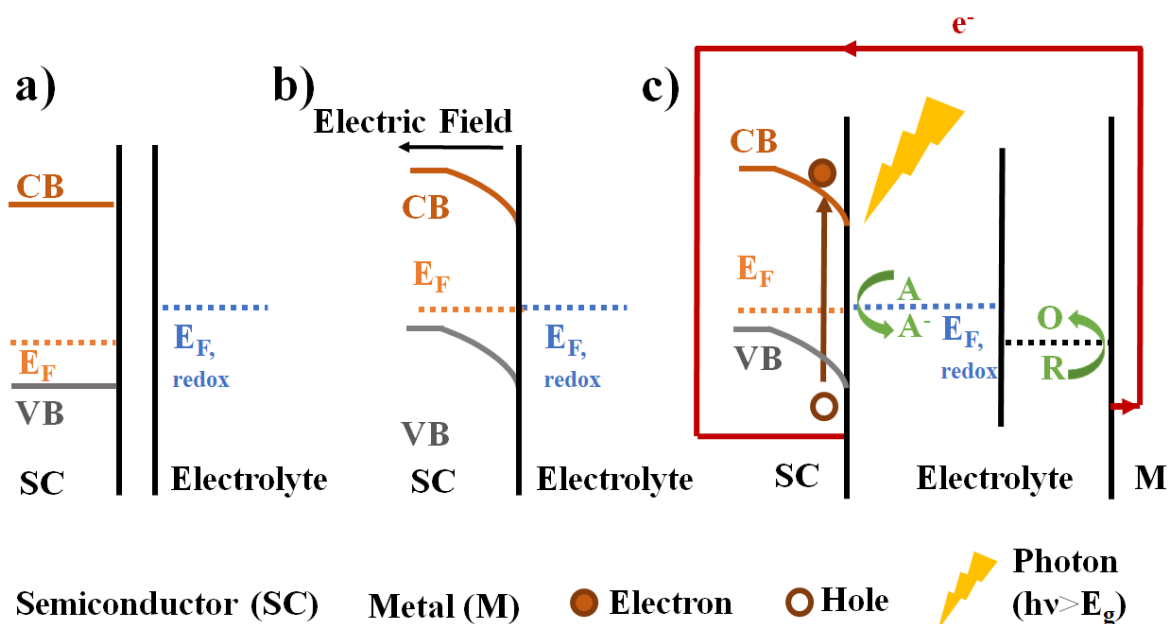


Figure 1.5 P-type semiconductor interface (a) before and (b) after immersion into redox electrolyte in a PEC cell setup upon illumination and in the presence of a counter metal electrode.

The direction of the photocurrent (anodic/cathodic) thus depends on the applied electric field and the position of the semiconductor Fermi level with respect to the EC potential, and by extension, the  $E_{F, \text{redox}}$  of the electrolyte (Figure 1.4 c, Figure 1.5 c). In general, the mobile charge carriers (electrons for n-type and holes for p-type semiconductors) in the semiconductor traverse the bulk of the electrode while minority carriers take part in the redox reactions at its surface.<sup>131</sup> Therefore, n-type semiconductors are generally used to produce anodic photocurrents and favour photoreductions while whereas p-type semiconductors are chosen for cathodic photocurrent generation and favour photooxidation.<sup>128,130</sup>

PEC bioanalysis represents a unique and dynamically developing methodology that offers an elegant route for sensitive biomolecular detection. Building on the principle of EC analysis, PEC biosensors harness the unique properties of optically active species to enhance analytical performance. The separation between the excitation source (light) and readout (EC current), offers this modality potentially higher sensitivity and high signal-to-noise ratio by reducing background contributions typically observed in conventional EC methods.<sup>132,133</sup> Benefitting from the ability to harness light to drive redox reactions at the transducing interface, PEC biosensors can operate with low to zero potential requirements, unlike their potential reliant EC counterparts; further minimizing inherent noise in such systems.<sup>134</sup> Furthermore, owing to the current based outputs evolved in PEC bioanalysis, they can be miniaturized and potentially integrated with handheld and portable analyzers, overcoming a key limitation of portable quantitative optical bioanalysis.<sup>135–137</sup> While no portable commercial PEC biosensor is currently available, these biosensors embody the virtues (sensitivity and specificity) of an ideal biosensing format by inheriting the advantages of optical and EC transducers and integrating advances in synthetic biology (i.e., high affinity functional nucleic acids). However, these devices are limited by long-term photocurrent stability, lifetime of photoactive species, sample turbidity and unstable light sources.<sup>134</sup>

While a brief overview of PEC sensing has been delineated in this section, a more detailed approach discussing materials, transduction methods used in PEC sensing and associated advantages and limitation will be elaborated on in chapter 2.

### 1.3 Motivation – Signalling Strategies to Enhance Analytical Performance in Biological Matrices

A noteworthy hurdle in quantitative POC diagnostics is that most of the biorecognition elements used lack inherent signaling capability upon target recognition, thereby necessitating the need for multistep

analysis or indirect quantification of bound analytes.<sup>138</sup> For instance, unmodified antibodies and nucleic acids, in their native forms, do not emit electrons or photons upon binding their target analytes (i.e., antigens and nucleic acids, respectively). To address this limitation, existing gold-standards for the quantitative analysis of proteins and nucleic acids—such as enzyme-linked immunosorbent assays (ELISAs), western blots, northern blots, and PCR—are multistep, reagent-intensive processes, typically reliant on labelling, and prohibitively complex; rendering them unsuitable outside laboratory settings (i.e., remote, low-resource settings and in-vivo applications).<sup>21,139</sup> Furthermore, optical readout centered around fluorophore/quencher interactions, is currently the most widely used method for transducing these biorecognition events into detectable signals.<sup>140,141</sup> However, the complexity of instrumentation and algorithms required by quantitative optical systems, resistance to miniaturization and susceptibility to matrix effects are barriers to POC implementation.<sup>103–105</sup>

As such, there is a growing interest in developing affinity-based disease diagnostics combining biorecognition with EC<sup>109,142</sup> and PEC<sup>127,143</sup> readout, owing to enhanced signal-to-noise ratio (SNR), ease of multiplexing, amenability to miniaturization, decreased complexity, and capacity for continuous and in-situ monitoring offered by these transducers.<sup>109,127,142,143</sup> These affinity-based biosensors rely on the use of label-free methods for direct quantification, or label-based methods for indirect detection of diagnostic targets.<sup>53</sup> Each of these strategies present unique advantages and limitations that require careful consideration in the rational design of functional, next generation molecular diagnostics.

Label-free methods reliant on direct binding mechanisms for transduction, such as signal-off DNA and immunoassays based on steric hinderance, are often susceptible to low analytical performance. The reason for this is two-fold – (1) as target detection is indicated by the decrease in a baseline signal (i.e., PEC/EC current), a magnitude of change beyond complete signal suppression is impossible thereby limiting detection sensitivity (nanomolar to picomolar range)<sup>127,144,145</sup>; and (2) non-specific adsorption by contaminants in biological matrices increase false-positive outcomes, thus compromising reliability and selectivity.<sup>138,143</sup> In such modalities, techniques to generate high baseline signals (hierarchical structuring, ligand modification, dye-sensitization of the photoactive or electroactive transducer) following transducer biofunctionalization are critical to their analytical success.<sup>146–148</sup> In contrast to signal-off readout, signal-on EC and PEC architectures dependant on direct (i.e., DNA intercalators<sup>149,150</sup>; and redox-<sup>151</sup>, quantum dot (QD)-<sup>152,153</sup>, dye-<sup>154</sup> or metal<sup>155–157</sup> labelled targets) or indirect labelling of bioanalytical targets (i.e., sandwich assays<sup>158,159</sup>) offer avenues to overcome barriers to analytical sensitivity.<sup>143,145,160,161</sup> However, steric limitation to kinetic binding in direct labeled detection and high background signals due to unbound labels hinder analytical performance. As mentioned earlier, high analytical sensitivity is critical to the deployment of bioassays in early-stage disease detection and progression monitoring. Many of these applications—including real-time pathogen detection—involve extremely small fractions of target analytes, with correspondingly few hybridization events, often outnumbered by matrix species.<sup>38</sup> Often, the detection of low abundance cancer biomarkers demands atto- to femtomolar quantification (sensitivity) in non-tumor environments such as blood, with recognition of disease-associated base-pair mutations (high selectivity),<sup>38,162</sup> to further inform early therapeutic intervention, serving as the ultimate aim in medical diagnostics.<sup>163,164</sup>

Dynamic biorecognition motifs such as aptamers, functional DNA structures and DNazymes present ways to address the shortfalls of traditional static recognition elements in diagnostic devices, given their compatibility with real-time monitoring; ability to target difficult-to-capture analytes such as small molecules; remarkable sensitivity; potential for reagentless transduction and facile conjugation with reporter probes.<sup>138,144,165,166</sup> Commonly used strategies for detection by these dynamic motifs range from unfolding/folding<sup>167</sup>, strand displacement/association<sup>168–170</sup>, degradation of DNA strands<sup>171</sup> and changes in secondary structure<sup>172</sup>.<sup>165</sup> While surface immobilized structure-switching constructs present the ability to realize reagent-less detection, they are limited by (1) background signals stemming from redox agents directly integrated onto switching entities,<sup>173,174</sup> emanating from thermodynamic imbalance in complex media<sup>175</sup> and/or the flexibility of the labelled single stranded DNA aptamer<sup>176–178</sup>; and (2) requirement for enzymatic amplification, in analyte sparse biological domains<sup>179</sup>. Techniques utilizing enzymatic elements for signal enrichment and transduction often require temperature stability, sample preparation to eliminate enzyme antagonistic agents, and the use of

enzyme-compatible reagents; inevitably resulting in compromises between analytical performance and assay complexity.<sup>180</sup>

Alternatively, aptamers relying on the displacement of a DNA barcode—labelled, single stranded oligonucleotide sequence—for signal transduction offer more precise thermodynamic control by tuning the length and complementarity of the displacement strand, while retaining assay simplicity.<sup>175,181–185</sup> Assays constructed using this format are pervasively signal-off modalities<sup>184,185</sup>, with the few reported instances of signal-on strand displacement assay suffering significant background noise<sup>183,186,187</sup>, making them error prone when bioanalyzing crude clinical samples with specimen variant backgrounds. There is, thus, an urgent need to develop elegant, simplified, signal-on strand displacement mediated strategies demonstrating low backgrounds for robust clinical detection in complex non-invasive biological media to enable the transition of disease diagnosis to the point-of-care.

While both PEC and EC biosensors hold great promise for sensitive bioanalysis, systems reliant on single-signalling mechanisms are highly affected by the variable backgrounds, variations in experimental conditions and false positives caused by biological matrices.<sup>58,188,189</sup> Recently, several instances of improved analytical performance in EC<sup>190–194</sup> and PEC<sup>195–197</sup> sensors incorporating dual-signalling, including both “signal-on” and “signal-off” modes that improve signal sensitivity, robustness, accuracy and reliability have begun to receive more attention.<sup>190–197</sup> For instance, Wu et al. developed an EC aptasensor for ATP detection based on a dual-signaling amplification strategy which enhanced the limit of detection (LOD; 1.9 nM) as compared to that using either methylene blue-modified probe (5.2 nM) or ferrocene-modified probe alone (4.8 nM).<sup>193</sup> Furthermore, building on prior work, Du et. al established that standard deviation between measurements obtained using different electrodes (via dual signalling) could be decreased by an order of magnitude less than that obtained using single signalling approach, thus demonstrating enhanced reproducibility, without sacrificing sensitivity or selectivity.<sup>194</sup> Despite the prevalence of EC readout strategies in dual-signal biosensing, redox based strategies are restricted in their environmental range as redox labels that can be used effectively in complex reductive or oxidative sample environments are extremely limited. In response, signal-combinatorial strategies harnessing the stability, ease of biofunctionalization, and versatility of noble metal/semiconductive labels and PEC readout are more amenable to ultrasensitive detection in a variety of complex environments.<sup>143</sup>

Embracing ratiometric signalling, Qui et al. demonstrated a spatially resolved technique to detect carcinoembryonic antigen (CEA)—an early cancer biomarker—in human serum, with a detection limit (LOD ~ 4.8 pg mL<sup>-1</sup> or 24 fM) exceeding that of commercial CEA ELISA kits (LOD ~ 50 pg mL<sup>-1</sup> or 250 fM) while exhibiting comparable accuracy.<sup>137</sup> A paper-based PEC assay devised by Yang et al. utilized dual-electrode ratiometric signalling to eliminate background fluctuations, displayed high sensitivity (LOD ~ 52 aM), persuasive selectivity (single-base-mismatch discrimination), and good feasibility for accurate microRNA-141 detection.<sup>197</sup> Furthermore, this combination of PEC sensing with a cheap paper-based POC friendly format performed comparably to commercial fluorescence qRT-PCR, in detecting microRNA-141 directly from human breast cancer cell lysates from. Despite the impressive analytical performance of dual-signal PEC biosensors, current differential/ratiometric PEC signaling designs typically rely on several photoactive reporters<sup>197,198</sup>, complex multi-species photoelectrode fabrication<sup>137,198</sup>, necessitate multiple bias voltage activation<sup>136,199–201</sup>, or simultaneously require different excitation wavelength regimes<sup>196,197</sup> for generating correlated or combinatorial signals. As high sensitivity and specificity, paralleled with facile operation and instrumentation is pivotal to the market adoption of dual-signalling PEC biodiagnostics; there is an urgent need for new approaches in ratiometric/differential signal transduction featuring a single photoactive species, operated at a single voltage using a single light source.

In theory, barcode-based biorecognition systems featuring the selectivity of functional-DNA motifs, the sensitivity of combinatorial signal transduction, and the miniaturization afforded by PEC and EC instrumentation; thus, hold the key to achieving the ultrasensitivity, reliability (minimizing false positive) and programmability necessary to advance molecular diagnostics towards the point-of-care.

Thus, the overarching goal of this dissertation is the development of ultrasensitive, dynamic, PEC and EC barcode-integrated biorecognition strategies, as tools for building translatable POC molecular diagnostics, capable of reliably detecting biomolecular targets in complex biological matrices by enhancing the analytical sensitivity, decreasing response time, and lowering background signals collected in such systems.

#### **1.4 Research Objectives**

To address the challenges presented in the ‘Motivation’ section of this dissertation and develop ultrasensitive, dynamic, PEC and EC barcode-integrated biorecognition strategies, tools for building translatable POC molecular diagnostics, capable of reliably detecting biomolecular targets in complex biological matrices, the following objectives are put forth:

1. Exploring surface-engineering strategies to develop robust, solution-processed, three-dimensional transducers for biosensing.  
In photoelectrochemical biosensing, the functionalization of photoactive transducers with biorecognition elements significantly reduces the baseline current and signal-to-background ratio of these devices. Additionally, the stability of photoactive electrodes created using photoactive nanomaterial assemblies is often insufficient to withstand the multiple washing and potential cycling steps that are involved in biosensing protocols. Here, we evaluate whether it is possible to engineer high performance photoelectrodes, (1) generated through facile synthesis amenable to mass-scaling; (2) capable of large baseline photocurrent generation, to counteract biofunctionalization induced signal loss; (3) demonstrating repeatable and stable photocurrents under cyclic operation; and (4) amenable to simple biofunctionalization with recognition elements.
2. Understanding the role of Au NPs in PEC transduction.  
The combination of plasmonic NPs such as gold (Au), silver (Ag) etc. with semiconductor nanostructures, in proximity of each other, allows researchers to tailor and engineer specific optical properties and observe new phenomena based on exciton–plasmon interactions (EPI).<sup>202</sup> However, the limitation of designing such structures lies in the fact that EPI have yet to be fully understood and mapped. For instance, Zhao et al. reported the attenuation photocurrent when a plasmonic NPs (Au) was placed in close proximity to a semiconductor NPs (CdS)<sup>203</sup> while Pu et al. reported the enhancement of photocurrent when a plasmonic NPs (Au) was shown to be in direct contact with a semiconductor nanowire (TiO<sub>2</sub>).<sup>204</sup> In order to effectively exploit the optical interaction of plasmonic and semiconductor NPs to enhance the analytical performance of engineered PEC transducers for ultrasensitive photoelectrochemical biosensing, it is of utmost importance to understand the mechanism of enhancement and attenuation of photocurrent and the conditions (type of semiconductor, material of plasmonic particle, separation distance, spectral overlap or lack thereof, etc.) that facilitate such processes. This objective, thus, probes – what reporter and associated signal generation mechanism offers us the highest magnitude of signal generation while enabling programmable signalling?
3. Investigating the role of light excitation regimes in metal-semiconductor systems (i.e., Au/TiO<sub>2</sub>) PEC transduction.  
While complexes resulting from the incorporation of Au NPs on TiO<sub>2</sub> surfaces have been extensively explored to enhance PEC activity, the current studies do not precisely investigate the impact of Au NP concentration on photocurrent enhancement for TiO<sub>2</sub>/Au NP systems under different excitation wavelengths that are linked to distinct interaction mechanisms. Here, we delved into understanding these mechanisms to effectively program and predict the PEC current response of TiO<sub>2</sub>/Au NP systems using different light excitation regimes.
4. Examining the influence of separation-distance in metal-semiconductor systems (i.e., Au/TiO<sub>2</sub>) PEC transduction.

We explore whether it is possible to use DNA capture probes as nanospacers to tap into the different nanoscale physical processes that occur between metallic NPs and semiconductors on different sensing channels of a single biosensor to predictively increase or decrease the PEC signal based on the separation between the metallic NP label and the semiconducting electrode.

5. Harnessing metal-semiconductor interactions to develop dual-signalling strategies for biomolecular detection.

While both PEC and EC biosensors hold great promise for sensitive bioanalysis, systems reliant on single-signalling mechanisms are highly affected by the variable backgrounds, variations in experimental conditions and false positives caused by biological matrices.<sup>58,188,189</sup> Biosensors incorporating dual-signalling, including both “signal-on” and “signal-off” modes offer avenues to improve signal sensitivity, robustness, accuracy and reliability.<sup>190–197</sup> Despite the impressive analytical performance of existing PEC dual-signal biosensors, these techniques typically rely on several photoactive reporters<sup>197,198</sup>, complex multi-species integrated systems for photoelectrode fabrication<sup>137,198</sup>, necessitate multiple bias voltage activation<sup>136,199–201</sup>, or simultaneously require different excitation wavelength regimes<sup>196,197</sup> for generating correlated or combinatorial signals. To make high performance PEC diagnostics amenable to POC operation, there is an urgent need to develop new streamlined dual-signalling approaches combining high sensitivity and specificity with facile operation and instrumentation. Here we explore the question – can we harness our understanding of light excitation regimes and separation distance in Au/TiO<sub>2</sub> systems to create ratiometric/differential signal strategies featuring a single photoactive species, operated at a single voltage and light excitation regime?

6. Engineering barcoded dual-signalling strategies for biomolecular diagnosis in complex biological matrices.

Direct labelling of bioanalytes in diagnostics is notoriously limiting due to high baseline signals prior to target capture, forced assay operation in diffusion limited regimes, unreliability (high incidences of false positives) and impracticality of direct bio-analyte labelling in real-world applications. As such, label-free strategies enabling reliable biomolecular detection in complex biological matrices—by enhancing analytical sensitivity; decreasing response time; and lowering background signals—are needed to realize the translation of quantitative EC and PEC systems to the point-of-care. In response to this, we investigate whether functional-DNA motifs, paralleled with the sensitivity and reliability of dual signal transduction, can be used to achieve ultrasensitive reagentless EC and streamlined PEC biorecognition in physiologically complex matrices (urine, saliva, plasma).

### ***1.5 Thesis Overview***

The remainder of this thesis is arranged as follows:

***Chapter 2*** – This chapter provides an in-depth review of PEC biosensors, with an emphasis on the various photoactive materials and transduction techniques used in PEC biosensing.

***Chapter 3*** – This chapter delineates a method to engineer high performance three-dimensional transducers for photoelectrochemical biosensing inspired by the remarkable adhesive properties of mussels. Surface modification of titanium dioxide (TiO<sub>2</sub>) with catechol-containing 3,4-dihydroxybenzaldehyde (DHB) and chitosan (CHIT) yielded photoelectrodes with high incident photon-to-electron conversion efficiency (IPCE) that are stable and robust upon repeated cyclic use in photoelectrochemical biosensing, thus achieving objective 1 as put forth in this thesis.

***Chapter 4*** – This chapter accounts the use of two different light excitation modes (UV and visible) to understand the effect of Au NP density, by varying surface loading of Au at TiO<sub>2</sub>, on PEC current generation. One wavelength mode (540nm) probed the localized surface plasmon resonance (LSPR) of Au NPs while the other (397nm) probed the interband excitation of Au NPs in conjunction with the bandgap excitation of TiO<sub>2</sub> NPs. In addition, the obtained bimodal

signal modulation was further demonstrated in the context of biosensing using Au NP-labeled DNA barcodes, optically excited at different wavelengths. The insight gained in this chapter, thus, contributes to objective 2 and 3 as outlined in this thesis report.

**Chapter 5** – This chapter demonstrates the use of DNA nano-spacers of varying lengths—integrated on a single multiplexed chip—to program signal modulation when exposed to same bioanalyte; thus, uncovering avenues for complex signal generation. Subsequently, a spatially-multiplexed PEC DNA detector was designed to achieve differential signaling (signal-on and signal-off readout) on a single device. This device yielded a limit-of-detection of 800 aM in buffer spiked samples, with a log linear dynamic range of three decades, which is significantly enhanced compared to previous semiconductive/plasmonic DNA biosensors using a single channel. Chapter 5 thus signifies the completion of objectives 2, 4 and 5 as put forth in this thesis report.

**Chapter 6** - While the previous work demonstrated single wavelength programmable DNA detection using labelled targets, this chapter describes the development of an innovative affinity-based, biobarcode differential PEC sensor to detect DNA based on a sequential partial hybridization strategy. This differential signal processing enhances the limit of detection and sensitivity of the assay by up to fifteen-and three-fold respectively, compared to the previously used PEC assays with single binding event, and boasts a limit of detection of 3 fM in buffer and 5 fM in urine. This chapter demonstrates the realization of objectives 5 and 6.

**Chapter 7** – While the previous chapter delineated a method of PEC detection of short DNA targets—without direct target labelling—and with potential applications in miRNA detection, this chapter details the development of a biobarcode EC diagnostic capable of reagentless, sensitive and specific detection of N-PEDv—a protein target with emerging global significance—in both buffer (LOD ~ 1.08  $\mu\text{g mL}^{-1}$ ) and urine (LOD ~ 1.09  $\mu\text{g mL}^{-1}$ ); thereby contributing to the completion of objective 6.

**Chapter 8** –This chapter summarizes the key finding of this research, contributions made to the field, and discusses potential future work.

## **Chapter 2: Overview of Photoactive species and PEC transduction**

### ***Preface***

This chapter presents an extensive literature review of affinity-based PEC sensor development. Here, three classes of photoactive materials used in PEC biosensing are reviewed, and their respective pros and cons carefully analyzed. Subsequently, different PEC transduction mechanisms pivotal to biosensor development are critically examined. By reviewing recent progress in this area, we explore the combination of strengths and deficiencies of these signal transduction systems and their respective building blocks. As a result, this review presents the author, and reader, with a complete understanding of the components of PEC biosensors, which is essential for the development of effective PEC diagnostic tools for POC translation.

### ***Authors***

Amanda Victorious, Sudip Saha, Richa Pandey, Tohid F. Didar and Leyla Soleymani (Authored in equal contribution with Sudip Saha and Richa Pandey)

In this paper, I was responsible for the paper structure and took the lead in organizing the paper's flow. In addition, I authored the following sections: Construction of a Photoelectrochemical Cell, Photoactive Species for PEC Biosensors (Inorganic semiconductors, Organic semiconductors, Hybrid semiconductors) and Challenges. In addition, alongside Dr. Saha and Dr. Pandey, I also jointly worked on the creation of all the tables used throughout the manuscript. I thank both Dr. Saha and Dr. Pandey for their expertise and collaboration during the authorship of this manuscript.

### ***Publication***

Frontiers in Chemistry, 7, 2019, 617

### ***Publication Date***

September 2019

## 2.1 Abstract

Detection and quantification of biologically-relevant analytes using handheld platforms are important for point-of-care diagnostics, real-time health monitoring, and treatment monitoring. Among the various signal transduction methods used in portable biosensors, photoelectrochemical (PEC) readout has emerged as a promising approach due to its low limit-of-detection and high sensitivity. For this readout method to be applicable to analyzing native samples, performance requirements beyond sensitivity such as specificity, stability, and ease of operation are critical. These performance requirements are governed by the properties of the photoactive materials and signal transduction mechanisms that are used in PEC biosensing. In this review, we categorize PEC biosensors into five areas based on their signal transduction strategy: a) introduction of photoactive species b) generation of electron/hole donors c) use of steric hinderance d) in situ induction of light, and e) resonance energy transfer. We discuss the combination of strengths and weaknesses that these signal transduction systems and their material building blocks offer by reviewing the recent progress in this area. Developing the appropriate PEC biosensor starts with defining the application case followed by choosing the materials and signal transduction strategies that meet the application-based specifications.

## 2.2 Introduction

Biosensors are devices that are used for analyzing biologically-relevant species using specific biorecognition elements and transducers<sup>205</sup>. Based on the nature of the biorecognition event, biosensors are classified into biocatalytic and affinity-based devices<sup>206</sup>. In biocatalytic biosensors, immobilized enzymes are used to recognize their specific substrate molecule, whereas affinity-based biosensors incorporate a synthetic or biological capture agent such as aptamers<sup>207</sup>, DNAzyme<sup>208</sup>, single stranded DNA<sup>209</sup>, or antibodies<sup>210</sup> to specifically capture the biologically-relevant target. The interaction between the analyte and the capture agent is translated into a readable signal by a transducer. To date, transduction methods relying on acoustic<sup>211</sup>, optical<sup>212</sup>, gravimetric<sup>213</sup>, electrochemical<sup>214</sup>, electronic<sup>215</sup>, and photoelectrochemical mechanisms<sup>206</sup> have been reported for use in biosensing systems. Researchers often choose a transduction method that offers the right level of sensitivity, specificity, speed, and multiplexing for the desired application, and meets requirements with respect to instrumentation cost, size, and ease-of-use.

Due to the growing demand for rapid clinical diagnosis and health monitoring using handheld systems, there has been an increasing push for the development of new bioanalytical techniques that combine high sensitivity, specificity, and speed with portable and inexpensive readout instrumentation. Photoelectrochemistry is an emerging signal transduction method that has the potential to meet the stringent requirements of the field of biosensing. In photoelectrochemical (PEC) bioanalysis, biological interactions between the analyte and the biorecognition element result in a change in the generated PEC current or voltage. In these systems, the photo-electrode or PEC label used in the biosensor is activated upon optical excitation. This optical excitation or biasing reduces the reliance of PEC systems on electrical biasing, which allows them to be operated under low or no applied electric potential. It has been shown that a lower limit-of-detection can be achieved using PEC signal readout compared to a similar assay that is coupled to electrochemical readout<sup>216,217</sup>. Although PEC biosensors rely on *both* optical and electrochemical mechanisms, they can be excited using low powered broad-spectrum light sources and read using inexpensive electrical circuits. As a result, it is possible to miniaturize PEC systems into inexpensive and integrated platforms that are similar in operation to handheld electrochemical readers<sup>217</sup>. Additionally, PEC biosensors can be easily multiplexed by incorporating multiple individually accessible electrodes on the same platform.

*Affinity-based* PEC biosensors combine the high specificity of biorecognition agents such as ssDNA, antibodies, and aptamers, with the sensitivity of PEC biosensors, and are the focus of this review article. There are previously-published review articles that are focused on a specific type of biorecognition-target interaction such as DNA sensing<sup>209</sup>, immunoassays<sup>210</sup>, enzymatic sensing<sup>208</sup>, and aptasensing<sup>207</sup>. However, our focus is on the elements that are important for building a PEC biosensor, regardless of the target analyte. Towards this goal we will discuss the construction of a photoelectrochemical cell,

photoactive materials used in creating these devices, and the signal transduction mechanisms that are employed in PEC signal generation (Figure 2.1).

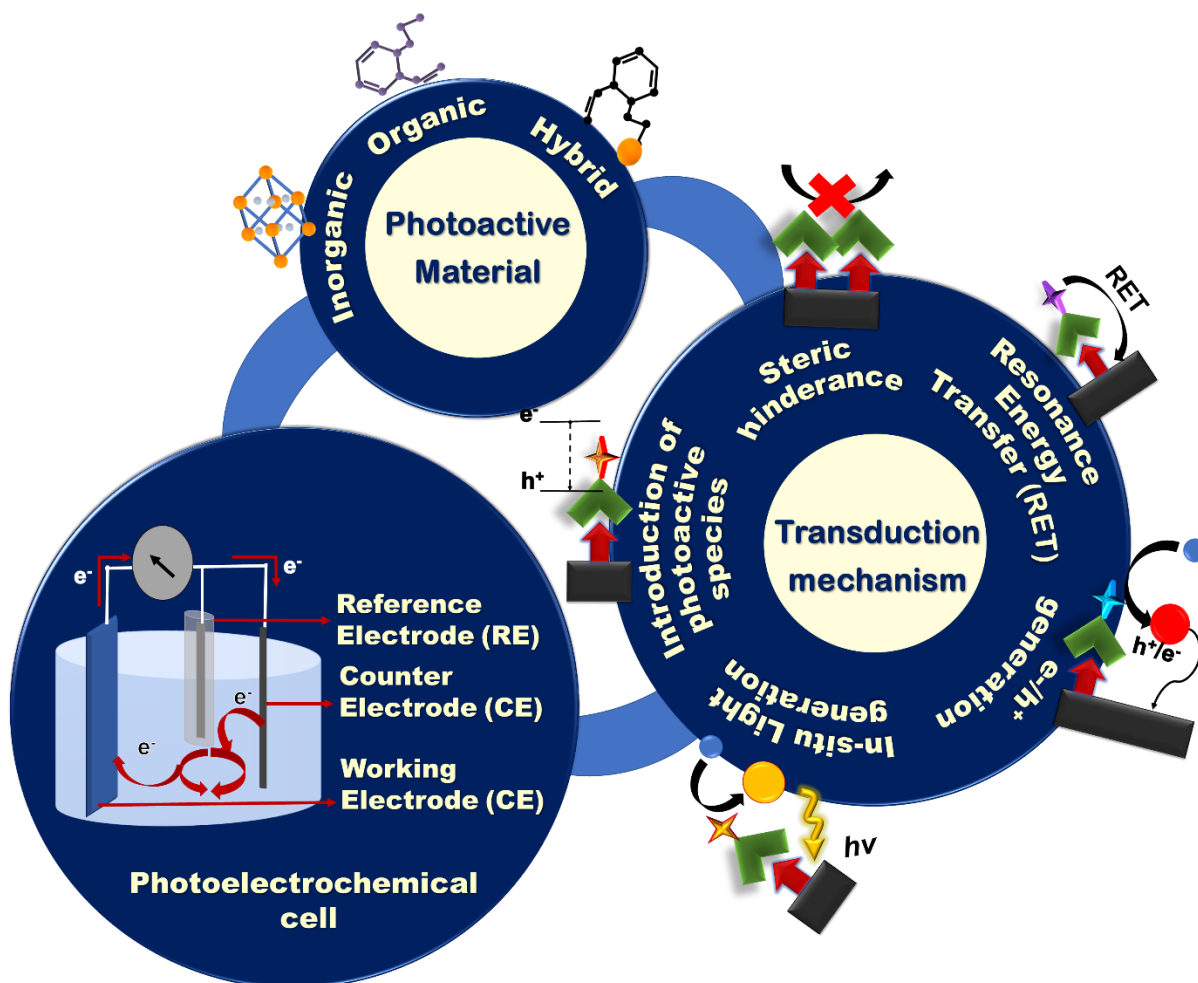


Figure 2.6 Schematic representation of the building blocks of a PEC biosensing system: the PEC cell, photoactive materials, and various signal transduction architectures.

### 2.3 Construction of a photoelectrochemical cell

Generally, a PEC cell consists of an optical excitation source, an electrochemical cell, and an electrochemical reader. The electrochemical cell consists of four main components (Figure 2.1): (i) a working electrode (WE) that is often constructed by immobilizing photoactive materials on a conductive substrate, (ii) a counter electrode (CE), (iii) a reference electrode, and (iv) an electrolyte to generate PEC signals using redox reactions. Upon illumination, the redox reactions driven by the electrochemically active species in the electrolyte generate an electric signal between the WE and the CE that is recorded by the electrochemical reader. To create an application-specific PEC biosensor, much attention has to be paid to the design of: (i) the sensing electrodes using photoactive species having the appropriate electronic and optical properties and/or conductive collectors; (ii) the transduction mechanism based on the target analyte and device application; and (iii) the electrolyte that contains the redox species that participate in the generation of the photoelectrochemical signal. The majority of the affinity-based PEC biosensing strategies reported to date rely on measuring photocurrents for signal readout<sup>210</sup>. To design a PEC bioassay, suitable for a specific application, it is

important to have a comprehensive knowledge of these components and the strategies that are used in incorporating them in a synergistic fashion.

#### **2.4 Photoactive species for PEC biosensors**

Photoactive species are materials that respond to optical excitation by generating excited electronic states and converting optical energy to chemical and electrical energy<sup>218</sup>. These species enable a PEC cell to generate or modify an electrochemical signal in response to light or electromagnetic radiation. In PEC biosensors, photoactive species are used as the building blocks of photoactive electrodes and/or as labels or reporters that associate with the biorecognition element<sup>219</sup>, target analyte<sup>220</sup>, or solution-borne surfaces such as magnetic beads and metallic nanoparticles (NPs)<sup>221</sup>. Due to its instrumental role in signal transduction, choosing the right photoactive material is critical to the development of PEC biosensors.

The photoactive materials used in PEC biosensing are chosen based on their electronic and optical parameters (incident photon-to-current conversion efficiency (IPCE), carrier mobility, response time, energy levels, and absorption spectrum), size/structure, stability against photobleaching, and ability to functionalize and integrate into devices. One of the most important parameters for evaluating photoactive materials used in PEC devices is IPCE. IPCE measures the photocurrent collected per incident photon flux as a function of illumination wavelength, which allows researchers to compare the efficiency of the photoactive species at different regions of the electromagnetic spectrum<sup>222</sup>. IPCE *collectively* evaluates the optical and electronic properties of materials such as their ability to absorb electromagnetic radiation and transport and collect charged carriers through the PEC cell. The electronic and optical properties of photoactive materials need to be selected such that the materials can supply charge carriers having sufficient energy (indicated by the band structure of the material) to drive the desired electrochemical reaction. It is also important for these electrochemical reactions to occur at high rates (measured using IPCE). The wavelength dependence of IPCE is important in understanding the type of optical excitation source that is required for designing a PEC biosensor<sup>223</sup>. Fine-tuning the size and shape of photoactive species in the nanoscale is also important for enhancing the PEC performance of the biosensor as structural tunability on the nanoscale changes the band structure of the materials, and can be used to enhance the surface-to-volume ratio of electrodes created from photo-active materials<sup>224</sup>. Resilience to photobleaching is important because photoactive materials that degrade due to multiple cycles of photoinduction do not allow the target-induced changes in the photocurrent to be reliably measured in a PEC biosensor<sup>225</sup>. Furthermore, for a photoactive material with the desired electronic, optical, and stability parameters to be used in a biosensing device, it is critical for it to have a chemical structure that can be easily functionalized with the typical termination chemistries of biorecognition elements (amine, thiol, carboxyl, aldehyde, to name a few). Finally, it is critical for these photoactive materials to have the sufficient level of mechanical robustness and adhesion to be integrated into miniaturized chips or strips used in biosensing platforms.

The three major classes of photoactive materials commonly used in PEC biosensors include (i) inorganic semiconductors, (ii) organic semiconductors and (iii) hybrid semiconductors<sup>226,227</sup>, which will be discussed in detail in this section.

##### **2.4.1 Inorganic Semiconductors**

Semiconductors from non-carbonous materials are known as inorganic semiconductors. Generally, in inorganic semiconductor transducers, electrons are excited from the valence band (VB) to the conduction band (CB) upon absorption of photons with energies higher than that of their band gaps. This results in the generation of electron-hole pairs that can engage in redox reactions at the surface of the working electrode. The direction of the photocurrent (anodic or cathodic) depends on the applied electric field and the position of the semiconductor Fermi level with respect to the electrochemical potential of the electrolyte (Figure 2.2). In general, the mobile charge carriers (electrons for n-type and holes for p-type semiconductors) in the semiconductor traverse the bulk of the electrode while minority carriers take part in the redox reactions at its surface<sup>228</sup>. Therefore, usually n-type semiconductors are

used to produce anodic photocurrents, whereas p-type semiconductors are chosen for cathodic photocurrent generation<sup>229</sup>.

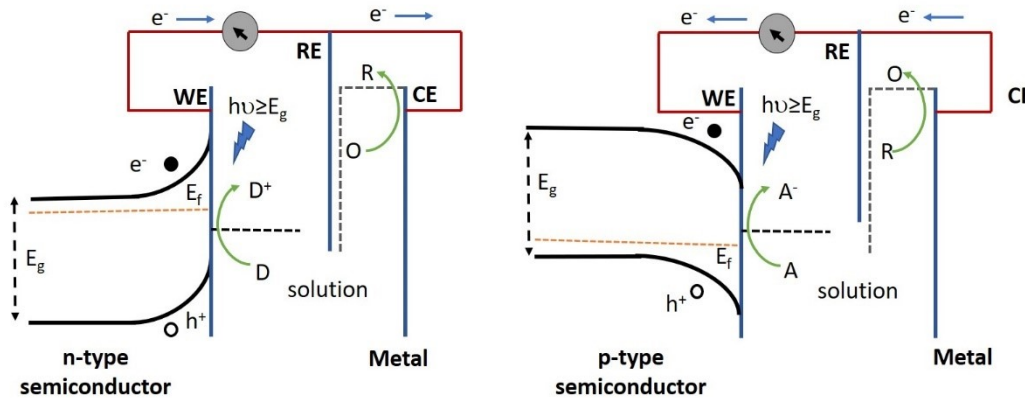


Figure 2.7 Operation of n-type semiconductor (left) and p-type semiconductor (right) in a PEC cell. Electron donors (D) in the redox couple are oxidized by the photoactive species, thereby resulting in the loss of an electron which is then relayed to the collector (underlying conductive substrate), thus yielding an anodic current. Alternatively, electron acceptors (A) in the redox couple gain an electron following their reduction upon light illumination, subsequently giving rise to a cathodic current.  $E_g$ ,  $E_f$ , WE, RE, CE represent band gap energy, fermi energy, working electrode, reference electrode and counter electrode respectively.

Inorganic semiconductors such as titanium dioxide ( $\text{TiO}_2$ )<sup>230</sup>, cadmium telluride ( $\text{CdTe}$ )<sup>231–233</sup>, cadmium sulphide ( $\text{CdS}$ )<sup>234–236</sup>, Molybdenum disulphide ( $\text{MoS}_2$ )<sup>237,238</sup>, cadmium selenide ( $\text{CdSe}$ )<sup>239,240</sup>, and zinc oxide ( $\text{ZnO}$ )<sup>241</sup> are used extensively in affinity-based PEC biosensors<sup>232,242–244</sup>. Inorganic semiconductors offer a few advantages over their organic counterparts as discussed in the following section. These materials typically exhibit longer stability under mechanical, electrical, and environmental stress<sup>245</sup>. High-performance inorganic semiconductors can be precisely fabricated into various structures at the nanoscale, matching the size of subcellular and molecular components and allowing better probing of biological targets<sup>246</sup>. Inorganic semiconductors usually require lower bias voltages (due to their higher charge mobility and charge-carrier separation efficiency)<sup>247</sup>, exhibit faster response time in the generation of charge carriers upon excitation, and allow for easier device passivation for use in physiological fluids as compared to organic SCs<sup>246</sup>.

Photochemical stability and high catalytic efficiency make  $\text{TiO}_2$  a promising material for affinity-based PEC biosensing<sup>248,249</sup>. While promising, pristine  $\text{TiO}_2$  suffers from a variety of problems such as poor response in the visible range owing to its wide band gap<sup>250</sup> and relatively fast recombination of photogenerated charge carriers<sup>251</sup>. In order to overcome these limitations, scientists are turning to hybrid  $\text{TiO}_2$  architectures that incorporate other materials such as metal cations and anions<sup>252</sup>, semiconductors of  $\text{M}_x\text{S}_y$ <sup>253</sup> and  $\text{M}_x\text{O}_y$ <sup>254</sup> configuration, and carbon-based materials<sup>255</sup>.  $\text{CdTe}$  is also widely used in PEC biosensing owing to its large bulk absorption coefficient ( $>10^4 \text{ cm}^{-1}$  in the red,  $\sim 10^5 \text{ cm}^{-1}$  in the blue)<sup>256</sup> and near-infrared band gap ( $E_g \approx 1.5 \text{ eV}$ )<sup>257</sup> making it suitable for operation in the visible region of the solar spectrum. One of the issues with  $\text{CdTe}$  is the low abundance of tellurium, which makes it economically inviable for biosensing<sup>258</sup>. Due to the availability of precursors and ease of crystallization<sup>259</sup>, there is a move towards other chalcogenides of  $\text{CdE}$  ( $E = \text{S}, \text{Se}$ ). These alternatives are mostly used as sensitizers due to their narrow band gaps ( $\text{CdS} = 2.4 \text{ eV}$ ,  $\text{CdSe} = 1.7 \text{ eV}$ )<sup>259</sup>. In addition, they offer higher conduction bands edges compared to most metal oxides ( $\text{ZnO}$ ,  $\text{TiO}_2$ ), making them useful for reactions where electrons need to be transferred from the conduction band of these materials<sup>259</sup>. However, their inability to integrate into device fabrication due to their poor adhesion onto the substrate and the inherent toxicity of Cd limit the possibility of using Cd-based materials in commercial biosensing platforms<sup>260</sup>.  $\text{ZnO}$  is another wide band gap (direct band gap of  $3.37 \text{ eV}$  in the near UV spectral region) semiconductor used in PEC biosensors, which offers biocompatibility, excellent photoactivity (large exciton binding energy at room temperature<sup>261</sup>, high charge carrier mobility, and thermal and chemical stability<sup>262</sup>.

ZnO can be structurally tuned and has been used in flower<sup>220</sup>, rod<sup>263</sup>, wire<sup>264</sup>, and pencil<sup>265</sup> architectures for biosensing applications. Nevertheless, the photocatalytic performance of ZnO diminishes in aqueous solutions due to the fast recombination of photogenerated charge carriers<sup>266</sup>. Apart from these materials, emerging inorganic semiconductors are being investigated for use in PEC biosensing. Specifically, MoS<sub>2</sub> is under investigation for use in PEC cells due to its ability to generate an internal electric field at the contact surface for photoinduced charge separation, which increases the carrier lifetime<sup>267</sup>. Additionally, Bi-X (X= S, V, O) materials are being investigated due to their tunable bandgap and photostability in acidic solutions<sup>267</sup>.

Inorganic semiconductors are widely used in developing PEC biosensors; however, a remaining challenge, as with other types of materials used in biosensors is related to non-specific adsorption causing interference to the signal by producing high noise levels or low reactivity<sup>268</sup>. Hydrophilic coating strategies have been employed for metal oxides and sulphides but most of these strategies have downsides under severe biological conditions or where long-term stability is needed. Furthermore, conditions such as high temperature, high salinity, and non-neutral pH, intensify these effects<sup>269,270</sup>. To overcome these challenges, researchers are focusing on integrating inorganic semiconductors into hybrid antifouling networks, which has been previously reviewed<sup>207</sup>.

### 2.4.2 Organic Semiconductors

Organic materials such as graphitic carbon nitride (g-C<sub>3</sub>N<sub>4</sub>), porphyrin, azo dyes, chlorophyll, bacteriorhodopsin, and polymers such as semiconducting polymer dots (Pdot), phthalocyanine, poly(thiophene), phenylenevinylene (PPV) and their derivatives have been used for constructing photoactive electrodes that can be applied to PEC biosensors<sup>271–273</sup>. Some of the main advantages offered by organic semiconductors lies in their improved mechanical compliance<sup>274</sup>, intrinsic stretchability<sup>274</sup>, and their amenability to low-temperature all-solution-based processing<sup>246,275</sup>. This allows inexpensive fabrication of large-area films on flat, irregular, and flexible substrates, which provides opportunities for the development of flexible and printed electronic based biosensors used in wearable technology<sup>276,277</sup>.

Graphitic carbon nitride (g-C<sub>3</sub>N<sub>4</sub>) is a metal-free two-dimensional polymeric semiconductor, which is attractive for PEC biosensing due to its high physicochemical stability and inexpensive and earth abundant nature<sup>278</sup>. It has a smaller band gap (~2.7 eV)<sup>279</sup> compared to commercial TiO<sub>2</sub> NPs (~3.0–3.2 eV) and is able to absorb light in the visible portion of the solar spectrum up to 460 nm<sup>280</sup>. G-C<sub>3</sub>N<sub>4</sub> has a desirable electronic band structure due to the presence of  $\pi$ -conjugated sp<sup>2</sup> hybridized carbon and nitrogen. It is also electron-rich and has basic surface functionalities due to the presence of Lewis and Brønsted basic functions<sup>281</sup>. This has enabled g-C<sub>3</sub>N<sub>4</sub> to be applied to the degradation of organic pollutants, hydrogen evolution reaction, biosensing, and energy conversion<sup>282–287</sup>. Da *et al.* constructed a novel “signal-off” PEC aptasensor using an aptamer bridged DNA network in conjunction with g-C<sub>3</sub>N<sub>4</sub> to detect vascular endothelial growth factor (VEGF165)<sup>272</sup>. This photo-electrode exhibited a stable photocurrent response with no severe decay under periodic off-on-off light excitation for nine cycles over a timeframe of 350 seconds. While g-C<sub>3</sub>N<sub>4</sub> is a promising material, its low quantum yield in its pristine form (0.1% at 420–460 nm)<sup>288</sup> remains an obstacle to its incorporation as a high-performance photoactive material for biosensing<sup>289,290</sup>. In order to enhance the efficiency of this material, the use of g-C<sub>3</sub>N<sub>4</sub> in conjunction with materials like TiO<sub>2</sub> and CdS has been reported for biosensing applications<sup>291–293</sup>. The formation of heterojunction with these materials helps to accelerate the charge transport and reduce the recombination rate by separating the charge carriers generated in g-C<sub>3</sub>N<sub>4</sub><sup>280</sup>.

Porphyrins, a group of macrocyclic organic compounds composed of four pyrrole rings joined via methine (=CH-) bonds are being investigated for use as photoactive materials or sensitizers in PEC systems<sup>294</sup> due to their wide availability in nature, high molar absorptivity and thermal stability<sup>295</sup>. One such example is the use of porphyrin derivative, iron(III) meso-tetrakis (N-methylpyridinium-4-yl) porphyrin (FeTMPyP), in a PEC DNA biosensor<sup>296</sup>. In this case, CdS quantum dots (QDs) modified with ssDNA formed the photo-active electrode. The porphyrin derivative specifically binds to dsDNA via groove interactions and reports the presence of dsDNA by catalyzing the oxidation of luminol to generate chemiluminescence. The photocurrent intensity of the biosensor did not show a detectable change after storage for 10 days, highlighting the stability of this biosensor. Porphyrin-based materials have been used

in conjunction with inorganic semiconductors such as  $\text{TiO}_2$ <sup>297</sup>,  $\text{ZnO}$ <sup>298</sup> and  $\text{CdTe}$ <sup>299</sup> to enhance the IPCE of these systems. A major difficulty in the wide spread use of porphyrin is that its chemical synthesis usually requires several steps with low overall yield, amounting to a high material cost<sup>300,301</sup>.

Pdots are a class of emerging photoactive nanomaterials that offer incredible photostability (photobleaching quantum yield of  $10^{-7}$  to  $10^{-10}$ ), tailorable electrical and optical properties, minimal toxicity, good biocompatibility and ease of processing<sup>273,302-304</sup>. Pdots and PPV derivatives have recently been used in PEC biosensors<sup>273,305</sup> due to their extraordinary light harvesting ability resulting from their large two-photon absorption cross sections<sup>306</sup>. However, their use in biosensing architectures are required to be thoroughly explored because of their pH dependence and tunability of photoelectrochemical properties according to their molecular weights<sup>307,308</sup>. Moreover, the photoelectrochemical properties of these materials are highly dependent on the electron transfer processes within the  $\pi$ -conjugated bonds<sup>309</sup>, requiring a fundamental understanding of these processes to be able to design highly efficient photoelectrochemical biosensing devices.

Organic semiconductors are attractive due to their tunability, low cost, metal free nature, and relative abundance; however, their low quantum efficiency often requires them to be coupled with other photoactive materials for creating photoelectrodes. Unlike the ionic or covalent bond in inorganic semiconductors, organic semiconductors are made of molecular units held together by weak van der Waals interactions<sup>310</sup>. As a consequence, the mobility of the charge carriers in organic materials is generally smaller with longer response times upon excitation as compared to their inorganic counterparts<sup>310</sup> leading to smaller conductivity<sup>311</sup>. Consequently, more research is needed towards creating *all organic* photoelectrodes that can be used in biosensing.

### 2.4.3 Hybrid semiconductors

Hybrid semiconductors are formed by: (i) coupling two inorganic semiconductors with different band gaps, (ii) complexation of organic and inorganic semiconductors<sup>229</sup>, and (iii) combining metal NPs (usually Au or Ag) with organic/inorganic semiconductors.

Coupling two or more inorganic semiconductors extends the absorption spectrum and increases the charge separation efficiency of the PEC system<sup>312</sup>. As a result, hybrid material systems offer a higher photon-to-current conversion efficiency, which is important for enhancing the performance of biosensors<sup>209</sup>. For example, when  $\text{TiO}_2$  NPs are used with CdS QDs in insulin detection<sup>312</sup>, CdTe is excited using visible light, and the photo-induced electrons are transferred from CdTe to the conduction band of  $\text{TiO}_2$  NPs. Liu *et al.* demonstrated improved sensitivity of microcystin detection by forming Z-scheme heterojunction of CdTe with  $\text{Bi}_2\text{S}_3$  nanorods<sup>313</sup> due to enhanced charge separation. Another strategy used to enhance the solar light harvesting efficiency of photoanodes composed of wide bandgap semiconductors (i.e.  $\text{TiO}_2$ ,  $\text{ZnO}$  etc.) is upconversion<sup>314</sup>. This is a type of anti-stoke process in which emission of higher energy photons is achieved by the absorption of two or more low-energy photons<sup>315</sup>. Qiu *et al.* developed a hybrid upconverting structure where the narrow absorption band of  $\text{TiO}_2$  was improved by the use of core-shell  $\text{NaYF}_4:\text{Yb},\text{Tm}@\text{TiO}_2$  upconversion microrods<sup>316</sup>. In this system, doped  $\text{Yb}^{3+}$  ions absorbed near-IR light, whereas the doped  $\text{Tm}^{3+}$  emitters produced the UV light through energy transfer upconversion (ETU). The upconverted photons were then absorbed by the  $\text{TiO}_2$  NPs, thereby, yielding effective IR-UV upconversion<sup>316</sup>. This core-shell  $\text{NaYF}_4:\text{Yb},\text{Tm}@\text{TiO}_2$  structure was used to detect carcinoembryonic antigen (CEA), which is a biomarker for colorectal cancer.

Complexation of organic and inorganic semiconductors are used to overcome the low charge conductivity, narrow absorption spectrum, and strongly bound excitons that are encountered in organic semiconductors<sup>276,317</sup>. This class of transducers typically demonstrates improved PEC response and physical and chemical properties compared to their purely organic or inorganic counterparts<sup>207,318</sup>. This type of complexation was demonstrated using  $\text{TiO}_2$  mesocrystals (inorganic semiconductor) sensitized with polyethylenimine (organic polymer)<sup>319</sup>. Polyethylenimine reduces the electron transport energy barrier of  $\text{TiO}_2$  mesocrystals by reducing the work function and thereby increasing the generated photocurrent. This type of performance enhancement was also seen in reduced graphene oxide

(RGO)/CdS/ZnS photoelectrode, where a widened light absorption range, spatial separation of photogenerated electron-hole pairs, accelerated electron transfer, and reduction of surface defects resulting from the coupling of ZnS (wide bandgap,  $\sim 3.8$  eV) and CdS (narrow bandgap,  $\sim 2.4$  eV) was observed<sup>264</sup>. By using RGO further enhancement of the photocurrent was achieved as it facilitates the excited electron transfer from the conduction band (CB) of CdS to the CB of ZnO. Ultrafast electron transport was also realized by Matylitsky *et al.* and Wang *et al.* by adsorbing an electron acceptor, methyl viologen (MV) on the surface of CdSe QDs. Here, MV acted as an electron relay and facilitated ultrafast electron transport in a timeframe of  $\sim 70$  fs<sup>239,240</sup>. The ability of MV in enhancing IPCE by working as an electron relay was exploited by Long *et al.* to demonstrate ultrafast electron transport in cysteine bioanalysis by using a MV coated CdS QD based system<sup>320</sup>. Surface sensitization of a wide band gap semiconductor with an organic material such as a dye is an alternative method of creating efficient hybrid materials. Here, an increase in efficiency of the excitation due to the injection of electrons directly into the CB of the semiconductor from the excited dye and expansion of excitation wavelength range results in higher photocurrent generation<sup>321–323</sup>. Neto *et al.* demonstrated the usefulness of such hybrid materials in sensing L-Dopamine by using iron phthalocyanine (FePc) dye sensitized TiO<sub>2</sub> system to enhance the PEC performance due to the charge transfer property of FePc<sup>324</sup>. Additionally, the antioxidant character of FePc is also hypothesized to enhance stability of the biorecognition units used in this study by inhibiting PEC-induced damage to the attached biomolecules typically seen in the case of wide band gap semiconductors such as TiO<sub>2</sub>.

The coupling of inorganic/organic semiconductors with metal nanoparticles is increasingly used in PEC devices due to the ability of metal NPs such as gold, platinum and silver to enhance the photoresponse of the system through surface-plasmon resonance (SPR). Han *et al.* detected  $\alpha$ -fetoprotein (AFP), a key clinical indicator used for diagnosing primary liver cancer, using Au-ZnO flower-rods<sup>220</sup>. Here, Au NPs enhanced the anodic photocurrent of ZnO flower-rods by extending the absorption to the visible region and by enhancing charge separation. Besides the SPR effect, Au NPs have been shown to improve the charge transfer properties of the substrate. For example, Lv *et al.* deposited Au NPs on p-CuBi<sub>2</sub>O<sub>4</sub> electrodes to reduce the charge transfer resistance and hence enhance the cathodic photocurrent of p-CuBi<sub>2</sub>O<sub>4</sub><sup>234</sup>. Another hybrid photoelectrode used in biosensing is created by Au NP-decorated hematite ( $\alpha$ -Fe<sub>2</sub>O<sub>3</sub>) nanorods<sup>325</sup>. Despite being widely used in other PEC applications (such as PEC water splitting, photovoltaic cells etc.),  $\alpha$ -Fe<sub>2</sub>O<sub>3</sub> has been rarely used in PEC biosensing due to poor electron mobility and lack of binding with capture biomolecules. Enhancement of electron mobility was achieved by decorating  $\alpha$ -Fe<sub>2</sub>O<sub>3</sub> with Au NPs. Moreover, Au NPs were also used to covalently attach capture biomolecules to the photoactive electrodes. Au NPs have also been used as anchors to deposit probe DNA and for improving the photocurrent of g-C<sub>3</sub>N<sub>4</sub>- based photoelectrodes<sup>326</sup>. In this work, Au NPs are used with g-C<sub>3</sub>N<sub>4</sub> for detecting zeatin, one of the main cytokines found in plant tissues responsible for promoting plant growth.

Hybrid semiconductors are gaining popularity as transduction elements for PEC biosensors owing to their performance enhancement resulting from the coupling of desirable qualities of its constituent materials and the unique properties generated as a consequence of their complexation. To be able to achieve higher IPCE from these hybrid structures, it is important to carefully choose the materials and control their composition and morphology. Controlling interfacial defects is an important consideration for designing hybrid PEC systems. A summary of the photoactive materials used in PEC biosensing is presented in Table 2.1.

*Table 2.1 Properties of various photoactive species used in PEC biosensing. RSD represents relative standard deviation, which signifies the reproducibility of the sensor.*

Photo electrode material	Excitation	Stability ('N' cycles, Rsd (%), period)	Base photo-current (A)	Enhanced absorption	Enhanced charge separation	Ease of functionalization	Reference
<b>1.1 Inorganic Semiconductors</b>							

TiO <sub>2</sub> NWs	Simulated sunlight	-	1.15 x10 <sup>-3</sup>	No	No	Yes TiO <sub>2</sub> NWs functionalized with HRP via APTES-glutaraldehyde coupling.	249
CdTe QD	Xenon lamp; 420 nm cut-off filter	Fairly stable. N=17, ~Rsd ~9.16%, 360 s	~2.17x10 <sup>-7</sup>	No	Decreased. Trap sites resulting from Ag <sub>2</sub> Te formation create new electron-hole recombination centers.	Yes; 3-Mercaptopropionic (MPA) modified CdTe via one pot synthesis; resultant carboxyl terminated surface.	327
CdTe QD	590 nm	Very stable. N=8, Rsd ~0.9%, 275 s	~3.80x10 <sup>-7</sup>	No	No	Yes; MPA modified CdTe via one pot synthesis; resultant carboxyl terminated surface.	232
CdTe QD	590 nm	Very stable. N=15, no decrease in photocurrent, 425 s	~2.10x10 <sup>-7</sup> (anodic) ~1.20x10 <sup>-7</sup> (cathodic)	No	No	Yes; MPA modified CdTe via one pot synthesis; resultant carboxyl terminated surface.	328

### 1.2 Organic Semiconductors

g-C <sub>3</sub> N <sub>4</sub>	Visible	Very stable. N=9, no significant decrease in photocurrent, 350 s	~3.00x10 <sup>-6</sup>	Yes	Yes; MB intercalators following duplex formation at g-C <sub>3</sub> N <sub>4</sub> enhance separation efficiency.	No	272
FeTMPyP	Chemiluminescence	Very stable. Rsd ~4.3%. Long term stability over 10 days.	~2.50x10 <sup>-7</sup>	Yes	No	No	329
PFBT Pdots (Polymer dots)	450 nm	Stable. N=20, 400 s	~3.00x10 <sup>-8</sup>	No	Yes; photogenerated electrons transferred to the proton in solution at low pH value.	Yes; Carboxylated surface obtained via synthesis procedure allows for easy immobilization of pDNA via amine-carboxyl interaction.	273

### 1.3 Hybrid Semiconductors

#### 1.3.1 Inorganic -Inorganic

CdTe-Bi <sub>2</sub> S <sub>3</sub>	Visible	Fairly stable. N=8, Rsd~7.3%, 350 s	~4.00x10 <sup>-7</sup>	Yes	Yes; Z-scheme heterojunction formation between CdTe and Bi <sub>2</sub> S <sub>3</sub> .	No	330
CdS/ZnS	Visible	Good long-term stability; 95.6% of its original value after 5 months	~3.00x10 <sup>-5</sup>	Yes	Yes; Formation of heterojunction allowed the transfer of photogenerated electrons to ZnS conduction band.	Yes; CdS was modified by carboxyl groups which was used to attach with amine terminated DNA.	331

Core-shell NaYF <sub>4</sub> :Yb, Tm@TiO <sub>2</sub>	Infrared	Fairly stable. N=10, Rsd ~7.9%, 250 s	~1.25x10 <sup>-7</sup>	Yes	Yes; Enhanced separation due to formation of Z-scheme heterojunctio n	No	316
<b>1.3.2 Organic-Inorganic</b>							
TiO <sub>2</sub> – polyethylen imine mesocrystal	Visible	Very stable. N=10, Rsd ~2.04%, 250 s Excellent long- term stability; 94.8% of initial value after 12 days	~4.00x10 <sup>-6</sup>	Yes	Yes; Improved charge separation via ligand (OAM/PEI) modification	Yes; Organic ligand (OAM/PEI) modification confers the complex with reactive amine terminations capable of further chemical reaction.	319
CdS - MV	Xenon lamp	Poor stability.	~1.00x10 <sup>-7</sup>	No	Yes; MV coating of CdS facilitates fast charge separation and a slow charge recom- bination upon irradiation.	Yes. Thioglycolic acid (TGA) capped CdS QDs formed via precipitation- based synthesis; resultant carboxyl terminated surface.	320
TiO <sub>2</sub> -EPM	380-480 nm	Very stable. N=10, Rsd ~2.04%, 400 s	~3.00x10 <sup>-6</sup>	Yes	No	Yes; Amine and hydroxyl terminations on TiO <sub>2</sub> conferred via EPM (ligand) conjugation.	323
<b>1.3.3 Metal NP -Inorganic/Organic</b>							
AuNP-ZnO FRs	Simulated sunlight	Very stable. N=15, no decrease in photocurrent, 300 s	~2.50x10 <sup>-5</sup>	Yes	Yes; Au NPs in the Au- ZnO FRs heterostructur e enhances charge separation. Yes; Au NPs, as a front contact of p- CuBi <sub>2</sub> O <sub>4</sub> enhance the efficiency of charge separation Yes; g- C <sub>3</sub> N <sub>4</sub> and GQD reduce the probability of recombinatio n of photogenerat ed electrons and holes.	No	220
AuNP on p-CuBi <sub>2</sub> O <sub>4</sub>	>420 nm	Good long-term stability; 99.8% of its original value after 3 weeks	~4.00x10 <sup>-7</sup>	No		Yes; Au NPs, as a front contact of p- CuBi <sub>2</sub> O <sub>4</sub> allow conjugation with thiol terminated biomolecules.	234
Au NP/Graphe ne QD/g- C <sub>3</sub> N <sub>4</sub> nanosheet	Xenon lamp	Very stable. N=15, Rsd ~1.5%, 20 s	~4.5x10 <sup>-7</sup>	No		Yes; Au NPs allow conjugation with thiol terminated biomolecules	326

## 2.5 Transduction mechanism

Several signal transduction strategies have been proposed to translate a biorecognition event to a PEC signal. The signal of a PEC biosensor depends on the properties of the photoactive material, applied potential, light intensity, wavelength, and the type and concentration of the electron donor or acceptor<sup>332</sup>. Depending on the mechanism chosen, the PEC biosensor operates in either *signal-on* or *signal-off* mode. In the former case, the PEC signal increases upon target recognition, and in the latter case it

decreases<sup>210</sup>. In this review, we have categorized the signal generation strategies used in affinity-based biosensors as: (i) introduction of photoactive species, (ii) generation of electron/hole donors, (iii) use of steric-hindrance, (iv) *in situ* induction of light, and (v) resonance energy transfer (Figure 2.3). In this section, we discuss the recent biosensing reports categorized under these mechanisms.

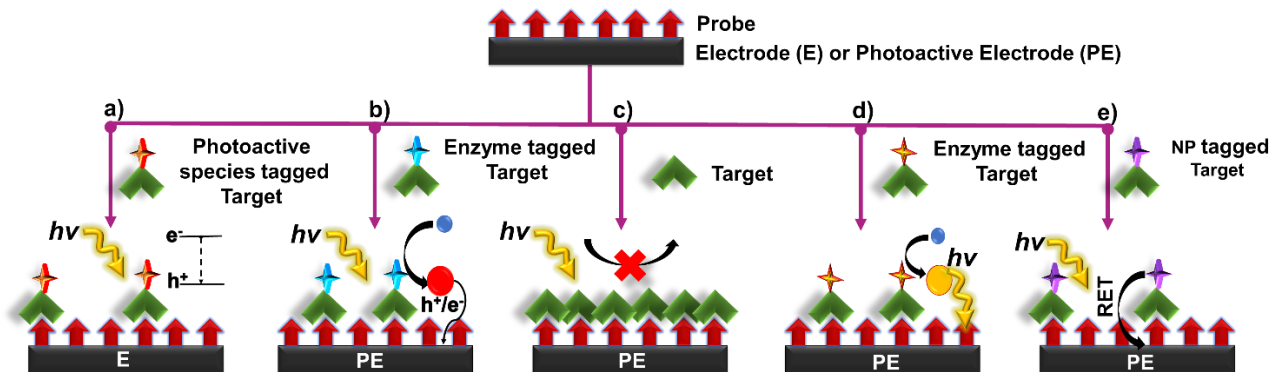


Figure 2.3 Principles of signal transduction in PEC biosensors a) Introduction of photoactive species b) Generation of electron/hole donors c) Use of steric hinderance d) *In situ* induction of light e) Resonance energy transfer.

### 2.5.1 Introduction of photoactive species

In this signal transduction strategy, the photoactive material is incorporated into the target/probe complex in the form of a label, which enhances or quenches the PEC response. Signal modulation is initiated by bringing the label into the close proximity of a conductive/ photoactive substrate following a biorecognition event. Once in proximity to the appropriate substrate, electron hole pairs are generated at the surface of the photoactive material upon light excitation. These electron-hole pairs then take part in chemical reaction with the redox species in the electrolyte or interact with the underlying substrate to either generate a measurable signal or enhance an existing one (Figure 2.3a). Different types of photoactive species, such as semiconductor nanocrystals<sup>260</sup>, metallic nanoparticles<sup>238</sup> and organic semiconductors such as g-C<sub>3</sub>N<sub>4</sub>, PFP (poly(9,9-bis(6'-(N,N,N-trimethylammonium)hexyl) fluorene-co-alt-1,4-phenylene) bromide, etc.<sup>333,334</sup> have been commonly used as a signal label. In this strategy, it is crucial to (i) minimize the size of bioconjugated labels to reduce steric hindrance, (ii) decrease the effect of the label on the mass transport and complexation of the biomolecule, and (iii) diminish nonspecific protein adsorption to develop labels that do not interfere with assay functionality. Semiconductor nanocrystals possess dimensions in the order of 1-100nm, making them an excellent choice as PEC labels. The PEC signal of QDs in a complex environment stem from a myriad of factors such as the intensity of excitation source, the magnitude of applied bias potential, the absence/presence of electron donors and acceptors, as well as the inherent photophysical properties of QDs<sup>335</sup>. These materials are particularly appealing owing to their tunable excitation spectrum resulting from quantum confinement, narrow and symmetrical emission spectrum, high quantum yield and good optical stability<sup>336</sup>. Noble metal NPs are also commonly exploited for this approach<sup>217,337</sup>. Plasmonic features of these particles such as intensive localized electric field generation in the near field, strong far-field light scattering, large absorption cross section in plasmonic resonance band, and light induced charge separation exhibited by these labels offer photocurrent modulation<sup>337,338</sup>.

In this sensing scheme, in addition to the type of labels used, the electrode material greatly influences the assay design. Here, the electrode is typically constructed from wide bandgap semiconducting materials such as TiO<sub>2</sub>, g-C<sub>3</sub>N<sub>4</sub>, ZnO, p-CuBi<sub>2</sub>O<sub>4</sub>, and hematite (Fe<sub>2</sub>O<sub>3</sub>), where the photoactive label extends the absorption to the visible wavelength and improves the charge separation efficiency of the electrode. However, given that signal transduction is induced using a photoactive label, non-photoactive electrodes can also be used in these assays<sup>217,339</sup>.

QDs are widely used as signal transduction reporters in PEC biosensors following the pioneering work of Wilner et.al. in the early 2000s<sup>217,339</sup>. In one of these works, ssDNA immobilized on a gold substrate was hybridized with CdS NP-tagged target DNA to create a crosslinked CdS/DNA network<sup>216,217</sup>. It

was observed that the photocurrent emanating from these networks could be switched ‘on’ and ‘off’ using the light source through the photoejection of conduction-band electrons of CdS particles that were in contact with or at tunneling distances from the electrode using  $\text{Ru}(\text{NH}_3)_6$  as an electron mediator. Using a similar strategy, Chai *et al.* reported an approach where they used DNA tetrahedron (TET) to deposit CdTe QDs and a methylene blue intercalator in the presence of the target analyte. Since the electrode was not photoactive, this system was operated at near-zero noise level and with a limit-of-detection of 17 aM and a linear range of 50 aM - 50 pM in the presence of target miRNA-141 under light excitation (590 nm). When the DNA TET-CdTe QDs-MB complex was used as a signal probe, the PEC response (0.82  $\mu\text{A}$ ) was  $\sim 2.5$  fold higher as compared to the PEC response based on the DNA TET-CdTe QDs complex alone<sup>232</sup> (Figure 2.4a). In contrast to the previously discussed assays, the introduction of photoactive materials can also occur in the *absence* of the target analyte<sup>340</sup>. In an assay of this type, the dsDNA capture probe contains a carboxyl-terminated ssDNA building block that is removed, through strand displacement, from the electrode upon target introduction. In the absence of the target strand,  $\text{CuInS}_2/\text{ZnS}$  (ZCIS) QDs and n-doped carbon dots are captured and increase the PEC signal under xenon lamp excitation (spectral range 200-1200 nm) (Figure 2.4b). This biosensor exhibited a limit-of-detection of 0.31 pM with a linear range of 1 pM - 100 nM in the presence of target miRNA-21. Furthermore, single base mismatch studies conducted using miRNA-21 (target), SM miRNA-21 and miRNA-141 showed  $\sim 4$ x higher response in the case of target as compared to the interfering miRNAs, showcasing the excellent selectivity of this sensor. In addition to nucleic acid sensing, QDs are widely used in PEC biosensors created for protein analysis. In an assay of this type, the presence of insulin instigated the formation of an immunocomplex containing DNA-labelled antibody, insulin, secondary DNA labelled antibody and CdTe-labelled reporter DNA<sup>312</sup>. CdTe induces a sensitization effect on the CdS/ $\text{TiO}_2$ /ITO electrode, thereby enhancing the photocurrent under white light excitation (spectral range 200-1200 nm) (Figure 2.4c). A limit-of-detection of 3 fM was exhibited by this sensor with a linear range of 10 fM - 10 nM using insulin as the target. The fabricated sensor exhibited desirable long-term stability with no significant change in photocurrent following storage for 10 days and excellent selectivity when incubated with a solution containing interfering agents (IGF-1 and C-peptide). Micro-RNA (miRNA-155) detection has been shown by introducing Au NP functionalized N-doped porous carbon ZnO polyhedra (NPC-ZnO) on CdSe QD based photoelectrode<sup>341</sup>. Following, miRNA hybridization with a hairpin structure probe, Au NP functionalized NPC-ZnO was brought close to the hybridized double-stranded RNA by using second hairpin DNA structure (Figure 2.4d). The NPC-ZnO is also photoactive and thereby generated a signal-on response under visible light excitation. This creative design strategy enabled ultrasensitive miRNA detection with a limit-of-detection of 49 aM (linear range of 0.1 fM – 10 nM), which is much lower than the previously reported photoelectrochemical miRNA detection bioassays<sup>312,340</sup>.

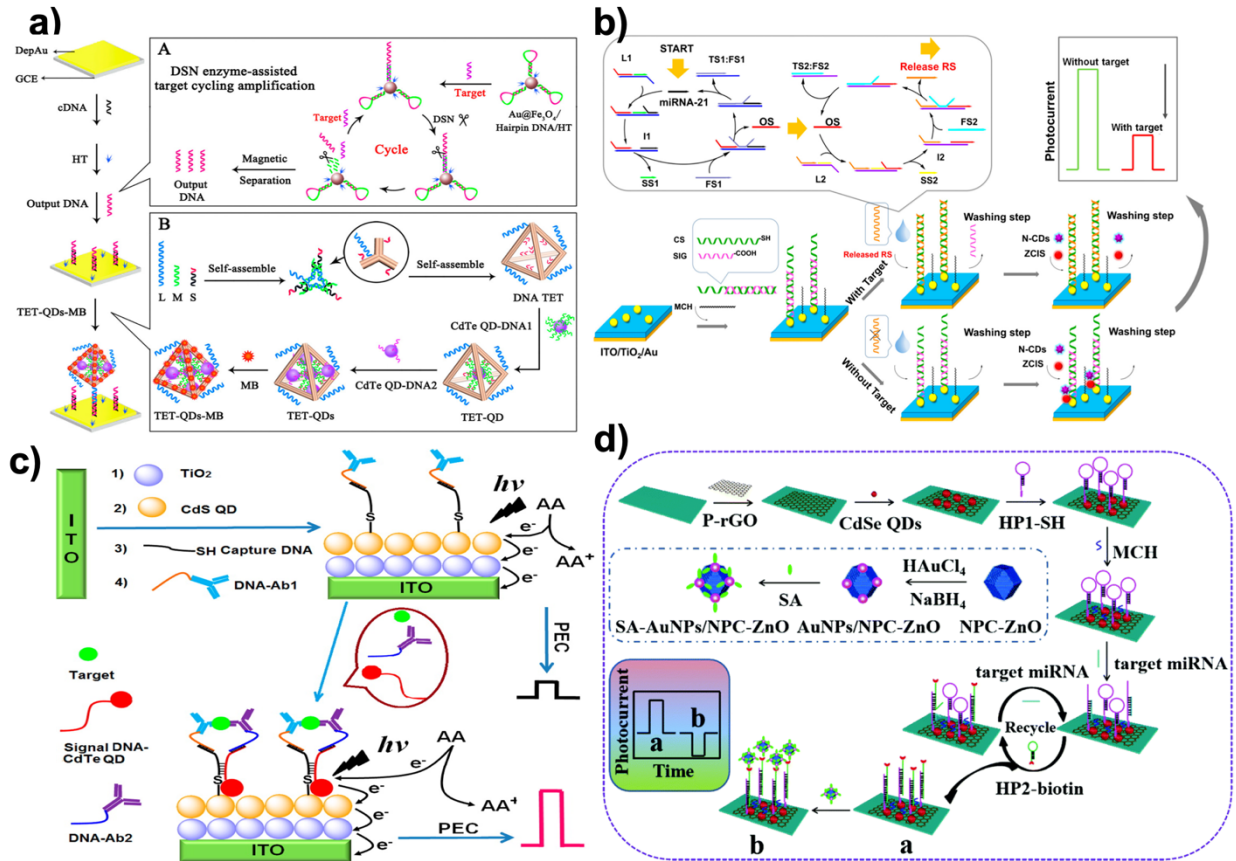


**Figure 2.4** Introduction of QDs as Photoactive species: a) Schematic Diagrams of PEC Biosensor for miRNA-141 detection using DSN enzyme-assisted target cycling amplification strategy and DNA TET-CdTe QDs-MB complex (Reprinted from <sup>232</sup> with permission from American Chemical Society); b) Schematic illustration of the PEC detection of miRNA-21 by bringing photoactive N-doped carbon dots following hybridization of the target RNA (Reprinted from <sup>340</sup> with permission from American Chemical Society); c) Schematic representation of ultrasensitive insulin detection based on CdTe QD labels brought into proximity of CdS/TiO<sub>2</sub>/ITO electrode upon affinity-based binding of CdTe QD labeled insulin target (Reprinted from <sup>312</sup> with permission from American Chemical Society); d) Schematic representation of the detection of miRNA-155 based on NPC-ZnO labelled target. Here, NPC-ZnO performs the role of electron scavenger, thus generating a signal-on response (Reprinted from <sup>341</sup> with permission American Chemical Society).

Dai *et al* demonstrated a multiplexed PEC immunoassay by using two different photoactive materials – graphitic carbon nitride (g-C<sub>3</sub>N<sub>4</sub>) which exhibited an anodic photocurrent and CS-AgI which exhibited a cathodic photocurrent – on a polyamidoamine dendrimer modified cube anatase TiO<sub>2</sub> mesocrystal (PAAD@CAM) substrate (Figure 2.5a) <sup>334</sup>. A competitive immunoassay was designed to analyze PSA and IL-6 biomarkers using anti-PSA and anti-IL-6 antibodies labelled with g-C<sub>3</sub>N<sub>4</sub> and CS-AgI respectively. Application of different bias voltages allowed each of the complexes to be individually analyzed with IL-6 having a dynamic range of 10<sup>-5</sup> - 90 pg mL<sup>-1</sup> (3.3×10<sup>-5</sup> pg mL<sup>-1</sup> limit-of-detection) and PSA having a dynamic range of 10<sup>-6</sup> - 90 ng mL<sup>-1</sup> (3.3×10<sup>-3</sup> pg mL<sup>-1</sup> limit-of-detection).

Metal nanoparticles are used in combination with photoactive materials as signal reporters in PEC biosensors. In an assay of this kind, liposomes loaded with AgNP were labelled with IgG antibodies to detect IgG on a BiOI/Ni electrode <sup>342</sup>. In a sandwich protein binding assay, the liposome-antibody conjugates were used to label the captured antigen. Upon binding, the Ag NPs were released using Triton X-100 and reacted with the p-type BiOI substrate to form an AgI/Ag/BiOI z-scheme heterojunction, enhancing the cathodic photocurrent of the electrode due to the reduction of dissolved O<sub>2</sub> by AgI and transferring electrons from the conduction band of BiOI to the valence band of AgI

through metallic Ag upon illumination (410 nm excitation light source) (Figure 2.5b). This assay demonstrated a limit-of-detection of  $100 \text{ fg mL}^{-1}$  and was linear in the  $100 \text{ fg mL}^{-1}$  -  $100 \text{ ng mL}^{-1}$  range.

As seen in the previous reports, target labeling provides the sensitivity and specificity that is needed for bioanalysis in complex biological samples. However, the introduction of photoactive species via labelling often impairs the rate and efficiency of bio-recognition, makes it difficult to perform quantitative analysis of biomolecular species in real time, and adds to the assay complexity due to the washing steps. An alternative method that can overcome some of the drawbacks of labeling is signal transduction via *in situ* generation of electron/hole donors, which is discussed in the following section.

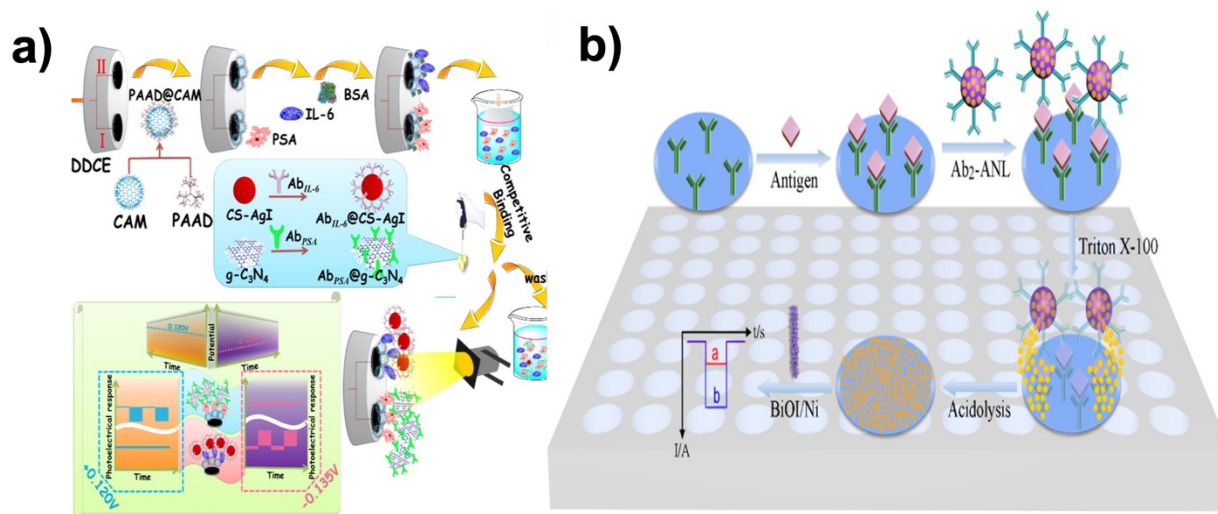


Figure 2.5 Introduction of photoactive species: a) Schematic representation of two potentiometrically resolvable protein detection assays for PSA and human interleukin-6 involving the affinity-based binding of CS-AgI tagged IL-6 and CS-AgI tagged PSA (Reprinted from <sup>334</sup> with permission from American Chemical Society); b) Liposomal PEC bioanalysis using photocathode and AgI/Ag; Reproduced with permission from (Reprinted from <sup>342</sup> with permission from American Chemical Society).

### 2.5.2 Generation of electron/hole donors

In this approach, target introduction releases free electron/hole donors (scavenging species) that interact with the photoactive electrode surface, induce charge separation, and modulate the photocurrent. A common method to produce electron/hole donors is by using an enzyme <sup>332</sup> to generate hydrogen peroxide ( $\text{H}_2\text{O}_2$ ) or ascorbic acid (AA). Alkaline phosphatase (ALP) is used in DNA and protein sandwich assays <sup>343,344</sup> to catalyze the conversion of ascorbic acid 2-phosphate (AAP) to ascorbic acid (AA) upon target binding. AA acts as a hole scavenger and increases the lifetime of photo-induced carriers, which enhances the PEC current <sup>345</sup>. Using a similar approach, an assay incorporating dual enzyme tags for multiplexed PEC detection was developed to differentiate between two cardiac markers – cardiac troponin I (cTnI) and C-reactive protein (CRP) <sup>346</sup>. ALP-tagged antibody was used for troponin T detection, and acetylcholine esterase (AChE)-tagged antibody was used for detecting C-reactive protein <sup>346</sup>. These tags generate electron donating ascorbic acid (AA) and thiocholine (TC) by specifically catalyzing the hydrolysis of AAP or acetylthiocholine (ATC) (Figure 2.6a). Under visible light irradiation, the generated electron donors scavenge photoinduced holes at the surface of the CdS QDs/ $\text{TiO}_2$  electrode, inhibiting the recombination of the holes and electrons, thus enhancing the photocurrent. A linear range of  $100 \text{ ng mL}^{-1}$  -  $0.1 \text{ mg mL}^{-1}$  (a limit-of-detection of  $50 \text{ ng mL}^{-1}$ ) was exhibited for CRP, and a linear range of  $1 \text{ ng mL}^{-1}$  -  $0.01 \text{ mg mL}^{-1}$  (a limit-of-detection of  $0.1 \text{ ng mL}^{-1}$ ) was exhibited for cTnI.

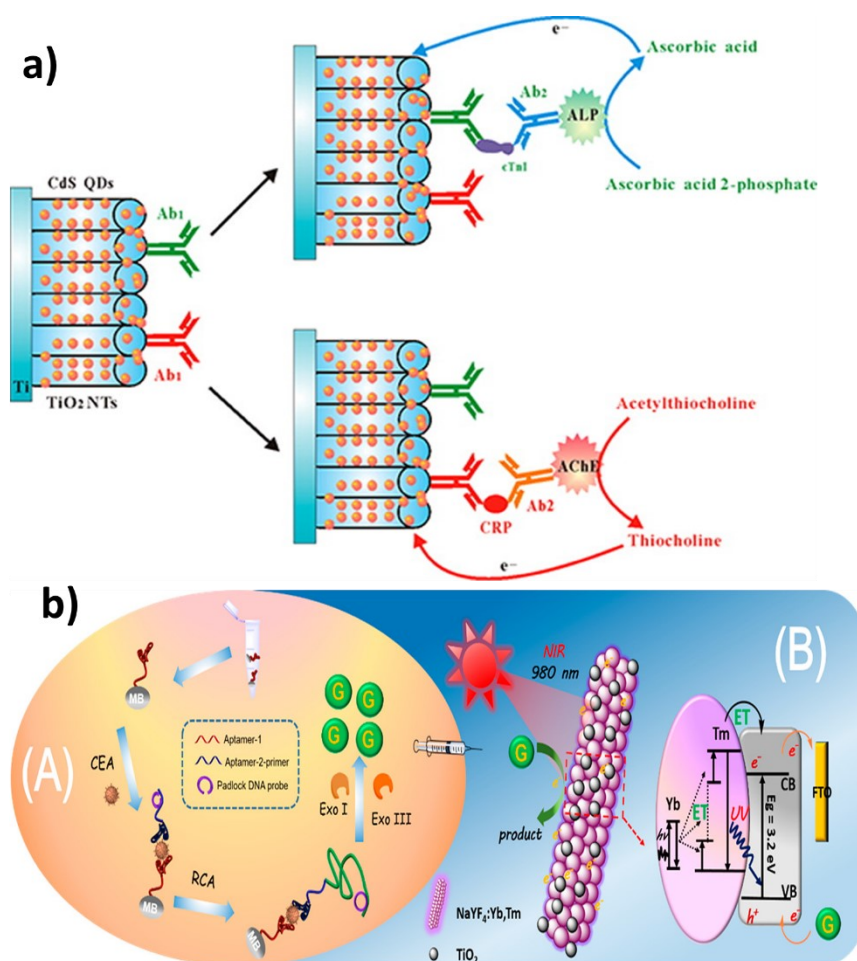


Figure 2.6 In situ generation of electron/hole donors : a) Incorporation of dual enzyme tags for multiplexed cardiac troponin I (cTnI) and C-reactive protein (CRP) detection (Reprinted from <sup>346</sup> with permission from American Chemical Society); b) Schematic Illustration of near infrared to ultraviolet light-mediated photoelectrochemical aptasensing for cancer biomarker detection and mechanism of signal generation in NaYF<sub>4</sub>:Yb,Tm@TiO<sub>2</sub> photoactive electrode (Reprinted from <sup>316</sup> with permission from American Chemical Society).

In the previous assays, the biorecognition event, the generation of electron/hole donors, and signal measurement were performed on the electrode surface. However, it is possible to perform biorecognition and generate electron/hole donating species in solution and use the resultant species to modulate the PEC signal at an electrode surface. An assay of this type detects carcinoembryonic antigen (CEA) using a sandwich assay on the surface of magnetic beads <sup>316</sup>. Upon aptamer–CEA–aptamer reaction, the primer DNA on the terminus of the secondary aptamer initiates rolling circle amplification (RCA) reaction, resulting in the generation of long guanine (G) rich oligonucleotide strands (Figure 2.6b). Subsequent introduction of exonuclease I and III releases guanine (G) bases following digestion of the RCA product. The free guanine bases function as electron donors and enhance the photocurrent of the NaYF<sub>4</sub>:Yb,Tm@TiO<sub>2</sub> microrod electrodes under near-infrared light excitation. The limit-of-detection of the assay for CEA target was 3 pg mL<sup>-1</sup> with a linear range of 10 pg mL<sup>-1</sup> to 40 ng mL<sup>-1</sup>. Furthermore, high specificity is demonstrated by this assay when tested against a complex mixture containing interferents such as PSA, TB, and human IgG.

In addition to using photoactive species and electron/hole donors separately, it is possible to combine these signal transduction mechanisms. For example, the synergistic effect of electron donor generation and photoactive species introduction was used to detect alpha-fetoprotein (AFP), which is a biomarker for liver cancer <sup>347</sup>. In this assay, AFP-CdS-GOD complex was formed by conjugating AFP with CdS QD and glucose oxidase (GOD). In this work, chitosan which helps to covalently bind anti-AFP

antibody was first deposited on the photoelectrode composed of ZnO inverse opal structure. Upon biorecognition with AFP-CdS-GOD, the photocurrent was enhanced. The enhancement of the photocurrent is attributed both to the increased absorption spectrum due to CdS QD and generation of H<sub>2</sub>O<sub>2</sub> by GOD as electron donor. This bioassay showed a limit-of-detection of 0.01 ng mL<sup>-1</sup> (linear range is 0.1 ng mL<sup>-1</sup> - 500 ng mL<sup>-1</sup>). Moreover, this assay showed good specificity against CEA, PSA and H<sub>2</sub>O<sub>2</sub>.

Although assays using electron/hole generation overcome the limitations encountered in labelled assays, they have some drawbacks that must be considered for using them in analyzing real-life samples. Enzymes that are typically used to induce the formation of local electron/hole donors are known for their instability, relatively low shelf life, and expensive reagent cost. Additionally, to ensure effective detection using this scheme, utmost importance must be paid to minimize interfering scavenging species found in native samples that may consume the locally generated electron/hole donors required to transduce the biorecognition events.

### 2.5.3 Steric-hindrance based assay

Introduction of a biomolecule at the biosensor surface can sterically hinder the access of electrolyte to the photoactive transducer to modulate the measured PEC current. This transduction approach is one of the simplest mechanisms for developing a biosensor because it usually does not require labeling steps following the target capture. However, most of these sensors operate in a signal-off fashion<sup>348-350</sup>.

In signal-off PEC biosensing, it is crucial to have a high photocurrent before target introduction because high concentrations of the target can completely diminish the PEC signal<sup>351</sup>. Different approaches have been used to obtain high baseline PEC currents. Depositing photoactive materials into three-dimensional scaffolds such as wrinkled electrodes has been used to increase the photocurrent of PEC biosensors<sup>352</sup>. The wrinkle electrodes showed 10 times higher photocurrent than a planar electrode composed of CdTe QDs. This wrinkled photoelectrode was used to detect single stranded DNA by simply hybridizing with the complementary sequence as a proof-of-concept. Moreover, it showed stable photocurrent following storage at 4°C in dark conditions for seven days and exhibited high specificity against single or multiple pair mismatch. Metal NPs are also deposited in combination with photoactive materials to enhance the photocurrent due to their plasmonic properties<sup>353,354</sup>. Wang *et al.* used Au NPs as a photoelectronic transfer promoter in photoactive molybdenum disulfide (MoS<sub>2</sub>) nanosheets to detect micro-RNA<sup>350</sup>. To obtain further reduction of photocurrent, bulky biotin-streptavidin coupling was used in conjunction with probe hairpin DNA and target microRNA to increase the signal changes caused by steric hindrance. This PEC sensor presented a broad linear range of 10 fM – 1 nM (limit-of-detection of 4.21 fM) (Figure 2.7b). Signal transduction using steric hindrance is ideally suited for cellular detection because the large size of cells compared to biomolecules enhances their steric hindrance effect. A signal-off sensor was constructed to rapidly detect early apoptotic cells using phosphatidylserine binding peptide (PSBP) bound to the surface of TiO<sub>2</sub>/Graphene/ZnIn<sub>2</sub>S<sub>4</sub> photoelectrode as the biorecognition element<sup>355</sup>. Here, the access of AA to the electrode surface was sterically hindered by the binding of the apoptotic cell decreasing the photocurrent. This biosensor exhibited an LOD of 3 cells mL<sup>-1</sup> with a linear range of 1×10<sup>3</sup> - 5×10<sup>7</sup> cells mL<sup>-1</sup> (Figure 2.7a). A paper-based cytosensor was reported for detecting breast cancer cells (MCF-7) constructed from ZnO spheres immobilized on Au nanorod-modified paper and sensitized with CdTe QDs and nanogold-assembled mesoporous silica nanoparticles (GMSNs) at their surface to create the photoactive portion of the biosensor<sup>356</sup>. Multiple horseradish peroxidase (HRP) molecules and branched capture sites were then immobilized onto the GMSNs using double stranded DNA (Figure 2.7c). HRP was used in this assay to generate optical excitation through chemiluminescence. A signal decrease is observed upon capture of graphene quantum dot (GQD) labelled cancer cells as H<sub>2</sub>O<sub>2</sub>, the oxidant of luminol based chemiluminescence, is sterically hindered. These biosensors demonstrated a linear range of 63 – 1.0×10<sup>7</sup> cells mL<sup>-1</sup> and limit-of-detection of 21 cells mL<sup>-1</sup>. Lymphoblast (CCRF-CEM) cells were also detected based on steric hindrance in a PEC biosensor<sup>357</sup>. These cells were captured using hairpin DNA targeting overexpressed protein tyrosine kinase-7 on their surface. A decrease in PEC signal was

exhibited on AgInS<sub>2</sub> NPs photoelectrodes due to steric hindrance of AA. A limit-of-detection of 16 cells mL<sup>-1</sup> and linear range of 1.5x10<sup>2</sup> - 3.0x10<sup>5</sup> cells mL<sup>-1</sup> were demonstrated.

Another interesting signal transduction method involves the generation of a passivating compound as a result of target capture, which is used to decrease the PEC current generated on the photo-electrode<sup>316,358</sup>. An assay of this type combines biorecognition and isothermal target amplification in solution with signal modulation on the photoelectrode to detect T4 polynucleotide kinase (PNK), an important cellular regulator<sup>358</sup>. In this detection scheme, a hairpin DNA (HP2) strand is phosphorylated upon the introduction of target PNK and is partially digested by λ-exo to yield an endogenous primer which initiates solution-based amplification generating DNA fragments. These DNA fragments activate the peroxidase-mimicking DNAzymes on the hairpin DNA probes immobilized on the photoelectrode (HP1) to catalyze the formation of insoluble precipitates at the electrode surface and attenuate the photocurrent response of the photoactive electrode. This target induced attenuation of current, and enabled PNK to be analyzed in the linear range of 2 to 100 mU mL<sup>-1</sup>. Zhang *et al.* used this strategy to detect prostate specific antigen (PSA) on a CdS nanorod electrode<sup>359</sup>. The presence of PSA led to the formation of a sandwich complex on Au NPs that contained DNAzyme concatamers that catalyzed the precipitation of 4-chloro-1-naphthol onto the photoactive electrodes in the presence of H<sub>2</sub>O<sub>2</sub>. The insoluble precipitate resulted in an attenuation of signal by inhibiting electron transfer from the electron donor AA to the photoelectrode. PSA detection was achieved in the 0.005 ng mL<sup>-1</sup> - 50 ng mL<sup>-1</sup> range with a limit-of-detection of 1.8 pg mL<sup>-1</sup>.

Multi-channel PEC biosensors operated based on steric hindrance have been developed for improved reliability<sup>360-362</sup>. In an assay that uses sunlight instead of an external light source, a two-channel design enables the device to calibrate its photoresponse by considering the incoming sun light intensity<sup>361</sup>. In this assay, biorecognition event of aflatoxin B1 by the covalently bound aptamer with the underlying Ag/TiO<sub>2</sub>/3D nitrogen-doped graphene hydrogel (3DNGH) resulted in a decrease of photocurrent. The decrement of the photocurrent is attributed to the enhanced steric hindrance of the electrolyte (0.1M PBS) to the electrode surface. Using this ratiometric approach an LOD of 2.5×10<sup>-4</sup> ng mL<sup>-1</sup> and linear range of 1.0×10<sup>-3</sup> ng mL<sup>-1</sup>-1.0×10<sup>3</sup> ng mL<sup>-1</sup> were achieved for the detection of aflatoxin B1 (AFB1), a highly toxic carcinogen mainly found in agricultural and sideline products such as cereals and dairy products. Building on this strategy, Hao *et. al.* developed another two channel device using CdTe-graphene oxide (GO) and CdTe photoelectrodes for detecting AFB1<sup>328</sup>. A signal increase was observed on the CdTe-GO electrode because the aptamer was released from the electrode surface upon target capture, which improved the access of electrolyte (0.1 M PBS) to the photoelectrode (Figure 2.7d). A signal decrease was observed on the CdTe electrode upon target capture by the immobilized aptamer. Using this detection strategy, a limit-of-detection of 0.01 ng mL<sup>-1</sup> and a linear range of 10 pg mL<sup>-1</sup> - 100 ng mL<sup>-1</sup> were observed. Compared to single channel PEC biosensors, this self-referencing design can provide better accuracy and reliability, thus providing a promising route for the future development of PEC biosensors.

Steric-hindrance based assays can also be combined with other strategies, for example p53 (cell cycle regulator and tumor suppressor) detection has been shown by combining two detection strategies – (i) *in situ* generation of electron donors and (ii) the subsequent hindering of AA<sup>363</sup>. A protein G molecular membrane was used to immobilize ALP conjugate anti-p53 antibody on ordered TiO<sub>2</sub> nanotubes containing Au NPs. ALP enzymatic reaction in the presence of AAP generates AA for scavenging the holes localized on Au NPs. In this system, immunocomplexation with the target (p53) decreases the photocurrent signal due to (i) increased steric hindrance caused by the immunocomplex and (ii) a change in dielectric permittivity of the Au NPs-TiO<sub>2</sub> NTs interface following target capture, which in turn influences the energy coupling between Au NPs and TiO<sub>2</sub> NTs. This sensor demonstrated a limit-of-detection of 0.05 ng mL<sup>-1</sup> and a linear range of 20 - 100ng mL<sup>-1</sup> under 410 nm light illumination. Additionally, excellent selectivity was demonstrated by the immunoassay when faced with interfering agents such as glucose oxidase (GOD), prostate specific antigen (PSA), lysozyme (LZM), and thrombin. Furthermore, given that the average level of p53 in lung cancer patient serum samples is 0.55 ng mL<sup>-1</sup>, the limit-of-detection of this assay, along with its excellent selectivity point to its applicability for clinical use.

The simplicity of steric hindrance based signal transduction makes it appealing for use in PEC biosensing. However, due to its signal-off nature, this transduction method is associated with a higher incidence of false positives as compared to the other transduction methods discussed in this section. To overcome this, strategies such as multi-channel sensing with built-in calibration<sup>328</sup> have been developed for more accurate and robust biosensing.

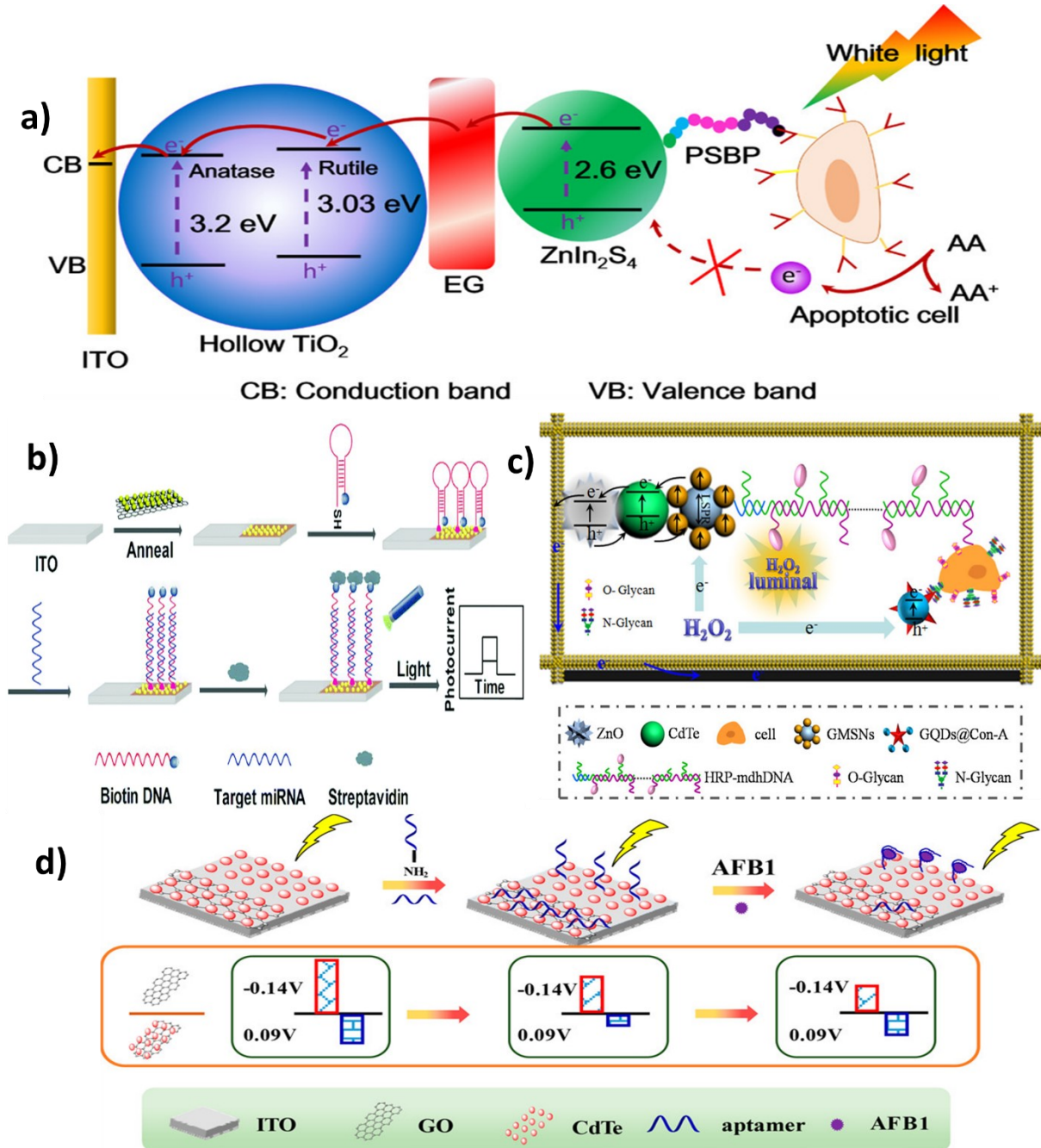


Figure 2.7 Steric-hindrance based biosensing: a) Detection of apoptotic cells by TiO<sub>2</sub>/EG/ZnIn<sub>2</sub>S<sub>4</sub> electrodes (Reprinted from<sup>355</sup> with permission from American Chemical Society); b) Use of Au NPs in conjunction with a semiconductor (MoS<sub>2</sub>) to achieve higher photoresponse (Reprinted from<sup>350</sup> with permission from The Royal Society of Chemistry); c) Detection of N glycan on ZnO<sub>2</sub>/CdTe/GMSNs electrode modified with GQD@conA (Reprinted from<sup>356</sup> with permission from American Chemical Society); d) Two-channel approach for detecting AFB1 (Reprinted from<sup>328</sup> with permission from American Chemical Society).

### 2.5.4 In situ induction of light

In conventional PEC biosensing, an external light-source is used for optical excitation, which imposes additional complexities for miniaturizing the biosensing platform<sup>221</sup>. Elimination of the external light source is often achieved by employing chemiluminescence (CL) in the PEC biosensor for generating *in situ* light of various emission wavelengths<sup>332,364</sup>. In an assay of this type, prostate specific antigen (PSA) was captured and labelled in a sandwich assay with Au NPs modified with glucose oxidase (pAb<sub>2</sub>-AuNP-GOx).<sup>365</sup> GOx generates H<sub>2</sub>O<sub>2</sub> enhancing the CL of the system, which in turn increases the photovoltage generated on the graphene oxide-doped BiVO<sub>4</sub> photoelectrode (Figure 2.8a). This system showed a detection limit of 3 pg/mL and good specificity against CEA and AFP. A similar approach was used in a paper-based PEC biosensor with porous Au/ SnO<sub>2</sub>/rGO photoelectrodes for detecting ATP<sup>366</sup>. In this assay, the aptamer for ATP detection was split into two oligonucleotides. One of them (SSDNA1) were immobilized initially at the electrode surface and the other (SSDNA2) was conjugated with luminol and GOx into Fe<sub>3</sub>O<sub>4</sub>@Au NP. This nucleotide conjugate NP was brought to the electrode surface following the ATP introduction and thereby formed the complex shown in Figure 2.8b. Once GOx is bound to the electrode, it catalyzes the CL reaction by generating H<sub>2</sub>O<sub>2</sub>, which further reacts with the luminol. The sensing platform demonstrated a limit-of-detection of 0.025 pM with specificity against guanosine triphosphate (GTP), cytidine triphosphate (CTP) and uridine triphosphate (UTP). A proof-of-concept PEC DNA assay was also shown using this approach on CdS/MoS<sub>2</sub> photoelectrodes<sup>237</sup>. In this assay, target DNA is captured using an immobilized hairpin probe. Following the target-induced unfolding of the probe, the target DNA is displaced by a hemin-labeled DNA recycling probe. Hemin catalyzes luminol oxidation and generates CL, exciting the photoelectrode. This assay demonstrated a limit-of-detection of 0.39 fM and specificity against other forms of DNA (smDNA, tmDNA). The elimination of external light source makes this form of signal transduction appealing for the development of point-of-care devices. Yet another advantage of this method lies in the tunability of chemiluminescence by changing environmental factors such as the concentration of oxidizing species, environmental pH value, hydrophobicity of the solvent, and solution composition<sup>367-369</sup>.

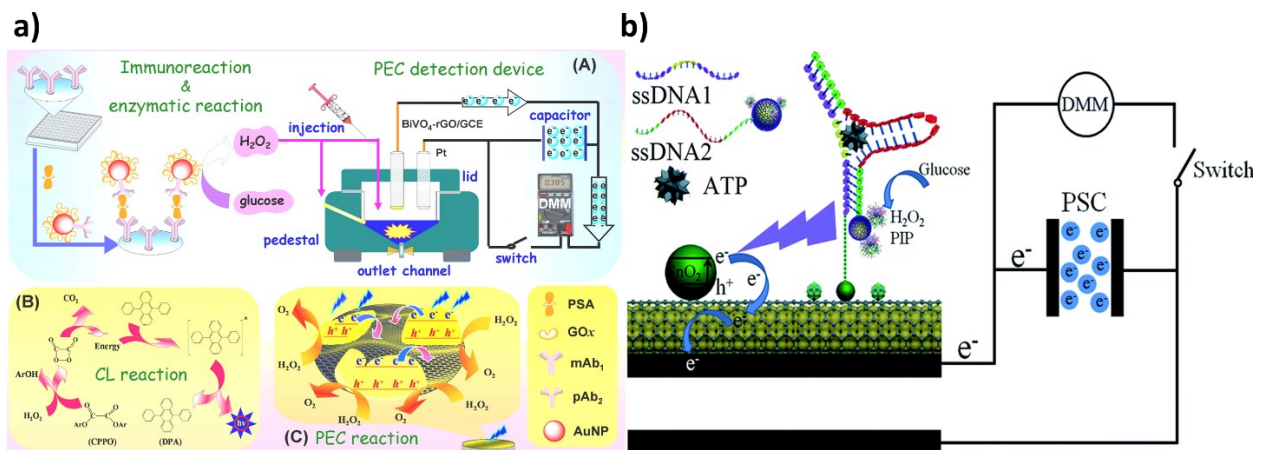


Figure 2.8 In situ generation of light. a) PSA detection by coupling H<sub>2</sub>O<sub>2</sub> – triggered peroxyoxalate self-illuminated system with an external capacitor on the photoanode and digital multimeter as readout device (Reprinted from<sup>365</sup> with permission from American Chemical Society); b) Schematic of the photocurrent generation mechanism in the modified paper sample zone of the Au-PWE under a CL light source (Reprinted from<sup>366</sup> with permission from Royal Society of Chemistry).

The signal transduction strategies elaborated thus far involved the reaction of photoactivated excitons with solution-based electron donors and acceptors to generate a measurable photocurrent, i.e, the signaling strategy established was based on the direct interfacial electron transfer between the photoactive material and ambient environment. The following section discusses signal transduction

based on resonance energy transfer that involves the transfer of acquired *electronic energy* following photo-excitation.

### 2.5.5 Resonance energy transfer

A powerful mechanism for modulating the PEC activity of the photoactive material in response to biorecognition is resonance energy transfer (RET)<sup>370</sup>. In this approach, the biorecognition event serves as a mediator to bring a noble-metal NPs (Generally Au or Ag) to the proximity of the photoelectrode<sup>332</sup>. Noble-metal NPs have very high extinction coefficients<sup>371</sup> and can function as either signal quenchers<sup>372</sup> or amplifiers<sup>373</sup> depending on the distance between the metal and the other photoactive materials. If the absorption spectrum of the metal NP overlaps with the emission spectrum of the photoactive material, a significant portion of the exciton energy is transferred to the metal NPs, subsequently decreasing the photocurrent<sup>374</sup>. However, when excited at plasmonic absorption wavelengths, a high electric field can surround the metal NPs and enhance the photocurrent generated by the photoactive material<sup>375</sup>. In these assays, metal NPs are excited by the emission of the semiconductor already present in the electrode which is different from the approach where to enhance the PEC current, metal NPs are introduced during biomolecule recognition followed by external light as described in section 4.1.

Semiconductor QDs are commonly used as photoactive materials for electrodes in this approach because it is possible to tune their emission wavelength by varying their size. Mi-RNA detection has been shown by using RET between CdS QDs and Ag NPs under the illumination at a wavelength of 410nm<sup>376</sup>. As shown in Figure 2.9a, target microRNA induces conformational change in the Au NP labelled hairpin probe deposited on CdS QD. ALP causes Ag deposition on the Au NPs, which significantly amplifies the signal decrease that is measured on the photoelectrode. This assay has demonstrated a detection limit of 0.2 fM with a linear range of 1 fM - 100 pM. The same group has also shown DNA detection without the Ag deposition-induced amplification strategy<sup>377</sup> using CdS QDs and Ag NPs and achieved a limit-of-detection of 0.3 pM and a linear range of 1 pM - 10 nM. Ma *et al.* also used energy transfer between CdS QDs and Ag NPs to detect tata binding protein<sup>378</sup> and achieved a limit-of-detection of 1.28 fM (linear range of 2.6 fM - 512.8 pM). The CdS QDs used in this work have an emission peak around 530 nm which overlaps with the absorption peak of Au NPs. DNA hybridization was used to bring Au NP into the proximity of the semiconductor QDs (Figure 9b). Tata binding protein can further bend this dsDNA structure and bring Au NPs even closer to the CdS QDs. The TATA binding protein increases the signal attenuation due to the combined effect of RET and steric hindrance. This assay showed excellent selectivity against AFP, CEA, lysozyme, PSA, and thrombin.

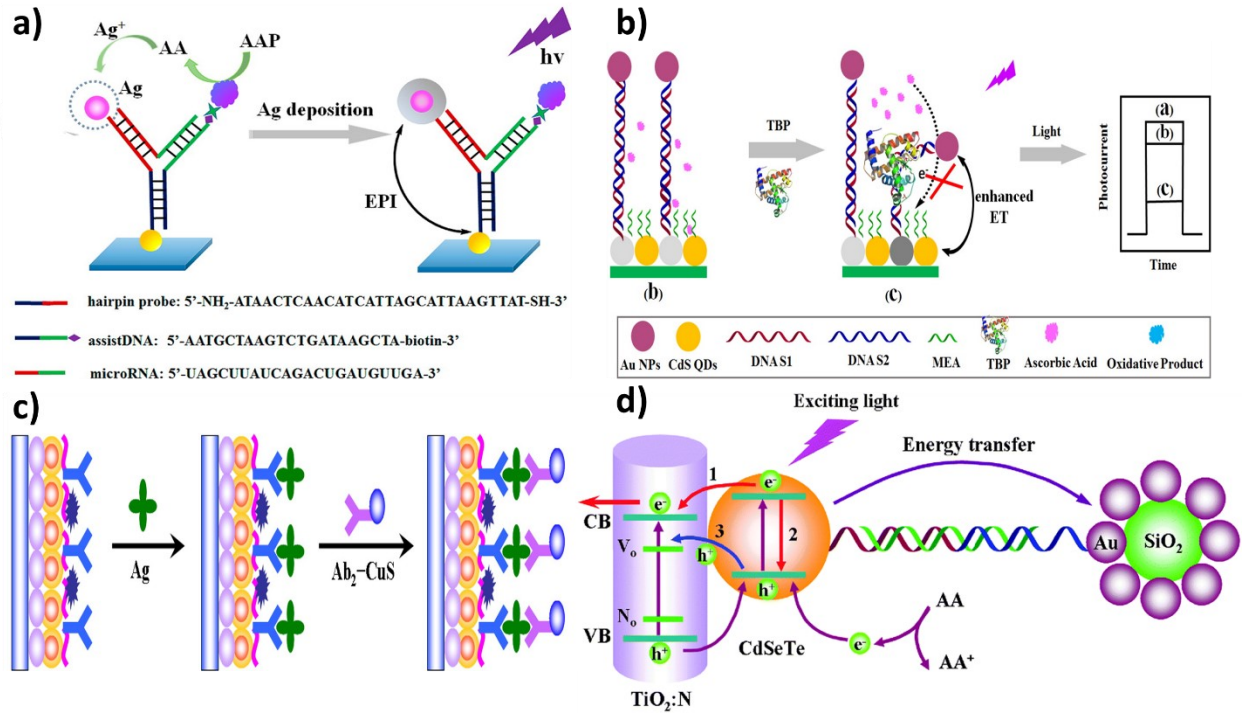


Figure 2.9 Resonance energy transfer based photoelectrochemical biosensors: a) Energy transfer between CdS QDs and Ag NPs upon the ALP induced Ag deposition on Au NPs (Reprinted from <sup>376</sup> with permission from American Chemical Society); b) Tata binding protein bends the double-stranded DNA structure and brings CdS QD and Au NPs closer (Reprinted from <sup>378</sup> with permission from American Chemical Society); c) Schematic illustration of the signal-off sandwich type immunoassay was developed by using CuS nanocrystals as photocurrent quencher for early detection of CEA (Reprinted from <sup>379</sup> with permission from American Chemical Society); d) Thrombin detection using a PEC aptasensing platform based on exciton energy transfer between CdSeTe alloyed quantum dots and  $SiO_2@Au$  nanocomposites. In this approach, RET significantly reduces the photocurrent, which is then quickly restored following the target's competitive binding and subsequent release of the metal NP tagged capture probe (Reprinted from <sup>380</sup> with permission from The Royal Society of Chemistry).

Although Au and Ag NPs are the most popular materials used for RET-based PEC biosensing, other materials can also be used in these assays. For example, a signal-off sandwich-type immunoassay was developed by using CuS nanocrystals as the photocurrent quencher for early detection of CEA on CdSeTe@CdS:Mn-sensitized  $TiO_2$  NPs <sup>381</sup>. In this assay, CEA target antigens were captured using anti-CEA antibodies immobilized on the electrode surface, and a signaling antibody labelled with CuS was introduced to reduce the PEC current (Figure 2.9c). A limit-of-detection of 0.16 pg/mL with a linear range from 0.5 pg mL<sup>-1</sup> to 100 ng mL<sup>-1</sup> were achieved using this assay. The specificity of this assay was validated against PSA, AFP, carbohydrate antigen 19-9 and 15-3.

PEC biosensors that operate based on RET are highly sensitive. However, many of the RET biosensing assays reported to date are signal-off <sup>332</sup>. It is possible to design a signal transduction method based on RET where the photocurrent is initially reduced and is *turned on* following target capture and the resultant removal of the metal NP <sup>382,383</sup>. Thrombin detection was demonstrated using this approach where AuNP-decorated  $SiO_2$  nanoparticles were initially immobilized on CdSeTe QD-photoelectrodes through a dsDNA construct containing a thrombin-selective aptamer. Upon target capture, the signal diminishing Au NPs were removed from the electrode vicinity and a limit-of-detection of 2.8 fM with a linear range of 10 fM - 50 pM was achieved <sup>380</sup> (Figure 2.9d). Consequently, it is possible to combine the high sensitivity of RET with reliability of signal-on sensing to create a high-performance biosensor.

Table 2.2 Summary of the recent affinity-based PEC biosensors

Photoactive Material	Target	Sensing Approach	Transduction mechanism	LOD, linear range	Reference	
AgI/Ag/BiOI	IgG	Immunosensor, Signal on	Introduction of photoactive species	100 fg mL <sup>-1</sup> 100 fg mL <sup>-1</sup> - 100 ng mL <sup>-1</sup>	342	
TiO <sub>2</sub> -CdS	Estradiol	Immunosensor, Signal off		2 pg mL <sup>-1</sup> 5 pg mL <sup>-1</sup> - 4 ng mL <sup>-1</sup>	384	
Donor-Acceptor-type PTB7-Th	Thrombin	Aptasensor, Signal on		34.6 fM 100 fM - 10 nM	385	
CdS NPs	Oligonucleotides	DNA sensor		-	386	
(PAAD)@TiO <sub>2</sub> CAM, g-C <sub>3</sub> N <sub>4</sub> , CS-AgI	PSA, IL-6	Immunosensor, Signal polarity change.		3.3×10 <sup>-5</sup> pg mL <sup>-1</sup> , 10 - 90 pg mL <sup>-1</sup> (IL-6) 3.3×10 <sup>-3</sup> pg mL <sup>-1</sup> , 10 <sup>-6</sup> - 90 ng mL <sup>-1</sup> (PSA)	334	
CdS QDs/ NPC-ZnO	miRNA-155	DNA sensor, Signal on		49 aM 0.1 fM - 10 nM	341	
CdS/TiO <sub>2</sub> , CdTe QDs	Insulin	Immunosensor, Signal on		3fM 10 fM to 10 nM	312	
Cationic polyfluorene derivative	Breast cancer cells (SKBR-3)	Cytosensor, Signal on		24 cells/mL <sup>-1</sup> 1.0×10 <sup>2</sup> to 5.0×10 <sup>5</sup> cell mL <sup>-1</sup>	333	
TiO <sub>2</sub> /ITO, Au NPs, [Ru(bpy) <sub>3</sub> ] <sup>3+</sup>	DNA	Peptide sensor, Signal on		5.0 × 10 <sup>-3</sup> U mL <sup>-1</sup> 10 - 50 U mL <sup>-1</sup>	387	
TiO <sub>2</sub> /Au, CuInS <sub>2</sub> /ZnS (ZCIS) QDS	miRNA-21	Aptasensor, Signal on		0.31 pM 1 pM - 100 nM	340	
CdTe, MB	miRNA-141	Aptasensor, signal on		17 aM 50 aM -50 pM	232	
MoS <sub>2</sub> /g-C <sub>3</sub> N <sub>4</sub> /black TiO <sub>2</sub> , Au NPs	miRNA	Aptasensor, Signal off		0.13 fM. 0.5 fM - 5000 fM	238	
GO/g-C <sub>3</sub> N <sub>4</sub>	Kanamycin	Aptasensor, Signal on		0.2 nM 1 nM - 230 nM	388	
TiO <sub>2</sub>	miRNA	DNA sensor, Signal Off-On		20 fM	389	
MB	miRNA	DNA sensor, Signal on		27 aM 80 aM -10 pM	390	
CdS/TiO <sub>2</sub> NT	cTnI, CRP	Immunosensor, Signal on		Generation of electron/hole donor	0.1 ng mL <sup>-1</sup> , 1 ng mL <sup>-1</sup> - 0.01 mg mL <sup>-1</sup> (cTnI). 50 ng mL <sup>-1</sup> , 100 ng mL <sup>-1</sup> - 0.1 mg mL <sup>-1</sup> (CRP)	346
NaYF <sub>4</sub> :Yb,Tm@TiO <sub>2</sub>	CEA	DNA sensor, Signal on			3.6 pg mL <sup>-1</sup> 10 pg mL <sup>-1</sup> to 40 ng mL <sup>-1</sup>	316
Au NPs, MoS <sub>2</sub>	mi-RNA	DNA sensor, Signal off		4.21 fM 10 fM-1 nM	237	

WS <sub>2</sub> , Au NP	MCF-7 cells	Aptasensor, Signal off	Steric-hindrance	21 cells mL <sup>-1</sup> 1x10 <sup>2</sup> to 5x10 <sup>6</sup> cells mL <sup>-1</sup>	391
AuNP/g-C <sub>3</sub> N <sub>4</sub>	PNK	Aptasensor, Signal off		1 mU mL <sup>-1</sup> 2 to 100 mU mL <sup>-1</sup>	358
Au NPs, TiO <sub>2</sub>	p53	Immunosensor, Signal off		0.05 ng mL <sup>-1</sup> 20 – 100 ng mL <sup>-1</sup>	392
Ag NPs, TiO <sub>2</sub>	AFB1	Aptasensor, Signal off		2.5×10 <sup>-4</sup> ng mL <sup>-1</sup> 1.0×10 <sup>-3</sup> -1.0×10 <sup>3</sup> ng mL <sup>-1</sup>	361
Graphene loaded carbon QDs, g-C <sub>3</sub> N <sub>4</sub>	E. Coli	Aptasensor, Signal off		0.66 cfu/mL 2.9 cfu/mL to 2.9x10 <sup>6</sup> cfu/mL	362
CuO nanopyramid-island, AO	ALP	Immunosensor, Signal off		0.33 U L <sup>-1</sup> 0.5 to 40.0 U L <sup>-1</sup>	393
TiO <sub>2</sub> sensitized with ZnIn <sub>2</sub> S <sub>4</sub>	Early apoptotic HL-60 cells	Aptasensor, Signal off		3 cells mL <sup>-1</sup> 1×10 <sup>3</sup> -5×10 <sup>7</sup> cells mL <sup>-1</sup>	355
ZnO, Au nanorods, CdTe QD	MCF-7	Aptasensor, Signal off		21 cells mL <sup>-1</sup> 63–1.0×10 <sup>7</sup> cells mL <sup>-1</sup>	356
TiO <sub>2</sub> /CdS:Mn, CuInS <sub>2</sub> nanoflower	PSA	Aptasensor, Signal off		0.32 pg mL <sup>-1</sup> 1 pg mL <sup>-1</sup> to 100 ng mL <sup>-1</sup>	394
CdS, Au NP	PSA	Aptasensor, Signal off		1.8 pg mL <sup>-1</sup> 0.005 ng mL <sup>-1</sup> - 50 ng mL <sup>-1</sup>	359
AgInS <sub>2</sub> NP	CCRF-CEM cells	Aptasensor, Signal off		16 cells mL <sup>-1</sup> 1.5 × 10 <sup>2</sup> to 3.0×10 <sup>5</sup> cells mL <sup>-1</sup>	357
CdS-MoS <sub>2</sub> QD	DNA	DNA sensor, Signal On		0.39fM 1fM -100pM	237
TiO <sub>2</sub> -CdS:Mn	PSA	Immunosensor, Ratiometric		0.32 pg/mL 1 pg/mL - 100 ng/mL	395
p-CuBi <sub>2</sub> O <sub>4</sub> -Au NP	AFP	Immunosensor, Signal Off		14.7 pg/mL 50 pg mL <sup>-1</sup> - 20 ng mL <sup>-1</sup>	234
TiO <sub>2</sub> -EG-ZnIn <sub>2</sub> S <sub>4</sub>	Apoptotic cells HL-60	Immunosensor, Signal Off		158 cells/mL 1000 – 50x10 <sup>7</sup>	355
TiO <sub>2</sub> Nanoneedles @MoO <sub>3</sub>	RAW264.7 Macrophage Cells	Immunosensor, Signal Off		50 cells/mL 50 cells/mL-1500 cells/mL	349
ZnO spheres Au nanorod- CdTe QDs	Breast cancer cells (MCF-7)	Immunosensor, Signal Off		21 cells/mL 100 - 10 <sup>7</sup> cells per mL.	356
t-mercaptopropionic acid capped AgInS <sub>2</sub> NP	Tumor cells	Aptamer sensor, Signal Off		16 cells/mL 1.5 × 10 <sup>2</sup> - 3.0 × 10 <sup>5</sup> cells/mL	357
CdS-TiO <sub>2</sub>	CEA	Dnazyme sensor, Signal Off		70 ag/ mL, 70 ag/mL – 500 fg/mL	396

CdTe, CdTe-GO	AFBI	Aptasensor, Simultaneous signal on-off	In-situ induction of light	10 pg mL <sup>-1</sup> 10 pg mL <sup>-1</sup> to 100 ng mL <sup>-1</sup>	328
BiVO <sub>4</sub> -rGO- AuNP	PSA	Immunosensor, Signal On		3 pg/mL 10 pg/mL- 80 ng/mL	365
SnO <sub>2</sub> QD-RGO	ATP	Aptamer sensor,		0.025 pM 0.1 pM -100 nM	366
CdS-Ag NP	Micro RNA/ ss DNA	Aptamer sensor, Signal Off	Resonance Energy Transfer	0.2 fM 1fM- 100 pM 0.3 pM 1pM – 10nM 0.1 fM	376,377
CdS- AuNP	Thrombin TATA binding protein	Aptamer sensor, Signal Off		1 fM- 10 pM 50 fg/mL 100 fg/mL – 10 ng/mL	378,397
TiO <sub>2-x</sub> - AuNP	ss DNA	DNA sensor, Signal On		0.6 pM 1 pM-10 nM	398
CdSeTe-SiO <sub>2</sub> @Au	Thrombin	Aptamer sensor, Signal On		2.8 fM 10 fM-50 pM	380

## 2.6 Challenges and Future Perspectives

Affinity based biosensors using photoelectrochemistry as their transduction mechanism have garnered a lot of interest over the past decade due to their exceptional limit-of-detection. Biosensor development starts with considering the target analyte of interest, required limit-of-detection and specificity, interference caused by the native sample, and constraints of the operating environment (point-of-care, lab-based, resource poor compatible). This review aims at helping the reader choose the building blocks – materials and signal transduction mechanisms – of a PEC biosensor based on the constraints imposed by the application.

Inorganic and organic semiconductors are used as the photoactive building blocks for PEC biosensors. In PEC devices, photoactive materials are primarily chosen based on their efficiency in converting optical energy to electrochemical current or voltage. Using these materials in PEC *biosensing* adds additional requirements in terms of stability, size/structure, integration, cost, and functionalization. Given that photoactive materials used in PEC biosensing directly interact with nanoscale biomolecules, solution-processed photoactive *nanomaterials* that can be readily used as labels, reporters, or building blocks for the photoelectrode are primarily used in these systems. An important challenge with using these materials is their varying performance and stability in biosensing conditions that often require operation in complex biological environments and under stringent washing protocols. Affinity-based PEC biosensors operate by measuring signal changes that occur upon target binding; consequently, the lack of stability can cause non-target related signal changes, leading to false-positive or false-negative results. A key development towards the practical use of PEC biosensors involves incorporating *in situ* calibration measures in the PEC system to account for signal variations that are caused by the instability of photoactive materials. It is also critical to integrate functionalized photoactive materials into biosensing chips, strips, or cartridges using fabrication methods that are amenable to large volume processing.

We have reviewed the five most widely used signal transduction mechanisms used in PEC biosensing: introduction of photoactive species, generation of electron/hole donating species, use of steric hindrance, *in situ* induction of light, and resonance energy transfer. It is evident that it is possible to use any of these mechanisms to detect various classes of targets including nucleic acids, proteins, and cells. Additionally, a low limit-of-detection is possible using all of these assays. However, these assays vary greatly in terms of their fabrication and operation complexity. Ultimately, biosensing devices that are fabricated using scalable materials and methods have a higher chance for commercialization. Additionally, assays that can be operated using robust reagents in a simple and rapid one-pot manner have a higher chance for wide-scale adoption and success compared to those that require a sequence of

washing and labeling steps. Consequently, choosing the right transduction method can be achieved by considering the collective requirements of a biosensing platform for use in real-life settings.

### **Chapter 3: Engineering a robust three-dimensional transducer for signal-off PEC biosensing (Objective 1)**

### **Chapter 4: Examining Au coverage density to design signal-on PEC TiO<sub>2</sub> architectures for biosensing (Objectives 2, 3)**

#### ***Preface***

While Chapter 3 demonstrated the development of novel surface functionalized TiO<sub>2</sub> NPs for creating high performance photoelectrodes, the biosensing system demonstrated here operated in a signal-off format. Label-free methods reliant on direct binding mechanisms for transduction, such as the signal-off DNA assays based on steric hinderance, are often susceptible to low analytical performance. The reason for this is two-fold – (1) as target detection is indicated by the decrease in a baseline signal (i.e., PEC/EC current), a magnitude of change beyond complete signal suppression is impossible thereby limiting detection sensitivity (nano- to picomolar range)<sup>127,144,145</sup>; and (2) non-specific adsorption by contaminants in biological matrices increase false-positive outcomes, thus compromising reliability and selectivity.<sup>138,143</sup> In order to enhance the analytical performance of the TiO<sub>2</sub> photoelectrodes demonstrated in Chapter 3, such that it may be a useful tool to build POC molecular diagnostics, it is critical to construct signal-on modalities using the same material system.

Au NPs have been widely used to modulate the PEC current of TiO<sub>2</sub> photoelectrodes in energy conversion and sensing systems. As such, we looked to Au NPs to explore whether the system could be translated to a signal-on format. Understanding the different mechanisms responsible for photocurrent modulation at different frequencies is important for building optimized PEC systems. This chapter, thus, discusses the use of two different illumination modes (UV and visible) to investigate the influence of Au NP density on PEC current generation by modifying the surface loading of Au at TiO<sub>2</sub>. It was revealed that by controlling surface density of Au, vastly different signal responses (signal-on and signal-off) can be attained at each light regime. The bimodal signal modulation resulting from this mechanistic investigation was subsequently harnessed to demonstrate a proof-of-concept DNA biosensor, where both *signal-on and signal-off* responses could be elicited on the same electrode by merely switching the illumination wavelength. The insight gained in this chapter, thus, contributes to objectives 2 and 3 as outlined in this thesis.

#### ***Authors***

Sudip Saha\*, Amanda Victorious\*, and Leyla Soleymani.

(\*indicates that Amanda Victorious and Sudip Saha contributed equally to this authorship and are co-first authors).

Here, I fabricated baseline electrodes by first patterning ITO onto glass slides, and then depositing DHB-CHIT-P25 (from the previous paper) NPs onto these ITO/glass substrates, following by baking of the substrates. Once fabricated, I modified the baseline electrodes by depositing gold NPs, previously synthesized by myself according to existing literature, onto the baseline electrodes for deposition times spanning from 5 to 45 min. Once synthesized, I carried out PEC characterization using chopped light amperometry under UV (397 nm) and visible excitation (540 nm) to observe the effect of Au surface density on photocurrent generation (Figure 4.2(b,c)). Subsequently, under the supervision of Dr. Saha, I performed Mott Schottky experiments on the baseline and Au modified photoelectrodes to correlate alterations to the flat band potential with increasing Au NP surface density (Figure 4.3(b)). Following this, I also measured the charge transfer resistance of the electrodes using electrochemical impedance spectroscopy for the baseline electrodes as well as those modified with Au for 5 minutes (Figure S4.3; baseline and 5 mins). Following photoelectrode characterization, I designed a DNA detection assay where detection of a gold labelled single stranded DNA strand would trigger signal-off (signal decrease) and signal-on (signal increase) response on the same electrode. Using this design, I fabricated electrodes and carried out DNA detection experiments on the baseline electrodes (DHB-CHIT-P25 without gold NP deposition) as illustrated in figure 4.5(a). In addition to experimentation, I also collaborated with

Dr. Saha to jointly come up with the hypothesis explaining the ongoing charge transfer mechanisms in this Au/TiO<sub>2</sub> system.

To summarize, I designed and performed the experimentation, data analysis, figure creation and manuscript write up for figures: 4.1(a), 4.2 (b,c), 4.5(a) in the main manuscript and data collection *only* for figure 4.3b (under the supervision of Dr. Saha). The rest of the data collection, design and data analysis was performed by Dr. Saha.

***Publication***

Electrochimica Acta 2021, 380, 138154

***Publication Date***

June 2021

#### 4.1 Abstract

Gold (Au) nanoparticles (NPs) have been widely used to modulate the photoelectrochemical current of TiO<sub>2</sub> photoelectrodes in energy conversion and sensing systems. Understanding the different mechanisms responsible for photocurrent modulation at different frequencies is important for building optimized photoelectrochemical systems. Herein, we investigated the photocurrent magnitude at different excitation wavelengths by varying Au NP concentration at the photoelectrode surface. Under UV illumination, increasing the surface loading of Au NPs initially increased the photocurrent, and above a threshold loading level, decreased the measured photocurrent. However, under visible light excitation, increasing the Au NP surface density resulted in a steady increase in photocurrent. Mott-Schottky measurements, incident photon to current conversion efficiency measurements, and electrochemical impedance spectroscopy were used to understand the mechanisms responsible for these different observations. It was found that both current loss – due to reduced light absorption by TiO<sub>2</sub> – and gain – due to direct charge transfer between Au and TiO<sub>2</sub> NPs were possible under UV light. Under visible light illumination, strong light absorption and localized surface plasmon resonance of Au NPs and negligible light absorption by TiO<sub>2</sub> NPs led to signal gain at varying Au NP surface concentrations. This bimodal signal modulation was further demonstrated in the context of biosensing using Au NP-labeled DNA barcodes, optically excited at different wavelengths. This study allows photoelectrochemical systems to be engineered for programmable signal-off, signal-on, or ratiometric biosensing combining the former sensing modes.

#### 4.2 Introduction

Titanium dioxide (TiO<sub>2</sub>) is among the most widely used semiconductive materials for photocatalysis and photoelectrochemistry<sup>484–486</sup>. TiO<sub>2</sub> nanoparticles (NPs) have recently attracted tremendous attention for use in the abovementioned areas, compared to bulk TiO<sub>2</sub>, because of their high surface-to-volume ratio, enhanced light absorption, and increased optically-excited carrier density<sup>487</sup>. In spite of this, TiO<sub>2</sub> NPs present low quantum efficiency and poor visible light absorption<sup>488</sup>. Plasmonic metal NPs such as gold (Au), silver (Ag), and platinum (Pt) have been previously used in conjunction with TiO<sub>2</sub> NPs to improve their quantum efficiency and visible light absorption<sup>489,490</sup>. The interaction between TiO<sub>2</sub> NPs and these plasmonic NPs is guided by their complementary optical properties: well-separated and long-lived excitons in semiconductors and localized electromagnetic modes in plasmonic NPs<sup>491</sup>. The integration of these two classes of NPs allows researchers to tailor and engineer materials systems with specific optical properties based on exciton–plasmon interactions. Au NPs have drawn a lot of interest when used in direct contact or close proximity to TiO<sub>2</sub> surfaces due to their photochemical and chemical stability, ease of preparation, and tailorable electronic and optical properties<sup>492</sup>. The complexes resulting from the incorporation of Au NPs on TiO<sub>2</sub> surfaces have been extensively explored to enhance photoelectrochemical (PEC) activity<sup>493–495</sup>. Various theories have been put forth to explain the enhancement demonstrated in these systems, which include the electron-sink effect, enhanced conductivity due to improved interfacial charge separation<sup>496</sup>, reduced bandgap energy of the resultant complex<sup>497</sup>, plasmon-induced resonance energy transfer<sup>498</sup>, and electric field amplification<sup>494</sup> to name a few.

Systems that use the direct contact of Au NPs with TiO<sub>2</sub> electrodes for PEC signal enhancement, require an optimized surface density of Au NPs for maximizing the PEC current. Rayalu et. al varied Au NP loading from 2.5% to 10% weight by weight (w/w) with respect to anatase and P25 TiO<sub>2</sub> and studied the effectivity of the resultant complex for photocatalytic water splitting under mercury light illumination<sup>499</sup>. An enhancement in the hydrogen evolution rate and yield, by a factor of 2 and 4 respectively, was exhibited upon increasing the concentration of Au NPs to 4% while an increase in concentration to 5% and beyond resulted in a significant decline in activity and yield. This was thought to be the result of a delicate tradeoff between loading-based enhancement and scattering caused by the increase in Au loading. At lower loading concentrations (4% w/w), the light path of incident radiation remains uninterrupted by the metal NPs. However, increasing the loading concentration (5% and 10% w/w) causes these metal NPs to act as half mirrors capable of reflecting incident radiations, consequently affecting the overall light absorption capacity and catalytic activity of the metal–semiconductor composite. This is in accordance with the report by Murdoch *et al.* where

Au NP loading of only 4 wt% on anatase TiO<sub>2</sub> NPs showed the highest H<sub>2</sub> production rate in a TiO<sub>2</sub>/Au NP system, where further loading of Au NPs reduced the photoreaction rate of hydrogen production<sup>500</sup>. Additionally, Kamat et al. investigated the Au NP loading effect on TiO<sub>2</sub> NPs and also found that the photocurrent under UV light excitation increases only for up to 2 wt% of Au NPs, beyond which a photocurrent decrease was observed<sup>501</sup>. Similar trends have also been observed using TiO<sub>2</sub> nanowires<sup>494</sup>.

The abovementioned studies do not precisely investigate the impact of Au NP concentration in photocurrent enhancement for TiO<sub>2</sub>/Au NP systems under different excitation wavelengths that are linked to distinct interaction mechanisms. In this study, we used two different light excitation modes to understand the effect of Au NP density on PEC current generation. In the same materials system, one wavelength mode probed the localized surface plasmon resonance (LSPR) of Au NPs; whereas the other probed the interband excitation of Au NPs in conjunction with the bandgap excitation of TiO<sub>2</sub> NPs. The new understanding generated here is utilized to design a DNA detection strategy, where both *signal-off* and *signal-on* responses can be achieved from the same electrode simply by changing the excitation wavelength. This bimodal readout system can be exploited for reducing background noise and enhance the sensitivity of the biosensor in the future<sup>502-504</sup>. The knowledge obtained from this study can be further used for effectively programming and predicting the PEC current response of TiO<sub>2</sub>/Au NP systems.

### 4.3 Materials and Methods

#### Chemicals

Phosphate buffer solution (PBS, 1.0M, pH 7.4), L-ascorbic acid (99%), sodium chloride (NaCl), chitosan (CHIT, from shrimp, degree of deacetylation of 85%, Mw=200,000), glacial acetic acid, 3,4-dihydroxybenzaldehyde (DHB), Chloroauric acid (HAuCl<sub>4</sub>), Trisodium citrate, Potassium chloride (KCl), Potassium ferrocyanide (K<sub>4</sub>Fe(CN)<sub>6</sub>), Potassium ferricyanide (K<sub>3</sub>Fe(CN)<sub>6</sub>), poly(diallyldimethylammonium chloride) (PDDA), and tris (2-carboxyethyl) phosphine hydrochloride (TCEP, 98%) were purchased from Sigma-Aldrich. 100 nm Indium Tin oxide (ITO) glass substrates were also bought from Sigma-Aldrich. P25-TiO<sub>2</sub> was obtained from Nippon aerosol Co. Ltd. Acetone and Ethanol were purchased from commercial alcohols (Brampton, ON). Milli-Q grade (18.2 MΩ cm) de-ionized (DI) water was used for all solution preparation and washing steps.

#### Synthesis of TiO<sub>2</sub> and Au nanoparticles (NPs)

Modification of TiO<sub>2</sub> NPs were completed by using the procedure reported earlier<sup>505</sup>. In brief, 16g L<sup>-1</sup> DHB solution was made in de-ionized (DI) water. CHIT solution with a concentration of 3 g L<sup>-1</sup> was made in acetic acid solution (1%). Then, DHB-modified CHIT solution was prepared with mass ratio 4:1 as DHB:CHIT. Finally, 20mg of P25-TiO<sub>2</sub> was added to the previously prepared DHB-modified CHIT solution. DHB enables superior signal generation by improving the electronic and optical properties of TiO<sub>2</sub> NPs<sup>506</sup>, while CHIT aids in the formation of uniform and stable films. The synergistic effects of these two materials were exploited to create a robust and reliable photoelectrode for our experimental design<sup>505</sup>.

The Au NP solution was synthesized according to the protocol reported by Grabar et al.<sup>507</sup>. Briefly, chloroauric acid (HAuCl<sub>4</sub>) of 1 mM was added onto 38.8 mM trisodium citrate solution with 10:1 ratio (volume). The mixed solution was heated at boiling temperature while stirring vigorously for 10 minutes. After that, stirring was continued at room temperature for 15 min. This procedure resulted in Au NPs with a diameter of 12 nm<sup>507</sup>.

#### Electrode fabrication

All ITO substrates were cleaned by sonicating in acetone, ethanol and DI water for 10 minutes. Vinyl tapes were used to mask the electrodes in order to preserve electrode contact area. The electrodes were plasma treated for one minute. Mesoporous P25-TiO<sub>2</sub> films were prepared by drop-casting 10 μl of solution onto the exposed electrode area and heated at 100°C for 5 minutes. The procedure was repeated

three times to deposit 30  $\mu\text{l}$  of P25-TiO<sub>2</sub> solution in total. The electrodes were washed and air dried prior to use.

#### *Photoelectrochemical characterization*

All PEC experiments were performed in a three-electrode cell setup where Ag/AgCl works as the reference electrode and Pt wire works as counter electrode. Zahner potentiostat was used for all the electrochemical and PEC measurements. Optical excitation was obtained using TLS03 LED light source (adjustable wavelength) from Zahner. Zahner CIMPS-QE/IPCE photo-electrochemical workstation was used for PEC measurements. Electrolyte for photocurrent and IPCE measurements consists of 0.1 M ascorbic acid (AA) in 0.1 M PBS solution. Photocurrents were calculated by subtracting the current with light from the dark current without any optical excitation. The measurements were performed under a bias voltage of 0 V vs. Ag/AgCl. Incident-photon-to-current-conversion efficiency (IPCE) was also measured by using the same electrolyte and bias voltage. IPCE can be defined as:

$$\text{IPCE}(\%) = \frac{1240 \times I(\text{A}/\text{cm}^2)}{\lambda(\text{nm}) \times P_{\text{inc}}(\text{W}/\text{cm}^2)} \times 100 \quad (1)$$

Where,  $I$  is the measured photocurrent,  $\lambda$  is the incident wavelength of light and  $P_{\text{inc}}$  is the incident optical power<sup>508</sup>.

#### *Electrochemical Impedance Spectroscopy (EIS) and Mott-Schottky*

EIS measurements were performed at room temperature by using Zahner potentiostat at open circuit potential by using 2 mM ferri/ferro cyanide in 0.1 M KCl as the electrolyte. The frequency range used for EIS was 100 kHz to 0.1 Hz and excitation amplitude was 5 mV. Mott-Schottky experiments were performed at a frequency of 1 kHz and using the same electrolyte and excitation amplitude as EIS.

#### *Scanning Electron Microscopy (SEM)*

The surface structure of the electrodes was visualized using FEI Magellan 400 scanning electron microscope (SEM). A Matlab code was used to calculate the Au NP density. At-least 5 different areas were used to calculate the Au NP density.

#### *Absorption spectroscopy*

UV-Visible (UV-VIS) absorption spectroscopy was performed using an ocean view Flame-S-XR1-ES assembly.

#### *Au NP-DNA conjugation*

For the DNA detection experiment, single-stranded DNA (ssDNA) target was conjugated with Au NPs according to the literature<sup>509</sup>. Briefly, 1 ml of the AuNP solution was (1 nM) suspended in 10 mM PBS buffer (pH 7.0). Target DNA (thiolated) of 100  $\mu\text{M}$  was reduced using TCEP and 35  $\mu\text{l}$  of the reduced DNA was added to the Au NP solution for creating the Au NP-labelled DNA barcode. This solution was then incubated for 16 h at room temperature (RT). After that, 2 M NaCl in 10 mM PBS was added slowly to make the final solution concentration of 0.1 M NaCl. This solution was kept at RT for 40 h while shaking continuously. Finally, the solution was washed with 10 mM PBS and 0.1 M NaCl buffer (pH 7.0).

#### *DNA sensing*

The electrodes were biofunctionalized by depositing ssDNA (1  $\mu\text{M}$ ) probe for 3 h. Following the probe deposition, electrodes were incubated in 100 pM solution of Au NP-labeled target. Electrodes were washed thoroughly between each step. The percentage change ( $\Delta I_{\text{DNA}}(\%)$ ) is calculated as:

$$\Delta I_{\text{DNA}}(\%) = (I_{\text{Target}} - I_{\text{Probe}}) / I_{\text{Probe}}$$

Where  $I_{\text{Probe}}$  and  $I_{\text{Target}}$  are the photocurrents after probe deposition and target hybridization, respectively.

The DNA sequences used in this work are as follows:

15-mer probe: 5'-NH<sub>2</sub>-AGG GAG ATC GTA AGC-3'

Complementary target: 5'-SH-TTT TTT TTT TGC TTA CGA TCT CCC T-3'

Non-Complementary target: 5'-SH-TTT TTT TTT TTT TTT TTT TTT T-3'

#### ***4.4 Results and Discussion***

In order to investigate the effect of Au NP surface density on modulating the PEC properties of TiO<sub>2</sub> NPs, we varied the deposition time of Au NPs (~12 nm, Supplementary Figure S1) from 5 to 45 minutes (Figure 4.1(a)). This in turn increased the surface density of Au NPs on TiO<sub>2</sub> photoelectrodes (Figure 1(b)). These photoelectrodes were created by drop casting a porous network of TiO<sub>2</sub> NPs, integrated within a catecholic polymeric network of chitosan (CHIT) and 3,4-dihydroxybenzaldehyde (DHB), onto conductive indium tin oxide (ITO) supports<sup>505</sup>. DHB enables superior signal generation by improving the electronic and optical properties of TiO<sub>2</sub> NPs<sup>506</sup>, while CHIT aids in the formation of uniform and stable films. The synergistic effects of these two materials were exploited to create a robust and reliable photoelectrode for our experimental design<sup>505</sup>. From the scanning electron micrographs (SEMs) obtained at different deposition time points (Figure 4.1(b)), the amount of Au NPs was calculated as 134, 181, 433 and 623 per μm<sup>2</sup> for 5 min, 10 min, 20 min and 45 min deposition times, respectively. The distance between the nearby Au NPs also decreased with the increase in deposition time.

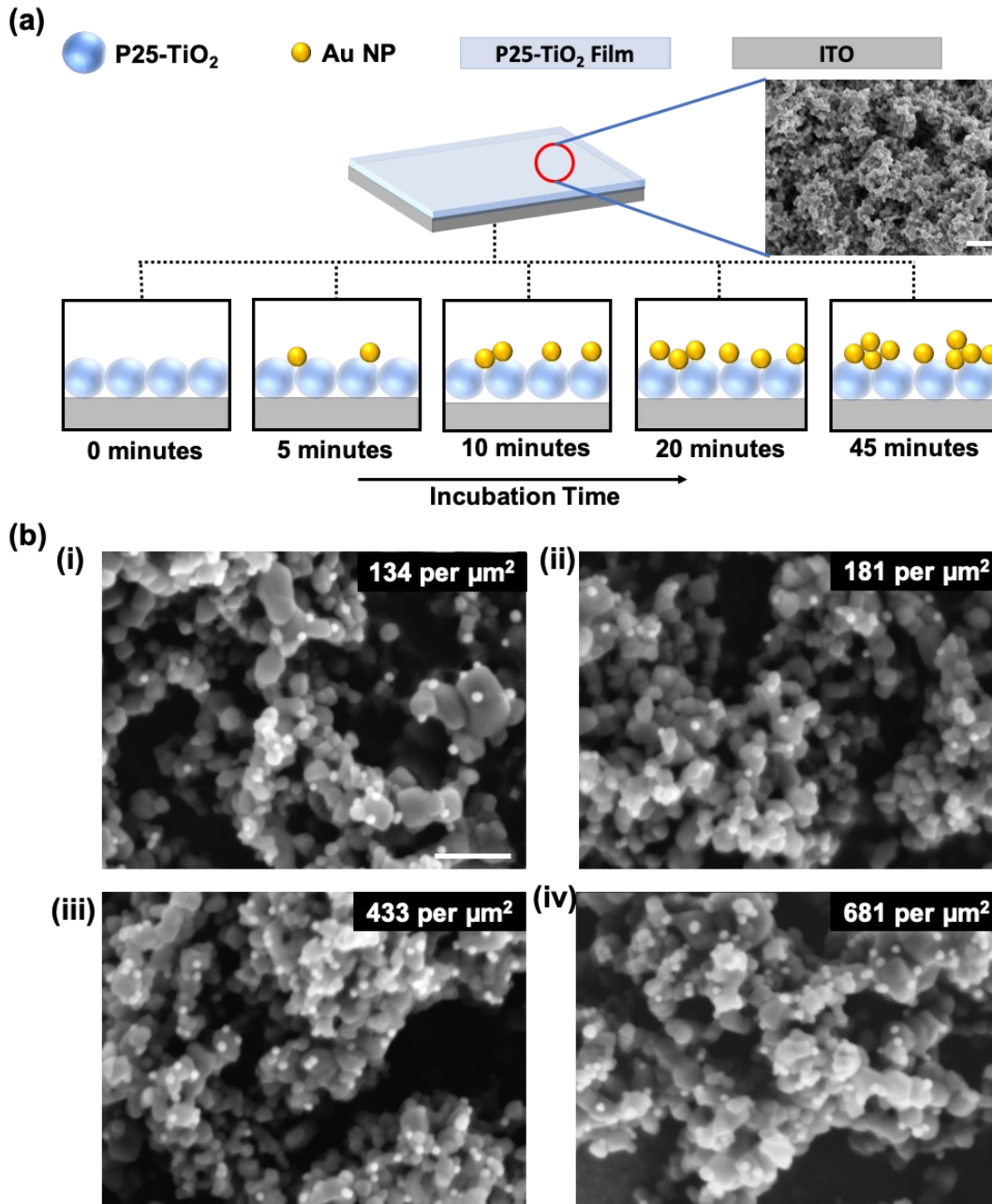


Figure 4.1: Development of the  $\text{TiO}_2$ -AuNP photoelectrodes. (a) Schematic diagram illustrating the Au NP deposition on P25- $\text{TiO}_2$  films by varying the deposition time from 5 minutes to 45 minutes with SEM image of the  $\text{TiO}_2$  electrodes (scale bar represents 200nm); (b) SEM image of the Au NP-deposited P25- $\text{TiO}_2$  electrodes for the deposition times of (i) 5min, (ii) 10min, (iii) 20min, (iv) 45min (scale bar represents 100 nm). The calculated density of Au NPs is shown at the top-right corner of each SEM image.

In this study, we investigated the PEC performance of the  $\text{TiO}_2$ /Au system under two wavelengths: 540 nm and 397 nm (Figure 4.2).  $\text{TiO}_2$  NPs have limited optical response and PEC current generation capability at 540 nm; however, Au NPs have strong absorption at this wavelength due to LSPR (Figure 4.2a), through which *intraband* carriers are generated<sup>510</sup>. The plasmon peak of Au in water occurs at approximately 525 nm (Figure 4.2a). However, as  $\text{TiO}_2$  shifts the plasmon peak of Au NPs<sup>511</sup>, a 540 nm excitation source was used in this work. At 397 nm,  $\text{TiO}_2$  NPs absorb light and generate electron-hole pairs; while *interband* hot carriers are generated in the Au NPs<sup>512,513</sup>. As a result, the 397 nm illumination is expected to generate charge carriers in both  $\text{TiO}_2$  and Au NPs, whereas the 540 nm

excitation is expected to only generate plasmonic hot carriers in Au NPs, which would be subsequently injected as hot electrons into the conduction band of the TiO<sub>2</sub> NPs<sup>514</sup>. We hypothesized the optimal surface concentration of Au NPs in TiO<sub>2</sub>/Au electrodes for PEC current generation to be wavelength dependent because of the strong wavelength dependence of the optical properties of the two materials.

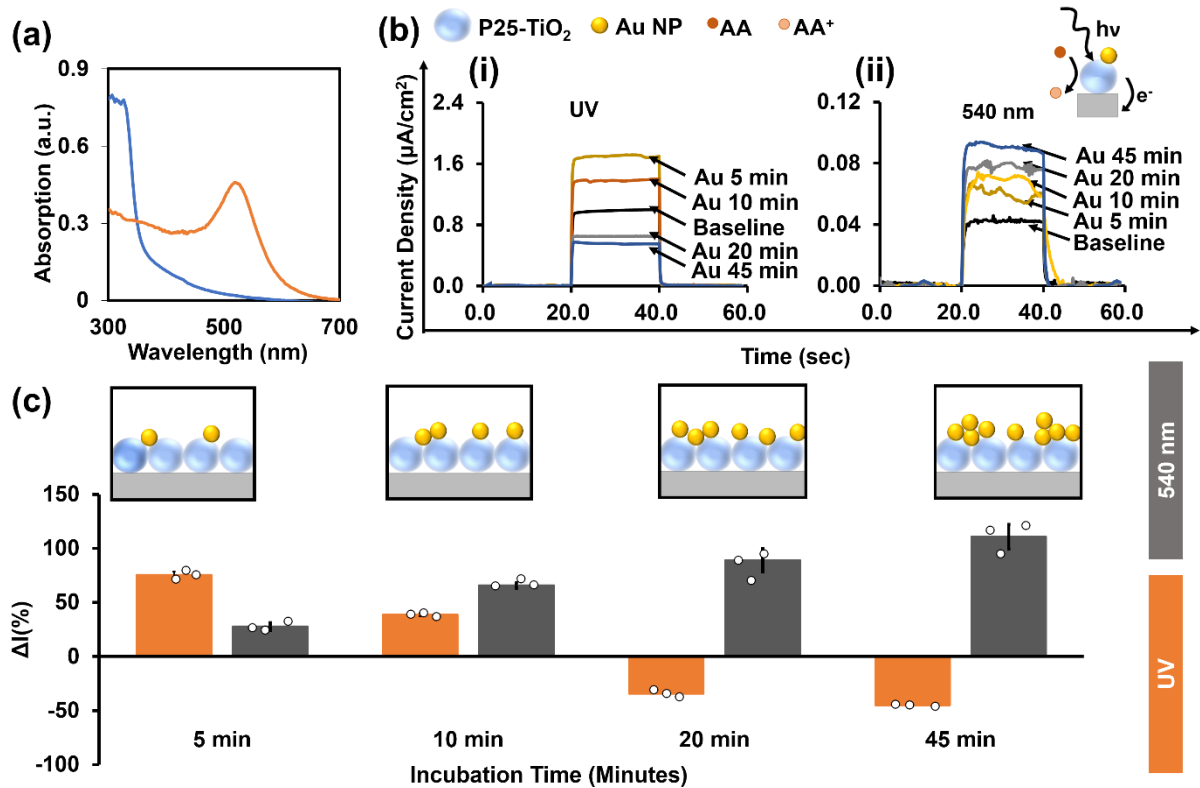


Figure 4.2: Photoelectrochemical characterization of the TiO<sub>2</sub>-AuNP photoelectrodes. (a) Absorption spectrum of TiO<sub>2</sub> NPs and Au NPs (b) Representative PEC curves of the photoelectrode obtained using chopped light chronoamperometry at 0 V bias versus Ag/AgCl at excitation wavelength of (i) 397 nm and (ii) 540 nm. (c) Bar plots summarizing the percentage change in photocurrents of the P25-TiO<sub>2</sub> electrodes following the immersion in Au NP solution. Error bars represent one standard deviation, with experiments performed using at least three separate electrodes.

The photocurrents of the TiO<sub>2</sub>/Au electrodes, with various surface concentrations of Au NPs, were measured under UV (397 nm) and visible (540 nm) illumination (Figure 4.2b), and the percentage change in photocurrent ( $\Delta I$ ) from the baseline photoelectrode (TiO<sub>2</sub> without Au NPs) was plotted for every deposition time (Figure 4.2c). Striking differences are observed in  $\Delta I$  values and trends between UV and visible light excitation. For visible light excitation,  $\Delta I$  increased steadily due to the increase in the Au NP deposition time; However, under UV illumination,  $\Delta I$  decreased starting at 5 minutes with negative values starting at 20 minutes. This indicates that, under UV illumination, increasing the Au NP surface concentration initially increases the photocurrent; however, beyond a certain surface concentration (between 10-20 minutes), it decreases the photocurrent below the baseline level.

We also measured the incident photon-to-electron conversion efficiency (IPCE) spectra of the baseline and TiO<sub>2</sub>/Au electrodes (Figure 4.3(a)). As demonstrated in the PEC measurements, for UV excitation (wavelengths below 450 nm), the IPCE increased from the baseline for the 5-minute Au NP deposition; however, it decreased (from 350-480 nm) with further increases in Au NP deposition times. In contrast, a peak appears in the IPCE spectra at 540 nm which increases from the baseline up until the 45-minute Au NP deposition time.

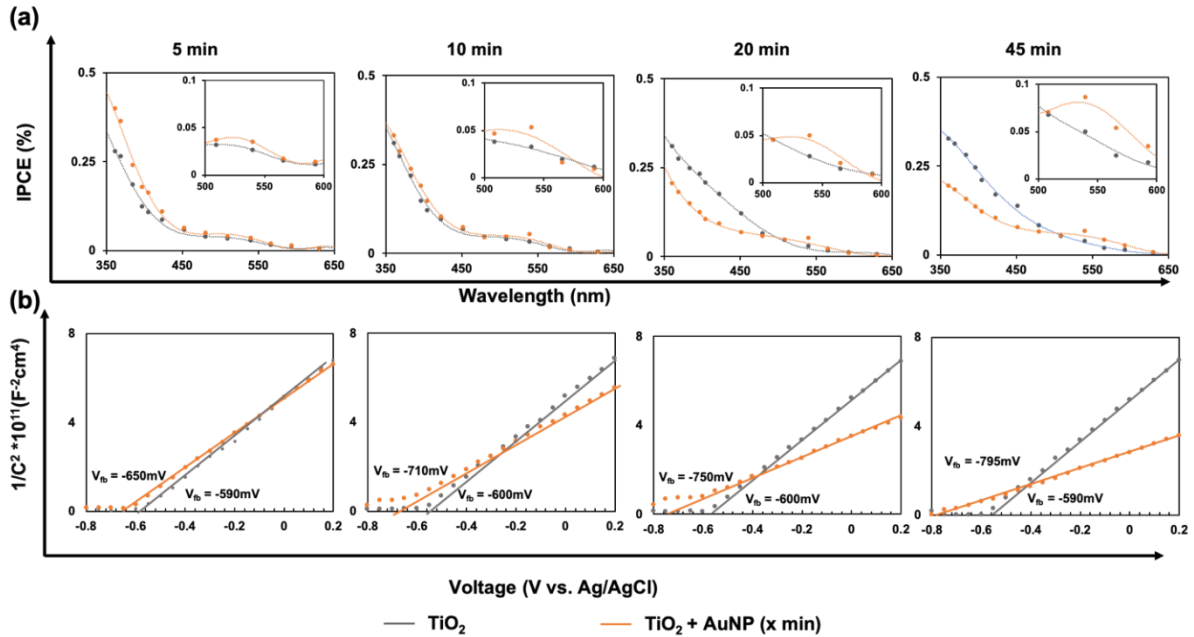


Figure 4.3: Understanding the mechanisms of photocurrent modulation in the TiO<sub>2</sub>-AuNP photoelectrodes. (a) IPCE spectrum of the photoelectrodes before and after Au NP deposition (inset shows zoomed in spectrum from 500 nm to 600nm). (b) Mott-Schottky ( $1/C^2$  vs. voltage) diagram for the photoelectrodes before and after AuNP deposition.

The negative shift in the flat-band potential from the base line value is measured as 60 mV, 110 mV, 150 mV and 205 mV for the 5, 10, 20 and 45-minute Au NP deposition time, respectively (Figure 4.3b). The flat-band potential becomes more negative with the increase in the Au NP density on the electrode. This is expected as the Fermi level of Au lies below the conduction band of TiO<sub>2</sub><sup>515</sup> and the shift of the flat-band potential is the direct consequence of Fermi-level equilibration<sup>516,517</sup>. The negative shift in the flat band potential after the addition of Au NPs to TiO<sub>2</sub> is associated with improved charge separation<sup>501</sup> and reduced charge recombination in the electrode<sup>508,518</sup>. Improved charge separation upon light illumination, through photocharging, enhances AA oxidation, augmenting photocurrent generation<sup>511,519</sup>. Furthermore, the positive slope of the M-S curve indicates that the photoelectrode is n-type<sup>520</sup>. The slope decreases with the addition of Au NPs, which also indicates a higher charge carrier density in the photoanode as the slope of the linear region of the M-S plot is inversely proportional to the electron density of the electrode (Table S1)<sup>521</sup>. This was further confirmed by measuring the charge transfer resistance of the electrodes using electrochemical impedance spectroscopy (Table S1), which showed a lower charge transfer resistance at a higher Au NP surface density (Figure S4.2).

We hypothesize the differences in the trends observed here under UV and visible light to be related to the different mechanisms for current generation under these light excitations. At 397 nm, both TiO<sub>2</sub> and Au NPs are excited. Electron-hole pairs are generated in the TiO<sub>2</sub>, whereas hot electrons and hot holes are induced in Au NPs (d-sp transition). Electrons from the conduction band of TiO<sub>2</sub> move to the Au NPs, which improves charge separation efficiency (Figure 4.4a). However, interband transition in Au NPs is also known to generate highly energetic hot holes and hot electrons that are also capable of taking part in redox reactions<sup>522-524</sup>. These hot holes, generated at the surface of Au NPs, can directly oxidize ascorbic acid (AA) in conjunction with the holes generated in the underlying TiO<sub>2</sub> matrix upon UV excitation (Figure 4.4a)<sup>513,525</sup>. Interband hot electrons may also possess sufficient energy to overcome the Schottky barrier at the TiO<sub>2</sub>/Au interface, causing electrons to move from the Au NPs to TiO<sub>2</sub><sup>526</sup>. This phenomenon can also be responsible for increasing the anodic current generated and collected at the working electrode.

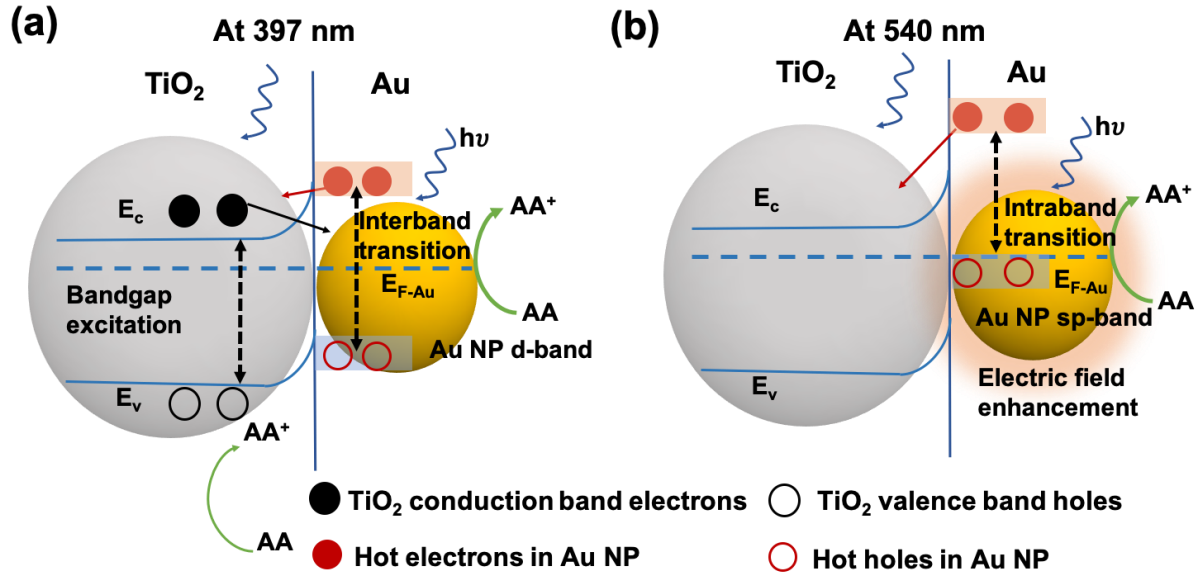
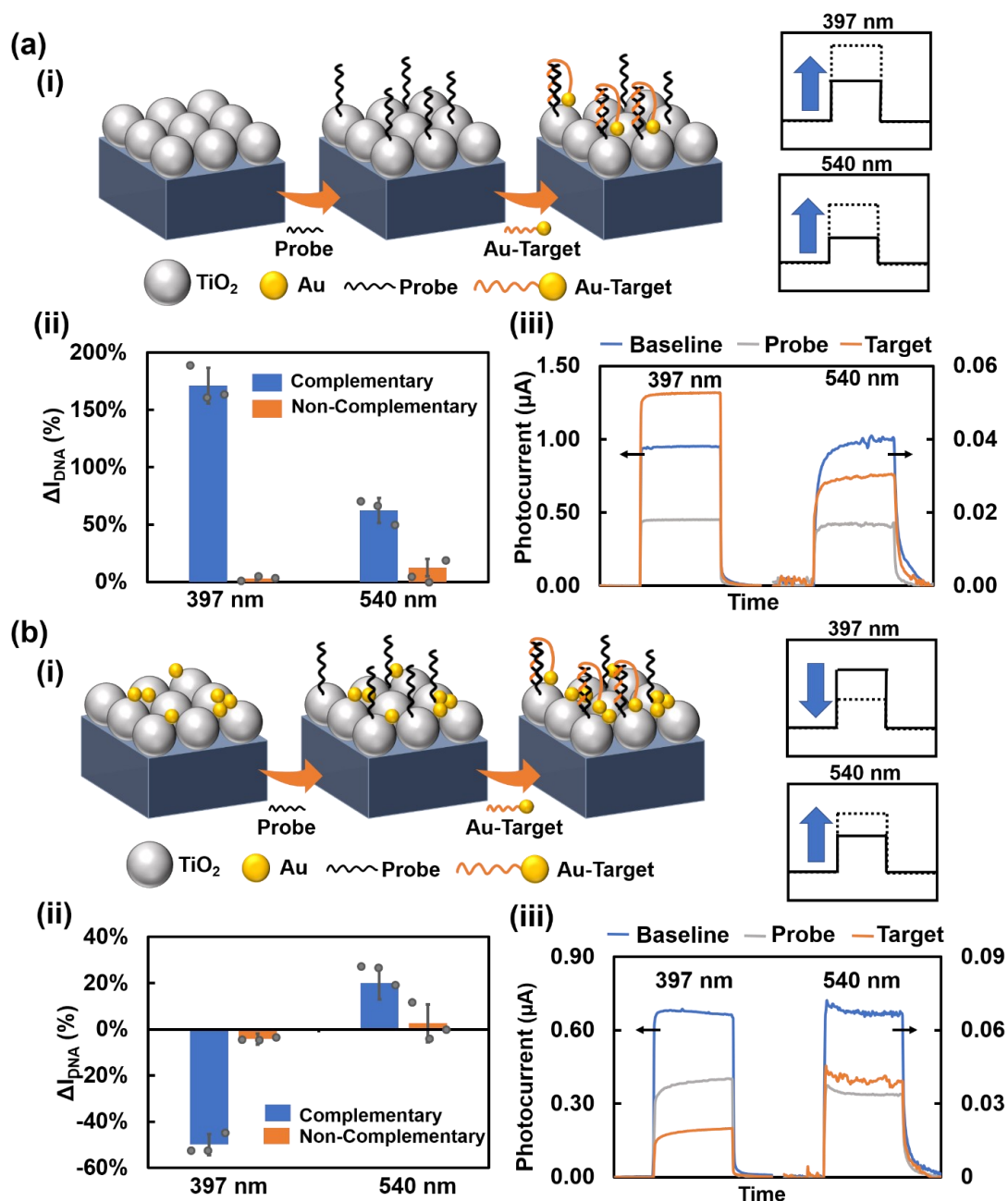


Figure 4.4: Schematic drawing showing the mechanisms of Au-TiO<sub>2</sub> interaction at UV (a) and visible (b) light excitation.

Both abovementioned charge transfer mechanisms would increase the PEC current in the UV regime with an increase in the surface density of Au NPs. In the light of this, what are the mechanisms responsible for the signal decrease observed here? To answer this question, we consider that the loading of Au NPs at the TiO<sub>2</sub> surface also influences the absorption and scattering of the incident light<sup>527,528</sup>. Au NPs can hinder the photoexcitation of the underlying TiO<sub>2</sub> in areas of high Au NP loading<sup>501</sup>. Additionally, the presence of Au NPs on the TiO<sub>2</sub> surface limits the direct access of TiO<sub>2</sub> to the electrolyte, potentially attenuating photocurrent generation<sup>527</sup>. While the direct charge transfer mechanisms discussed above, photocharging and hot electron transfer, both increase the generated photocurrent, the reduced access to light and electrolyte decreases the photocurrent generated by TiO<sub>2</sub>. As a result, these enhancement and loss effects become competitive with a delicate optimum occurring at low Au NP concentrations. At lower Au NP loadings (incubation times < 20 minutes), the influence of charge transfer is dominant, yielding enhanced photocurrents while at higher loadings a higher prevalence of loss mechanisms yields to decreasing photocurrents. This is in accordance with prior studies that demonstrate for TiO<sub>2</sub>/Au interfaces under UV excitation, enhancement of photocurrent is obtained at only very small amounts of AuNPs<sup>526,529,530</sup>. It should be noted that increased light absorption and scattering can also enhance the local electric field surrounding Au NPs, which can in turn increase the photocurrent generated by TiO<sub>2</sub><sup>494,531</sup>. However, this becomes negligible for small Au NPs (diameter < 30nm) at UV excitation<sup>532</sup>. For TiO<sub>2</sub>/Au systems, Au NPs can also transfer their absorbed energy to TiO<sub>2</sub> via plasmon-induced resonance energy transfer (PIRET)), which is only evident when the Au NPs are excited at their LSPR wavelengths<sup>532</sup>.

Interestingly, under the 540 nm illumination, the photocurrent increases with the increase of Au NP surface density on the electrode. Au NPs exhibit strong absorption under 540 nm excitation due to their LSPR properties and generate hot electron-hole pairs through *Landau damping*<sup>533</sup>. These hot carriers lose their energy through electron-electron scattering on time scales of less than 100 fs<sup>533</sup>. It is important to have high density of electron-accepting states in the semiconductor in order to transfer these hot electrons into the conduction band of semiconducting nanoparticles. TiO<sub>2</sub> has a large density of states in the conduction band, and exhibits efficient coupling with Au NPs<sup>534</sup>. Due to this efficient coupling, the plasmonic excitation of Au NPs (540nm) exhibits steadily increasing photocurrent with increasing Au NP concentration (Figure 4.2b, c). Moreover, exciting Au NPs at the plasmonic wavelength significantly increases the electric field in their surrounding region (Figure 4.4b)<sup>531</sup>, which can enhance the photocurrent by energy transfer to TiO<sub>2</sub> via PIRET<sup>535</sup>.

As the photocurrent generation mechanism differs for the two excitation wavelengths used here, we probed whether this effect could be utilized to design a DNA detection assay where an analyte was able to provide both *signal-off* (signal decrease) and *signal-on* (signal increase) responses on the same electrode. Although TiO<sub>2</sub>/Au electrodes have been used in biomolecular detection<sup>536,537</sup>, there is no report of obtaining both signal-on and signal-off response on a *single electrode* for these systems. Both baseline and TiO<sub>2</sub>/Au (20 min) electrodes were used to examine wavelength-dependent photocurrent modulation in the presence of a DNA linker. Au NP-labeled DNA was used as a target that hybridizes with the capture probes immobilized at the surface of the photoelectrode (Figure 4.5). Due to the differences in the length of probe (15-mer) and target (25-mer) DNA strands, target hybridization is anticipated to bring the Au NP label present at the single stranded end of the target to the vicinity of the electrode surface (Figure 4.5a(i)), effectively increasing the concentration of Au NPs on the electrode<sup>502</sup>. We expect a *signal-on* response for the baseline electrodes for both excitation wavelengths (Figure 4.5a(i)) and a combination of *signal-off* (at 397 nm) and *signal-on* (at 540 nm) responses for the TiO<sub>2</sub>/Au electrodes (Figure 4.5b(i)) as DNA binding is hypothesized to increase the AuNP concentration beyond the threshold loading level after which a signal loss would be expected for UV excitation.



*Figure 4.5: DNA detection assay built on the interactions between Au and TiO<sub>2</sub> NPs (a) DNA detection assay on baseline TiO<sub>2</sub> electrode. (i) Schematic illustration of the assay design. (ii) Percentage change in PEC current showing signal-on response for UV and visible light excitation. (iii) Representative PEC graphs obtained on the baseline TiO<sub>2</sub> electrode. (b) DNA detection assay on TiO<sub>2</sub>/Au electrode. (i) Schematic demonstration of the assay design. (ii) Percentage change of PEC current for showing signal-off response for UV and signal-on response for visible light excitation. (iii) Representative PEC graphs obtained on the TiO<sub>2</sub>/Au electrodes. Photocurrent measurements were performed at a bias voltage of 0 V vs. Ag/AgCl and 0.1 M PBS with 0.1 M ascorbic acid was used as the supporting electrolyte. Error bars represent one standard deviation from the mean for the PEC measurements performed with at least three separate devices.*

As expected, target binding on the baseline electrode increased the PEC current for both UV (171%) and visible (61%) light excitations (Figure 4.5 a(ii)). In contrast, a 50% decrease and a 20% increase in PEC currents were exhibited by the TiO<sub>2</sub>/Au electrode following target binding (Figure 4.5b(ii)) for the UV and visible excitations, respectively. The concentration of Au NP labeled target DNA bound by surface immobilized probe DNA dictates the amount of Au NPs anchored at each electrode. The low concentration (1 pM) of target DNA utilized here is anticipated to increase Au loading by a small amount following hybridization. As the TiO<sub>2</sub>/Au electrode contains Au NPs prior to the introduction of DNA target, it exhibits a markedly different behavior as that of the baseline electrode. A *signal-off* response is yielded under the UV regime while a *signal-on* response is yielded under visible light excitation. The introduction of additional Au NPs via target hybridization disrupts the delicate optimum of Au loading on the TiO<sub>2</sub>/Au electrode, triggering loss effects (reduced access to light and electrolyte) to dominate enhancement mechanisms (photocharging and hot electron transfer) at the UV regime. Conversely, under visible light illumination, increased electric field effects (PIRET) stemming from enhanced Au loading augments the resultant PEC current. It should be noted that the absolute value of the percentage changes of photocurrent, following target hybridization, at both UV and visible light illumination is significantly lower in case of TiO<sub>2</sub>/Au electrodes as compared to baseline TiO<sub>2</sub>. Increased concentration of Au NPs at the TiO<sub>2</sub>/Au electrodes beyond a certain threshold have been shown to introduce recombination centers, thereby reducing carrier lifetime<sup>538</sup>. Nevertheless, the TiO<sub>2</sub>/Au electrodes provide different responses for the same DNA target (1 pM) on a single electrode, dynamically controlled by illumination wavelength (397nm and visible) alone. Obtaining both *signal-on* and *signal-off* responses for a single target has been shown to improve specificity, sensitivity and *signal-to-noise ratio* in biosensing<sup>502,539,540</sup>.

#### 4.5 Conclusions

In this study, the distinct interaction mechanisms between Au NPs and TiO<sub>2</sub> NPs were probed under varied excitation regimes (397 nm and 540 nm) to understand the effect of Au NP density on PEC current generation. SEM micrographs demonstrated a rise in Au NP loading (134, 181, 433 and 623 per  $\mu\text{m}^2$ ) on P25-TiO<sub>2</sub> photoelectrodes with increasing deposition time (5, 10, 20 and 45 min). Negative shifts in flat-band potential, as calculated from Mott Schottky measurements, indicated enhanced charge separation at greater Au NP surface concentrations, which has been linked to enhanced photocurrent generation<sup>500</sup>. Under UV illumination, increasing the surface loading of Au NPs initially increased the photocurrent; however, beyond a certain surface loading (between 10-20 minutes), it attenuated the photocurrent. In contrast, under visible light excitation, a steady increase in photocurrent was depicted upon increasing the surface loading of Au NPs. It was hypothesized that under UV illumination, Au NPs contribute to both current enhancement and current loss mechanisms. Current loss is possible due to the absorption and scattering of light by Au NPs, and the reduction of bandgap light absorption by TiO<sub>2</sub>, which in turn reduces the photo-excited charge carriers participating in PEC oxidation reactions. Current enhancement was possible due to the direct charge transfer from TiO<sub>2</sub> to AuNPs through Fermi level equilibration, and possibly due the transfer of hot interband carriers, generated under UV excitation, from AuNPs to TiO<sub>2</sub>. Both of these mechanisms increase the photocurrent by increasing the concentration of photo-excited holes for participating in PEC oxidation of ascorbic acid. The loss and enhancement mechanisms can compete, and their extent can be controlled by the density of Au NPs on the electrode surface. Under visible light excitation, the light absorption of TiO<sub>2</sub> becomes negligible;

however, intraband hot carriers are generated in Au NPs through *Landau damping*. Hot electrons are transferred to the conduction band of TiO<sub>2</sub>, enabling hot holes to participate in oxidation reactions. These intraband carriers are the main driving force in generating the photocurrent in this wavelength regime.

The knowledge obtained from this study was used to design a DNA detection assay using TiO<sub>2</sub>/Au electrodes where both signal-on and signal-off responses were achieved depending on the excitation light wavelength employed. Hybridization of an Au NP-labelled DNA strand on a TiO<sub>2</sub> photoelectrode caused a signal increase under visible illumination and a signal decrease under UV illumination. The ability to achieve both signal-on and signal-off behavior on a single photoelectrode can be exploited to enhance the limit-of-detection of biosensors by achieving differential or ratiometric signal processing possible through combining the two signal transduction modalities.

#### **4.6 Acknowledgements**

The authors acknowledge support from Natural Science and Engineering Council of Canada (NSERC) and the Ontario Early Researcher Award granted to L.S., as well as a salary award to L.S. from the Canada Chairs Program. Scanning electron microscopy was performed at the Canadian Centre for Electron Microscopy (CCEM), which is a national facility supported by NSERC and McMaster University. S.S. and A.V also receive NSERC doctoral scholarships.

#### **4.7 Supplementary Information**

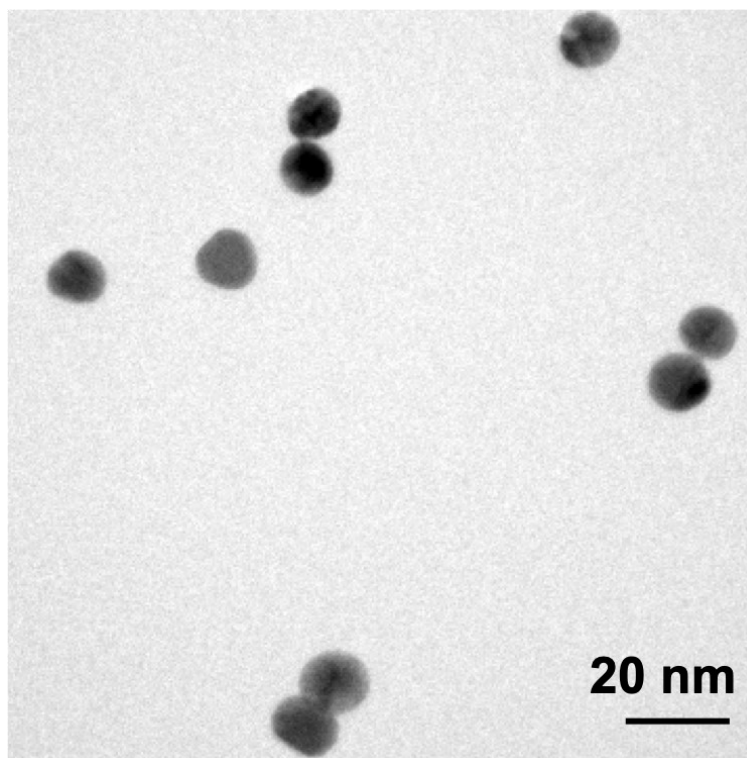


*Figure S4.1: TEM image of Au nanoparticles*

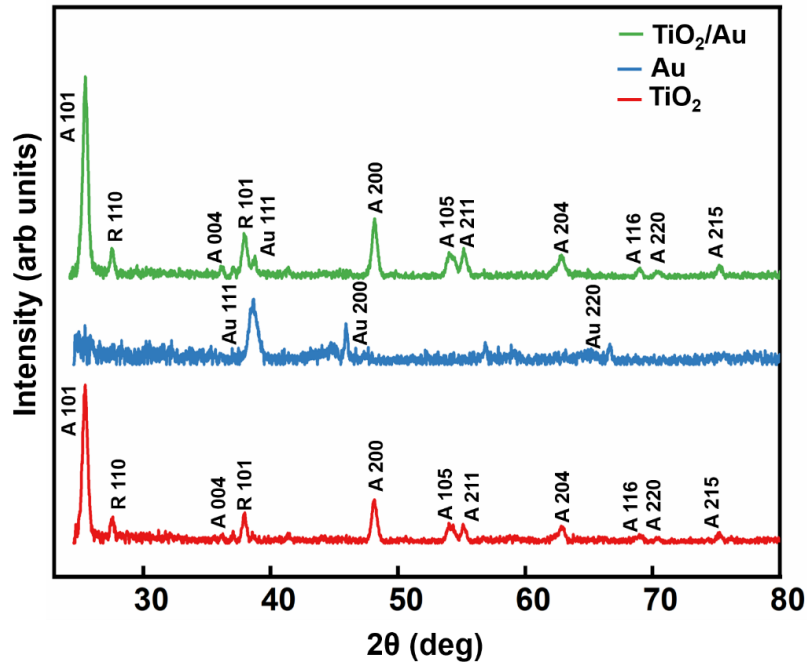


Figure S4.2: X-ray diffraction analysis of the photoelectrodes. A and R refer to the anatase and rutile phases, respectively.  $\text{TiO}_2/\text{Au}$  (40 min) samples were used as an example of hybrid samples.

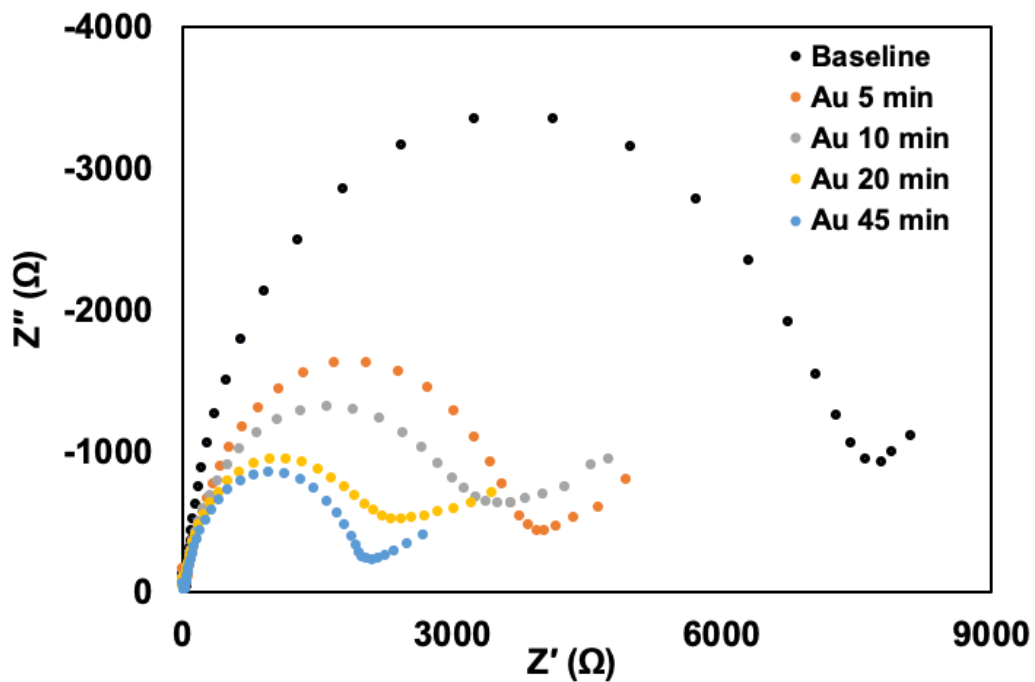


Figure S4.3: Nyquist plots for the photoelectrodes at open circuit voltage. The charge transfer resistance ( $R_{ct}$ ) decreases as the amount of Au NP increases in the electrode.

Table S4.1: Charge-transfer resistance ( $R_{ct}$ ), charge carrier density ( $N_d$ ) and flat-band potential ( $V_{FB}$ ) of the electrodes used in this work

Sample	$R_{ct}$ (k $\Omega$ )	$N_d$ (cm $^{-3}$ )	$V_{FB}$ (mV)
--------	------------------------	---------------------	---------------

TiO <sub>2</sub>	8.5	0.99-1.062x10 <sup>17</sup>	-590 to -600
TiO <sub>2</sub> -Au (5 min)	4.0	1.15 x10 <sup>17</sup>	-650
TiO <sub>2</sub> -Au (10 min)	3.5	1.41 x10 <sup>17</sup>	-710
TiO <sub>2</sub> -Au (20 min)	2.8	1.94 x10 <sup>17</sup>	-750
TiO <sub>2</sub> -Au (45 min)	2.2	2.27 x10 <sup>17</sup>	-795

## Chapter 5: Investigating spatial dependency in TiO<sub>2</sub> /Au NP systems for differential PEC biosensing (Objectives 2, 4, 5)

### *Preface*

While the last chapter yielded a bimodal bio-signalling system operated at two individual excitation frequencies, the subsequent goal of the investigation was to transform this bimodal current modulation to operate at a single excitation wavelength while simultaneously exhibiting programmable signal switching behaviour. Towards this end, we explored yet another degree of freedom to program signal responses in the Au/TiO<sub>2</sub> PEC systems—i.e, the modulation of separation distance between the metal NPs and the semiconductive species. In order to examine this spatial dependency, DNA nano-spacers of varying lengths—integrated on a single multiplexed chip—were used to assess PEC response when exposed to same bioanalyte. The dynamic motion of these constructs was then experimentally characterized and statistically modelled. By building on the knowledge attained in Chapters 3 and 4, Chapter 5 details the design of a spatially-multiplexed PEC DNA detector capable of differential signaling – signal-on and signal-off readout – on a single device, at a single illumination wavelength; thus, offering the building blocks to construct PEC systems for POC analysis. Chapter 5, thus, contributes to objectives 2, 4 and 5 as put forth in chapter 1 of this thesis.

### *Authors*

Sudip Saha\*, Amanda Victorious\*, Richa Pandey, Amanda Clifford, Igor Zhitomirsky and Leyla Soleymani. (\*indicates that Amanda Victorious and Sudip Saha contributed equally to this authorship and are co-first authors).

In order to integrate the motional dynamics dependant and programmable responses exhibited by Au/TiO<sub>2</sub> onto a single device, I designed the signal-on (15-mer channel) component of plasmonic ruler and collaborated with colleague (Dr. Saha) who developed the signal-off (20-mer channel) system. Jointly, we integrated the two systems to generate a coherent signalling scheme using a single assay designed to detect Au labelled 25-mer single stranded target DNA. Once the assay design was finalized, I developed the electrode design spatially incorporating both systems (electrical channels) onto a single ITO/glass substrate, which was used for integrated (dual channel) experiments throughout the course of this project.

Prior to integrating both the electrical (*on and off*) channels onto a single device, I performed chopped light chronoamperometry before modification, following modification with 15-mer (signal on) or 20-mer probe signal (off), and after hybridization with a 25-mer complementary or non-complementary (NC) Au NP-labelled DNA target to measure the PEC performance on each of the designed channels (on and off) individually. In this manner, I proved that both signal on and off responses could be programmed using the motional dynamics of DNA (Figure 5.2 (b, c)). I then experimentally obtained Mott-Schottky plots for the 15-mer channel (Figure 5.3 (c; 15-mer)). Once the Mott-Schottky data was obtained, I worked with my colleague Dr. Saha to generate a hypothesis explaining these results. Dr. Saha then developed the algorithmic simulation that then went on to further corroborate our hypothesis. In order to further corroborate the validity of this dynamically switchable system developed in this work, I along with Dr. Saha designed various iterations of switchable DNA systems incorporating 34-mer AuNP-labelled complementary DNA targets hybridized with electrodes housing 20-mer DNA probes. After settling on a design, I carried out the experimental work and data analysis (Figure S5.12). As the same trend depicted in the 15-mer channel following hybridization with 25-mer target was also shown in the 20-mer channel hybridized with 34-mer target, the predictive design of the signal on channel was verified. In a similar fashion, in order to experimentally corroborate the signal on behaviour expected when the Au labels contact the underlying TiO<sub>2</sub> photoelectrode, I designed one iteration of the DNA assay forcing the labels to contact the TiO<sub>2</sub> surface using the 15-mer channel (Figure S5.13 a(i)) while Dr. Saha designed one for the 20-mer channel. Using this design, I carried out chopped light

amperometry to investigate the signal responses following target hybridization on the 15-mer channel, analyzed the collected data and plotted the subsequent signals (Figure S13b, 15-mer only).

Next, I devised and fabricated a spatially multiplexed differential biosensor incorporating these two channels by patterning ITO onto glass substrates (Figure 5.4a, Figure S5.1). I subsequently performed chopped light amperometry to obtain the signal changes generated upon incubation with blank and target DNA sample drops on the 15-mer and 20-mer channels. In order to avoid researcher bias, Dr. Saha and I divided the data acquisition such that half of the data sets for 15-mer and the 20-mer were obtained by myself while the other half of both data sets (15-mer and 20-mer) were obtained by Dr. Saha (Figure 4b). Once this data was acquired, I generated calibration curves and calculated the limit-of-detection (LOD) for both systems (Figure S5.14). I was also responsible for data acquisition and analysis for figure 5.4(a) and the creation of the schematic depicted in figure 5.4(a). Lastly, I probed the stability of the 15-mer channels using chopped light amperometry to obtain photocurrent density measurements over 15 illumination cycles (Figure S5.15, 15-mer). Aside from the aforementioned experiments depicted in the main manuscript, I also generated Au labelled 25-mer strands, carried out IPCE experiments (and analysis) comparing baseline ( $\text{TiO}_2$ ) and Au-modified  $\text{TiO}_2$  electrodes (Figure S5.7), fabricated substrates and was part of the electrochemical impedance spectroscopy (EIS) analysis of the phase diagrams exhibited by 15-mer and 20-mer channel before and after hybridization (Figure S5.8).

To summarize, I performed the experimentation, data analysis, figure creation and manuscript write up for figures: 5.2 (a; 15-mer), 5.2(b, c), 5.3(c; 15-mer), 5.4(a), 5.4(b) (half the data sets for 15-mer and 20-mer; the other half was done by Dr. Saha). In addition, I also performed the experimentation, data analysis, figure creation for figures: S5.1, S5.7, S5.8 (prepared substrates for and was part of analysis), S5.12, S5.13a (i) (only designed 15-mer but illustrated both), S5.13(b) (15-mer only), S5.14, S5.15 (15-mer) in the supplementary information. I thank Dr. Saha for his support, guidance, contribution, and collaboration demonstrated throughout the course of this project.

***Publication***

ACS Appl. Mater. Interfaces 2020, 12, 36895–36905

***Publication Date***

August 2020

### 5.1 Abstract

As dynamic biorecognition agents such as functional nucleic acids become widely used in biosensing, there is a need for ultrasensitive signal transduction strategies, beyond fluorescence, that are robust and stable for operation in heterogeneous biological samples. Photoelectrochemical readout offers a pathway towards this goal as it offers the simplicity and scalability of electrochemical readout, in addition to compatibility with a broad range of nanomaterials used as labels for signal transduction. Here, a differential photoelectrochemical biosensing approach is reported, in which DNA nano-spacers are used to program the response of two sensing channels. The differences in the motional dynamics of DNA probes immobilized on different channels are used to control the interaction between Au and TiO<sub>2</sub> nanoparticles positioned at the two ends of the DNA nano-spacer to achieve differential signal generation. Depending on the composition of the DNA constructs (fraction of the DNA sequence that is double stranded), the channels can be programmed to produce a signal-on or a signal-off response. Incident photon-to-current conversion efficiency, UV/VIS spectroscopy, and flat band potential measurement indicate that direct transfer of electrons between metallic and semiconductive nanoparticles is responsible for the signal-on response and incident light absorption and steric hindrance are responsible for the signal-off response. The differential photoelectrochemical signal readout developed here increases the device sensitivity by up to three times compared to a single channel design and demonstrates a limit-of-detection of 800 aM.

### 5.2 Introduction

Biosensors combine biorecognition with signal transduction to analyze biologically-relevant targets.<sup>541,542</sup> Dynamic biorecognition agents such as structure switching aptamers and DNazymes<sup>541,543–545</sup> are increasingly used in biosensing due to their compatibility with real-time monitoring,<sup>546</sup> ability to target difficult-to-capture analytes such as small molecules,<sup>547</sup> and facile conjugation with reporting probes.<sup>548,549</sup> Optical readout, based on fluorophore/quencher interactions, is currently the most widely used method for transducing these biorecognition events into detectable signals.<sup>549</sup> There is a growing interest in combining these biorecognition systems with electrochemical readout due to the enhanced signal-to-noise ratio (SNR) offered by these transducers, ease of multiplexing, and their applicability to continuous and *in situ* monitoring.<sup>209,550–552</sup> Inspired by the electronic amplifier circuits, differential (also referred to as ratiometric) signal readout has been used in electrochemical biosensors to enhance their SNR and suppress the effect of background currents generated in unprocessed biological samples resulting from non-specific adsorption.<sup>539,553–555</sup> The current differential signaling designs typically rely on multiple redox labels for generating correlated or combinatorial signals. This presents a challenge in applying these systems to a wide range of sample environments since the number of redox labels compatible with bio-conjugation that can be used effectively in complex reductive or oxidative sample environments is extremely limited.

Our vision was to create a differential electrochemical readout strategy that used non-redox labels for operation in complex environments. For this purpose, we explored photoelectrochemical (PEC) signal generation that combines optical biasing with electrochemical current measurement. PEC signal readout is possible with a wide range of robust and stable nanomaterial labels (i.e. metal NPs,<sup>556,557</sup> semiconductive quantum dots,<sup>558</sup> organic semiconductors<sup>559</sup> etc.). There is a growing interest in combining plasmonic nanoparticles with semiconducting nanoparticles.<sup>560–564</sup> The main attraction of these two types of nanoparticles (plasmonic and semiconducting) lies in their complementary optical properties, i.e., well separated and long lived excitons in semiconductors and localized electromagnetic modes in plasmonic nanoparticles, capable of interaction used in proximity of each other.<sup>491,561</sup> The use of both plasmonic and semiconducting nanoparticles in proximity of each other holds great potential to allow researchers to observe new phenomena that are based on exciton-plasmon interactions and engineer specific optical properties for applications such as data storage,<sup>565</sup> water splitting,<sup>494,560</sup> light harvesting<sup>562</sup> and photocatalysis.<sup>564</sup>

Differential PEC readout is currently possible using two different bias voltages and applied wavelengths,<sup>539,554,566,567</sup> which result in assays with increased instrumentation complexity. We sought to overcome this complexity by developing a differential PEC biosensor that used a single label, voltage,

and light source by controlling the nanoscale interactions of the system using DNA nano-spacers, rather than tuning the parameters of external stimuli. To achieve differential PEC signaling that generates signal increase (signal-on) on one channel and signal decrease (signal-off) on another, we employed the nanoscopic interactions between metallic nanoparticles (NPs) and semiconductor electrodes. PEC assays that use metallic NPs in conjunction with semiconducting photoactive materials build on the foundation that when metallic NPs are in direct contact or close proximity (~10 nm) with semiconducting materials having the desired energetics, the carrier lifetime increases or decreases,<sup>532,561</sup> which modulates the PEC current.<sup>563,564</sup> Au and Ag NPs have been widely used in these assays in conjunction with metal oxide electrodes (such as TiO<sub>2</sub>,<sup>522</sup> SnO<sub>2</sub>,<sup>556</sup> Fe<sub>2</sub>O<sub>3</sub><sup>568</sup> etc.) to design biosensors for detecting various biomolecules (e.g. oligonucleotides,<sup>522</sup> protein,<sup>569</sup> enzyme<sup>568</sup> etc.). We explored whether it would be possible to use DNA capture probes as nano-spacers to tap into the different nanoscale physical processes that occur between metallic NPs and semiconductors on different sensing channels of a single biosensor to predictively increase or decrease the PEC signal based on the separation between the metallic NP label and the semiconducting electrode.

### 5.3 Materials and Methods

#### *Chemicals*

Phosphate buffer solution (PBS, 1.0M, pH 7.4), L-ascorbic acid (99%), sodium chloride (NaCl), chitosan (CHIT, from shrimp, degree of deacetylation of 85%, Mw=200,000), glacial acetic acid, 3,4-dihydroxybenzaldehyde (DHB), and tris (2-carboxyethyl) phosphine hydrochloride (TCEP, 98%) were purchased from Sigma-Aldrich. P25-TiO<sub>2</sub> was obtained from Nippon aerosol Co. Ltd. Acetone and Ethanol were purchased from commercial alcohols (Brampton, ON). Milli-Q grade (18.2 MΩ cm) deionized (DI) water was used for all solution preparation and washing steps.

#### *Surface modified TiO<sub>2</sub> and Au NP preparation*

A 3 gL<sup>-1</sup> CHIT solution was prepared in DI water using 1% acetic acid. The concentration of DHB aqueous solution was 16 gL<sup>-1</sup>. DHB-modified CHIT solution was obtained by modifying CHIT in the liquid phase. DHB modified CHIT solution (mass ratio 4:1 as DHB: CHIT) was prepared by adding DHB solution to the CHIT solution. P25-TiO<sub>2</sub> was added to the DHB-modified CHIT solution.

#### *TiO<sub>2</sub> substrate preparation*

Fisherband premium plain glass microscope slides were used for substrate preparation. The glass slides were cut into desired dimensions and sonicated using acetone, ethanol and DI water for 15 minutes before using. A 100 nm film of indium tin oxide (ITO) was sputtered onto glass slides using a radio-frequency magnetron sputtering from angstrom science. A 90% In<sub>2</sub>O<sub>3</sub> and 10% Sn<sub>2</sub>O<sub>3</sub> target was used for the sputtering under the argon gas. All glass/ITO substrates were masked using vinyl tape to preserve electrode contact area and oxygen plasma treated for one minute. All films were fabricated by dropping 10 microliters of solution onto exposed glass/ITO substrate surface and baked at 100°C for 5 minutes. This procedure was repeated for a total of three deposition steps. The resulting electrodes were then air dried and washed prior to use.

#### *Gold (Au) nanoparticle synthesis*

Au NPs were synthesized using the protocol reported in literature.<sup>507</sup> Briefly, a 1 mM gold chloride (HAuCl<sub>4</sub>) solution was added into 38.8 mM trisodium citrate solution with a volume ratio of 10:1. This solution was boiled with vigorous stirring for 10 min, and then the stirring was continued for an additional 15 min without applying heat. This synthesis protocol produced the Au NPs with size approximately 12 nm. The size of the Au NPs were further confirmed by imaging in TEM (Supplementary figure S9).

#### *AuNP-DNA conjugation*

DNA conjugated Au NPs were prepared according to the literature.<sup>509</sup> Briefly, 1 ml of AuNPs were suspended in 10 mM PBS buffer (pH 7.0). 100 μM of thiolated DNA was reduced using TCEP and 35 μl of the reduced DNA was added to the AuNP solution. The solution was incubated for 16 h at room temperature (RT). After that, 10 mM PBS and 2 M NaCl solutions were added slowly to make the final

salt concentration of 0.1 M NaCl. This solution was incubated for 40 hours at room temperature. Finally, the solution was washed three times and re-suspended in 10 mM PBS with 0.1 M NaCl buffer (pH 7.0).

#### *Photoelectrochemical Characterization*

PEC measurements were carried out in a three-electrode cell setup with an ultraviolet flashlight to facilitate illumination of the photoelectrode surface. The intensity of the flashlight was measured as 470 W/m<sup>2</sup>. A Pt wire was used as the counter electrode, Ag/AgCl as the reference electrode, and the glass/ITO/TiO<sub>2</sub>NP substrates acting as the working electrode. A 0.1 M PBS solution with 0.1 M ascorbic acid (AA) was used as the supporting electrolyte. Amperometric i-t curve were measured by a CHI 660D electrochemical station, under UV illumination at every 20 s for a period of 100 s. Photocurrents were reported as the difference in current with and without incident light on the face of the TiO<sub>2</sub> electrode.

The IPCE measurements were carried out in a three-electrode cell setup with Pt as the counter, Ag/AgCl as the reference electrode, and a solution of 0.1 M AA in 0.1 M PBS as the electrolyte. All IPCE measurements were performed under *zero* bias voltage and light illumination in the range of 350–650 nm using a Zahner CIMPS-QE/IPCE Photo-Electrochemical workstation.

IPCE is defined as:

$$IPCE(\%) = \frac{1240 \times I(A/cm^2)}{\lambda(nm) \times P_{inc}(W/cm^2)} \times 100$$

Where, I is the photocurrent,  $\lambda$  is the incident wavelength and  $P_{inc}$  is the incident optical power of the excitation light.<sup>508</sup>

#### *Electron Microscopy*

The surface structure of the prepared substrate was analyzed using FEI Magellan 400 scanning electron microscope (SEM). UV-Visible (UV-VIS) absorption spectroscopy was measured using Infinite M200 pro (Tecan) plate reader.

#### *X-ray photoelectron spectroscopy (XPS)*

XPS measurements were performed using Kratos AXIS supra X-ray photoelectron spectrometer. The survey scan analysis was carried out over an area of 300 X 700  $\mu$ m using a pass energy of 160 eV.

#### *Mott-Schottky measurements*

Mott-Schottky experiments were performed in a three-electrode setup using Ag/AgCl as a reference electrode and Pt as counter electrode. The electrolyte contained 2 mM potassium ferro/ferricyanide in 0.1 M KCl and 10 mM PBS. The experiments were performed with an AC excitation of 5 mV. From the Mott-Schottky plot, flat-band potential and charge carrier density were calculated by using the following formula:<sup>570</sup>

$$\frac{1}{C^2} = \frac{2}{\epsilon\epsilon_0 A^2 e N_D} (V - V_{fb})$$

Where,  $\epsilon$  and  $\epsilon_0$  are the dielectric constant of the semiconductor and vacuum permittivity, respectively.  $N_D$  is the charge carrier density,  $V_{fb}$  is the flat band potential, C is capacitance and A is the area of the electrode.

#### *DNA hybridization experiments*

Electrodes were fabricated using a layer-by-layer drop casting method, followed by ssDNA (1 $\mu$ M) probe deposition for 3 hours and incubation with a blank solution containing 1.2 nM of non-complementary target or complementary targets (100 aM-1 nM) spiked in the blank solution. Electrodes were washed thoroughly between each deposition step. The measured percentage change in signal for each concentration is calculated as:

$$\begin{aligned} \Delta I &= I_{Target} - I_{Probe} \\ \% \Delta I_{15-mer} &= (\Delta I_{15-mer} \times 100) / I_{Probe 15-mer} \\ \% \Delta I_{20-mer} &= (\Delta I_{20-mer} \times 100) / I_{Probe 20-mer} \\ \% \Delta I_{15-mer} &= (\Delta I_{15-mer} \times 100) / I_{Probe 15-mer} \\ \% \Delta I &= | \% \Delta I_{15-mer} | + | \% \Delta I_{20-mer} | \end{aligned}$$

$I_{15\text{-mer}}$  indicates the percentage change in photocurrent following hybridization of Au NP-labelled target with the 15-mer probe while  $I_{20\text{-mer}}$  indicates the percentage change in photocurrent following hybridization of Au NP-labelled target with the 20-mer probe.

The DNA sequences used in this work are as follows:

15-mer probe: 5'-NH<sub>2</sub>-AGG GAG ATC GTA AGC-3'

20-mer probe: 5'-NH<sub>2</sub>-AGG GAG ATC GTA AGC AAA AA-3'

Complementary target: 5'-SH-TTT TTT TTT TGC TTA CGA TCT CCC T-3'

Non-Complementary target: 5'-SH-TTT TTT TTT TTT TTT TTT TTT T-3'

Target sequence for the experiment where Au NP is hybridized to be in proximity of TiO<sub>2</sub> is:

5'-TGC TTA CGA TCT CCC TTT TTT TTT T-SH-3'

#### *Limit-of-Detection*

To calculate the limit-of-detection of the differential assay, we plotted the photocurrent change versus the log of target concentration in the linear range (10 aM – 100 fM). The linear equation for the regression line is  $\Delta I (\%) = 22.35 \log C + 5.55$  with a correlation coefficient of 97.5% (Figure 4(b)-inset). The limit-of-detection is determined by calculating the concentration where the y-value of the regression line becomes equal to the limit-of-blank (LOB). LOB is defined as:

$$LOB = \Delta I_{blank} + 1.96 \times \sigma_{blank}$$

Where,  $\sigma_{blank}$  is the standard deviation of the blank signal and the factor 1.96 is used to calculate the limit-of-detection within a 95% confidence interval.

#### **5.4 Results and Discussion**

To assess the role of DNA probes as nano-spacers for tuning the sensing response of different channels, we created two classes of biofunctionalized photoactive electrodes (Figure 5.1(a)). Both of these photoactive electrodes were created from a porous network of TiO<sub>2</sub> NPs deposited on indium tin oxide (ITO) substrates (Figure 5.1(b,i)). However, one was biofunctionalized with single stranded DNA (ssDNA) probes having 15 nucleotides (15-mer), and the other harbored a 20 nucleotide (20-mer) long ssDNA probe (Supplementary Figure S5.1). Upon hybridization with AuNP-labelled complementary DNA targets (25-mer), we expected these two classes of photoactive electrodes to experience different Au-TiO<sub>2</sub> NP collision probabilities caused by the differences in the DNA motional dynamics.<sup>571-574</sup> High magnification backscattered electron microscopy demonstrates that Au NPs are indeed introduced to the TiO<sub>2</sub> NP matrix by complementary DNA target strands following hybridization (Figure 5.1(b)). As a result, we expect a fraction of the TiO<sub>2</sub> NPs to experience nanoscale interactions with Au NPs.

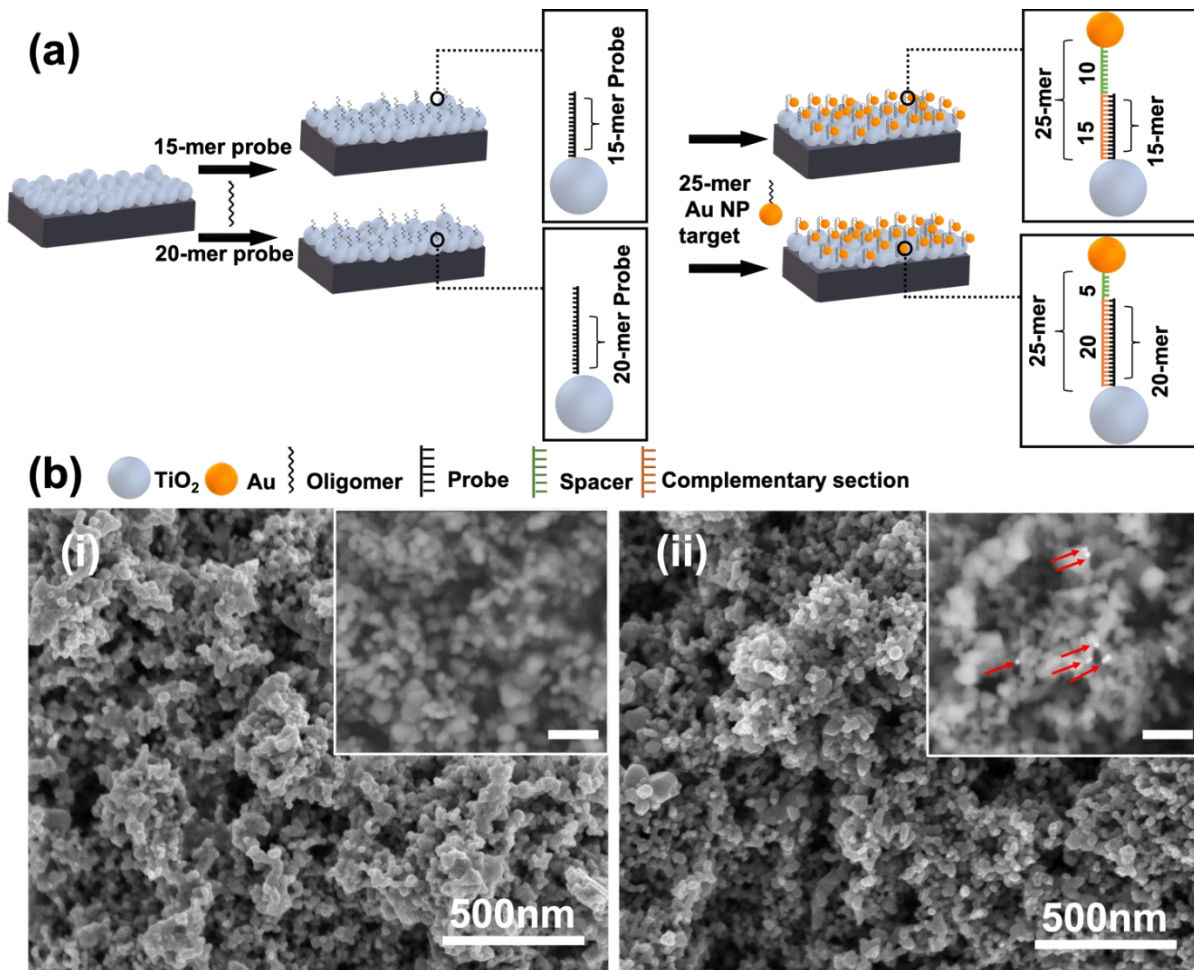


Figure 5.1 Differential photoelectrochemical biosensor. (a) Channels are created by depositing 15-mer or 20-mer probe DNA nano-spacers on photoactive TiO<sub>2</sub> substrates. Au NP-labelled 25-mer targets are hybridized onto the two channels. (b) SEM image of the electrode before (i) and after (ii) DNA hybridization with Au NP-labelled DNA target. The insets show the magnified image of the substrate acquired using the backscatter detector, with the red arrow pointing to Au NPs (scale bar in the inset represents 100 nm).

The incident photon to current conversion efficiency (IPCE) spectrum, which is defined as the number of electrons collected by the electrode per incident photon,<sup>494</sup> was measured to evaluate the wavelength dependence of the PEC response for the 15-mer and 20-mer channels (Figure 5.2(a)). Remarkably, on the 15-mer channel, the IPCE increases after hybridization with the complementary target, whereas for the 20-mer channel, the IPCE decreases. The increase or decrease in the IPCE after target hybridization is observed over the entire absorption spectrum of our photoelectrodes (from 350 nm to 550 nm). It should be noted that absorption of photons with energy lower than the bandgap of TiO<sub>2</sub> NPs (3.09 eV/400 nm as determined from supplementary Figure S5.2) is achieved using our photoelectrodes because of the use of chitosan and 3,4-Dihydroxybenzaldehyde (DHB) in preparing nanoporous photoactive films (Figure 5.2(a)-inset).<sup>505</sup>

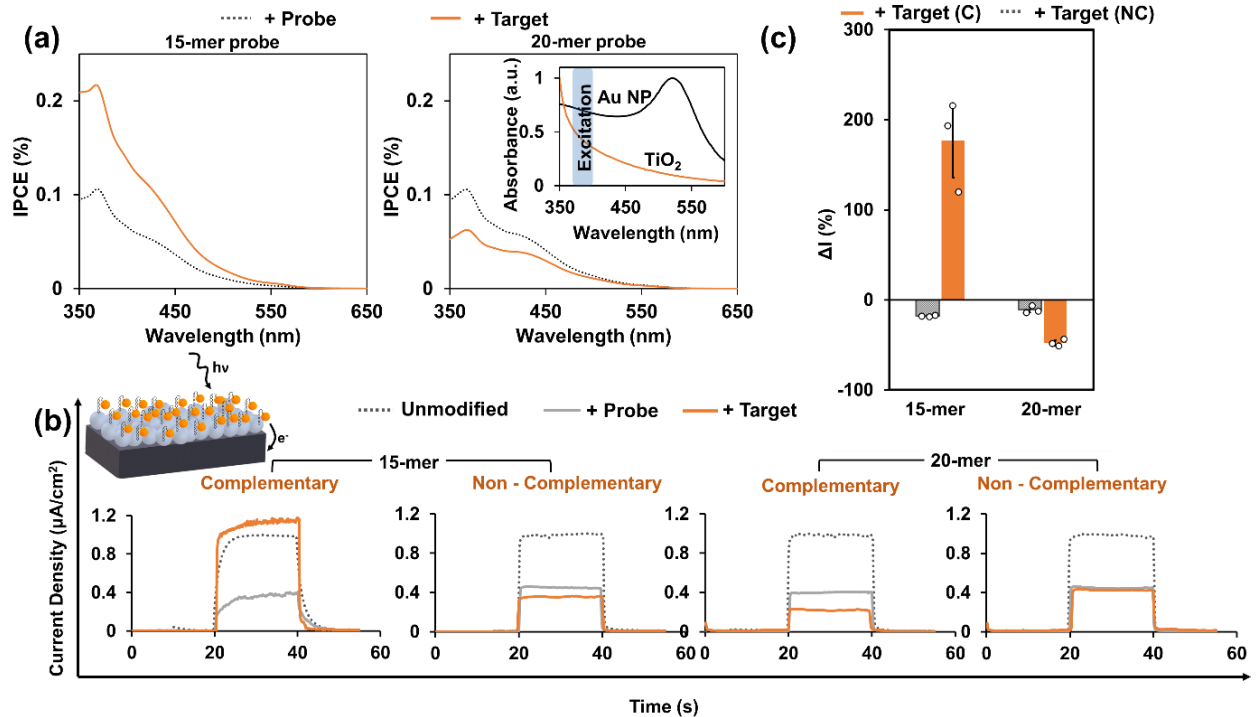


Figure 5.2 Photoelectrochemical characterization of the two sensing channels (a) IPCE spectrum of the photoactive electrode after probe attachment and after hybridization with Au NP-labelled complementary DNA targets (inset shows the absorption spectrum of AuNPs and TiO<sub>2</sub> NPs and the spectral range of the light source). (b) Representative PEC curves of the photoelectrode obtained using chopped light chronoamperometry at 0 V bias versus Ag/AgCl, before modification, following modification with 15-mer or 20-mer probe, and after hybridization with a 25-mer complementary or non-complementary Au NP-labelled target. The photoelectrodes were illuminated at 395 nm for 20 seconds starting at 20s (light on) and ending at 40 s (light off) with 0.1 M ascorbic acid in 0.1 M phosphate buffered solution used as the supporting electrolyte. The inset schematically demonstrates photoelectrochemical readout. (c) Bar plots summarizing the percentage change in photocurrents following hybridization of 15-mer and 20-mer channels with Au NP-labelled complementary (C) and non-complementary (NC) targets. Error bars represent one standard deviation with experiments performed using at least three separate devices.

In addition to the IPCE measurements, we evaluated the sensing capability of the system using PEC readout (Figure 5.2(b)). We optically excited the system using a single light source that operated at a wavelength range at which we observed a large signal change in the IPCE spectrum (Supplementary Figure S5.3 and Figure S5.4). We used ascorbic acid (AA) as the hole scavenger to generate a photocurrent upon optically exciting the TiO<sub>2</sub> photoelectrode. In both channels, an anodic current is generated, which was decreased upon functionalization with probe DNA. The anodic current is generated due to the annihilation of the photo-generated holes in TiO<sub>2</sub> by AA, and the movement of electrons from the conduction band of TiO<sub>2</sub> to the ITO electrode.<sup>556</sup> Modifying the electrode surface with biorecognition elements decreases the PEC signal by hindering the access of AA to the electrode surface.<sup>575</sup>

As hinted by the IPCE results, striking differences were observed in the signal change when the 15-mer and 20-mer channels were hybridized with complementary 25-mer DNA targets. The 15-mer channel demonstrated a signal increase (~177%), whereas the 20-mer channel yielded a signal decrease (~48%). It should be noted that incubating the probe-modified electrodes with non-complementary target produced a small signal decrease (~2%) in both channels (Figure 5.2(b), (c)), demonstrating the specificity of this readout strategy and its applicability to biosensing. The incubation of the probe-

modified electrodes with non-complementary DNA strands served as a control experiment to examine the effect of non-targeted AuNP-labelled DNA sequences on the generated PEC signal.

X-ray photoelectron spectroscopy (XPS) analysis of both channels showed gold to be present at the electrode surface at 0.2 at% (Supplementary Figure S5.5). Although this does not directly measure the amount of the AuNPs present at each channel, it provides a representative snapshot of the amount of gold at the electrode surface, suggesting that the Au NP amounts are similar in both channels. This indicates that the observed differences in signal change on the 15-mer and 20-mer channels are not due to the concentration difference of Au NPs on these two channels.

The signal-on versus the signal-off response observed on the 15-mer and 20-mer channels, respectively is hypothesized to be related to the different collision probabilities experienced between the AuNPs and TiO<sub>2</sub> matrix on the two channels. In our designed architecture, following hybridization, the 15-mer channel holds a 15 nucleotide double stranded segment with an estimated length of 5 nm and a 10 nucleotide single stranded segment with a length of 3.33 nm (Figure 5.1a). On the 20-mer channel, the 20 nucleotide double stranded segment is estimated to be 6.67 nm in length, and the 5 nucleotide segment is estimated to be 1.66 nm in length (Figure 5.1a). Double stranded DNA is considered to be significantly more rigid than single stranded DNA having the same number of nucleotides.<sup>576</sup> It is hypothesized that because a larger portion of the DNA nano-spacer is single stranded for the 15-mer channel compared to the 20-mer channel, there is smaller average separation between the AuNP and TiO<sub>2</sub> surface.

Previous voltametric studies performed using redox labelled-DNA constructs anchored on the electrode surface using a six-carbon (C<sub>6</sub>) linker indicate that the rotational motion of double stranded DNA (dsDNA) around the surface anchoring point allows the redox label to sufficiently approach the electrode for successful electron transfer.<sup>574</sup> Additionally, the probability of electron transfer is influenced by the length of the linker that connects the redox label to the DNA strand, with longer linkers resulting in increased electron transfer.<sup>571</sup> This system can be envisioned as a double hinged system with a spring-like anchor (C<sub>6</sub> linker, Hinge 1), rigid rod-like structure (dsDNA), and a flexible signaling linker connecting the DNA to the label (Hinge 2). Given that our system uses a C<sub>6</sub> linker, includes a double stranded segment, and is terminated by a ssDNA segment conjugated with a AuNP, it can be modelled using the abovementioned double-hinged system (Figure 5.3a). For the 15-mer channel, the single stranded portion of the target DNA is 40% of the total nominal DNA length; whereas for the 20-mer channel, the single stranded portion constitutes only 20% of the total nominal construct length. This indicates that the 20-mer channel includes a longer rod-like segment and a shorter flexible portion, which will have a dual effect on the probability of charge transfer between the AuNP and the TiO<sub>2</sub> matrix. The longer rod-like segment increases the bending radius of the DNA construct, and the shorter flexible segment decreases the probability of AuNP/electrode collisions. We expect this dual effect to result in a smaller probability of charge transfer between the AuNP and the TiO<sub>2</sub> matrix for the 20-mer channel in comparison with the 15-mer channel.

In order to calculate the relative collision rate of Au NPs with TiO<sub>2</sub>, we performed conformational analysis of the DNA nano-spacers on the 15-mer and 20-mer channels considering the worm-like chain model.<sup>576,577</sup> We modeled the DNA nano-spacers on each channel by considering each nano-spacer as two separate DNA segments (ssDNA and dsDNA) with different persistence lengths (Supplementary Figure S5.6). Although this model considers probe DNA to be anchored on a planar substrate, it is expected that to provide an estimate of the relative collision rate for the rough surface used in this work due to the stochastic motions of DNA strands.<sup>578</sup> This model indicates that a 5.77-5.83 times higher collision rate is expected on the 15-mer channel compared to the 20-mer channel.

Our experimental results demonstrate that signal enhancement occurs on the 15-mer channel, while signal decrease is seen on the 20-mer channel. We hypothesize that, on average, a larger number of AuNPs contact the TiO<sub>2</sub> surface more often on the 15-mer channel than on the 20-mer channel. This difference in signal generation on the two channels is evident despite the uneven surface of the TiO<sub>2</sub>

electrodes because the measured current is a collection of the aggregated response of all of the nanoparticles present at the electrode surface.

We further explored whether direct contact between Au NPs and TiO<sub>2</sub> electrodes would result in an enhancement in photocurrent, similar to what was observed on the 15-mer channel. We designed an experiment in which AuNPs were deposited directly on the TiO<sub>2</sub> electrodes. Au NPs deposited on TiO<sub>2</sub> electrodes showed a higher photocurrent compared to bare TiO<sub>2</sub> electrodes (Supplementary Figure S5.7). Additionally, the IPCE spectrum (Supplementary Figure S5.7) obtained on bare and AuNP-modified TiO<sub>2</sub> electrodes showed a similar behavior to that observed on the 15-mer channel, further corroborating that direct Au NP/ TiO<sub>2</sub> contact could be responsible for the photocurrent enhancement seen on this channel.

Previous studies have demonstrated that AuNPs in direct contact with TiO<sub>2</sub> substrates alter the carrier lifetime measured on the TiO<sub>2</sub> surfaces alone due to the increased recombination probability.<sup>538,579</sup> We measured the changes in carrier lifetime by performing electrochemical impedance spectroscopy (EIS) on the two channels before and after hybridization. The phase diagram of EIS shows a positive phase shift after hybridization which delineates a decrease in carrier lifetime on the 15-mer channel, whereas no significant shift is observed for the 20-mer channel (Supplementary Figure S5.8). Reduction of carrier lifetime between probe-modified and hybridized electrodes is calculated as 46.8% and 2.1 % for 15-mer and 20-mer channel, respectively. The change in carrier lifetime suggests that Au NPs are directly contacting the TiO<sub>2</sub> NPs on the 15-mer channel, which is not observed on the 20-mer channel. This is in line with our hypothesis that the AuNPs on the 15-mer channel have a higher chance of collision with the TiO<sub>2</sub> NPs compared to the 20-mer channel.

To understand the link between the changes in the DNA motional dynamics and the PEC response of the two channels, we consider the possible mechanisms for signal generation. Upon optical excitation of this Au-TiO<sub>2</sub> NP complex, electron/hole pairs are generated at the surface of TiO<sub>2</sub> NPs and interband carriers are generated in Au NPs<sup>513</sup> as the d-band energy lies only 2.4 eV below the Fermi levels of Au<sup>580</sup> (Figure 5.3(b)). When Au NPs are in proximity or contact to the surface of a semiconductor, it is possible to induce multiple effects on the photocurrent of the semiconductor,<sup>515,534</sup> including catalysis, surface passivation, Fermi-level equilibration/photocharging, incident energy absorption,<sup>581</sup> plasmonic-enhancement (light scattering, hot electron injection<sup>582</sup>, enhanced semiconductor absorption due to local electric field enhancement,<sup>583</sup> plasmon-induced resonance energy transfer (PIRET)), and Förster resonance energy transfer (FRET).<sup>584,585</sup>

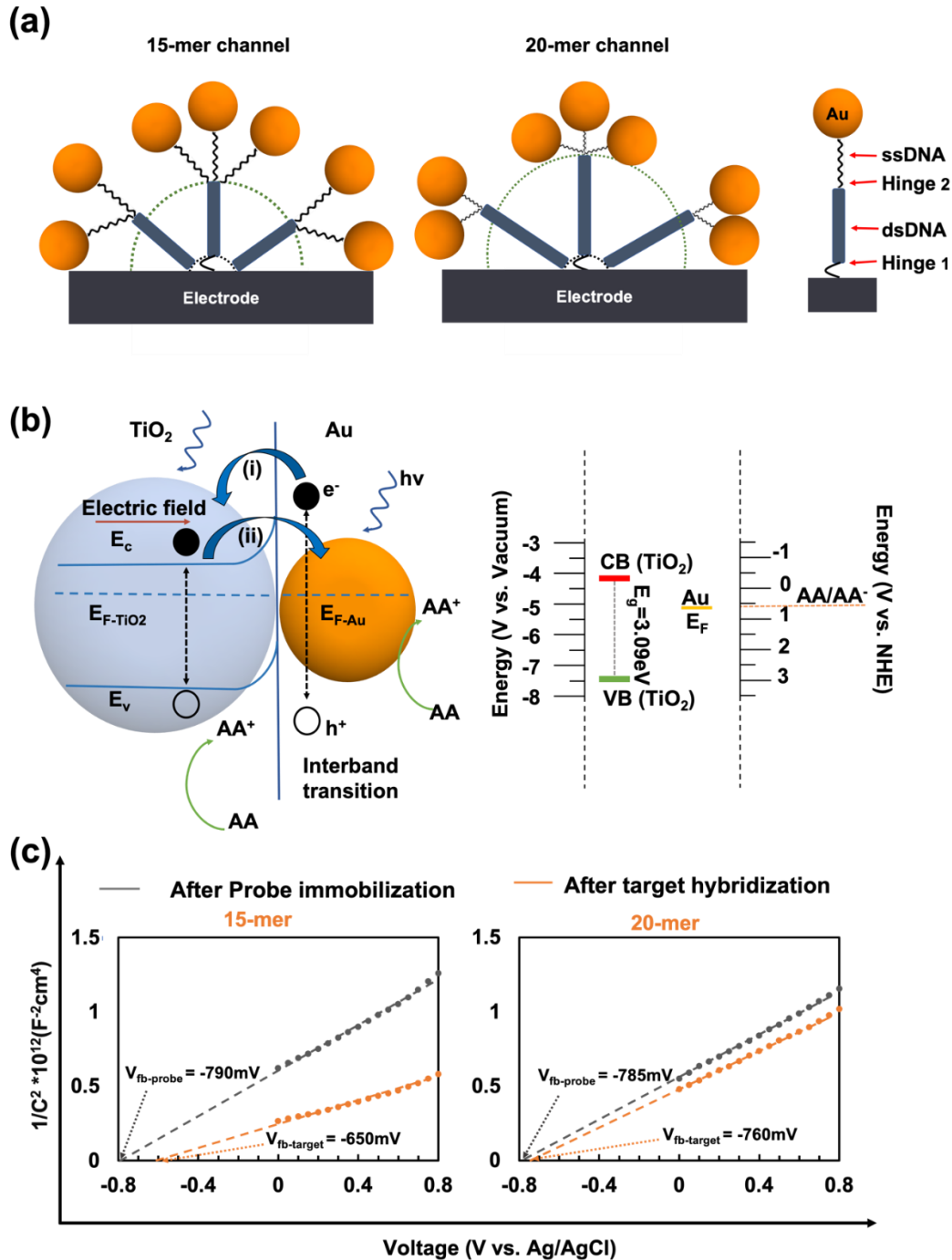


Figure 5.3 The physics of differential signaling in the 15-mer and 20-mer channels. (a) Schematic diagram of the molecular building blocks of the 15-mer and 20-mer channels by considering the dsDNA as a rod-like structure and ssDNA as a flexible string-like structure on a model planar surface. (b) Band diagram and Schottky contact formation at the TiO<sub>2</sub>-Au interface (left). Valence and conduction band energy level for TiO<sub>2</sub> and Fermi energy level for AuNP are drawn with respect to vacuum and NHE (right). Ascorbic acid oxidation potential is depicted here using a dotted red line. For photocharging process, electrons from TiO<sub>2</sub> will transfer to Au NP (i) and in hot electron transfer process, hot electron from Au NP will transfer to TiO<sub>2</sub> (ii) (c) Mott-Schottky ( $1/C^2$  vs. voltage) plots for 15-mer and 20-mer channels, before and after hybridization with the Au NP-labelled 25-mer target.

Regarding the signal increase observed on the 15-mer channel and noting that catalysis is insignificant in our electrolyte system, we consider Fermi-level equilibration/photocharging, light scattering,

plasmonic hot electron injection, enhanced semiconductor absorption due to local electric field enhancement, and PIRET. Since the gold nanoparticles are 12 nm in size (Supplementary Figure S5.9), plasmonic light scattering is negligible.<sup>585,586</sup> Enhancement of the local electric field at the surface of AuNPs through localized surface plasmon resonance can enhance the photocurrent induced in TiO<sub>2</sub> nanoparticles through radiative and non-radiative (PIRET)<sup>532,584</sup> mechanisms.<sup>534</sup> Radiative energy transfer from metal NPs to the semiconductor enhances absorption cross-section by enhancing electron-hole pair generation in the semiconductor.<sup>583</sup> However, for smaller Au NPs (diameter <30 nm) such as those used here, the efficiency of radiative energy transfer drops significantly, making it an unlikely enhancement mechanism.<sup>534</sup> PIRET is the non-radiative energy transfer process that can increase the electron-hole pair in TiO<sub>2</sub> NPs.<sup>586,587</sup> PIRET occurs as a result of dipole-dipole coupling between the plasmon of the metal NP and the electron-hole pairs in the semiconductor due to the spectral overlap of the plasmonic resonance band of the metal NP and the semiconductor's absorption band.<sup>498</sup> Cushing et al. performed an experiment using transient absorption spectroscopy to investigate whether charge transfer or PIRET is the dominant mechanism for photoconversion efficiency enhancement in the metal NP-semiconductor heterojunctions.<sup>587</sup> It was shown that there is no detectable PIRET effect for the wavelength range of 350-750 nm when Au NP is in contact or proximity with TiO<sub>2</sub>. PIRET requires strong dipole generation in a metal, which occurs by exciting plasmons. From the absorption spectra of Au NPs (Figure 5.2(a)-inset), it can be seen that the significant plasmon excitation occurs in the range of 515-525 nm. Due to the fact that the UV excitation used in this work (395 nm) does not include the plasmonic band of Au NPs (in the range of 515-525 nm), we can exclude PIRET mechanism for the photocurrent enhancement seen in 15-mer channel.<sup>532,534</sup> It is important to note that although our materials architecture is not identical to that used in Cushing's work, in both cases, the TiO<sub>2</sub> shows an absorption tail at 395 nm (the excitation wavelength used in this work) and the plasmonic excitation of the gold falls within the 515-530 nm range.

Hot electron transfer and Fermi-level equilibration/photocharging are both potential mechanisms for signal enhancement, suggesting that the 15-mer/25-mer DNA construct enables direct charge transfer to occur between the Au NPs and TiO<sub>2</sub> matrix.<sup>587,588</sup> A large shift in the flat band potential (~140 mV) observed in the 15-mer channel after target hybridization (Figure 5.3(c)) compared to the much smaller shift in the 20-mer channel confirms that there is a larger probability for direct charge transfer in the 15-mer compared to the 20-mer case. This potential shift was not evident when unlabelled target DNA was used (Supplementary Figure S5.10), indicating the importance of the interaction between Au and TiO<sub>2</sub> NPs. The shift in flat band potential has been previously observed in Au NP modified semiconductors and is attributed to Fermi level equilibration,<sup>589,590</sup> which occurs due to the metal deposition at the semiconductor electrode (Figure 5.3(b)) and the direct charge transfer from the semiconductor to the metal.

Photocharging occurs when light-induced electrons move from the semiconductor conduction band to the surface of Au NPs, and is a special case of Fermi level equilibration under light excitation.<sup>515,591</sup> This directional electron movement occurs if the Fermi energy of Au NPs lies below the conduction band energy of TiO<sub>2</sub>,<sup>592</sup> which is the case in our experiments (Figure 5.3(b)). Au NPs have been reported to exhibit this electron-sink (photocharging) effect and can minimize charge recombination owing to enhanced charge separation (Supplementary S5.11).<sup>527,593</sup> This enhanced charge separation is supported by the increased carrier density observed from the slope of the Mott-Schottky curve measured after hybridization on the 15-mer channel (Figure 5.3(c) and supplementary Table S1).

Hot electron injection or the direct transfer of excited charge carriers also explains the signal enhancement seen on the 15-mer channel, in which there is a large probability for direct electron transfer.<sup>492</sup> Hot holes/electrons are generated by plasmon dephasing<sup>585,586</sup> with the energetics of the hot carriers depending on the excitation energy (Intraband/interband excitation).<sup>594,595</sup> The energy of the hot electrons is higher for intraband excitation; whereas hot holes are more energetic for interband excitation<sup>519,596,597</sup> that is used in our experiments.<sup>512,598</sup> It is hypothesized that interband d-sp transitions in the Au NPs following UV excitation generate highly energetic hot holes and hot-electrons that are capable of taking part in redox reactions.<sup>526,530,599</sup> For interband transitions, the energy of the hot holes can be as high as ( $E_{F-Au} - h\nu_{excitation}$ ), whereas the energy of hot electrons lies near the Fermi level of

Au,<sup>530</sup> where  $E_{F-Au}$  denotes the Fermi level of Au NPs and  $v_{excitation}$  is the excitation wavelength. These hot holes, generated at the surface of the Au NPs can directly oxidize AA in conjunction with the holes generated upon UV excitation of the underlying TiO<sub>2</sub> matrix.<sup>583,600</sup> Interband hot electrons can also have sufficient energy to overcome the Schottky barrier at the Au-TiO<sub>2</sub> interface and therefore the electrons can move from Au NPs to the TiO<sub>2</sub> matrix.<sup>601</sup> This phenomenon can also increase the anodic current generated and collected at the 15-mer channel.

Regarding the signal decrease observed on the 20-mer channel, we expect the DNA motional dynamics to lower the probability of direct charge transfer between the Au NPs and the TiO<sub>2</sub> matrix. Consequently, photocharging and plasmonic hot electron injection can be considered negligible. The 12 nm Au NPs can strongly absorb the incident light;<sup>602</sup> however, the energy uptake by the Au nanoparticles cannot transfer to TiO<sub>2</sub> due to the low probability of charge transfer. Therefore, these gold nanoparticles partially block the incident light received by TiO<sub>2</sub>, leading to the reduction of photocurrent in TiO<sub>2</sub>. Moreover, DNA labelled Au-NPs are negatively charged<sup>603</sup> and sterically and electrostatically hinder the access of AA to the electrode system, which reduces the system's electrochemical activity.

To confirm that the change in photocurrent is driven by the probability of charge transfer between the Au NPs and TiO<sub>2</sub> matrix and is not sequence-specific, we designed an experiment where the longer probe sequence (20-mer) was hybridized with a longer Au NP-labelled target sequence (34-mer). In this case, the target/probe length ratio was kept the same as the 15-mer/25-mer channel. Similar to the 15-mer/25-mer complex, the 20-mer/34-mer DNA construct demonstrated a signal increase upon hybridization (Supplementary Figure S5.12), indicating the importance of the length ratio between the single stranded and double stranded segments of DNA complexes in controlling their interaction with the electrode surface. In order to further verify that the signal-on and signal-off responses were related to the different collision probabilities experienced between the Au NPs and the TiO<sub>2</sub> matrix on the two channels, hybridization experiments with Au NPs attached to the proximal end of the target DNA were conducted. It was hypothesized that a similar enhancement in photocurrent would be exhibited in both the 15-mer and 20-mer channels as the Au NPs, when positioned at the proximal end of the DNA target, would have very similar interactions with the TiO<sub>2</sub> NPs. As expected, PEC measurements (Supplementary Figure S5.13) revealed similar enhancements in photocurrent (~174.33% and ~172.38% on the 15-mer and 20-mer respectively) on both channels, thereby confirming that the signal-on and signal-off responses were related to the different collision probabilities experienced between the Au NPs and the TiO<sub>2</sub> matrix on the two channels.

We used the knowledge obtained from this DNA nano-spacer study to create an ultra-sensitive differential DNA biosensor. For this purpose, we integrated the 15-mer and 20-mer channels onto a single spatially-multiplexed substrate (Figure 5.4(a)), allowing both channels to be interfaced with a *single* solution. As expected, when a heterogeneous solution containing both complementary and non-complementary DNA sequences was introduced to the device (target drop), the electrodes on the 15-mer channel showed a PEC current that monotonically increased with increasing the concentration of complementary DNA, whereas the 20-mer channel demonstrated a monotonically decreasing current (Figure 5.4(a)). We then plotted the percentage change that was measured on each channel before and after the introduction of blank and target drops containing 100 aM-1 nM of complementary DNA suspended in the blank solution (Figure 5.4(b)). Additionally, we plotted the differential response of the device by adding the magnitude of changes obtained using the 20-mer and 15-mer channels. This differential processing increased the signal magnitude at every target concentration point. For example, a signal change of 186% for the 15-mer channel at 1 nM was increased to 227% upon differential processing. Moreover, this signaling strategy increased the sensitivity of the measurement from 14% per log for the 15-mer channel and 7% per log for the 20-mer channel to 23% per log for the differential approach (Supplementary Figure S5.14) resulting in a limit-of-detection of 800 aM, with a log linear dynamic range of three decades, which is significantly enhanced compared to previous semiconductive/plasmonic DNA biosensors using a single channel (Supplementary Table S2).

The Stability of both channels was evaluated by illuminating the electrodes after target recognition repeatedly for 15 cycles for a period of 600 s (Supplementary Figure S5.15). Through this repeated

cycling, both of the 15-mer and 20-mer channels showed stable photocurrents with relative standard deviations of 1.35 % and 1.29 %, respectively.

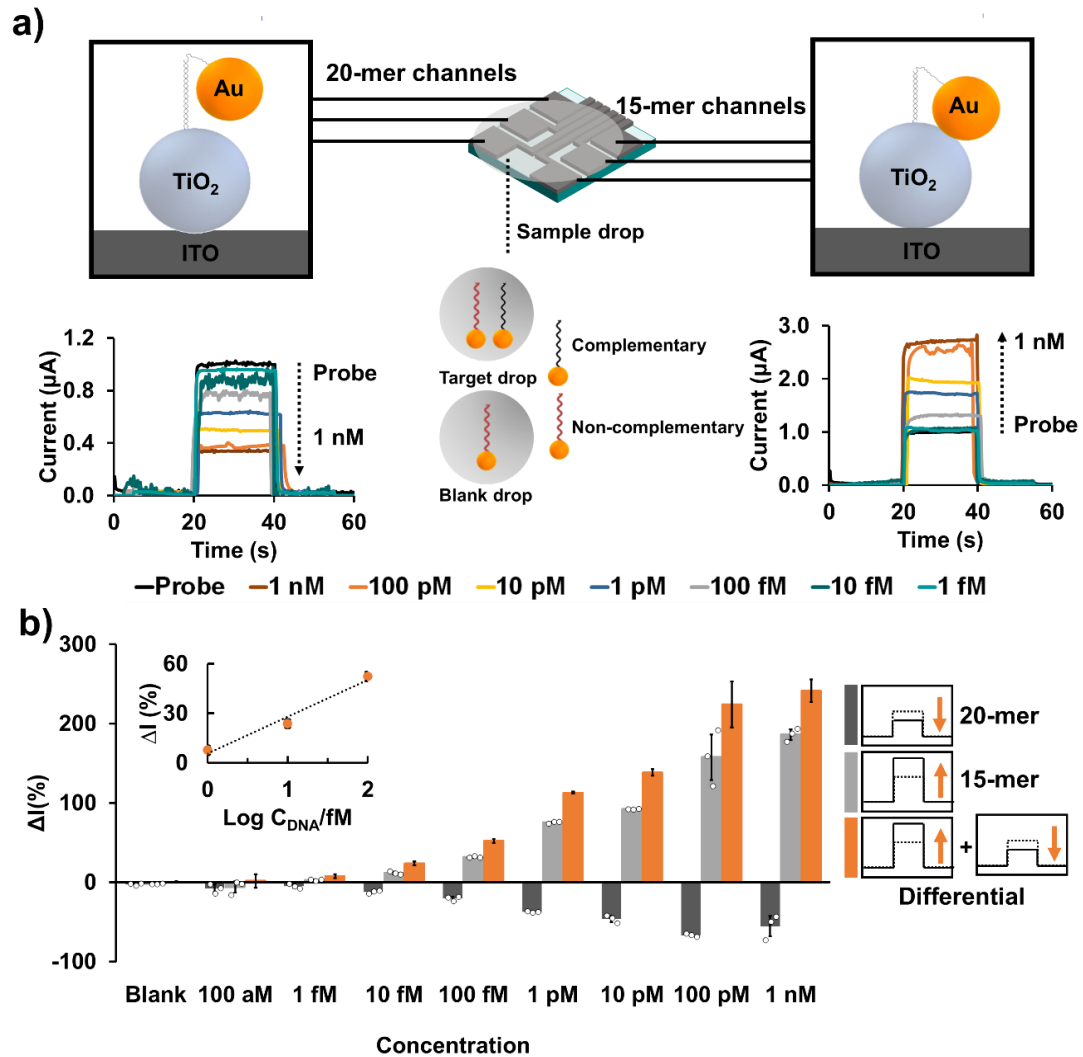


Figure 5.4: Differential biosensing enabled by DNA nano-spacers. (a) Illustration of the spatially-multiplexed differential biosensor design (top) and the corresponding PEC data for various concentrations of target 25-mer AuNP-labeled DNA on the 20-mer and 15-mer channels (b) Signal change obtained upon incubation with blank and target drops on the 15-mer and 20-mer-channels. The differential signal changes are calculated by adding the magnitude of signal changes obtained from the 15-mer and 20-mer channels. The inset shows the calibration curve for determining the limit-of-detection. Error bars represent one standard deviation, with experiments performed using at least three separate devices.

### 5.5 Conclusions

In this work, we sought to create a differential photoelectrochemical biosensor that uses a single label for obtaining signal-on and signal-off responses on a single multiplexed chip. Single stranded DNA probes of different lengths were used as nano-spacers that modulate direct electron transfer between Au NP-labelled DNA targets and TiO<sub>2</sub> NPs on the electrode surface. DNA sensing channels with 15-mer probes demonstrated a signal increase upon hybridization with a 25-mer Au NP-labelled target DNA; whereas channels with 20-mer probes demonstrated a signal decrease. Measuring the changes in charge carrier density and lifetime, as well as theoretical DNA conformation calculations indicated that

increasing the probe length from 15 to 20 nucleotides significantly reduced the probability of direct electron transfer between Au and TiO<sub>2</sub> NPs, and is responsible for changing the sensor response from signal-on (15-mer) to signal off (20-mer).

We combined these signal-on and signal-off PEC channels on a single device to create a differential DNA biosensor, which increased the device sensitivity by a factor of 1.5 or 3.2 compared to using only the 15-mer or 20-mer channels, respectively and resulted in the remarkable limit-of-detection of 800 aM. Given its performance and reliance on robust materials, we expect this differential PEC readout strategy to be applicable to a wide range of electrochemical biosensors where enzymes and redox species are currently used as labels. Although this study demonstrates a proof-of-concept differential signal transduction assay, in the future, it can be extended for analyzing clinically-relevant samples by its integration with DNA machines<sup>604-608</sup> where target capture is translated to the release of Au NP-labelled DNA barcodes<sup>609</sup>.

### 5.6 Acknowledgements

This work was supported by NSERC and Ontario Early Researcher Award grants to L.S., and a salary award to L.S. from the Canada Research Chairs Program, The electron microscopy was carried out at the Canadian Centre for Electron Microscopy (CCEM), a national facility supported by the NSERC and McMaster University. S.S and A. V are the recipients of NSERC doctoral scholarships.

### 5.7 Supplementary Information

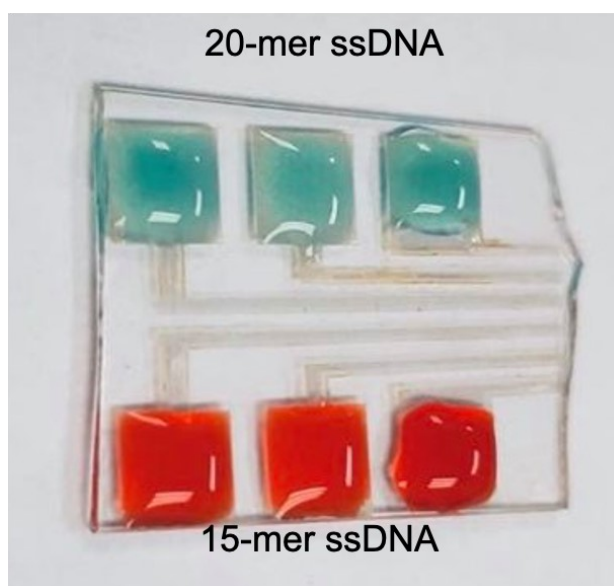


*Figure S5.1 Biofunctionalization of photoelectrodes with 15-mer and 20-mer ssDNA probes by drop-depositing the target on the electrodes. Green and Red colors are used to emphasize the spatial difference among the target solutions.*

Figure S5.1 shows the photograph of the spatially-multiplexed electrodes. It shows the manual modification of separate areas of the photoactive TiO<sub>2</sub> electrodes with probe.

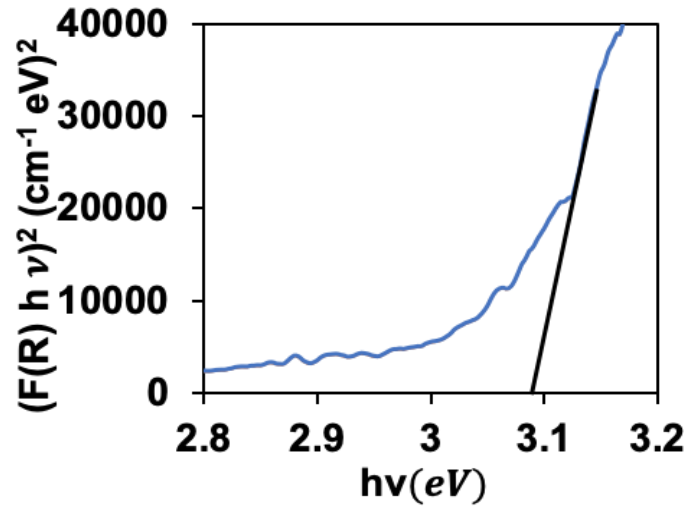


Figure S5.2 Determining the bandgap of the TiO<sub>2</sub> NP films. The intersection of the slope and x-axis determines the bandgap.

It has been shown that the bandgap of TiO<sub>2</sub> nanoparticles (NPs) can be determined from diffuse reflectance spectroscopy.<sup>1</sup> In this work, the Kubelka-Munk (K-M or F(R)) method was applied for the bandgap estimation.<sup>2</sup> By plotting  $(F(R)h\nu)^n$  as a function of  $h\nu$ , one can determine the bandgap. For indirect bandgap,  $n=0.5$ , whereas for direct bandgap,  $n=2$ . From the above plot in Figure S5.2, we determine the bandgap of the P25-TiO<sub>2</sub> NPs used in this work to be 3.09 eV.

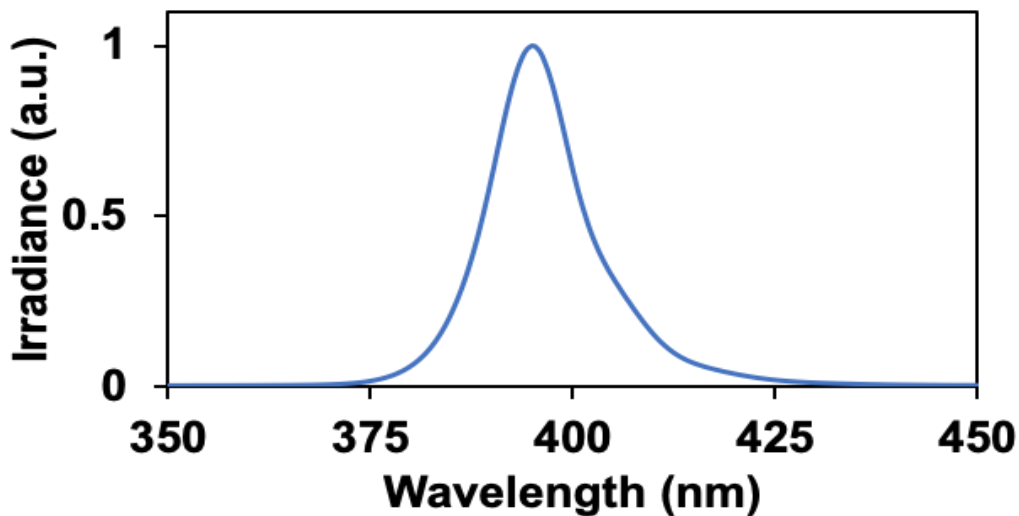


Figure S5.3 Irradiance spectrum of the excitation source used in obtaining the PEC measurements

Figure S5.3 shows the irradiance spectrum of the LED flashlight used in this work for exciting the photoelectrodes. Peak wavelength of the excitation is determined as 395 nm.

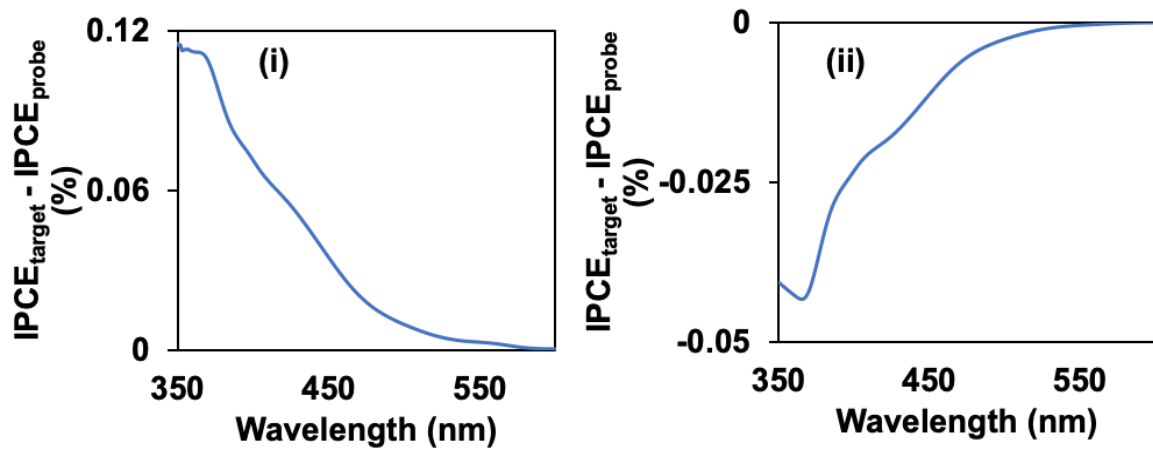


Figure S5.4 Difference of the IPCE values obtained before and after target hybridization for the (i) 15-mer and (ii) 20-mer probes.

The differential IPCE value is calculated to illustrate the wavelength (Figure S5.4) variation of hybridization-induced signal change.

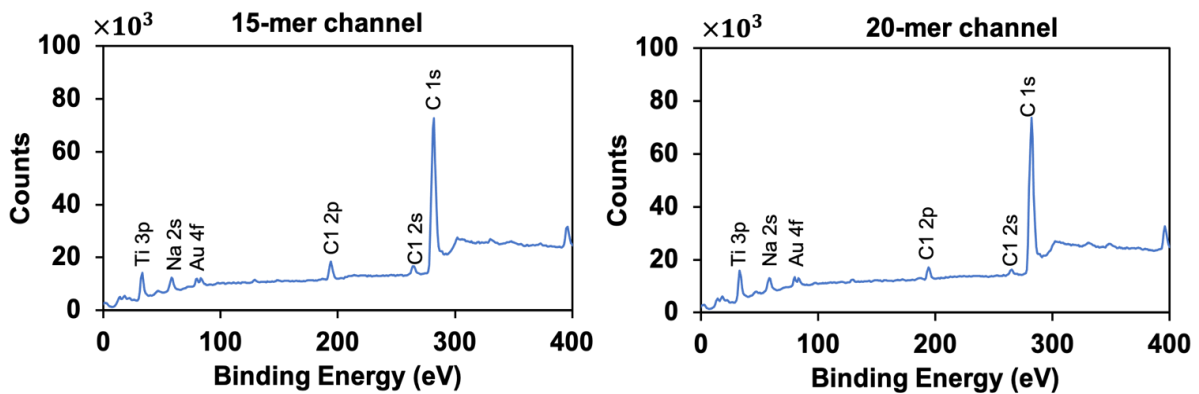


Figure S5.5: XPS analysis of the 15-mer and 20-mer channels. Both channels showed similar amount of Au.

Figure S5.5 shows the spectra obtained by X-ray photoelectron spectroscopy (XPS) technique for the 15-mer and 20-mer channels. Presence of Au NPs on the channels can be confirmed from the characteristic Au 4f spectral line at 83.8 eV. XPS intensity for both channels are similar, which indicates relatively similar amount of surface Au atom on both the 15-mer and 20-mer channels.

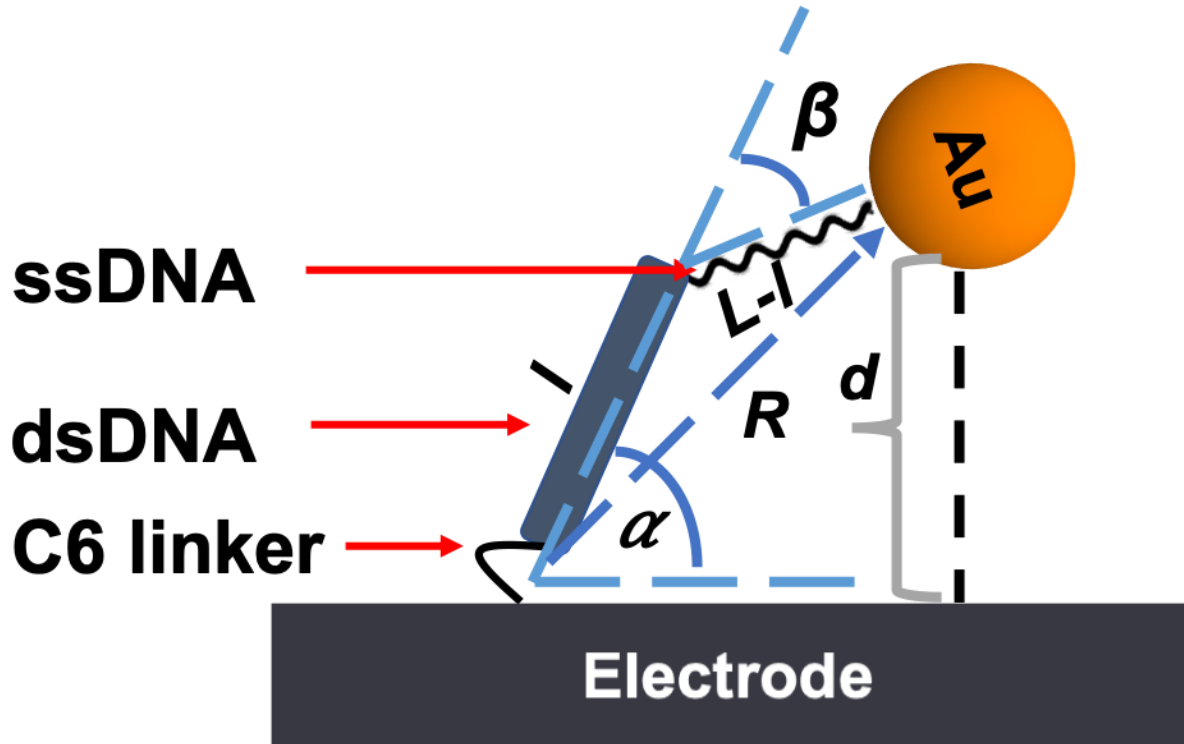


Figure S5.6: Schematic model depicting the DNA structure used in this work having two separate sections (ssDNA and dsDNA) with different persistence length.

Figure S5.6 shows the schematic model of the DNA structure after hybridization. The contour length,  $L$  of the DNA is 8.34 nm (25-mer) as each base-pair is shown to be 0.34 nm in length.<sup>3</sup> The overall structure has four sections: C6 linker, dsDNA, ssDNA, Au NP. Length of the C6 linker is considered to be 1 nm.<sup>4</sup> The diameter of the Au NP used in this study is 12 nm. The length of the dsDNA is denoted by  $l$ , which is 5 nm for 15-mer channel and 6.67 nm for 20-mer channel. The motion of the structure is governed by the stochastic motion of the dsDNA and ssDNA sections. Therefore, the angle between electrode and dsDNA ( $\alpha$ ), and the angle between dsDNA and ssDNA ( $\beta$ ) will vary with the movement of these two sections. Rivetti et al. showed that the end-to-end distance,  $R$ , of the two DNA polymer sections with different flexibility can be calculated as:<sup>5</sup>

$$\begin{aligned} \langle R^2 \rangle = & 2P_1l \left( 1 - \frac{P_1}{l} \left( 1 - e^{-\frac{l}{P_1}} \right) \right) + 2P_2(L-l) \times \left( 1 - \frac{P_2}{(L-l)} \left( 1 - e^{-\frac{(L-l)}{P_2}} \right) \right) \\ & + 2P_1P_2 \left( 1 - e^{-\frac{l}{P_1}} \right) \left( 1 - e^{-\frac{(L-l)}{P_2}} \right) \end{aligned}$$

Here,  $P_1$  is the persistence length of the dsDNA (45-55nm)<sup>3</sup> and  $P_2$  is the persistence length of ssDNA (2 nm)<sup>6</sup>. In order to calculate the collision rate, we calculate the distance,  $d$  from electrode to Au NP. Au NP will be in contact with  $\text{TiO}_2$  if  $d$  is equal zero. The combination of angle  $\alpha$  and  $\beta$  for which the distance ( $d$ ) becomes negative is considered not real and therefore neglected.

From the above model, distance can be calculated as:

$$d = (1 + l) * \sin \sin (90 - \alpha) - (L - l + R_{Au}) * \sin (\alpha + \beta - 90)$$

Where,  $R_{Au}$  is the radius of Au NPs, which equals 6 nm for this calculation.

By following the above procedure relative collision rate for 15-mer channel to 20-mer channel was calculated. The collision rate for 15-mer channel is 5.77-5.83 times higher than the 20-mer channel.

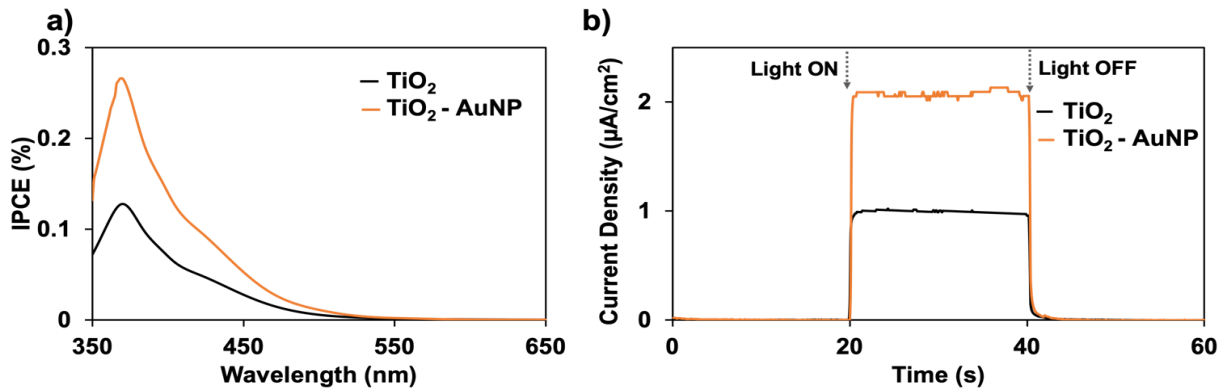


Figure S5.7 Photoelectrochemical comparison between  $\text{TiO}_2$  and  $\text{TiO}_2 - \text{Au NP}$  samples. (a) IPCE spectrum of the photoactive electrodes (b) PEC curves of the photoelectrodes obtained using chopped light chronoamperometry. Both measurements were performed at 0 V bias versus Ag/AgCl and the electrolyte used was 0.1 M ascorbic acid in 0.1 M phosphate buffer solution.

$\text{TiO}_2$  matrix was modified with Au NPs by using electrostatic attraction.  $\text{TiO}_2$  substrates were immersed into Polydiallyldimethylammonium chloride (PDDA) solution which will have positive surface charge and then the substrates were immersed into Au NP solution. Figure S7a shows the IPCE spectrum of the samples before and after modification with Au NPs. In this case, Au NPs are directly in contact with  $\text{TiO}_2$  and therefore we expect the behaviour to be similar of 15-mer channel. Chopped light voltammetry at UV showed more than 2 times photocurrent enhancement (Figure S5.7b).

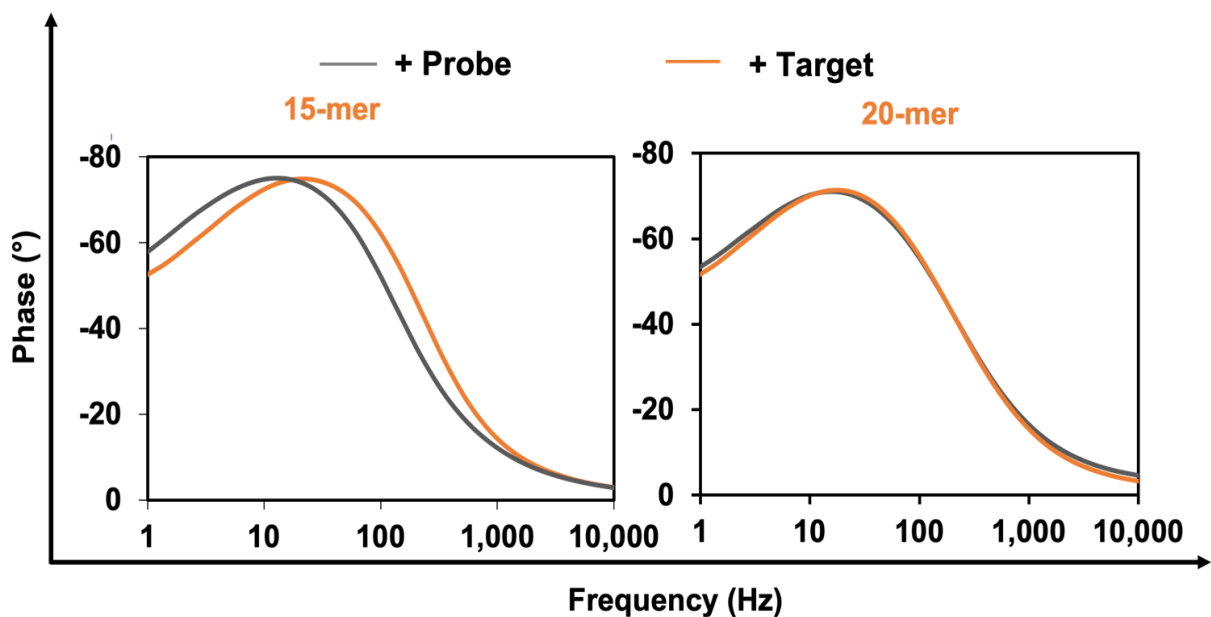


Figure S5.8 Phase diagram of 15-mer and 20-mer channel before and after hybridization obtained from electrochemical impedance spectroscopy (EIS).

Figure S5.8 shows the phase diagram on both 15-mer and 20-mer channel before and after hybridization with a 25-mer Au NP-labelled complementary target using electrochemical impedance spectroscopy (EIS). From the phase response measured using EIS, we can deduce the carrier lifetime as:

$$\tau = \frac{1}{2\pi f_{peak}}$$

where  $f_{peak}$  is the peak frequency for the capacitor element in the phase vs. log frequency curve of the Bode plot (Figure S5.8). We observed that after target hybridization on the 15-mer channel,  $f_{peak}$  shifted towards higher frequency, indicating a decrease in carrier lifetime. Whereas, for the 20-mer channel, no significant shift in the peak frequency was observed. For probe-modified substrate, carrier lifetime is 13.9 ms, whereas after target introduction carrier lifetime becomes 7.4 ms for the 15-mer channel and 13.6 ms for the 20-mer channel. The carrier lifetime significantly decreased for the 15-mer channel and experienced a much smaller change for the 20-mer channel.

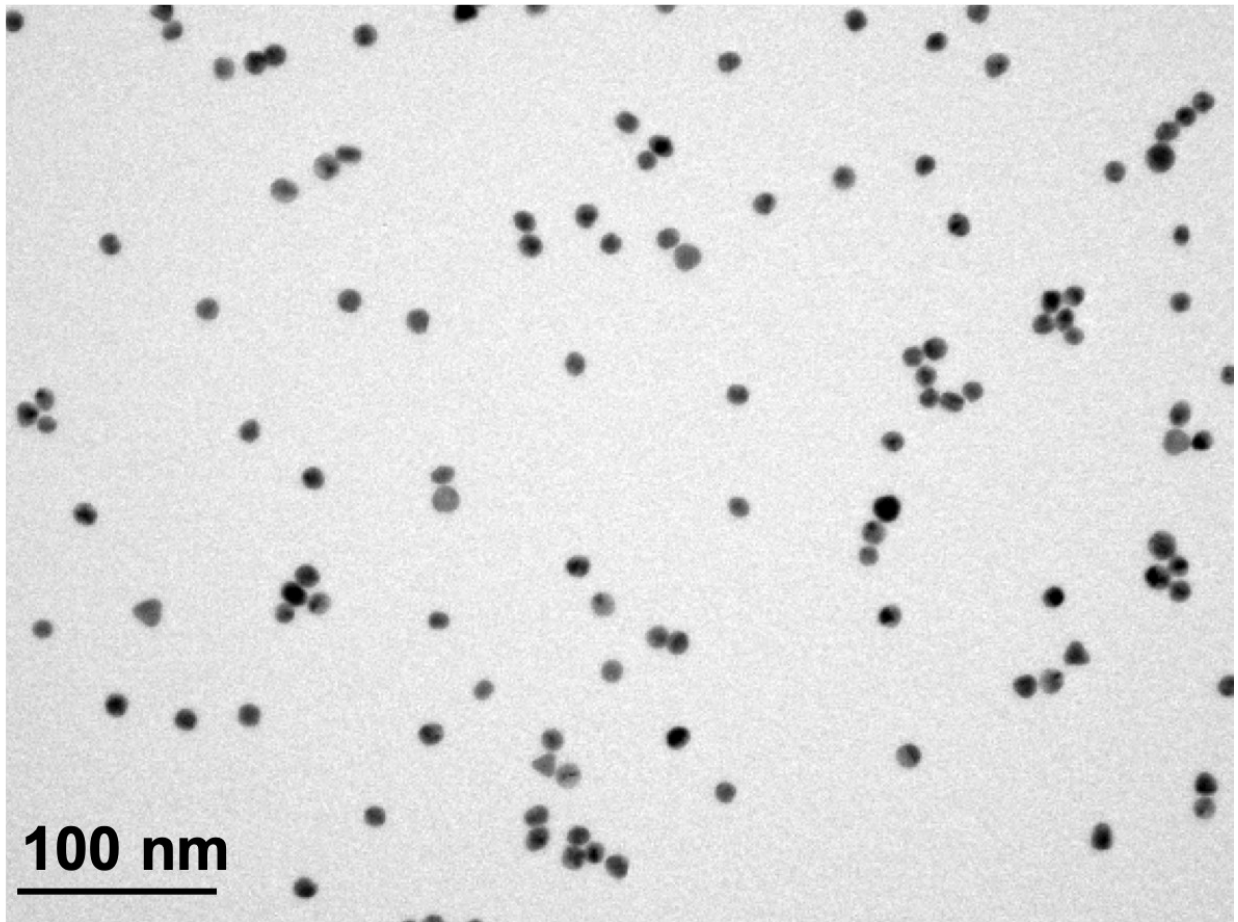


Figure S5.9 Au NPs used in this work imaged using transmission electron microscopy (TEM) showing an average size of 12 nm.

Figure S5.9 shows TEM image of Au NPs. The diameter of the Au NPs were determined as 12 nm.

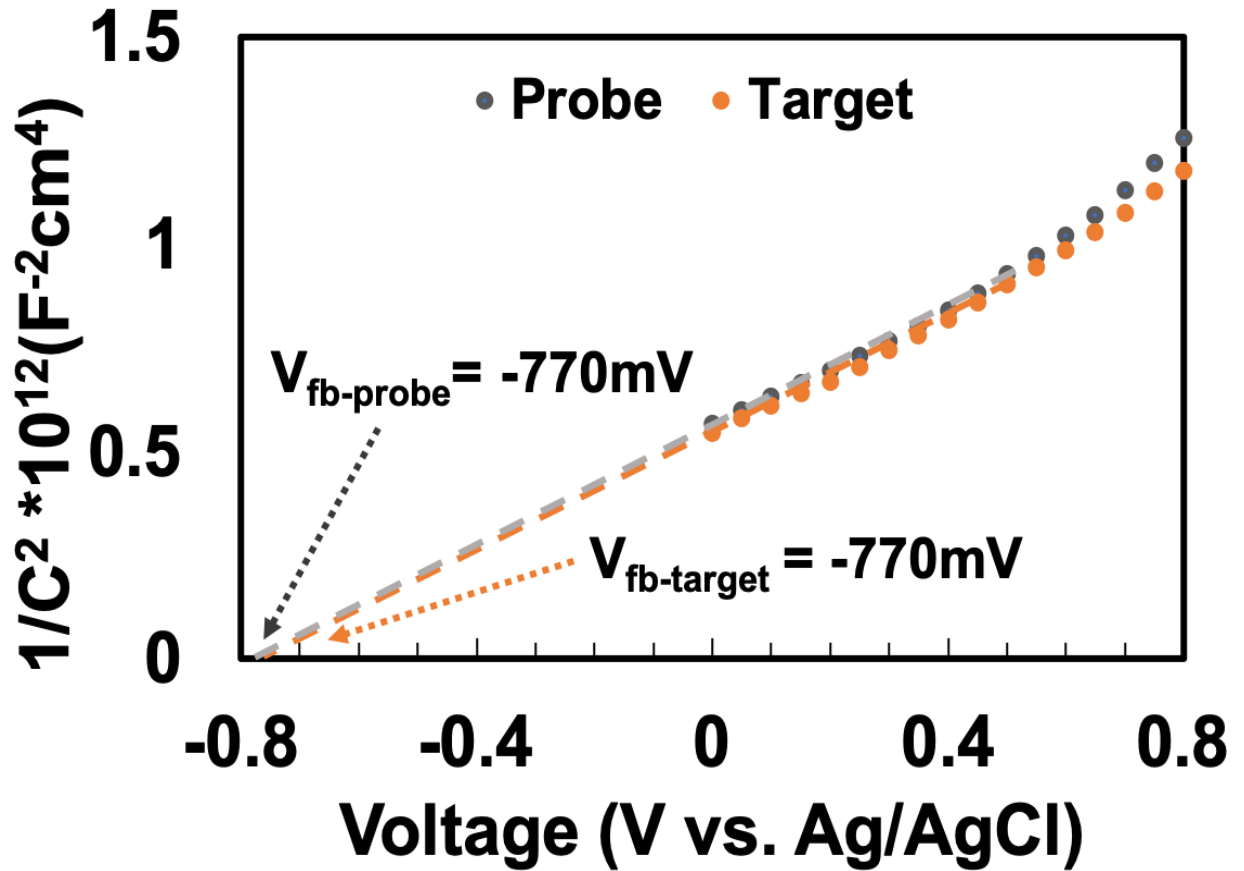


Figure S5.10: Mott-Schottky plot for the hybridization of un-labelled 25-mer DNA targets on the 15-mer channel.

Figure S5.10 shows the Mott-Schottky plot with an un-labelled 25-mer target DNA hybridized on the 15-mer channel. Both the slope and flat-band potential remain unchanged after target hybridization. From the Mott-Schottky plot, flat-band potential and charge carrier density were calculated using the following formula:<sup>7</sup>

$$\frac{1}{C^2} = \frac{2}{\epsilon\epsilon_0 A^2 e N_D} (V - V_{fb})$$

Where,  $\epsilon$  and  $\epsilon_0$  are the dielectric constant of the semiconductor and vacuum permittivity, respectively.  $N_D$  is the charge carrier density,  $V_{fb}$  is the flat band potential,  $C$  is capacitance and  $A$  is the area of the electrode. The values of the carrier density and the flat-band potentials for different experimental conditions are given in table S5.1:

Table S5.1 Flat-band potential ( $V_{fb}$ ) and charge carrier density ( $N_D$ ) for the 15-mer and 20-mer channels

Material-architecture	$V_{fb-probe}$ (mV)	$V_{fb-target}$ (mV)	$N_{D-probe}$ ( $cm^{-3}$ )	$N_{D-target}$ ( $cm^{-3}$ )
15-mer channel with AuNP labelled complementary target	-790	-650	$1.29 \times 10^{17}$	$2.69 \times 10^{17}$
20-mer channel with AuNP-labelled complementary target	-785	-760	$1.28 \times 10^{17}$	$1.43 \times 10^{17}$
15-mer channel with AuNP labelled non-complementary target	-770	-770	$1.30 \times 10^{17}$	$1.31 \times 10^{17}$

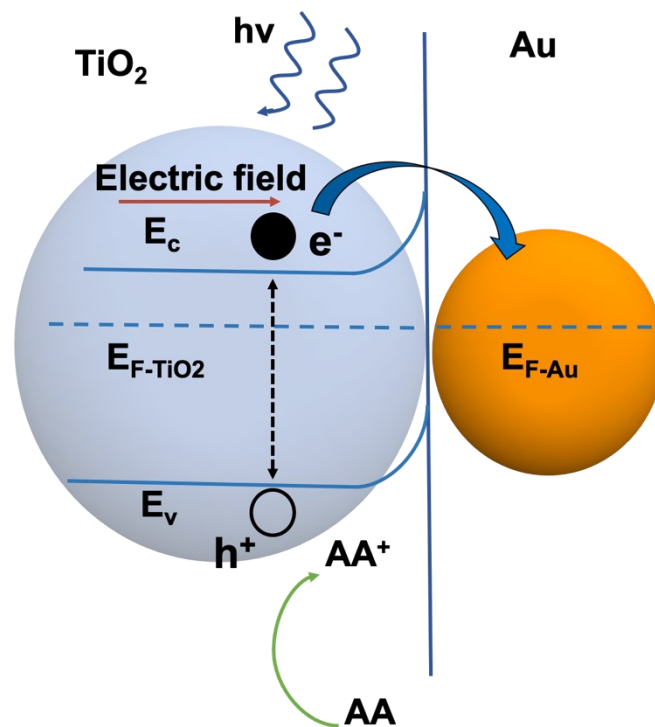


Figure S5.11 Schematics illustrating Photocharging process. Under light excitation, conduction band electrons move to Au NPs and improve electron-hole separation.  $E_c$  and  $E_v$  denotes the conduction band and valence band position, respectively.  $E_F$  denotes the fermi-level position. Holes ( $h^+$ ) from  $TiO_2$  oxidize ascorbic acid (AA) to produce photocurrent

Figure S5.11 shows the photocharging process. UV excitation generates electron-hole ( $e^- - h^+$ ) pairs in the  $TiO_2$ . The Au NPs act as an electron sink thereby allowing the conduction band electrons ( $e^-$ ) to move from the  $TiO_2$  to the Au NP, thus enhancing electron-hole separation. This in turn, increases the charge carrier lifetime and consequently the photocurrent.

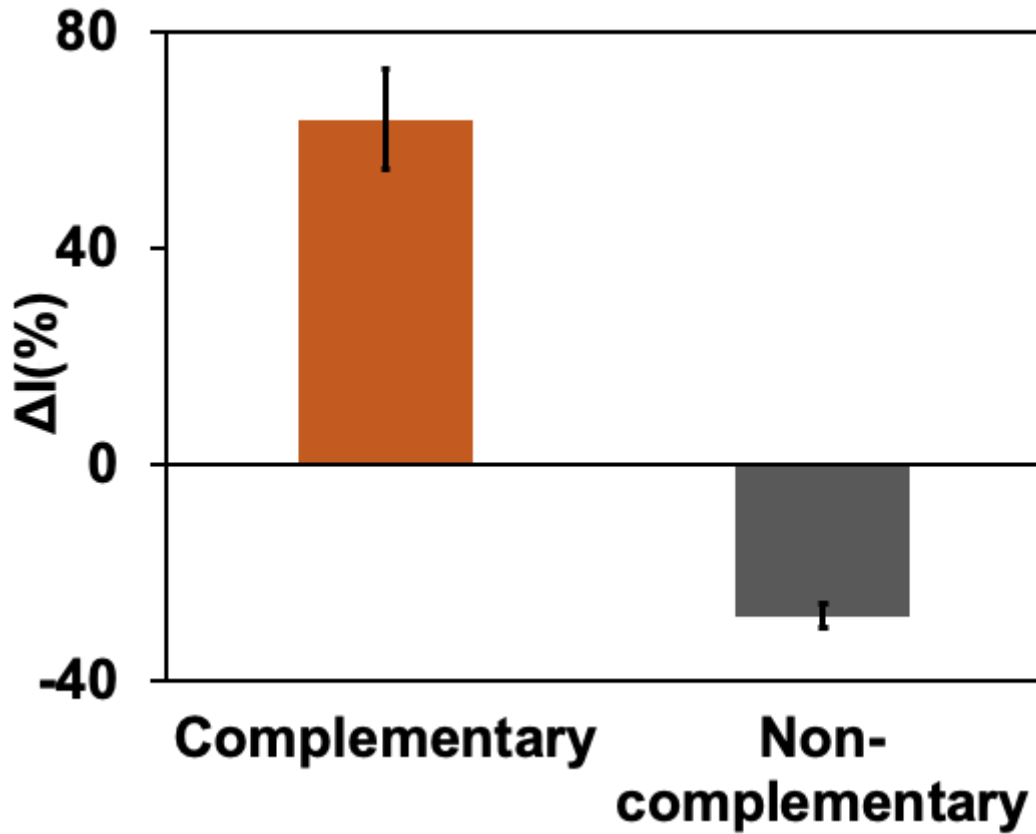


Figure S5.12: Bar plot illustrating the percentage change in photocurrents following hybridization of the 20-mer probes with 34-mer Au NP-labelled complementary targets. The error bars represent standard deviation from at least three separate trials.

Figure S5.12 shows the photocurrent change when 34-mer AuNP-labelled complementary targets were hybridized with electrodes having 20-mer probe. The same trend as the 15-mer channels hybridized with 25-mer AuNP-labelled target was also seen for the 34-mer case. An enhancement in signal of 64 % was seen for the complementary case while a decrease of 28 % observed for the non-complementary case.

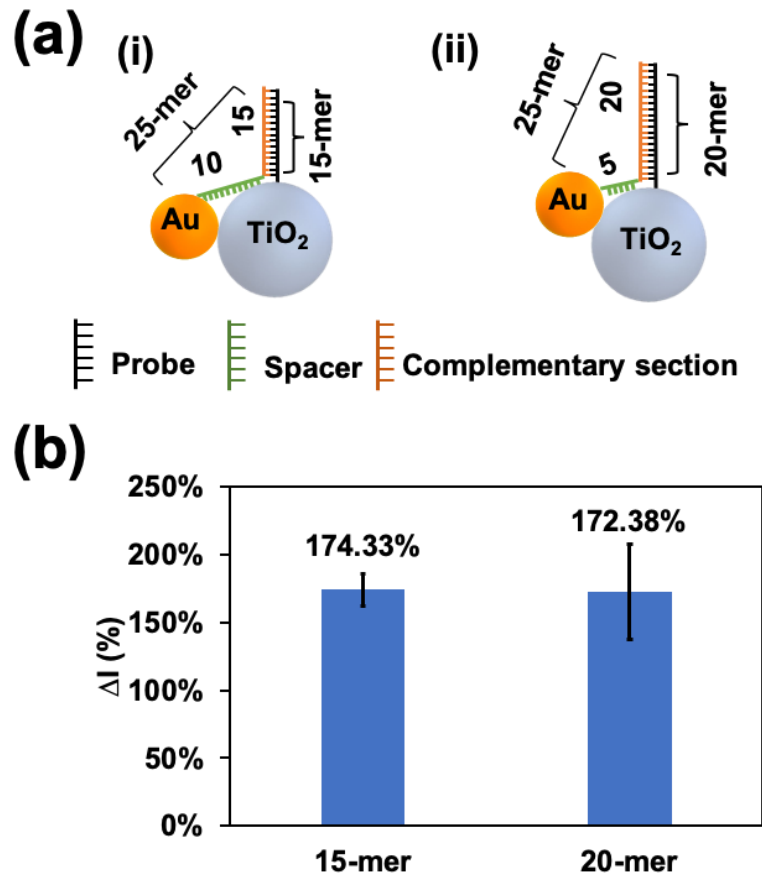


Figure S5.13 Hybridization experiments with Au NP attached to the proximal end of 25-mer DNA and hybridized with 15-mer and 20-mer probes. (a) Schematic illustration of (i) 15-mer and (ii) 20-mer channels after hybridization with AuNP-labelled target. (b) Photocurrent enhancement for 15-mer and 20-mer channels.

Figure S5.13a shows the schematics of both 15-mer and 20-mer channels when hybridized with AuNP-labelled target where Au NP is attached to the proximal end of the target. As it can be seen from the schematics, in both channels, Au NP is expected to directly contact the TiO<sub>2</sub> nanoparticles surface. Figure S13b shows the bar plot of the photocurrent enhancement after target introduction for the systems used in a). As the Au NP is expected to contact TiO<sub>2</sub> in both 15-mer and 20-mer channels, we observe similar signal enhancements in both channels.

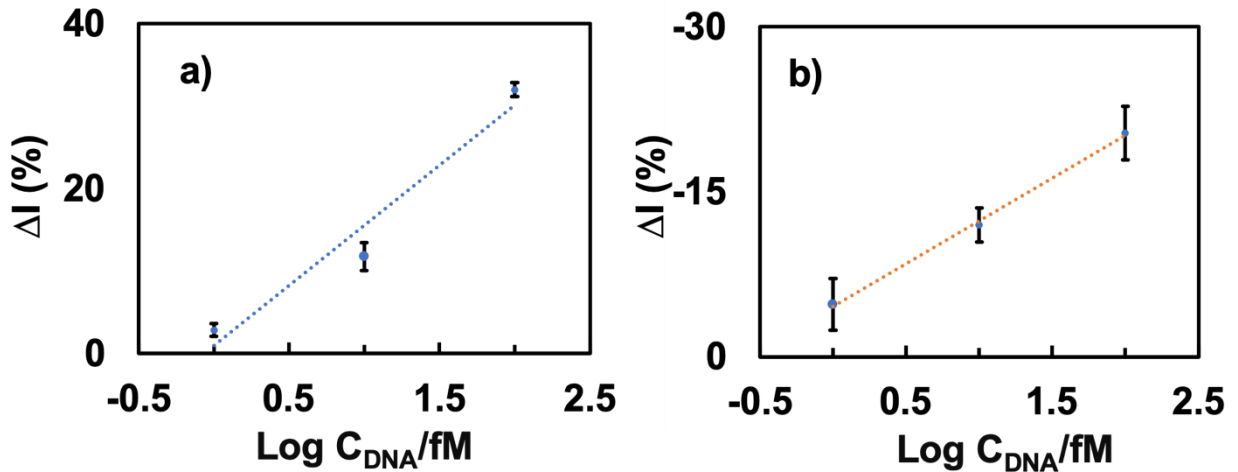


Figure S5.14: Calibration curves for the (a) 15-mer and (b) 20-mer channels for various concentration of target DNA as tested in figure 4.

The linear regions of the calibration curve as shown in Figure S5.14 were fitted using the following equations: (a)  $\Delta I (\%) = 14.56 \log C + 0.98$ ; correlation coefficient 95.2%, (b)  $\Delta I (\%) = 7.78 \log C + 4.57$ ; correlation coefficient = 99.8%.

A summary of the recent works for developing PEC DNA sensor using plasmonic properties is provided in table S5.2. As can be seen from the table, implementing dual channel strategy helps to achieve sub femtomolar sensitivity.

Table S5.2 Summary of the recent PEC DNA sensor utilizing plasmonic properties of metal NPs

Semiconductor-Plasmonic material	Target	Sensing Approach	Channels	LOD, linear range	References
CdS Quantum dots -Ag Nanocluster	DNA	Signal Off	1	0.3 pM, 1pM – 10nM	8
TiO <sub>2-x</sub> – Au NP	DNA	Signal On	1	0.6 pM, 1pM – 10nM	9
Polymer dots – Au NP	DNA	Signal off	1	0.97 fM, 1 fM – 10pM	10
TiO <sub>2</sub> NP – Au Nanorod	Micro-RNA	Signal On	1	20 fM, N/A	11
TiO <sub>2</sub> NP – Au NP	DNA	Signal On	2	0.8 fM, 1fM – 100fM	This work

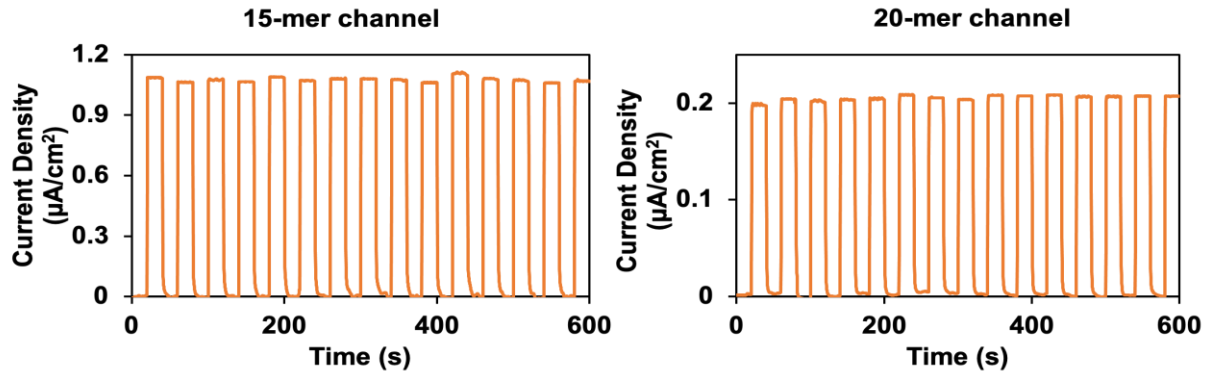


Figure S5.15 Stability test of both 15-mer and 20-mer channels over 15 illumination cycles

Figure S5.15 showed the photocurrent density measurement over 15 illumination cycles. The period of each cycle was 40s with 50% times of illumination. Both 15-mer and 20-mer channel showed stable photocurrents.

## Chapter 6: Dynamic DNA barcodes - A differential strategy for single-electrode PEC nucleic acid detection in urine (Objectives 5, 6)

### *Preface*

While the previous work demonstrated single wavelength programmable DNA detection using labelled targets on *dual-electrodes*, this chapter relays the development of an innovative affinity-based differential PEC sensor that integrates dynamic DNA barcodes to detect nucleic acids on the basis of a sequential partial hybridization strategy on a *single-electrode*, without directly labelling the bioanalyte. The ability to constrain dual-signal generation—at a single illumination wavelength—to a single electrode further streamlines this PEC strategy, making it more amenable to POC translation. Building on the knowledge gleaned from the previous chapter, the detection strategy developed in chapter 6 utilizes predictive dual-signal modulation in Au/TiO<sub>2</sub> systems to initiate a reverse signal-to-concentration effect, where the largest signals are obtained at the lowest concentrations. Subsequently, the use of combinatorial dual-signal processing enhances the limit of detection and sensitivity of the assay by up to 15- and three-fold respectively, as compared to analogous PEC assays with a single binding event (signal-off or signal-on alone) and exhibits a limit of detection of 3 fM in buffer and 5 fM in urine. Furthermore, this differential biosensor is capable of discerning single-base mismatched sequences. As this dynamically barcoded PEC sensor, integrating biorecognition with dual-signal transduction, demonstrates robust nucleic acid detection in urine, it thus presents potential applications in short-sequence DNA detection such as the sensing of miRNA biomarkers linked to diseases such as cancer, heart disease, etc. Additionally, this chapter demonstrates the realization of objectives 5 and 6 stated in Chapter 1 of this thesis.

### *Authors*

Amanda Victorious\*, Sudip Saha\*, Richa Pandey, and Leyla Soleymani.

(\*indicates that Amanda Victorious and Sudip Saha contributed equally to this authorship and are co-first authors).

Here my colleague Dr. Saha and I jointly devised a novel detection scheme to eliminate the labelling of target DNA. In this work, I synthesized the photoactive nanoparticles and fabricated photoelectrodes using ITO patterning, solution-based NP deposition and baking of the photoelectrodes. I then biofunctionalized the electrodes using single stranded DNA and an anti-fouling agent (Figure 6.1). Once fabricated, I performed experiments utilizing chopped light amperometry to ascertain the photocurrent response to various concentrations of target DNA spiked in phosphate buffered saline (Figure 6.2 (a, b), Figure 6.3 (b)) and urine (Figure 6.3 (d)). In order to avoid researcher bias, I obtained the data for all the results in spiked buffer and the data pertaining to 100 pM – 1 pM of target DNA spiked in urine while Dr. Saha acquired the rest of the data in urine. Jointly, we then extracted the differential response of the sensor (Figure 6.3 (b, i), 6.3 (d, i)). I then plotted the LOD calibration curves for both data sets and extracted the LOD for both the buffer and urine data using the differential approach (Figure 6.3 (b, ii), 6.3 (d, ii)) and their signal-off analogues (Figure S6.5). Dr. Saha and I designed a couple of iterations of base-mismatches to evaluate the specificity of the system. Following design finalization, I fabricated all the electrodes for the experiment but only performed chopped light amperometry on the 2-base mismatched, and non-complementary (NC) data set (Figure 6.4 (2-base mismatch, NC)). Furthermore, I performed preliminary kinetic assessments of the system (Figure S6.4) and compared the systems response to 1 pM DNA target spiked in buffer *versus* urine (Figure S6.6) using chopped light amperometry. It is important to note that Dr. Saha acquired the comparative response for figure S6.6 in plasma.

To summarize, I was responsible for the experimentation, data analysis, figure (and/or schematic) creation and manuscript write up for figures: 6.1, 6.2 (a, b), 6.3 (b (i, ii)), figure 6.3 (d (i,ii)) ( I acquired the data for 100 pM – 1 pM while Dr. Saha acquired the rest (NC - 100fM), data acquisition for 6.4 (2-base mismatch, NC). In addition, I also performed the experimentation, data analysis and figure creation for figures: S6.4, S6.5 and S6.6. I thank Dr. Saha for his support and collaboration demonstrated throughout the course of this project.

***Publication***

Angew. Chem. Int. Ed. 2021, 60, 7316 –7322

***Publication Date***

January 2021

## 6.1 Abstract

PEC biosensors hold great promise for sensitive bioanalysis; however, similar to their electrochemical analogues, they are highly affected by the variable backgrounds caused by biological matrices. We developed a new PEC biosensing strategy that uses differential signal generation, combining signals from two separate but correlated binding events on the biosensor, for improving the limit-of-detection, sensitivity, and specificity of PEC DNA biosensors in biological samples. In this assay, the binding of unlabeled target DNA is followed by the capture of a signal amplification barcode featuring a plasmonic nanoparticle. The interaction of the plasmonic barcode with the semiconductive building blocks of the biosensor results in significant signal amplification, and together with differential signal processing enhances the limit-of-detection and sensitivity of the assay by up to 15 and three times, respectively, compared to the previously-used PEC assays with a single binding event, demonstrating a limit-of-detection of 3 fM.

## 6.2 Introduction

Photoelectrochemical (PEC) biosensors have been heavily explored over the past decade due to their promise for improved signal-to-noise ratio and enhanced limit-of-detection.<sup>495,610,611</sup> These biosensors translate specific biorecognition events into a change in the output PEC signal.<sup>495,612</sup> As with their electrochemical analogues, the limit-of-detection of PEC transducers is often compromised due to signal fluctuations caused by environmental interferences and minute variations in experimental conditions.<sup>613–615</sup> In response, ratiometric or differential assays, combining two or more PEC signals, have been implemented to reduce the effect of interference and experimental variations, enhance detection accuracy at trace analyte concentrations, and improve analysis reliability.<sup>539,554,566</sup>

The existing ratiometric PEC biosensors typically use multiple photoactive species – signal reporters<sup>555,566,567</sup> or labels<sup>554</sup> – that need to be activated at various voltages<sup>555,567</sup> or wavelengths<sup>554</sup> in order to obtain multiple signal readings for each biorecognition event. Although this multi-species approach is effective in increasing the signal-to-noise ratio of PEC biosensors, it increases the complexity of the measurement instrumentation and the calibration algorithms needed to deal with the varying baseline signals and chemical and optical stability observed when multiple photoactive materials are used in a single system. For PEC biosensors to be translated from the laboratory to the market, it is highly desirable for high sensitivity and specificity to be paralleled with facile operation and instrumentation. As a result, new approaches for ratiometric/differential PEC signal transduction using a single photoactive species, operated at a single voltage using a single light source are needed.

Several PEC biosensors have recently been developed that use the interaction between plasmonic nanoparticles (NPs) such as Au and Ag with semiconductive photoelectrodes to translate biomolecular recognition to a change in the PEC signal.<sup>550,616</sup> Among these, systems that use robust and stable materials are highly desired for use in biosensing devices that undergo multiple washing, incubation, and potential scan steps. Au/TiO<sub>2</sub> systems offer excellent chemical and photostability and have been used in protein,<sup>557</sup> heavy metal,<sup>617</sup> glucose<sup>618</sup> and nucleic acid detection.<sup>502</sup> The major role of Au NPs in these sensing systems is to improve the photoconversion efficiency of the functionalized TiO<sub>2</sub> electrodes upon biorecognition, thereby enhancing the photocurrent. Depending on the assay design, different roles – injection of hot charge carriers, extending the light absorption range, and excitation of charge carriers in TiO<sub>2</sub> via plasmon energy transfer – can be played by the Au NPs upon target binding to modulate the photocurrent.<sup>619–621</sup> More specifically, biorecognition causes the Au NPs to either come into proximity<sup>622</sup> of (*signal-on*) or move away<sup>623</sup> from (*signal-off*) the TiO<sub>2</sub> electrodes. However, these bioassays only focus on harnessing the modulation of photocurrent influenced by Au NPs.

In this work, we sought to answer the question: Is it possible to effectively utilize and combine photocurrent modulation – both upon the capture of the unlabeled target and the binding of a plasmonic barcode (Au NP-modified DNA strand) – to achieve improved analytical sensitivity?

We aimed at developing a differential biosensor using the TiO<sub>2</sub>/Au system, using Au NPs as the sole PEC species. To achieve this, we investigated the use of two subsequent and correlated PEC measurements. First, we measured the change in PEC current induced by the binding of an unlabeled

target to a probe DNA. Second, we measured the additional PEC current change obtained when the unreacted probes were bound to a signal amplifying barcode (SAB) generated from AuNP-labeled DNA strands, for signal amplification. The signal changes measured during the two binding events were differentially combined to enhance the limit of detection (LOD) of the system. The use of SAB as an amplification sequence builds on the premise that plasmonic NPs in direct contact or close proximity to semiconducting materials possessing favorable energetics, modulate carrier lifetime,<sup>532,624</sup> thus, altering the PEC current. Using this differential strategy, the influence of background contributions is effectively suppressed, which in turn enhanced sensitivity by more than three times and LOD by 14 times compared to an analogous assay that measured a single binding event.

### 6.3 Methods and Materials

#### *Reagents*

Phosphate buffer solution (PBS, 0.1 M, pH 7.4), Potassium ferricyanide(III) ( $K_3Fe(CN)_6$ ), potassium hexacyanoferrate(II) trihydrate ( $K_4Fe(CN)_6 \cdot 3H_2O$ ), L-ascorbic acid (99%), sodium chloride (NaCl), Magnesium chloride ( $MgCl_2$ ), ethanolamine (MEA), chitosan (CHIT, from shrimp, degree of deacetylation of 85%,  $M_w=200,000$ ), glacial acetic acid, 3,4-dihydroxybenzaldehyde (DHB), Hexaammineruthenium (III) chloride ( $Ru(NH_3)_6Cl_3$ ), Tris buffer, 4-arm polyethylene glycol (PEG) with molecular weight 5000 (PEG-5K), and tris (2-carboxyethyl) phosphine hydrochloride (TCEP, 98%) were purchased from Sigma-Aldrich. P25-titanium dioxide ( $TiO_2$ ) was obtained from Nippon aerosol Co. Ltd. Acetone and Ethanol were purchased from commercial alcohols (Brampton, ON). Milli-Q grade (18.2  $M\Omega\text{-cm}$ ) de-ionized (DI) water was used for all solution preparation and washing steps. 100 nm indium tin oxide (ITO) glass slides were purchased from Sigma- Aldrich.

#### *Preparation of surface-modified $TiO_2$ Nanoparticles (NPs)*

$TiO_2$  NPs were prepared using the protocol reported by Victorious et al.<sup>[1]</sup> Briefly, 3gL<sup>-1</sup> CHIT solution was prepared in 1% acetic acid. A 16gL<sup>-1</sup> DHB solution was prepared in DI water. A DHB-modified CHIT solution was prepared by maintaining the mass ratio of 4:1 for DHB:CHIT. This solution was obtained by adding DHB solution to the CHIT solution. Finally, 60 mg of P25- $TiO_2$  was added to 15 ml of the DHB-modified CHIT solution.

#### *$TiO_2$ substrate preparation*

ITO glass substrates were treated with air plasma for 1 minute. Prior to the plasma treatment, substrates were masked using vinyl tape for separating contact area and electrode area. This was also used to ensure the uniformity of the geometric surface area of the electrode.  $TiO_2$  films were prepared by placing 10  $\mu\text{L}$  of the surface modified  $TiO_2$  solution onto the ITO substrate surface and subsequently baking at 95°C for 5 minutes. This last step was repeated 3 times. Finally, the electrodes were washed and then air dried before using.

#### *Gold (Au) NP synthesis*

Citrate capped Au NPs were synthesized according to the protocol reported by Grabar et al.<sup>[2]</sup> Briefly, aqueous gold chloride ( $HAuCl_4$ ) solution (1 mM) was mixed with 38.8 mM trisodium citrate solution with a volume ratio of 10:1. This solution was heated under vigorous stirring for 10 minutes, and then the stirring was continued for an additional 15 minutes without applying heat. The diameter of the prepared Au NPs was approximately 12 nm.

#### *AuNP-DNA conjugation*

DNA conjugation with Au NPs was accomplished by using the protocol provided by Zhang et al.<sup>[3]</sup> Briefly, 1 ml of 1.2 nM AuNPs was resuspended in 10 mM PBS (pH 7.0). A 100  $\mu\text{M}$  solution of thiolated DNA was reduced by mixing 1  $\mu\text{l}$  of 10 mM TCEP with 35  $\mu\text{l}$  of the DNA. DNA was incubated in this solution for 30 minutes. Reduced thiolated DNA was added to the AuNP solution and this was incubated for 16 hours at room temperature. After the incubation step, 10 mM PBS and 2 M NaCl solutions were added to the DNA mixture as slowly as possible to make the final salt concentration as 0.1 M NaCl. This solution was incubated for 40 hours at room temperature. This solution was

occasionally shaken in order to avoid aggregation. Finally, the solution was washed three times and resuspended in 10 mM PBS with 0.1 M NaCl (pH 7.0) and stored at 4°C.

#### *Photoelectrochemical (PEC) Characterization*

PEC measurements were conducted in a three-electrode electrochemical cell using a Zahner CIMPS system. Optical excitation was achieved using a 405 nm LED from the tunable optical light source (TLS03). A Pt wire was used as the counter electrode, Ag/AgCl as the reference electrode, and the deposited TiO<sub>2</sub> photoelectrode as the working electrode. All PEC measurements were performed at an applied potential of 0 V (vs. Ag/AgCl). The electrolyte used for all PEC measurements was 0.1 M PBS with 0.1 M ascorbic acid (AA), where AA served as hole scavenger. Period of light excitation was 40s with a 50% duty cycle (illumination time 20s). Baseline correction was performed on the measured photocurrents prior to plotting to the data for the manuscript figures.

#### *Electrochemical Characterization*

Electrochemical impedance spectroscopy (EIS) measurements were performed on the Zahner potentiostat under the open circuit potential. The measurements were performed within the frequency range of 100 kHz to 0.1 Hz in a solution containing 2 mM [Fe(CN)<sub>6</sub>]<sup>3-/4-</sup>, 0.1 M PBS, and 0.1 M KCl. Cyclic voltammetry was performed by using 10 mM PBS as electrolyte and 50 mV/s scan rate.

#### *Probe density measurement*

The Probe density of the DNA modified TiO<sub>2</sub> electrodes was measured by following the protocol described by *Steel et al.*<sup>625</sup> In short, chronocoulometry was performed sequentially in 10 mM Tris-buffer and in 100 μM Hexaammineruthenium (III) chloride in 10 mM Tris-buffer, on the DNA modified photoelectrodes. From the two graphs, the difference between y-axis intercepts were measured to determine the charge (Q) of the redox marker (Ruthenium ion in this case). From the charge, surface density of the redox marker is calculated using the following formula:

$$Q = nFA\Gamma_0$$

Where, n indicates the number of electrons per molecule for a redox reaction, F is the faraday constant, A is the area of the surface, and  $\Gamma_0$  is the density of adsorbed ruthenium ion. Redox marker density can be converted to DNA probe coverage using the following formula:

$$\Gamma_{DNA} = \Gamma_0 \left( \frac{z}{m} \right) N_A$$

Where,  $\Gamma_{DNA}$  is the density of probe, m is the number of bases in probe DNA, z is the charge of the redox molecule, and  $N_A$  is the Avogadro's number.

#### *DNA hybridization experiment*

Electrodes were modified with probe DNA by drop depositing 35 μl of 1 μM single stranded probe DNA and incubated for 3 hours at room temperature. Afterwards, a 1 mM MEA solution was deposited as a surface blocker with an incubation time of 50 minutes. A 20 μl solution of unlabeled target DNA with different concentrations was drop deposited on the electrode and incubated for one hour at room temperature. Finally, a 100 pM solution of the AuNP-conjugated DNA (signal amplification barcode (SAB)) was deposited on the electrode and incubated for another 40 minutes at room temperature. After each step, electrodes were rinsed in a wash solution (25 mM PBS, 25 mM NaCl). Percentage change of the photocurrent was calculated in two steps. After target deposition, the measured percentage decrease in signal is:

$$\Delta I_{target} = I_{target} - I_{block}$$

$$\% \Delta I_{target} = (\Delta I_{target} \times 100) / I_{block}$$

' $\% \Delta I_{target}$ ' indicates the percentage change in photocurrent following hybridization of the unlabeled target with immobilized probe, while ' $I_{block}$ ' and ' $I_{target}$ ' represent the signals obtained following MEA incubation and target hybridization, respectively. Similarly, percentage increase after SAB hybridization is calculated as follows:

$$\Delta I_{SAB} = I_{SAB} - I_{target}$$

$$\% \Delta I_{SAB} = (\Delta I_{SAB} \times 100) / I_{target}$$

Here, ' $\% \Delta I_{SAB}$ ' indicates the percentage change in photocurrent upon SAB binding by available probe sites following target hybridization. ' $I_{SAB}$ ' represents the signal obtained following the anchoring of SABs at the photoelectrode surface.

The signal for the developed bioassay ( $\% \Delta I_{diff}$ ) is the algebraic sum of both percentage changes calculated above and is computed according to the following equation:

$$\% \Delta I_{diff} = \% \Delta I_{target} + \% \Delta I_{SAB}$$

The DNA sequences used in this work are as follows:

Probe DNA: 5'-NH<sub>2</sub>-AGG GAG ATC GTA AGC-3'  
 Complementary target: 5'-TTT TTT TTT TGC TTA CGA TCT CCC T-3'  
 Non-complementary (NC) target: 5'-TTT TTT TTT TTT TTT TTT TTT TTT T-3'  
 DNA for Au NP conjugation: 5'-SH-TTT TTT TTT TGC TTA CGA TCT CCC T-3'  
 1-base mismatch: 5'-TTT TTT TTT TGC ATA CGA TCT CCC T-3'  
 2-base mismatch: 5'-TTT TTT TTT TGC ATA CGA TGT CCC T-3'

#### *Sensitivity and Limit-of-Detection Calculations*

In order to determine the limit-of-detection (LOD) of the assay, we plotted the photocurrent change ( $\% \Delta I_{diff}$ ) versus the log of target concentration in the linear range (1 fM – 100 pM) for both steps of hybridization. These changes are algebraically added to obtain the differential signal. The linear equation for the regression line is  $\% \Delta I_{diff} = -49 \log_{10}C + 173$  with a correlation coefficient of 97.97% when the target is in the buffer and  $\% \Delta I_{diff} = -25 \log_{10}C + 106$  with a correlation coefficient of 99.84% when the target is in diluted urine. The correlation coefficient for both cases is written in Figure 3(b). The limit-of-blank (LOB) was calculated as [4]:

$$LOB = \mu_B - 1.645 * \sigma_B$$

Here, ' $\mu_B$ ' is the mean and ' $\sigma_B$ ' is the standard deviation of the background signal, *i.e.* the signal obtained upon incubation of the photoelectrodes with non-complementary target DNA. The LOD was calculated by determining the concentration where the ' $\% \Delta I_{diff}$ ' value of the regression line becomes equal to the LOB. This was done using the following equation:

$$LOD = 10^{\frac{LOB-x}{m}}$$

Here, ' $x$ ' is the x-intercept of the regression line while ' $m$ ' denotes the sensitivity of detection and was obtained from the slope of the regression line of the LOD curve.

Similarly, for the signal-off assay, the photocurrent change ( $\% \Delta I_{target}$ ) versus the log of target concentration in the linear range (1 fM – 100 pM) was plotted following target hybridization alone. The linear equation for the regression line obtained for this data set is  $\% \Delta I_{target} = -14 \log_{10}C - 3$  with a correlation coefficient of 98.83% when the target is in the buffer and  $\% \Delta I_{target} = -8 \log_{10}C - 4$  with a correlation coefficient of 99.13% when the target is in diluted urine. The LOD was calculated by determining the concentration where the ' $\% \Delta I_{target}$ ' value of the regression line becomes equal to the LOB. The LOB and LOD of the signal-off assay were then calculated as per the aforementioned protocol.

#### *Urine Sample Analysis*

Urine samples were collected from a healthy patient cohort. The urine was diluted 10 times and the target DNA was spiked into the diluted urine. All experiments were performed using the methods in the previous section, except for the shortened, 40-minute, hybridization time.

#### *Plasma Sample Analysis*

Human plasma was donated by the Canadian Plasma Resources (Saskatoon, Canada). Target DNA (1 pM) was spiked into the 5 times diluted plasma samples. All experiments were performed similarly to the Urine sample analysis, except 1mM PEG-5K was used as the surface blocker instead of 1 mM MEA.

#### 6.4 Results and Discussion

We created the differential PEC biosensor by combining two sequential but correlated binding events on a single photoelectrode. A porous network of TiO<sub>2</sub> NPs was deposited on ITO substrates to create the photoelectrode, yielding the initial photocurrent profile (Figure 6.1a(i)). These photoelectrodes were then bio-functionalized with 15-nucleotide long single stranded DNA (ss-DNA) probes and subsequently blocked with monoethanolamine (MEA) to prevent nonspecific adsorption. The immobilization of probe DNA on the photoelectrode surface was verified using chronocoulometry and the probe coverage was measured as  $5 \times 10^{11}$  molecules/cm<sup>2</sup> (Supporting Figure S6.1).

A resulting decrease in photocurrent was anticipated following bio-functionalization due to the induction of steric hindrance between the photoelectrode and the species in the electrolyte (Figure 6.1a(ii)). Upon incubation with 25-mer complementary DNA targets (unlabeled), hybridization occurs between a fraction of the total probe population and the targets, leaving behind a population of available unhybridized probe strands. A further decrease in photocurrent is expected due to steric hindrance (Figure 6.1a(iii)). The SAB strand is then hybridized with the available probe strands. The length of the ssDNA probe (15-mer) is shorter than the length of the SAB strand (25-mer), with the resulting DNA complex containing both double and single stranded regions.<sup>571,576</sup> It has been previously demonstrated that the Au NPs on the SAB have a high probability of coming into direct contact with TiO<sub>2</sub> NPs owing to the dynamic motion of the DNA complex used in this work.<sup>502</sup> Direct contact between Au and TiO<sub>2</sub> NPs facilitates charge transfer between the two particles, thereby enhancing the anodic photocurrent (Figure 6.1a(iv)).<sup>492,514</sup> The presented DNA sensing approach, involving two hybridization steps, presents two benefits: 1) the target DNA strand does not need to be labeled prior to introduction on the chip, and 2) the combination of the signal changes induced from the two hybridization steps is expected to increase the assay sensitivity (Figure 6.1(b)). It should be noted that this two-hybridization approach makes it possible for the SAB binding to result in the displacement (completely or partially) of the target strands.<sup>626,627</sup> Partial hybridization of the SAB with the existing target-hybridized probes becomes more probable at longer nucleic acid strands.<sup>626,628</sup> Under the conditions used here, the use of a 15-mer DNA probe, a 25-mer DNA target, a 25-mer SAB strand with the same sequence as the target strand, and a room temperature hybridization step, we expect less than 10% of target strands to be removed by the SAB strand,<sup>626,627,626,627</sup> thus not making competitive strand replacement a significant contributor to the assay performance. As a result of the assay design, we expect it to be ideally-suited for detecting short nucleic acid targets such as microRNA (18-25 mer) or short DNA barcodes released from DNA machines.<sup>609</sup> MicroRNAs have been identified as clinically important diagnostic biomarkers for various diseases including cancer<sup>629,630</sup>, cardiovascular conditions,<sup>631</sup> and infectious diseases.<sup>632</sup>

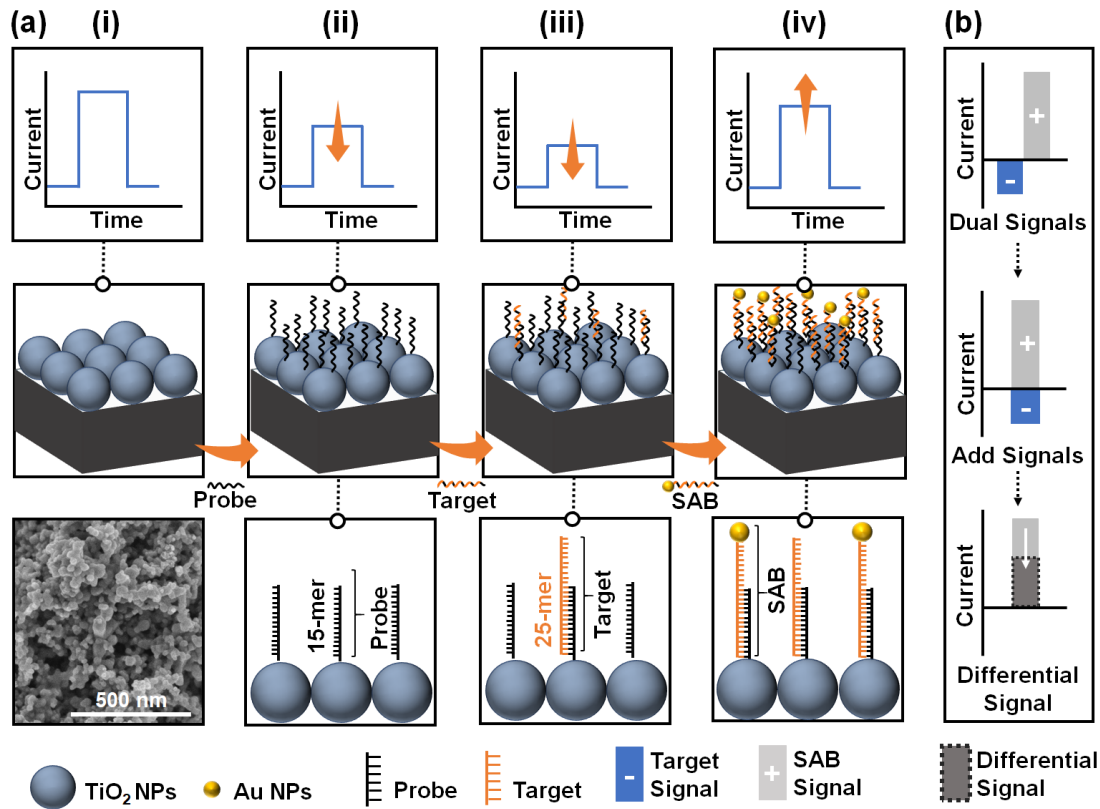
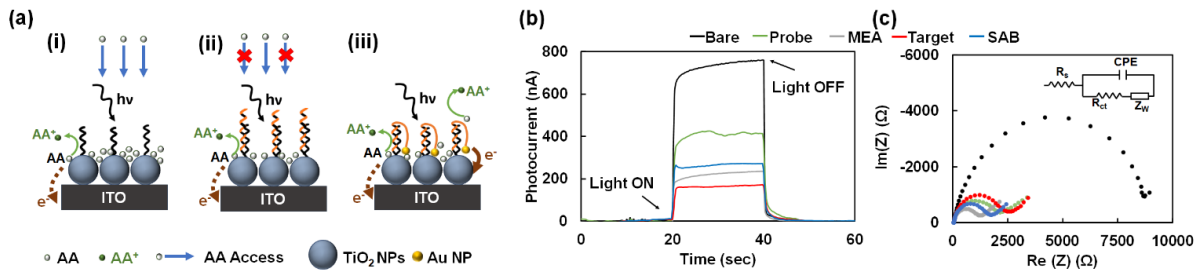


Figure 6.1 The operation of the differential PEC biosensor (a) Schematic illustration depicting the development of the PEC biosensor with the expected change in photocurrent profile depicted at each stage of sensing. A scanning electron micrograph (SEM) demonstrates the photoelectrode surface structure (bottom left). (i) Baseline photoelectrodes are created via solution deposition of  $\text{TiO}_2$  NPs onto ITO substrates, yielding an anodic photocurrent upon 405 nm illumination (ii) Bio-functionalized photoelectrodes are created by depositing 15-mer DNA probes on photoactive  $\text{TiO}_2$  substrates, yielding a decrease in photocurrent. (iii) 25-mer nucleotide targets are hybridized onto the transducer, resulting in a further decrease in photocurrent. (iv) Introducing SABs gives rise to an amplified photocurrent following hybridization. (b) A depiction of the combination of signals following target and SAB hybridization to yield the differential signal processing scheme used in this study.

The differential sensor design was verified by measuring the photocurrent and charge transfer resistance in each step of the sensor development process (Figure 6.2). For the photocurrent measurements, we used an LED light source with an excitation wavelength of 405 nm and an intensity of  $160 \text{ W/m}^2$ . Ascorbic acid (AA) was used as the hole scavenger to generate anodic current upon optically exciting the electrode (Figure 6.2a). A 45% photocurrent decrease was observed after probe deposition due to the steric hindrance of AA caused by the single stranded capture probe (Figure 6.2b).<sup>575</sup> Subsequently, MEA was used to block the unbound sites of the working electrode which further decreased the photocurrent by 35% as MEA impedes the access of AA to the surface of  $\text{TiO}_2$  nanoparticles. Following this, target DNA was introduced on the surface and a 45% photocurrent reduction was observed. As target DNA hybridizes with the capture probe on the photoelectrode, it further hinders the access of AA (Figure 6.2a). Finally, a 105% enhancement in photocurrent was observed upon the introduction of the SAB to the substrate (Figure 6.2b). Enhancement of photocurrent under UV excitation has been reported in similar systems due to Fermi level equilibration as optically-excited electrons from the conduction band of the semiconductor move to the Au NPs, thereby reducing the carrier recombination rate.<sup>515,591</sup> Optical excitation at 405 nm can also generate hot electron and hot holes via d-sp transition in Au NPs.<sup>510,633,634</sup> It is possible that these hot holes directly oxidize AA, while the hot electrons are transferred to  $\text{TiO}_2$  NPs, thereby increasing the photocurrent (Figure 6.2a).

Electrochemical impedance spectroscopy (EIS) at open circuit potential was also used to characterize the stepwise fabrication process of the proposed assay design (Figure 6.2c). The charge transfer resistance ( $R_{ct}$ ) of the photoelectrode decreased by 78% after DNA probe attachment (Supporting Table S1 and Supporting Figure 6.S2). This is contrary to the usual observation found in the literature where probe immobilization increases  $R_{ct}$ .<sup>343,635,636</sup> A study reported by Imani *et al.* showed that the addition of ssDNA on dopamine modified  $TiO_2$  NPs results in a higher electron transfer rate due to the quantum mechanical tunneling effect by bridging the molecular medium between the donor and the acceptor sites of ssDNA and  $TiO_2$  NPs, respectively.<sup>637</sup> Therefore, the observed reduction in  $R_{ct}$  in this work can also occur due to the amine-modified ssDNA covalently bonding with the aldehyde groups on the 3,4-dihydroxybenzaldehyde (DHBA) linker on the  $TiO_2$  NP surface having the same linker chemistry as dopamine, thereby enhancing the probability of quantum tunneling. It has also been hypothesized that DNA functionalization reduces carrier trapping sites by passivating the semiconductor ( $TiO_2$ ) surface, thereby reducing charge recombination.<sup>638</sup> In order to further validate this finding, we performed a study by performing cyclic voltammetry (CV) in 0.1 M phosphate buffer (PBS) to show changes in charge transfer kinetics (Supporting Figure S6.3). This study showed that the amount of stored charges in the photoelectrodes were increased from 0.59 mC to 0.72 mC after DNA functionalization, indicating longer lived excitons. Similarly, the addition of MEA as a surface blocker further decreased the charge transfer resistance by 43%. Upon the hybridization of target DNA, the  $R_{ct}$  increased by 110%, which is attributed to increased steric hindrance between the redox species in the solution and the surface of the photoelectrode.<sup>537</sup> Introduction of the SAB resulted in a 33% decrease in  $R_{ct}$ , which is attributed to improved charge transfer kinetics due to the addition of Au NPs into the electrode film.<sup>562,639</sup>



**Figure 6.2** Photoelectrochemical signal generation on the differential DNA biosensor. (a) Schematics showing the mechanism for photocurrent generation (i) bare TiO<sub>2</sub> electrode (ii) after hybridization with complementary target (iii) after hybridization with SAB (b) Photocurrent measurement after each step of the biosensor operation with 1 pM target in buffer using a 405 nm LED as excitation source at 160 W/m<sup>2</sup>. All photocurrent measurements were performed at 0 V bias vs. Ag/AgCl. using 0.1 M ascorbic acid (AA) in 0.1 M PBS as electrolyte at each step of the biosensor construction. (c) Electrochemical impedance spectroscopy measurements were performed in dark at open circuit potential vs. Ag/AgCl reference electrode using 2 mM [Fe(CN)<sub>6</sub>]<sup>3-/4-</sup> in 0.1 M PBS and 0.1 M KCl as electrolyte. The equivalent circuit based on the shape of the Nyquist diagram is shown in the inset. Charge transfer resistance between the redox couple and the electrode is denoted by R<sub>ct</sub>, which can be determined from the diameter of the semicircle. R<sub>s</sub>, Z<sub>w</sub> and CPE denote the solution resistance, Warburg impedance and constant phase element, respectively.

To assess the ability of the differential PEC biosensor in analyzing DNA targets, we analyzed unlabeled DNA targets within a concentration range of 1 fM to 100 pM. As expected, when a solution containing target DNA was introduced to the device, the electrodes showed a PEC current that monotonically decreased with increasing target concentration (Figure 6.3a). As the concentration of target DNA in the first hybridization step decreases, there is a larger population of residual unhybridized probes, allowing more SAB strands to bind to the photoelectrode yielding a signal increase. As expected, this signal increase is larger at lower target DNA concentrations (Figure 6.3a, b(i)).

The differential PEC sensing strategy is then developed by combining the photocurrent change after target and SAB binding steps. More specifically, the absolute value of photocurrent decrease after target hybridization was subtracted from the absolute value of photocurrent enhancement after SAB binding. The differential signal for each concentration was plotted to generate a calibration curve (Figure 6.3b). A linear fit to the calibration curve yields a sensitivity of 49 % / log<sub>10</sub> M and LOD of 3 fM in buffer. The reverse signal-to-concentration effect observed here, where the largest signals are obtained at the lowest concentrations, allows high signal-to-noise ratios to be obtained at low concentrations that are often needed for clinical analysis, a feature that is not possible with traditional sandwich assays. This increase in signal at lower concentrations comes with the inherent drawback of differential signal processing: the experimental errors obtained from each measurement accumulate in the differential signal, leading to a loss of precision at all concentrations. Additionally, the use of two hybridization steps increases the overall assay time; however, preliminary experiments demonstrate that it may be possible to reduce the duration of each hybridization step (Supporting Figure S6.4).

In order to assess the applicability of the differential biosensor in analyzing DNA targets in complex biological matrices, we spiked target DNA at various concentrations into healthy patient urine (Figures 6.3c-d). The differential assay yielded a sensitivity of 25 % / log<sub>10</sub> M and LOD of 5 fM in urine. Both LOD and sensitivity deteriorate moderately in urine compared to buffer (less than a factor of two). This can be attributed to the biofouling of the photo electrode caused by the biological components present in urine.<sup>640</sup>

Adding the signal amplification step using the SAB significantly enhances the LOD of the system in both buffer (from 11 fM to 3 fM) and urine (from 73 fM to 5 fM) compared to using a single target binding step (Supporting Figure S6.5). The large enhancement in LOD (~15 times) observed in urine

indicates that the differential signaling strategy is particularly important for compensating for the performance loss that is observed in complex biological samples. In addition to LOD, the differential strategy enhanced the assay sensitivity by about three times compared to the single binding assay for both buffer and urine samples. We further challenged the bioassay by spiking 1 pM target DNA into human blood plasma (Supporting Figure S6.6). It should be noted that the bioassay utilized polyethylene glycol (PEG), in place of MEA, to reduce non-specific adsorption at the biosensor surface. The photocurrent changes observed after incubating the sensor with the target and SAB strands were similar to when human urine was used, indicating the potential use of this assay for biomarker detection in blood plasma.

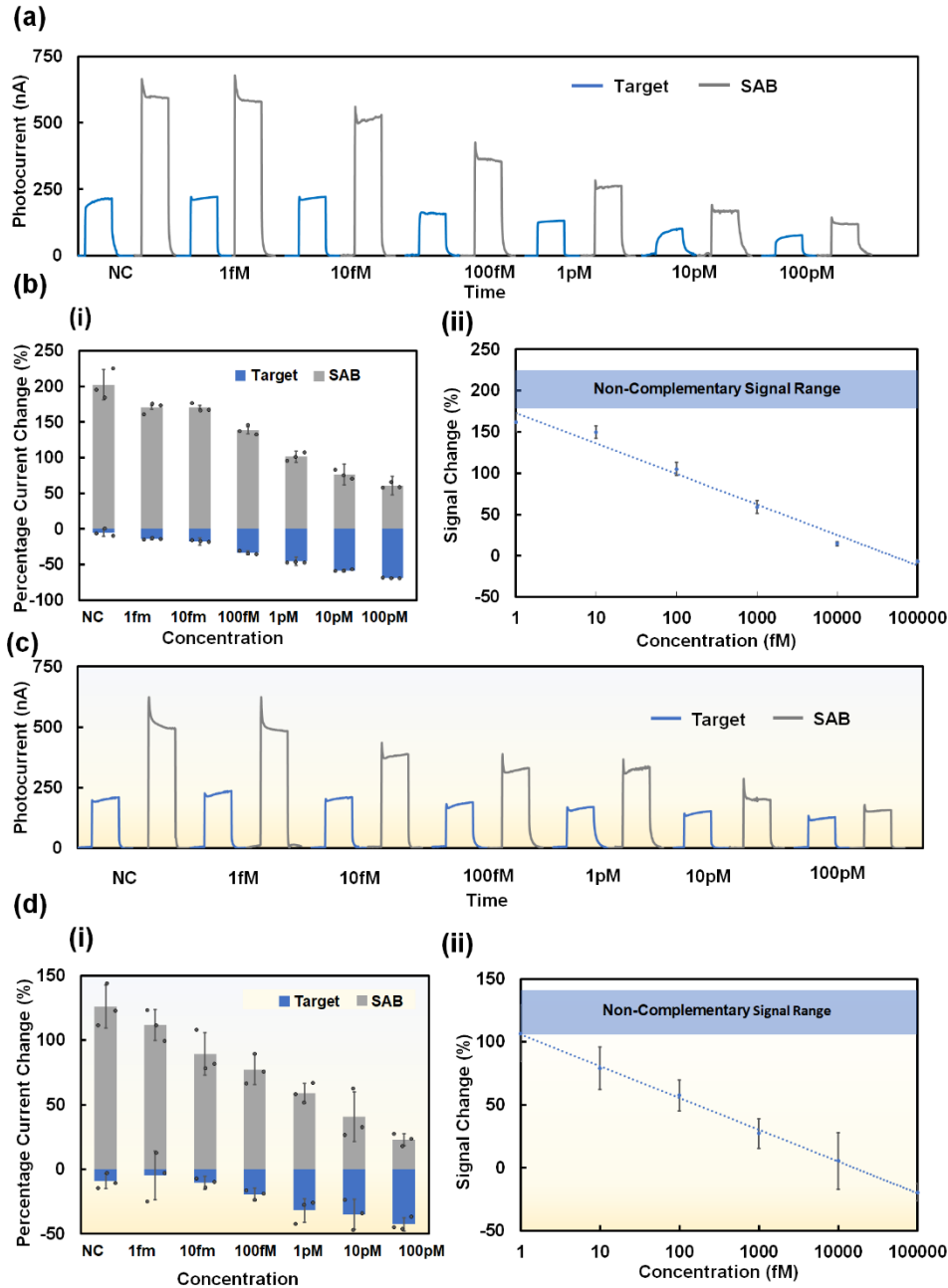


*Figure 6.3 Limit-of-detection and sensitivity of the differential assay. All photocurrent measurements were performed at 0 V versus Ag/AgCl in 0.1 M ascorbic acid in 0.1 M PBS as electrolyte, illuminated using a 405 nm LED excitation source at 160 W/m<sup>2</sup> (a, c) PEC graphs demonstrate signal responses following target and SAB binding in PBS and urine respectively. (b, d) Jitter plots (i) demonstrating the signal changes obtained from target and SAB binding in buffer and urine respectively, obtained from (a) and (c). Representation of the differential signal (ii) obtained from the data presented in (i). The linear region of the calibration curve of the PBS graph was fitted using the equation  $\Delta I \% = -49 \log_{10}C + 173$  (correlation coefficient of 97.97%) while the equation  $\Delta I \% = -25 \log_{10}C + 106$  (correlation coefficient of 99.84%) was used to fit the urine data. This graph is depicted using a semi-log format, with the x-axis representing the logarithmic concentration ( $\log_{10} M$ ) of the target analyte.*

To assess the specificity of the nucleic acid biosensor and its ability in distinguishing between fully-matched and mismatched targets presenting point mutations, detection was carried out for targets with sequences having 1-base, 2-base and 3-base mismatches with the original sequences. The photocurrent changes obtained following each hybridization stage (after target and SAB binding) were then evaluated against those obtained for a perfectly complementary and a fully mismatched sequence tested in the same manner (Figure 6.4).

Following target binding, the current decreased by  $48\% \pm 6\%$ ,  $16\% \pm 4\%$ ,  $14\% \pm 9\%$ , and  $6\% \pm 3\%$  for matched, 1-base mismatched, 2-base mismatched, and non-complementary (NC) sequences, respectively (Figure 6.4a). This trend is largely attributed to the varying hybridization efficiency in each scenario, with fewer base mismatches resulting in more efficient target binding.<sup>641,642</sup> The matched, 1-base mismatched, 2-base mismatched, and NC sequences exhibited a  $109\% \pm 6\%$ ,  $160\% \pm 9\%$ ,  $179\% \pm 8\%$ , and  $202\% \pm 4\%$  increase in signal magnitude respectively, following SAB binding (Figure 6.4a). In the case of the mismatched sequences, albeit inefficient, a fraction of the target sequences binds to available probe sites, still decreasing the available binding sites for SAB binding, which in turn reduces the SAB-induced signal enhancement. The differential signal enables highly distinguishable signal footprints to be realized for the different sequences with 60%, 123%, 163%, and 201% signal changes measured for matched, 1-base mismatched, 2-base mismatched, and NC sequences (Figure 6.4b). A statistical t-test was performed to assess the ability of the assays using one or two binding steps in distinguishing between different degrees of probe/target complementarity. Using differential signaling, we were able to distinguish between matched, 1-base mismatched, 2-base mismatched, and NC sequences (Figure 6.4b). On the contrary, the single target binding event can only distinguish matched from the 1-base mismatched sequence. The differential approach achieves a superior mismatch specificity with a high confidence level ( $p < 0.05$  for all scenarios) as compared to its *signal-off* analogue.

We further assessed the static and dynamic stability of the differential PEC biosensor. PEC measurements of the electrodes stored under static conditions over a 7-day period following probe deposition (Supporting Figure S6.7 a) revealed a small decrease in biosensor photocurrent (8% decrease from day 1 to day 7). Furthermore, the stability of the photoelectrodes under dynamic conditions, multiple light excitation, and potential application, was assessed for 15 measurement cycles within a period of 800 s (Supporting Figure S6.7 b), indicating stable photocurrents with a relative standard deviation of 6 %

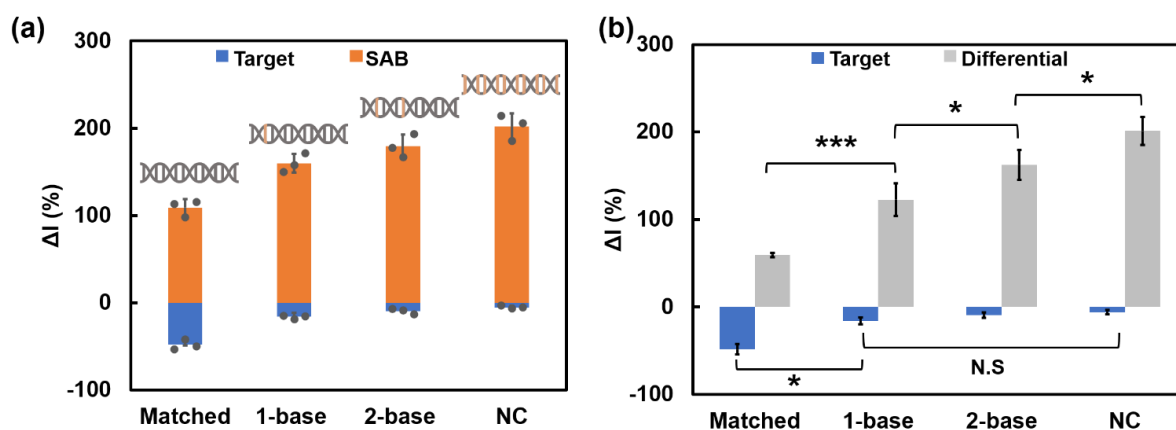


Figure 6.4 Specificity of the differential assay. (a) Change in PEC current following hybridization with 1 pM of matched, 1-base mismatched, 2-base mismatched, and NC targets and SAB binding measured in 0.1 M PBS with 0.1 M AA. (b) Differential and signal-off responses for the target sequences in (a) with \* and \*\*\* representing  $p < 0.05$  and  $p < 0.001$ , respectively.

## 6.5 Conclusion

In this work, we demonstrate a differential PEC assay using two subsequent and correlated hybridization events, first with an unlabeled target and then with a single amplification barcode tapping into the interaction of plasmatic and semiconductive nanoparticles, to detect unlabeled target DNA in both buffer and urine. The differential strategy exhibited a LOD of 3 fM in buffer and 5 fM in diluted urine, demonstrating significant improvement over a conventional signal-off strategy that used a single binding event (11 fM in buffer and 72 fM in urine) respectively. In addition to LOD, this assay enhanced the analytical sensitivity by a factor of three compared to an analogous assay that did not use differential signaling. The differential assay also demonstrated the ability to distinguish between sequences that were matched or contained 1- or 2-base mismatches with the detection probe, which was not possible using the non-differential approach. This work offers a new strategy for enhancing the limit-of-detection, sensitivity, and specificity of PEC biosensors, performance metrics that are key to the use of PEC biosensors in clinical decision making. The assay presented here, in terms of target length (25-mer) and concentration range (1 fM – 100 pM), is ideally-suited for the analysis of short nucleic acid strands such as microRNA or DNA barcodes released from DNA machines such as DNAzymes,<sup>643</sup> CRISPR-Cas systems,<sup>644</sup> and strand displacement-based systems.<sup>645</sup>

## 6.6 Acknowledgements

This work was supported by NSERC, the Ontario Early Researcher Award granted to L.S., and a salary awarded to L.S. from the Canada Research Chairs Program. The electron microscopy was carried out at the Canadian Centre for Electron Microscopy (CCEM), a national facility supported by the NSERC and McMaster University. A.V and S.S. are recipients of the NSERC doctoral scholarships.

## 6.7 Supplementary Information

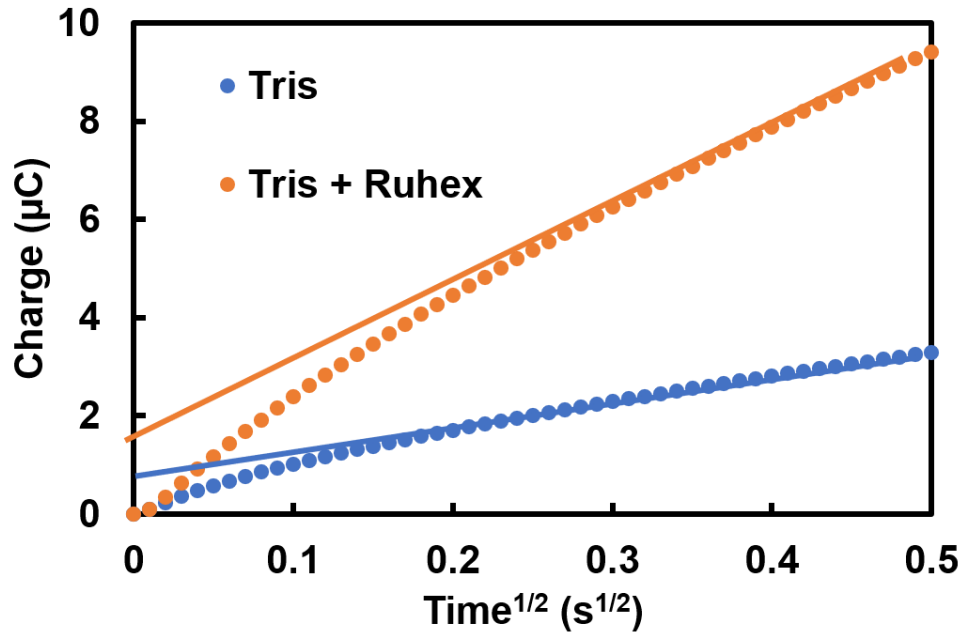


Figure S6.1 Chronocoulometric measurement of probe density. Blue dots represent the data obtained by running the scan with 10 mM Tris-buffer and orange dots represent the data obtained by running the scan with 100  $\mu$ M Hexaamineruthenium (III) chloride in 10 mM Tris-buffer. Corresponding solid lines indicate the linear fit that was used to obtain the y-axis intercept.

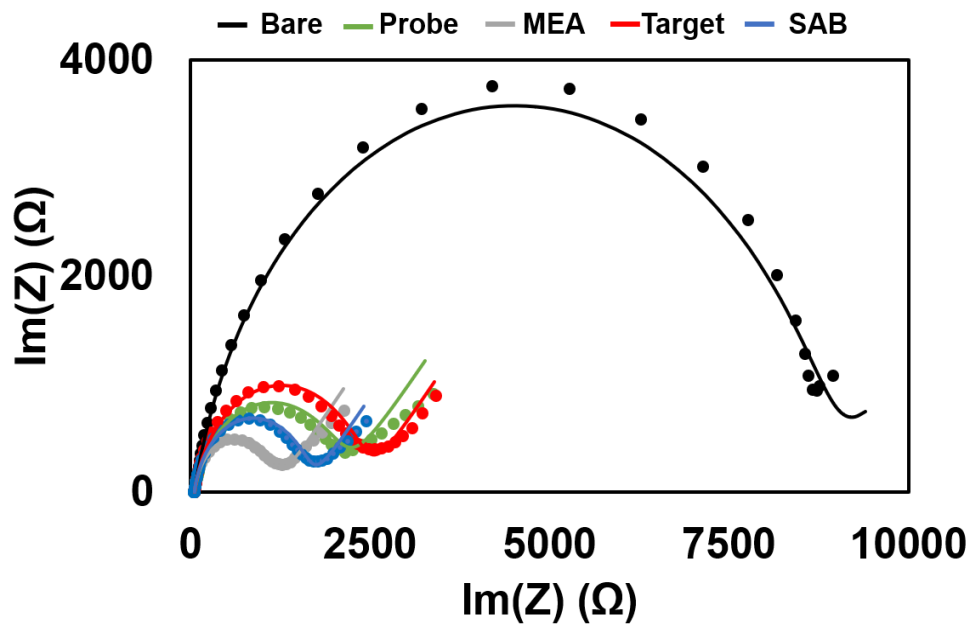


Figure S6.2 EIS measured at different fabrication steps of the differential PEC biosensor. The dots indicate the raw data points, whereas the solid line indicates the fit with the circuit model

Table S6.1 Values of the charge transfer resistance ( $R_{ct}$ ), constant phase element (CPE) and  $n$ , indicating the constant phase ( $-90*n$ ) of the CPE for each step of the construction of the differential biosensor extracted from Figure S6.1.

	$R_{ct}$ (k $\Omega$ )	CPE ( $\mu$ F)	$n$
Bare	8.8	8	0.9
Probe	1.96	4.6	0.85
MEA	1.12	5.43	0.91
Target	2.36	4.07	0.87
SAB	1.58	5.54	0.9

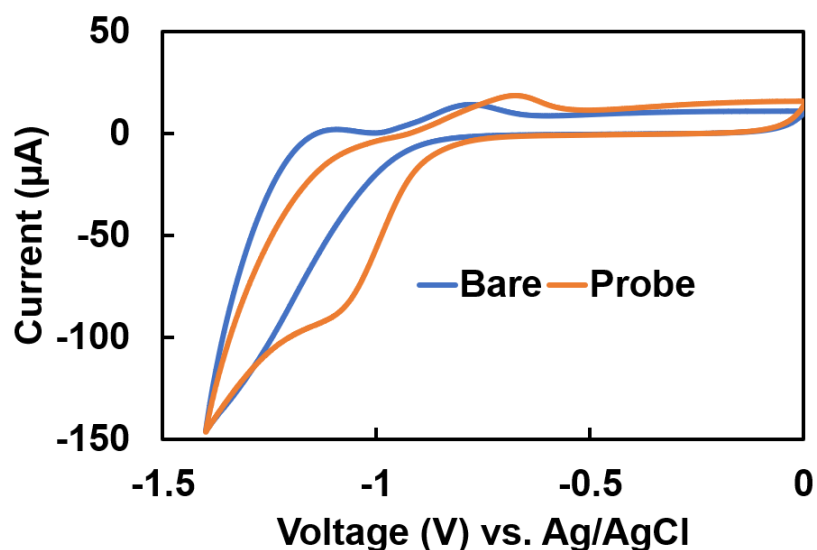


Figure S6.3 Cyclic voltammety scan for TiO<sub>2</sub> electrodes before and after modification with ssDNA using 10 mM PBS as electrolyte and 50 mV/s scan rate

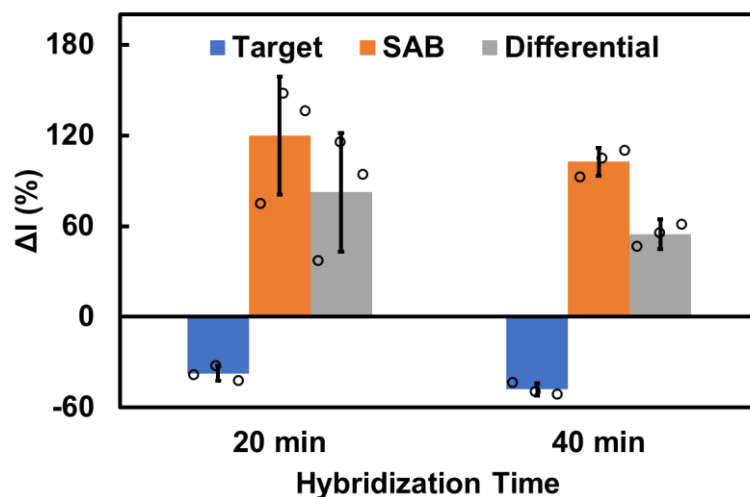


Figure S6.4 Comparison of photocurrent change in detecting 1 pM DNA targets spiked in buffer (PBS) at 20-minute and 40-minute hybridization times. The error bars indicate one standard deviation from the mean and calculated from at least three measurements performed at 0 V versus Ag/AgCl in 0.1 M ascorbic acid in 0.1 M PBS as electrolyte, illuminated using a 405 nm LED excitation source at 160 W/m<sup>2</sup>.

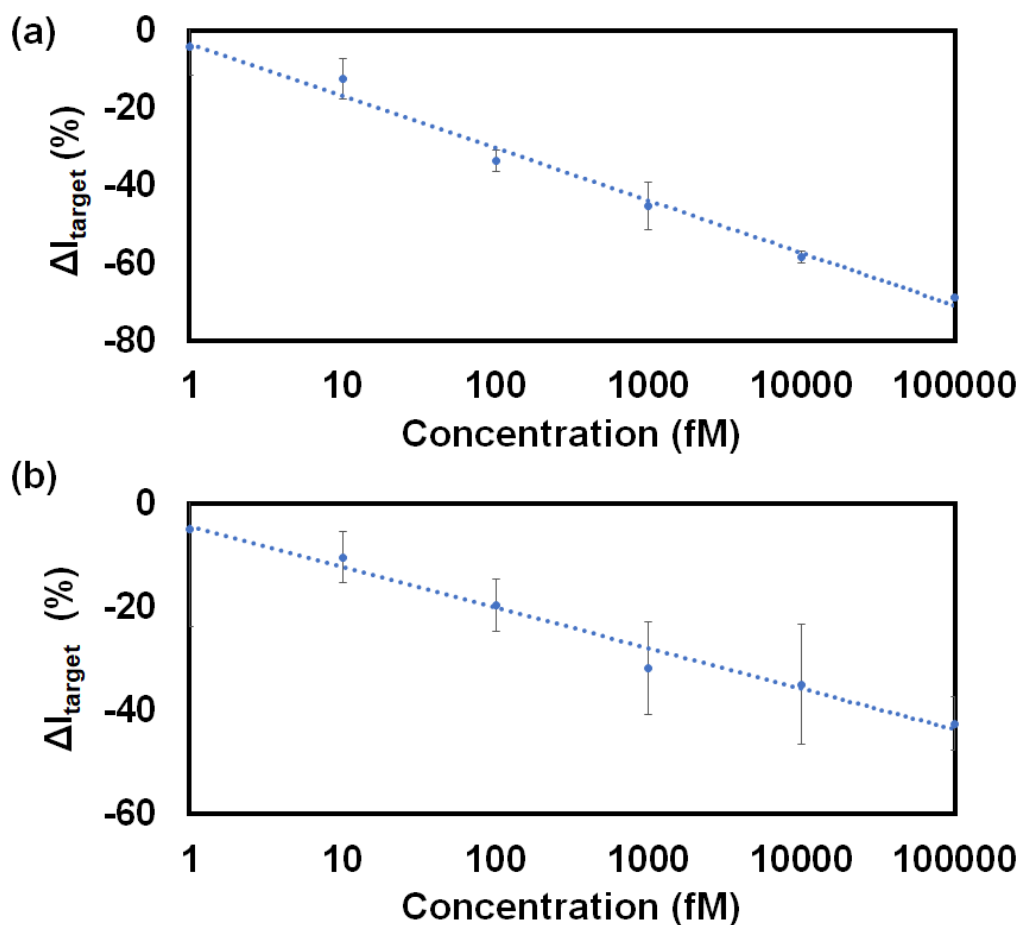


Figure S6.5 The limit-of-detection of the signal-off-detection mode in (a) PBS and (b) urine.

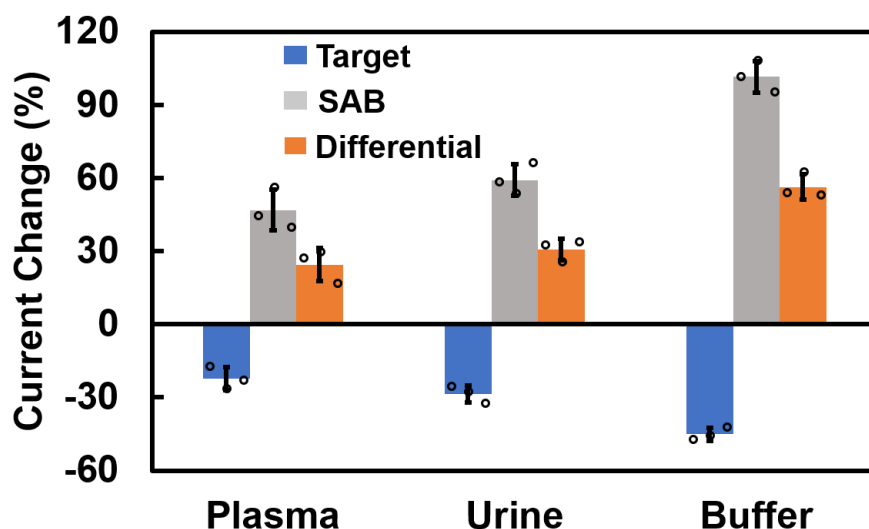


Figure S6.6 Signal changes measured with 1 pM DNA target spiked into human plasma, urine, and buffer. The error bars indicate one standard deviation from the mean, calculated from at least three measurements

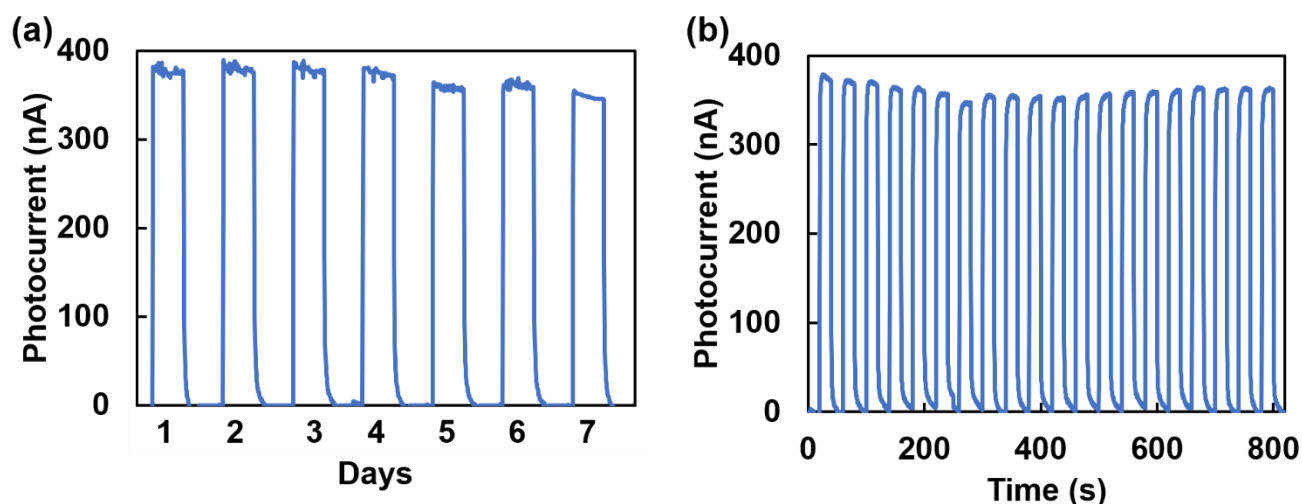


Figure S6.7 Evaluation of the stability of the PEC biosensor. (a) Photocurrent measurement following the storage of probe modified electrodes for a period spanning 1-7 days. (b) Photocurrent measurement for 15 repeated cycles after probe modification. All photocurrent measurements were performed by applying 0 V vs. Ag/AgCl using 0.1 M ascorbic acid in 0.1 M PBS as electrolyte.

## **Chapter 7: Dynamic DNA barcodes - A reagentless strategy for dual-electrode EC protein detection in saliva (Objective 6)**

### ***Preface***

While the previous chapter delineated a method of target amplification-free, sensitive PEC detection of short DNA targets with potential applications in miRNA detection, this chapter details the development of a biobarcode EC assay capable of reagentless, sensitive and specific detection of N-PEDv—a protein target with emerging global significance—in swine saliva. Here, barcoded dynamic DNA motifs—electrochemical biobarcodes hybridized with surface anchored aptamers—integrate biorecognition with dual-signal generation on Au patterned dual-electrode electrochemical (DEE) chips. To make the assay amenable to the constraints of POC detection, mass transport control strategies (i.e., reduced inter-electrode spacing and electrical field mediated transport) were employed to enable faster kinetics and expedite assay operation (60 min). This DEE-Chip successfully analyzed 91.6% (and 100% of all samples for  $C_t \leq 33.17$ ) of the clinically sourced swine saliva with a clinical sensitivity of 83%, specificity of 100%, and an AUC > 0.83 (extracted from an ROC plot) in 60 minutes without target amplification and target enrichment; thus, fulfilling the need for a non-invasive PEDv sensor capable of potential on-farm operation. As a result, the scientific study presented in this chapter satisfies objective 6 as stated in Chapter 1 of this thesis. Furthermore, while these structure-switching functional DNA motifs have been demonstrated in EC detection, the technique described in this chapter may also be extended to PEC systems in the future. PEC systems based on the same principle may be constructed by (1) swapping the nanotextured Au electrodes with 3D TiO<sub>2</sub> photoelectrodes such as the ones developed in Chapter 3 and (2) replacing methylene blue tagged biobarcodes with Au terminated biobarcodes, such as the ones used in chapters 4-6.

### ***Authors***

Amanda Victorious\*, Zijie Zhang\*, Richa Pandey, Dingran Chang, Jianrun Xia, Jimmy Gu, Roderick Malachlan, Todd Hoare, Leyla Soleymani, and Yingfu Li.

(\*indicates that Amanda Victorious and Zijie Zhang\* contributed equally to this authorship and are co-first authors).

Here, I fabricated all the DEE-chips used in this work and carried out experimental design and validation of the design in buffer and saliva (Figure 7.2, 7.3, S7.5). I then examined the cross reactivity of this system to ensure specificity (Figure 7.4). Subsequently, I devised an experiment to probe the kinetic limitations of the system and devised avenues to overcome these limitations (Figure 7.5). Once a suitable detection time was devised, I designed and carried out the device validation using clinically sourced samples, formulated a hypothesis for anomalous responses and further probed anomalous responses (Figures 7.6, S7.7, S7.8). The experimental design, validation and analysis that was solely carried out by me pertain to figures: 7.2, 7.3, 7.4, 7.5, 7.6, S.7.5, S.7.7 and S7.8). In addition, I also co-lead the authorship of the manuscript, created figures (7.2, 7.3, 7.4, 7.5, 7.6, S.7.5, S.7.7 and S7.8) and carried out the writing pertaining to the introduction, figures 7.2, 7.3, 7.4, 7.5, 7.6, S.7.5, S.7.7 and S7.8 and the conclusion. I thank Dr. Zhang for this responsiveness, collaboration, expertise, and support exhibited during this project.

### ***Publication***

Under review at Angewandte Chemie International

### 7.1 Abstract

Rapid testing of farm animals for infectious diseases is critically needed to reduce transmission in herds and enable timely intervention strategies for reducing economic loss, food security disruptions, environmental impacts of farming, and animal-to-human transmission. Despite this need, especially with the recent occurrence of emerging viral diseases in animals, pen-side and rapid infectious disease testing in animal farms remain elusive. Most existing testing strategies rely on sample collection and transport to centralized labs resulting in sample-to-result times of 2-4 days. In response, we introduce a rapid, simple, and reagent-less dual-electrode electrochemical (DEE) chip featuring a barcode-releasing electroactive aptamer for on-farm detection of porcine epidemic diarrhea viruses (PEDv). The inclusion of mass transport enhancement strategies for expediting the movement of DNA barcodes from the electroactive aptamers to the detection electrode – via reduction of the inter-electrode spacing and active field mediated transport – enables faster kinetics and expedites assay operation. The DEE-Chip yielded a clinically relevant limit-of-detection of  $1.1 \mu\text{g mL}^{-1}$  in buffer and saliva-spiked PEDv samples. The clinical evaluation of this biosensor using 12 porcine saliva samples demonstrated a diagnostic sensitivity of 83% and specificity of 100% with a concordance value of 92% at an analysis time of one hour.

### 7.2 Introduction

It is widely disseminated that human, animal, and environmental health are tightly interconnected. Pathogens such as coronaviruses (CoVs) cause severe respiratory, enteric, and systemic infections in human and animal hosts,<sup>646,647</sup> jeopardize animal husbandry and food supply,<sup>648</sup> and have potentially devastating environmental and global biodiversity consequences.<sup>649</sup> Furthermore, viral outbreaks in poultry and livestock pose continuous threats to human health, carrying risks of sporadic human zoonotic infections or the emergence of transboundary viral strains with pandemic potential, as evidenced by the recent COVID-19 pandemic.<sup>650</sup> In fact, more than 70% of all emerging infections are believed to have animal origins.<sup>651</sup> Additionally, infectious animal diseases pose a clear economic threat, affecting local production, national economies and global trade. In 2013, the introduction of porcine epidemic diarrhea virus (PEDv) – an emerging and highly transmittable CoV – devastated 10% of the US commercial swine population in 31 states within a span of 18 months, leading to economic losses of > US \$400 million.<sup>647</sup>

Although biosecurity in the commercial swine industry is comprehensive in many countries including Canada and United States, the rapid and recurrent spread of PEDv demonstrates the vulnerability of the farming industry to emerging pathogens. The current biosecurity surveillance measures for animal diseases such as PEDv rely on polymerase chain reaction (PCR) testing, which requires analysis at centralized laboratory, specialized equipment and technical expertise, and transport and turnaround times between sample submission and diagnosis spanning 2-4 days.<sup>652</sup> The lack of rapid and on-farm testing allows emerging animal pathogens to spread, increasing morbidity and mortality rates in animals.<sup>653</sup> Immunoassays are popular alternatives to PCR for PEDv detection, which reduce sample-to-result time and assay complexity by eliminating the need for target amplification. These assays rely on the use of antibodies as bio-recognition elements and are often integrated into engineered detection platforms or devices for rapid testing such as lateral flow assays (LFAs),<sup>654-656</sup> enzyme-linked immunosorbent assays (ELISA),<sup>657-667</sup> and electrochemical assays.<sup>668-670</sup> Although rapid, these methods, all based on antibody-based sandwich assays, either require multi-step processing such as washing, labeling, or addition of reagents (ELISA and electrochemical assays) or suffer from low clinical sensitivity and specificity partly stemming from the poor stability and cross-reactivity of the antibodies (LFAs).<sup>652</sup> It is thus of utmost importance to develop rapid, simple and reagent-less on-farm tests capable of precise and reliable detection of PEDv.

DNA aptamers, a class of functional nucleic acids selected *in vitro* for specific target binding, offer several key advantages over antibodies for the development of rapid tests such as their small size, high chemical and thermal stability, easy and precise modification, compatibility with DNA machines and consequently reagent-less sensing, scalable production and minimal batch-to-batch variation.<sup>79</sup> In addition, it has been shown that aptamers can be used to directly detect targets present in clinical

samples,<sup>81,82</sup> making these molecular recognition elements increasingly important for developing rapid diagnostic devices. In the past few decades, many important DNA aptamers have been selected for rapid diagnosis of viral diseases including human immunodeficiency virus (HIV), influenza, porcine reproductive and respiratory and coronaviruses (PRRSv), African swine fever virus (ASFv) and coronaviruses like SARS-CoV and MERS.<sup>671</sup> However, there are no aptamers currently available for detecting PEDv.

We sought to develop a reagent-less electrochemical aptamer-based sensor for rapid PEDv sensing to combine the advantages of aptamers with the ultra-sensitivity of electrochemical readout. The existing aptamer-based electrochemical sensors typically employ target-induced structure switching.<sup>166,175,672</sup> These assays offer a breakthrough because they enable reagent-less sensing; however, the integration of the redox label directly on the structure-switching aptamer that is immobilized on the sensing electrode often results in large background signals even before target capture due to thermodynamic imbalance in complex media<sup>175</sup> and/or the flexibility of the labelled single-stranded DNA aptamer.<sup>176-178</sup> Alternatively, while aptamers relying on the displacement of a labelled single-stranded DNA strand for signal transduction offer more precise thermodynamic control by tuning the length and complementarity of the displacement strand,<sup>175,181,183-185</sup> such assays typically operate in a signal-off configuration<sup>184,185</sup> or carry a large background current in the few reported signal-on designs,<sup>183,186</sup> both prone to introducing errors in heterogeneous clinical samples that generate varying backgrounds.

In order to develop a reagent-free, signal-on, and low background sensor for detecting PEDv, we first discovered a PEDv-specific aptamer that we later integrated into a dual-electrode electrochemical (DEE) aptasensor. The DEE aptasensor is designed to house the aptamer bound to a DNA barcode onto one electrode and detect the released barcode on another electrode. The separation of the analyte capture and signal reporting on two different electrodes enables signal-on sensing with almost no redox background. Mass transport enhancement strategies, such as reduction of inter-electrode spacing and active field mediated transport, were also effectively harnessed to overcome slow kinetics, enabling the dual-electrode sensor to discriminate between healthy and diseased samples from 12 clinically derived porcine oral fluids in 60 minutes without necessitating target labelling, amplification, or enrichment techniques.

### 7.3 Methods and Materials

#### *Reagents*

All oligonucleotides were purchased from Biosearch and Integrated DNA Technologies (IDT), and purified by standard 10% denaturing (8 M urea) polyacrylamide gel electrophoresis (dPAGE) before use. The sequences are listed in Table S1 and S2. The nucleocapsid protein of PEDv (N-PEDv, molecular weight: 60 kDa) was expressed from *E. coli* cells and purified using standard methods (see details below). Bovine serum albumin (BSA) and human- $\alpha$ -thrombin were purchased from Sigma-Aldrich (Oakville, Canada). SARS-CoV-2 nucleocapsid protein (catalog number: 40588-V08B) and spike protein (catalog number: 40591-V08B1) were purchased from Sino Biological Inc. RNase H2 was expressed from *E. coli* and purified in the Li's lab at McMaster University.<sup>673</sup> Taq DNA polymerase was purchased from GenScript.  $\gamma$ -[<sup>32</sup>P]-ATP was acquired from PerkinElmer. Phosphate buffer solution (1.0 M, pH 7.4), sodium chloride (NaCl,  $\geq 99.0\%$ ), magnesium chloride (MgCl<sub>2</sub>,  $\geq 99.0\%$ ), 4-(2-hydroxyethyl)-1-piperazineethanesulfonic acid (HEPES), sodium phosphate dibasic (Na<sub>2</sub>HPO<sub>4</sub>), potassium phosphate monobasic (KH<sub>2</sub>PO<sub>4</sub>), potassium chloride (KCl), Tween-20, polyethylene glycol 6000 (PEG 6000), 6-mercapto-1-hexanol (MCH, 99%), tris(2-carboxyethyl)phosphine hydrochloride (TCEP), potassium hexacyanoferrate(II) trihydrate ([Fe(CN)<sub>6</sub>]<sup>4-</sup>,  $\geq 99.95\%$ ), gold(III) chloride solution (HAuCl<sub>4</sub>, 99.99%) were purchased from Sigma-Aldrich. HisPur Ni-NTA magnetic beads (catalog number: 88831), T4 DNA ligase, T4 polynucleotide kinase (PNK), adenosine triphosphate (ATP) and deoxyribonucleoside 5'-triphosphates (dNTPs) was from Thermo Scientific. Sulfuric acid (H<sub>2</sub>SO<sub>4</sub>, 98%) and 2-propanol (99.5%) were purchased from Caledon Laboratories. Hydrochloric acid (HCl; 37% w/w) was purchased from LabChem. Swine saliva samples were obtained from South West Vets, Ontario. Milli-Q water was used for all experiments.

#### *Expression and Purification of N-PEDv*

The nucleocapsid protein of PEDv (N-PEDv) was produced as described by Deejai et al. 2017.<sup>673</sup> The optimized sequence coding N-PEDv was purchased from GENEWIZ (Suzhou, China) based on the genome of strain CH/HNQX-3/14 and cloned in pET28-a (+) vector for expression in E. coli. The E. coli BL21-DE3 clones harboring the pET28-a (+) vector was cultured in Luria-Bertani (LB) broth medium containing 50 µg/mL kanamycin with shaking at 210 rpm at 37 °C for 16 h. Isopropyl-β-d-thiogalactoside (IPTG, 1 mL, 5 M) was added to the culture when the optical density of cells at 600 nm (OD<sub>600</sub>) reached 0.5 to induce expression of N-PEDv for 24 hours. The harvest cells from 1 L of culture were suspended in 20 mL of PBS and lysed by sonication. After centrifugation at 40000 g for 40 mins, the supernatant fraction of recombinant N-PEDv was purified using His-trap-affinity column (catalog number: 45-000-323, Fisher Scientific) run on Cytiva AKTA Start chromatography system (36-104-1137, Fisher Scientific). Purity of >90% N-PEDV was eluted in PBS with 400 mM imidazole. The imidazole was removed by dialysis in PBS with 50 mM Arginine. Purified N-PEDv protein aliquots were stored at -80 °C for aptamer selection and tests.

#### *Conjugation of N-PEDv protein on magnetic beads*

HisPur Ni-NTA magnetic beads (16 µL, 5% w/v, 12.5 mg/mL) were first washed with PBST buffer (0.5 mL, 1.8 mM KH<sub>2</sub>PO<sub>4</sub>, 10 mM Na<sub>2</sub>HPO<sub>4</sub>, 2.7 mM KCl, 137 mM NaCl, 0.01% v/v Tween-20). Magnetic bead pellets were then resuspended in 5× PBST buffer (40 µL). Imidazole (4 µL, 1 M), N-PEDv protein with His-tag (100 µL, 0.5 mg/mL) and water (60 µL) were mixed with the magnetic beads and incubated at 4 °C for 12 h. The protein-conjugated magnetic beads (20 µL) were then washed twice with PBST and resuspended in PBST buffer with 200 mM imidazole. The free and bound N-PEDv were analyzed by SDS PAGE and the bound N-PEDv on magnetic beads was determined to be 0.16 mg/mL. The protein-conjugated magnetic beads were stored at 4 °C for selection.

#### *Selection of DNA aptamers for N-PEDv*

DNA aptamers for N-PEDv protein were selected using magnetic bead-based SELEX method as described in our previous study.<sup>674</sup> Briefly, the DNA library was diluted in selection buffer (1× SB; 50 mM Tris-HCl, pH 7.26, 150 mM NaCl, 1 mM MgCl<sub>2</sub>, 0.01% Tween-20, 10 mM Imidazole) and heated at 90 °C for 1 min, followed by annealing at room temperature for 10 min. Then, the N-PEDv protein-conjugated magnetic beads were washed twice with 1× SB and mixed with the DNA library at 23 °C for 30 min. After washing three times with 1× SB (1 mL), the magnetic beads were resuspended in elution buffer (50 mM Tris-HCl, pH 7.26, 150 mM NaCl, 1 mM MgCl<sub>2</sub>, 0.01% Tween-20, 500 mM Imidazole) to elute the bound DNA on magnetic beads. The eluted DNA in the supernatant was collected by magnetic separation, followed by the addition of the reverse primer RP1 (10 µL, 10 µM), the forward primer FP1 (10 µL, 10 µM), Taq DNA polymerase (2 µL, 5 U/µL), Taq buffer (200 µL, 50 mM KCl, 10 mM Tris-HCl, 1.5 mM MgCl<sub>2</sub>, 1% v/v Triton X-100, pH 9.0) and dNTPs (20 µL, 2 mM) for PCR1. PCR1 was carried out using the following temperature profile: preheating at 94 °C for 30 s; thermo cycles of 94 °C for 30 s, 50°C for 30 s, and 72 °C for 30 s; annealing at 72 °C for 5 min. Next, the PCR1 product was used as the template for PCR2. The PCR2 mixture was prepared by mixing the PCR1 product (50 µL), FP1 (25 µL, 10 µM), RP2 (25 µL, 10 µM), 10× Taq buffer (50 uL), Taq DNA polymerase (5 µL, 5 U/µL), dNTPs (10 µL, 10 mM), and water (335 uL). The amplification reaction used the same temperature profile as PCR1. After amplification, the PCR2 product was pelleted by ethanol precipitation, purified by dPAGE, quantified by UV-Vis absorbance at 260 nm and utilized for the next round of selection. A total of 10 rounds of selection were carried out. The SELEX pressure was gradually increased by decreasing the concentrations of the DNA library and N-PEDv target (from 1 – 10 round: DNA library (nM): 2000, 200, 200, 200, 200, 50, 10, 5, 2.5, 2.5 nM; N-PEDv (nM): 100, 100, 50, 25, 10, 5, 5, 1.6, 1, 0.5 nM). Selected DNA libraries were amplified by PCR using primers with sequencing tags and analyzed with the MiSeq (Illumina) sequencing platform using our previously published protocols.<sup>675</sup>

#### *Radiolabelling of DNA Aptamers*

DNA aptamers were labeled with γ-[<sup>32</sup>P] ATP at the 5'-end using PNK reactions according to the manufacturer's protocol. Briefly, 2 µL of 1 µM DNA aptamers were mixed with 2 µL of γ-[<sup>32</sup>P] ATP, 1

$\mu\text{L}$  of  $10 \times$  PNK reaction buffer A, 10 U (U: unit) of PNK and 4  $\mu\text{L}$  water. The mixture was incubated at 37 °C for 20 min, and then purified by 10% dPAGE.

#### *Electrophoresis mobility shift assays (EMSA)*

$\gamma$ -[ $^{32}\text{P}$ ] labelled DNA aptamers (1 nM) were dissolved in 1xSB and heated at 90 °C for 5 min, and then cooled at room temperature for 20 min. N-PEDv protein were dissolved and diluted in the same buffer. 5  $\mu\text{L}$  of the above aptamer solution was mixed with 15  $\mu\text{L}$  of N-PEDv solution with different concentrations. The mixture was incubated at room temperature for 1 h, followed by adding 6  $\times$  glycerol loading buffer (4  $\mu\text{L}$ ) and analyzed by native PAGE (10% w/v, 100 V, 20 min, room temperature). The PAGE gel was then analyzed using a Typhoon 9200 imager. Aptamer binding with other proteins were tested using the same method.

#### *DEE-Chip Fabrication*

The DEE-Chip was fabricated on polystyrene sheets (Graphix Shrink Film, Graphix). The polystyrene was cleaned with ethanol and deionized water, after which a vinyl mask (FDC 4304, FDC Graphic Films) was applied onto the sheet. The vinyl mask was then patterned (as defined by Adobe Illustrator) using a Robo Pro CE5000-40-CRP cutter (Graptect America). A 100 nm gold film was sputtered onto the masked substrate using direct current sputtering (MagSput, Torr International) and the vinyl mask was removed. Subsequently, gold nanostructures were electrodeposited onto the two working electrodes by applying a static potential of  $-0.6$  V for 600 s in a solution of 10 mM gold chloride ( $\text{HAuCl}_4$ ) and 5 mM HCl using a potentiostat (Palmsens) with Ag/AgCl as the reference and platinum wire as the counter electrode.

#### *DEE-Chip Biofunctionalization*

All of the electrochemical measurements were performed using a potentiostat (Palmsens). The DEE-Chips were rinsed in isopropanol and ddH<sub>2</sub>O. This was followed by electrochemical cleaning using cyclic voltammetry in 0.1 M H<sub>2</sub>SO<sub>4</sub> (0–1.5 V, 100 mV s<sup>-1</sup>, 40 cycles). After cleaning of the DEE Chips, the sensing electrodes (E<sub>1</sub> and E<sub>2</sub>) were functionalized with their respective biorecognition elements. To functionalize E<sub>1</sub>, 0.5  $\mu\text{M}$  thiol-terminated e-aptamer sequence was reduced with 150  $\mu\text{M}$  TCEP for 2 h in the dark at room temperature and then deposited onto the sensing electrode. Simultaneously, TCEP reduced single-stranded DNA (ssDNA) capture probes (3  $\mu\text{L}$ , 1.5  $\mu\text{M}$ ) specific to the biobarcode sequence of the e-aptamer were drop functionalized onto E<sub>2</sub>. The DEE-chips containing their respective solutions were then enclosed in foil-backed petri dishes at room temperature and stored in a dark environment for 20 h.

#### *Electrochemical Characterization*

Electrochemical characterization of the DEE-chips was carried out using square wave voltammetry (SWV) over a voltage range of 0 V to  $-0.6$  V (all of the voltages are reported as anodic negative) before and after the e-aptamer deposition in 25 mM PBS and 25 mM NaCl buffer (25:25 buffer). The immobilization of a thiol-terminated ssDNA probe on the capture channel was characterized using a cyclic voltammetry scan from 0 V to 0.5 V at a scan rate of 50 mV s<sup>-1</sup> in 2 mM potassium hexacyanoferrate(II) solution.

#### *Detection in Buffer and Saliva*

Following biofunctionalization, a 100 mM MCH solution was used to backfill the surface for 10 mins in the dark at room temperature prior to buffer (50 mM Tris (pH 7.4), NaCl 150 mM, MgCl<sub>2</sub> 1 mM, Tween-20 0.01%) based analysis. Buffer spiked N-PEDv samples (8  $\mu\text{L}$ ) of varying concentrations were then deposited onto the DEE-chips such that both E<sub>1</sub> and E<sub>2</sub> were covered at the same time. The sample containing DEE-chips were subsequently incubated for a period of 45 min.

For saliva spiked analysis, a 1mM PEG 6000 solution was used to backfill the sensing surfaces for 100 mins in the dark at 4°C. Healthy swine saliva samples were then thawed, redispersed and diluted to 30% (v/v) in buffer. N-PEDv proteins of various concentrations were subsequently spiked into these saliva samples (10  $\mu\text{L}$ ) and incubated on the DEE-chips at room temperature for 120 min.

Following incubation, redox currents on each electrode were probed using SWV over a voltage range of 0 V to -0.6 V (all voltages are reported as anodic negative) in 25 mM PBS and 25 mM NaCl buffer (25:25 buffer).

#### *Specificity Testing*

Individual sets of DEE-chips ( $n > 3$ ) were incubated with 250 nM N-PEDv (target protein), bovine serum albumin (BSA), thrombin and ribonuclease (RNase) spiked in 30% porcine saliva as per the protocol for detection in saliva (described above). Square wave voltammograms for each of the sensing electrodes were subsequently acquired in a 25 mM phosphate buffer solution containing 25 mM NaCl (25/25 buffer) against a silver/silver chloride (Ag/AgCl) electrode and a platinum (Pt) counter electrode in a potential range of 0 to -0.6 V and a scan rate of 0.1 V sec<sup>-1</sup>.

#### *Kinetic Characterization*

Three different electrode configurations were designed to manipulate mass transport times. Towards this end, DEE-chips pertaining to the first two configurations were obtained by vinyl masking and sputtering gold star electrodes with interelectrode distances of 500  $\mu\text{m}$  and 300  $\mu\text{m}$ , respectively. A third configuration was then generated by applying a positive potential bias (+0.5 V) across  $E_2$  for a set ( $n = 3$ ) of DEE-chips possessing an interelectrode spacing of 300  $\mu\text{m}$ . Each set of electrode configurations was then cleaned, characterized and incubated with 500 nM of N-PEDv (10  $\mu\text{L}$ ) spiked in 30% porcine saliva samples for incubation times spanning 0 – 120 mins. Square wave voltammograms for each of the sensing electrodes were subsequently acquired at each predetermined incubation interval. All electrochemical measurements were performed in 25 mM phosphate buffer solution containing 25 mM NaCl (25/25 buffer) against a silver/silver chloride (Ag/AgCl) electrode and a platinum (Pt) counter electrode in a potential range of 0 to -0.6 V and a scan rate of 0.1 V sec<sup>-1</sup>.

#### *Preclinical Study*

A set of 12 porcine saliva samples was obtained through Southwest Vets following a PEDv outbreak. Of these, six were established as PEDv-positive and six were determined to be PEDv-negative by RT-PCR (Figure S7.6). Each of these 12 samples was then anonymized and tested in a double-blind study. Following sample dilution (30% saliva) in buffer, whole saliva samples were heat lysed at 60°C for 25 mins to release N-PEDv proteins from within the viral cells, if present. A sample volume of 10  $\mu\text{L}$  was then added to each DEE-Chip, with a positive potential bias (+0.5 V) applied across  $E_2$  using a potentiostat (Palmsens). The DEE-chips were incubated for 60 mins at room temperature and scanned using a lightweight benchtop potentiostat (Palmsens). All electrochemical measurements were performed in 25 mM phosphate buffer solution containing 25 mM NaCl (25/25 buffer) against a silver/silver chloride (Ag/AgCl) electrode and a platinum (Pt) counter electrode in a potential range of 0 to -0.6 V and a scan rate of 0.1 V sec<sup>-1</sup>. Changes in signal were then reported against the potential window according to the following equation:

$$\begin{aligned} \text{Fold Change } E_1 &= I E_1 \text{ after} \div I E_1 \text{ before} \\ \text{Fold Change } E_2 &= I E_2 \text{ after} \div I E_2 \text{ before} \end{aligned}$$

Clinical sensitivity and specificity were calculated as:

$$\text{Sensitivity} = \text{True positive} \div (\text{True positive} + \text{False negative})$$

$$\text{Specificity} = \text{True negative} \div (\text{True negative} + \text{False positive})$$

Every data point corresponds to the mean of three ( $n = 3$ ) individual data points measured for the same conditions on three separate devices, with the error bar indicating the standard deviation.

## **7.4 Results and Discussion**

### **Aptamer selection and characterization**

In order to develop the DEE aptasensor for detecting PEDv, we selected DNA aptamers specific to the nucleocapsid protein of PEDv (N-PEDv) using our previously described magnetic bead-based SELEX technique (Figure 7.1a).<sup>674,676</sup> We chose N-PEDv as the target analyte due its high degree of expression and ability to conserve large genetic regions during PEDv infection, which minimizes the extent of mutation relative to the spike (S) protein sites.<sup>677,678</sup>

Following ten rounds of selection with a library containing  $6 \times 10^{14}$  DNA molecules (see Table S1 for the sequences of the DNA library and primers used), high-throughput sequencing was conducted using the 10<sup>th</sup> selection pool, consistent with a previously described protocol.<sup>679</sup> Many aptamers were discovered; the top 50 aptamer sequences based on their abundance in the final pool are listed in Table S2 (named according to their rank). The top five ranked aptamers (PEA1-PEA5) were selected for binding studies using a gel-based electrophoresis mobility shift assay (EMSA). The extracted  $K_d$  values (binding affinity) of these aptamers ranged from 2.3 to 26.3 nM (Table S2), values that are comparable with most reported aptamers for pathogen detection and thus validate the quality of the selected sequences for subsequent use in diagnostic assays.<sup>680</sup> As PEA1 yielded the highest affinity ( $K_d = 2.3$  nM) compared to the other 4 sequences, it was chosen for further investigation.

It is widely disseminated that shorter aptamers are more stable, cheaper to produce and easier to immobilize onto electrodes.<sup>681</sup> Considering these factors, we truncated PEA1 (containing 79 nucleotides; Figure 7.1b) to yield shorter variants. In total, 8 variants (named PEA1-1 to PEA1-8) were designed and tested for N-PEDv binding using EMSA (Figure S7.1). A close analysis of the data revealed that PEA1-3 (shortened to 54 nucleotides; Figure 7.1c) possessed an affinity ( $K_d = 2.8$  nM, Figure 7.1d and Figure S7.2) similar to that the full length PEA1, while a significant loss in affinity was observed for all other derivatives (Figure S7.1). This result suggests that the L1 and L2 loops in PEA1 play important roles in recognizing the protein target (Figure 7.1b).

In addition to affinity, we also tested the specificity of PEA1-3 by evaluating its binding to the following four proteins: bovine serum albumin (BSA), human  $\alpha$ -thrombin (Tb), RNase H2 of *Clostridium difficile* (RNase H2) and the target N-PEDv protein (Figure 7.1e). BSA is commonly used as a control protein to test the aptamer specificity. Human  $\alpha$ -thrombin, on the other hand, was chosen due to the existence of a high-affinity DNA aptamer that specifically recognizes this human protein<sup>682</sup> while RNase H2 was chosen to represent a nucleic acid binding protein. We did not observe any significant binding of PEA1-3 to the control proteins. We further tested aptamer-specific interactions of PEA1-3 with the spike (S) and nucleocapsid (N) proteins of SARS-Cov-2 (another virus from the coronavirus family) and did not observe any significant binding (Figure S7.3), further validating the specificity of the aptamer. Owing to its ability to specifically identify N-PEDv, we chose PEA1-3 for constructing the reagent-less electrochemical assay for detecting PEDv.

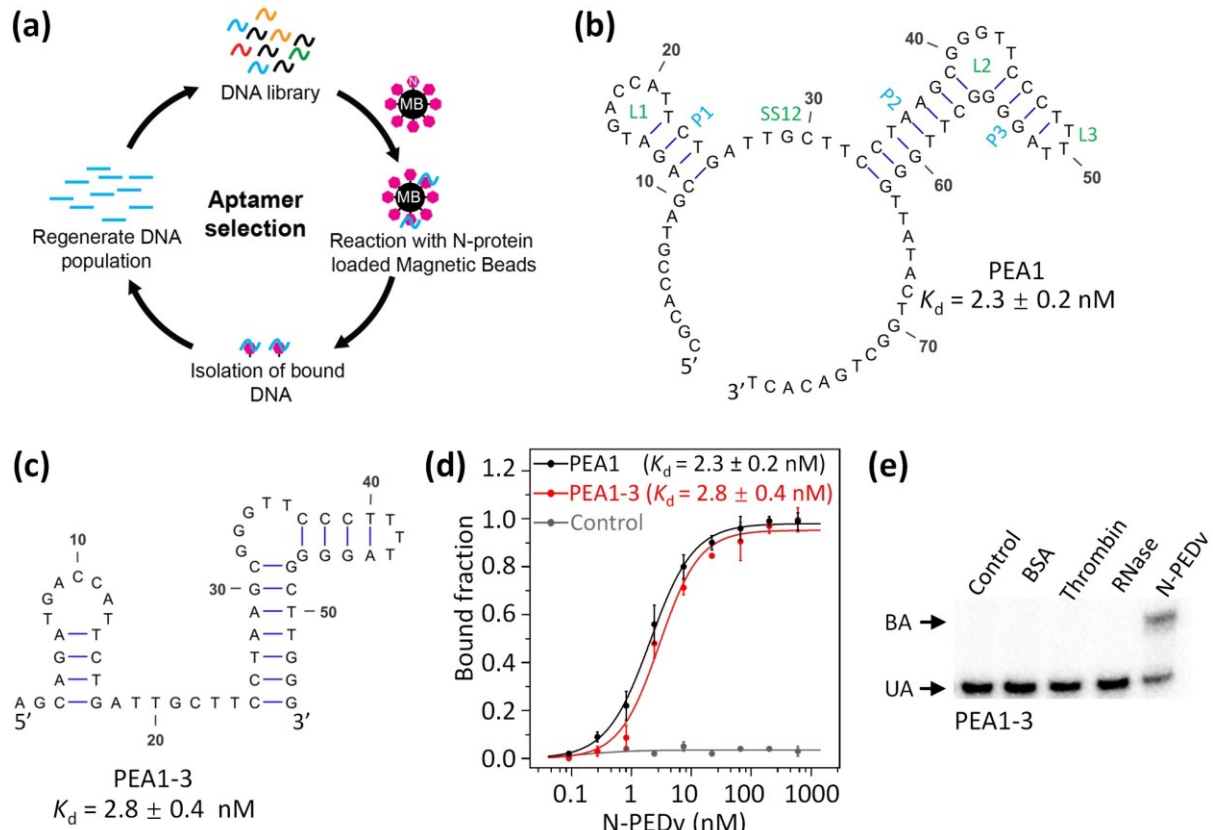


**Figure 7.1** Aptamer selection and characterization. (a) Depiction of the aptamer selection process. The secondary structures of (b) full-length aptamer PEA1 and (c) truncated PEA1-3. (d) Binding curves and resultant affinity values ( $K_d$ , nM) extracted from the aptamers binding to the nucleocapsid protein of PEDv (N-PEDv). Aptamer PEA1-3 was chosen for subsequent testing. (e) Selectivity tests demonstrating PEA1-3 binding of N-PEDv (target protein) in comparison with the control proteins bovine serum albumin (BSA), thrombin and ribonuclease (RNase). A concentration of 5 nM of each protein was used in this study (BA: bound aptamer; UA: unbound aptamer).

### Engineering the dual-electrode electrochemical chip (DEE-chip)

In order to integrate PEA1-3 into a reagentless electrochemical biosensor, we annealed the newly developed aptamer sequences (PEA1-3) with a methylene-blue (redox-active) tagged bio-barcode to create an electroactive aptamer (e-aptamer), the sequence of which is given in Table S1. The e-aptamer was then integrated into a *dual-electrode electrochemical chip (DEE-chip)* with two sensing electrodes,  $E_1$  and  $E_2$  (Figure 7.2). In this assay,  $E_1$  is used for housing the e-aptamers on the electrochemical chip at the time of fabrication to enable reagent-less operation and for validating the chip and assay quality whereas  $E_2$  is designed for generating the electrochemical signal needed for sample analysis. For constructing the DEE-chip, we immobilized the e-aptamers onto  $E_1$  and modified  $E_2$  with single-stranded DNA (ssDNA) capture probes specific to the biobarcode sequence of the e-aptamer (Figure 7.2). In the presence of the target protein, the redox barcode is designed to be released from  $E_1$ , diffuse on the DEE-chip, and then be recaptured on  $E_2$  for signal generation. The two related yet separate events on  $E_1$  and  $E_2$  are expected to yield a signal attenuation on  $E_1$  and signal increase on  $E_2$ , which is used for sample analysis.

Electrochemical chips comprised of star-shaped  $E_1$  and  $E_2$  gold electrodes patterned onto polystyrene substrates were fabricated for small volume (10  $\mu$ L) bioanalysis. Electrodeposition of gold was then employed to derive the three-dimensional nanostructured architecture required for sensitive detection at both electrodes (Figure S7.4). Diffusion-limited growth stemming from the presence of sharp edges along the star electrodes served as the main driving force in generating this dense nanostructured topography.<sup>683,684</sup> To ensure successful reproducibility and function of the devised

platform, (1) extensive electrochemical cleaning of the electrodes was conducted prior to e-aptamer and probe bio-functionalization, (2) reproducible electroactive surface area generation was conducted on both  $E_1$  and  $E_2$  (Figure S7.5a), and (3) sufficient e-aptamer and probe bio-functionalization was qualitatively verified for  $E_1$  and  $E_2$  using cyclic-voltammetry measurements (Figure S7.5b).

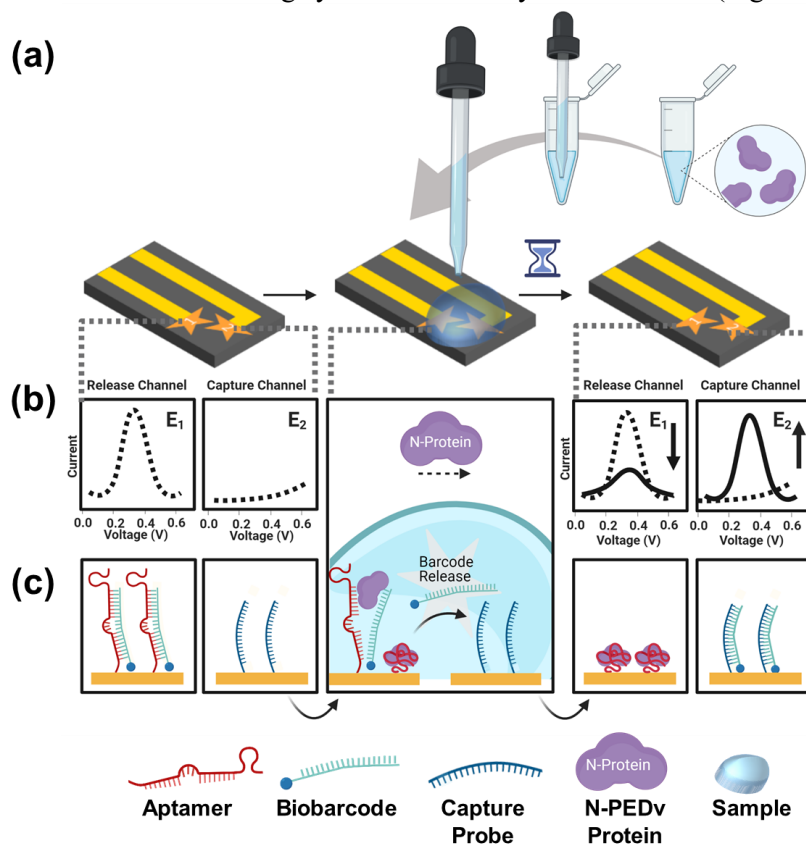


*Figure 7.2 Schematic illustration of the operating principles and the components of the DEE-chem assay. (a) Sample-to-test workflow: liquid samples comprising of N-PEDv are introduced to the DEE-Chip using a dropper. (b) Signal changes: (Left) Prior to sample introduction, a methylene blue (MB) redox peak is exhibited by  $E_1$  while an absence of this peak is exhibited on  $E_2$ . (Right) Following N-PEDv introduction, target induced displacement of the redox barcode on  $E_1$  and subsequent capture on  $E_2$  yields a decrease in the MB peak on  $E_1$  while a signal increase is seen on  $E_2$ . (c) Molecular Operation: (Left) E-aptamers comprised of redox barcodes are immobilized on  $E_1$  while single-stranded DNA (ssDNA) capture probes are anchored on  $E_2$ . (Middle) In the presence of the target protein (N-PEDv), these redox barcodes are released from  $E_1$  and diffuse towards  $E_2$ . (Right) Following diffusion, the redox barcodes are subsequently captured on  $E_2$ , yielding a decrease in the redox peak on  $E_1$  and a signal increase on  $E_2$ .*

### Electrochemical assessment against viral protein load

Given its importance to the farming industry and the lack of rapid tests currently available, we chose PEDv as our clinical target. However, this assay design can be easily adapted to other viral and non-viral targets by swapping out the e-aptamer to one specific to the newly chosen analyte.<sup>685–690</sup>

Aiming to assess the performance of the DEE-Chip in detecting clinically relevant amounts of viral protein, we first challenged the platform with known concentrations of N-PEDv spiked in buffer. Measured current changes at both  $E_1$  and  $E_2$  (using square wave voltammetry, SWV), were used to probe the DEE-Chip response to viral protein loads of 10 nM ( $0.6 \mu\text{g mL}^{-1}$ ) to 500 nM ( $29 \mu\text{g mL}^{-1}$ ) following an incubation period of 45 mins and a small sample volume of 10  $\mu\text{L}$  (Figure 7.3a). The redox currents on each electrode were generated through the electrochemical reduction of methylene blue that was tagged on the DNA barcode. Biofunctionalization with mercaptohexanol (MCH) was utilized to combat biofouling at both electrodes on the DEE-chip. The ensuing fold-changes were quantified by measuring the redox current before (baseline;  $I_{E_1 \text{ before}}$ ,  $I_{E_2 \text{ before}}$ ) and after (signal;  $I_{E_1 \text{ after}}$ ,  $I_{E_2 \text{ after}}$ )

viral protein loading of the DEE-chip, with the resultant fold-changes ( $Fold\ Change\ E_1 = I_{E_1\ after} / I_{E_1\ before}$  and  $Fold\ Change\ E_2 = I_{E_2\ after} / I_{E_2\ before}$ ) then extracted to yield the sensor response calibration curve (Figure 7.3b). Prior to target introduction, e-aptamers immobilized on  $E_1$  bring methylene blue moieties close to the gold surface. As this electrode is stepped through a series of potential pulses, reduction of methylene blue at the electrode gives rise to a characteristic voltametric peak at -0.3 V (baseline; Figure 7.3b (left, inset)).<sup>691</sup> Concurrently, an absence of this redox signature is observed on  $E_2$  due to the lack of methylene blue (baseline; Figure 7.3b (right, inset)). In this manner, a device comprising of a signal-off ( $E_1$ ) electrode and a signal-on electrode ( $E_2$ ) is designed on a single chip, in which both electrodes are operated under identical experimental conditions.

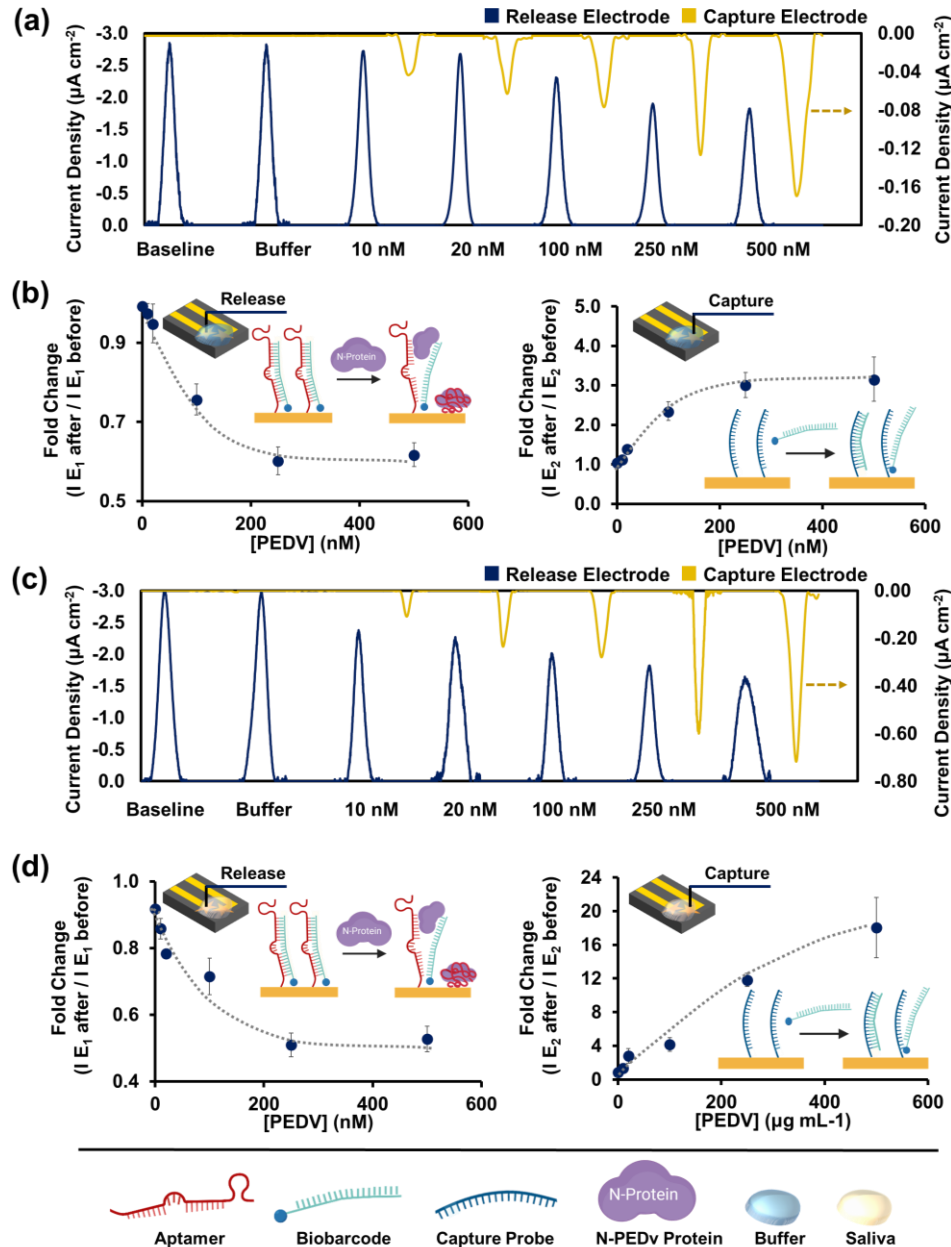


Figure 7.3 Dual electrode electrochemical assay for detecting PEDv nucleocapsid protein. (a) Raw square wave voltammetry (SWV) curves obtained from  $E_1$  and  $E_2$  following incubation with various concentrations of target protein spiked in buffer and incubated on the electrode for 45 min. (b) Calibration plots depicting the associated fold-changes in signals attained on  $E_1$  and  $E_2$  following incubation with target concentration of 10 nM ( $0.6\ \mu g\ mL^{-1}$ ), 20 nM ( $1.2\ \mu g\ mL^{-1}$ ), 100 nM ( $5.8\ \mu g\ mL^{-1}$ ), 250 nM ( $14.5\ \mu g\ mL^{-1}$ ) and 500 nM ( $29.0\ \mu g\ mL^{-1}$ ) in buffer. (c) Raw square wave voltammetry (SWV) curves obtained from  $E_1$  and  $E_2$  following incubation with various concentrations of target protein spiked in 30% porcine saliva and incubated on the electrodes for 120 min. (d) Calibration plots

*depicting the associated fold-changes in signal attained on  $E_1$  and  $E_2$  for target concentrations of 10 nM ( $0.6 \mu\text{g mL}^{-1}$ ), 20 nM ( $1.2 \mu\text{g mL}^{-1}$ ), 100 nM ( $5.8 \mu\text{g mL}^{-1}$ ), 250 nM ( $14.5 \mu\text{g mL}^{-1}$ ) and 500 nM ( $29.0 \mu\text{g mL}^{-1}$ ) in porcine saliva. All electrochemical measurements were performed in a 25 mM phosphate buffer solution containing 25 mM NaCl (25/25 buffer) against a silver/ silver chloride (Ag/AgCl) reference electrode and a platinum (Pt) counter electrode in a potential range of 0 to - 0.6 V and a scan rate of  $0.1 \text{ V sec}^{-1}$ . Error bars depict the standard deviation from the mean obtained using three ( $n=3$ ) separate devices per sample.*

As anticipated, the programmed release and subsequent capture of redox barcodes triggered by target proteins generated opposing trends in fold-changes on  $E_1$  and  $E_2$  that monotonically decreased (Figure 7.3b, left) and increased (Figure 7.3b, right) with target concentration, respectively. It is interesting to note that while a signal saturation is exhibited at both electrodes at a target concentration of 250 nM ( $14.5 \mu\text{g mL}^{-1}$ ), the fold-changes evoked at  $E_1$  are consistently lower than one-fold while fold-changes greater than one-fold are observed on  $E_2$ . A regression fit to the linear region of the calibration curve yielded a LOD of 25.7 nM ( $1.49 \mu\text{g mL}^{-1}$ ; 1.49 ng for a sample volume of  $10 \mu\text{L}$ /electrode) for the signal-off electrode, whereas a LOD of 18.6 nM ( $1.08 \mu\text{g mL}^{-1}$ ; 1.08 ng) was exhibited by the signal-on electrode (Fig 3b).

As PEDv is a disease occurring in porcine populations, we then sought to challenge the DEE-chem assay with viral protein targets ( $10 \mu\text{L}$  sample volume) spiked in 30% swine saliva. However, in order to compensate for the increased non-specific adsorption in this biological matrix, polyethylene glycol (PEG) was used as the anti-fouling agent in place of MCH. Furthermore, the incubation period was increased from 45 mins to 120 mins to account for the increased diffusion time required by the bio-barcode to traverse this viscous media.<sup>692</sup> Trends mirroring those demonstrated in the buffer-spiked study were seen in SWV curves obtained using saliva-spiked samples (Figure 7.3 c). The fold-change extracted from the voltammetry curves revealed that while both the buffer and saliva study were able to distinguish between samples with and without PEDv on  $E_1$ , starting at a concentration of 10 nM ( $0.6 \mu\text{g mL}^{-1}$ ), the fold-change was considerably higher in the saliva study (Figure 7.3d). This is largely attributed to the increased diffusion time used in the saliva-spiked study. The associated calibration curve, pertaining to the fold-changes at  $E_1$  and  $E_2$ , revealed a LOD of 37.8 nM ( $2.19 \mu\text{g mL}^{-1}$ ; 2.19 ng) for  $E_1$  and a LOD of 18.8 nM ( $1.09 \mu\text{g mL}^{-1}$ ; 1.09 ng) for  $E_2$  in saliva (Fig 3d). While the LOD obtained for  $E_2$  in saliva is similar to that obtained in buffer (25.7 nM), the LOD for  $E_1$  is reduced by 1.5x in saliva as compared to buffered samples. This signal drop is expected to be caused by increased matrix viscosity and non-specific binding in saliva compared to the buffered samples. Despite this, both samples yielded LODs that fall well within the clinically relevant range reported in the literature (440 ng on day 3 or 66.3 ng on day 7 in rectal swabs).<sup>693</sup> Most specimens exhibit noticeable physiological symptoms within 4 days post infection.<sup>693,694</sup> This is further bolstered by the finding that a significantly higher magnitude of shedding is observed in oral fluids as compared to rectal swabs during the 14 days-post-infection.<sup>695</sup> The large fold-changes achieved on  $E_2$  is facilitated by our unique two-electrode design that suppresses background contributions on  $E_2$ , facilitating the detection of 10 nM N-PEDv in both buffer and saliva (Figure 7.3b, d).

### **Specificity of the DEE-chem assay**

To further explore the integrity of the devised platform, we investigated whether the engineered DEE-chem assay could specifically recognize N-PEDv targets. We challenged the sensor by introducing a panel of non-target proteins including thrombin, bovine serum albumin (BSA), and ribonuclease (RNase) spiked in 30% healthy porcine saliva. The DEE-Chip displayed remarkable specificity, accurately distinguishing the N-PEDv samples from the nonspecific panel on both  $E_1$  and  $E_2$ . Square wave voltammograms revealed negligible fold-change attenuations in response to thrombin, BSA, and RNase, each of which presented fold-changes less than 0.9-fold on  $E_1$  compared to the 0.5-fold change exhibited by the N-PEDv samples (Figure 7.4a, b). Moreover, a remarkable 12-fold increase in current was observed on  $E_2$  when it was incubated with the N-PED sample compared to much smaller fold-changes of 1.0, 1.1, and 1.4 for thrombin, BSA and RNase respectively, demonstrating the exceptional specificity of the assay. The use of two separate, yet related biorecognition events – target

binding on  $E_1$  and barcode binding and signal transduction on  $E_2$ —reduces the effect of nonspecific binding occurring on  $E_1$  on the signal generated on  $E_2$ , contributing to the high specificity of this assay.

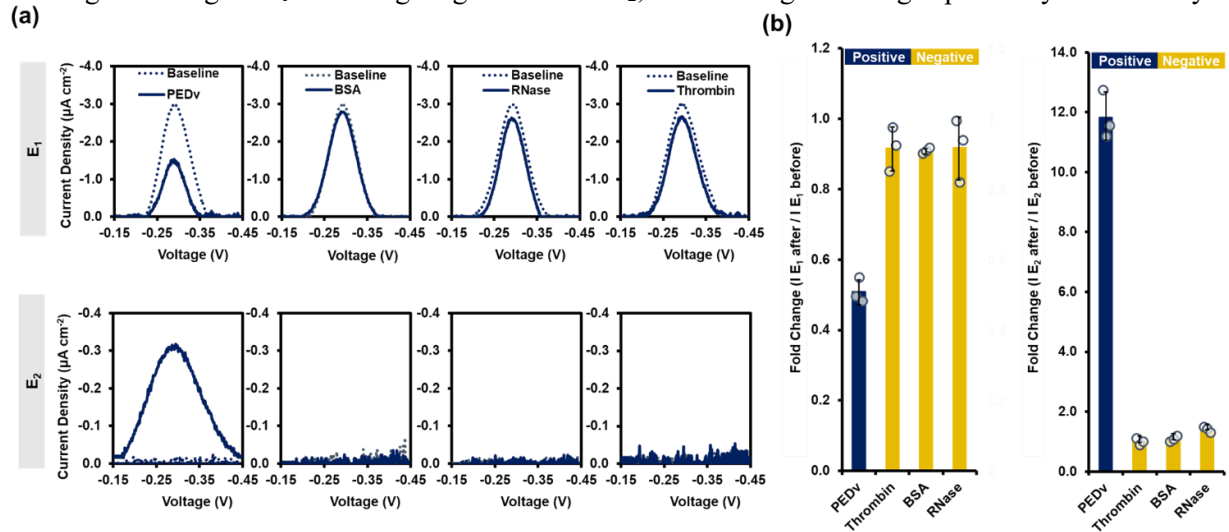


Figure 7.4. Specificity testing of the DEE-Chip in 30% porcine saliva. (a) Square wave voltammograms representing the fold-changes obtained from a pair of  $E_1$  and  $E_2$  electrodes. Each pair was separately incubated with of 250 nM N-PEDv (target protein), bovine serum albumin (BSA), thrombin and ribonuclease (RNase) spiked in 30% porcine saliva. (b) Jitter-plots comparing the signal responses obtained from  $E_1$  and  $E_2$  in the presence of target (N-PEDv) and control (thrombin, BSA, RNase) proteins. All electrochemical measurements were performed in a 25 mM phosphate buffer solution containing 25 mM NaCl (25/25 buffer) against a silver/ silver chloride (Ag/AgCl) electrode and a platinum (Pt) counter electrode in a potential range of 0 to -0.6 V and a scan rate of  $0.1 \text{ V sec}^{-1}$ . Error bars depict the standard deviation from the mean obtained using three ( $n=3$ ) separate devices per sample.

### Kinetic analysis and optimization

While the engineered DEE-Chip embodies the analytical sensitivity and specificity required for N-PED detection in saliva, a detection period of 120 minutes is undesirable for on-farm testing. To overcome this limitation, we explored whether strategies such as reduction of inter-electrode distance and electric field-mediated barcode transport could be leveraged to accelerate mass transport and reduce the required incubation times. Towards this end, we examined the kinetics of the sensor response by measuring the fold-changes on the two electrodes as a function of incubation time (Figure 7.5) for three different electrode configurations designed to manipulate mass transport times (Figure 7.5a). The first configuration represents the original assay design, wherein an original inter-electrode spacing ‘x’ of 500  $\mu\text{m}$  exists between  $E_1$  and  $E_2$  (Figure 7.5a i). This was used to probe and identify the limitations inherent to our original design (as used in Figure 7.3). The second configuration features a reduced inter-electrode spacing ‘y’ of 300  $\mu\text{m}$  between the two electrodes (Figure 7.5a ii), allowing us to directly probe whether decreasing the inter-electrode distance is sufficient to overcome the challenge of transporting the barcode through the viscous salivary medium to  $E_2$  in under 120 min. The last configuration explores the use of a positive bias potential, applied across  $E_2$ , in conjunction with an interelectrode spacing of 300  $\mu\text{m}$  (Figure 7.5a iii) to drive the negatively charged DNA barcode via electro-migration from  $E_1$  to  $E_2$ . We hypothesized that reducing the inter-electrode distance and designing sensors featuring field-mediated transport could enhance the transport of the DNA barcode from its release site to its capture location.

On  $E_1$ , a linear decrease in fold-change is observed between 15 mins and 60 min, with the slope of the curve decreasing after 60 mins (Figure 7.5b). Redox-tagged barcodes are increasingly released between 15 and 60 mins as target proteins bind to the surface immobilized e-aptamers. A plateau in fold-change is subsequently attained at 120 mins as accessible e-aptamer sites on  $E_1$  are exhausted. In case ‘i’ ( $x = 500 \mu\text{m}$ ), capture of the released barcodes begins at 42 min, rising exponentially until a capture of  $>50\%$

is attained by 120 mins (Figure 7.5c i). Using a diffusion coefficient ( $D$ ) of  $\sim 1.18 \times 10^{-10} \text{ m}^2 \text{ s}^{-1}$ , as deduced from a fluorescein-tagged 33-nucleotide oligomer navigating an aqueous solution,<sup>696</sup> we calculate that it takes 17.7 mins ( $\tau = x^2/2D$ ) for the barcode to diffuse through an inter-electrode distance ( $x$ ) of 500  $\mu\text{m}$ . Given that the signal onset (42 min) takes longer than the diffusion time (estimated  $\sim 18$  min in aqueous media), we hypothesize that the viscosity of the salivary matrix lowers the reaction kinetics. Reducing the inter-electrode distance to 300  $\mu\text{m}$  to overcome this inherent diffusion time barrier causes the theoretical diffusion time to reduce to 6.4 min, which correlates to a practical observed signal onset at 30 mins (Figure 7.5c ii). Inspired by the electrophoretic motion of DNA fragments through gels, we applied a positive potential bias across  $E_2$  to further aid in diffusion of the barcode through saliva. Time-resolved electrochemical measurements revealed that while signal onset mirrored that of detection without the application of a bias-potential (case ii), the fold-change increased at a much faster rate between 30 and 60 min, reaching 75% of its final value at 60 minutes compared to much lower values for the first (20%) and second (45%) configurations (Figure 7.5c iii). The improved signal detection achieved for sensors employing both the reduction of inter-electrode distance and the application of a bias potential in tandem supports the reduction of detection time from 120 mins (case i; *original design*) to 60 mins (*optimized design*), adapting the DEE-chip design to a more on-farm testing friendly format.

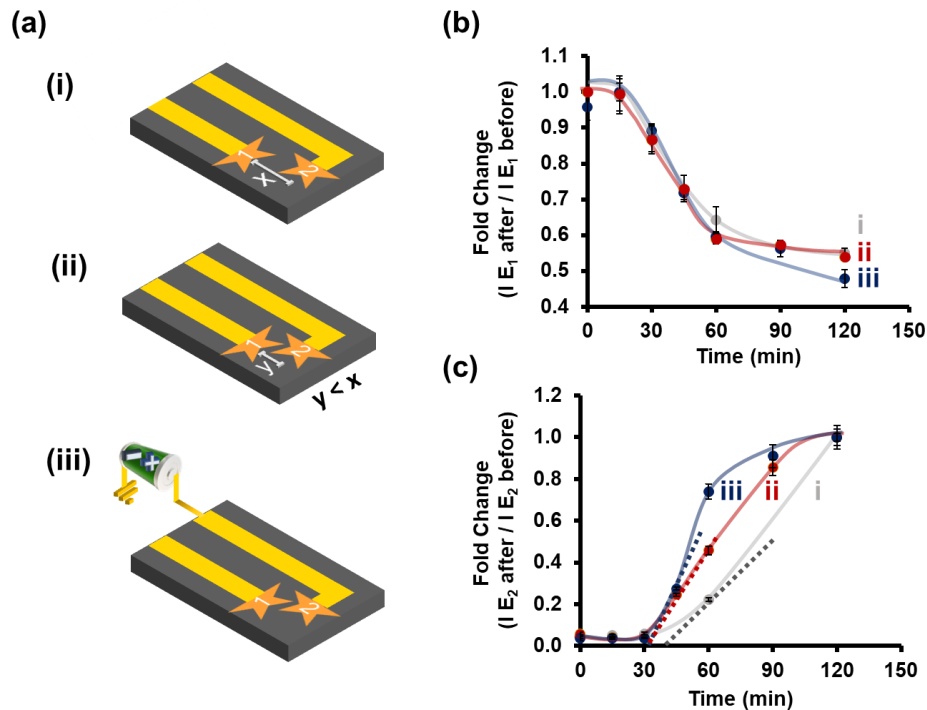


Figure 7.5 (a) A visual representation of the engineering changes made to the DEE-Chip for reducing assay time. The first case (i) demonstrates the original inter-electrode spacing ' $x=500 \mu\text{m}$ ' between  $E_1$  and  $E_2$ . Scenario (ii) depicts the reduction of this inter-electrode spacing to yield the new inter-electrode distance ' $y=300 \mu\text{m}$ '. Scenario (iii), on the other hand, portrays the use of inter-electrode spacing ' $y$ ' in conjunction with an applied positive potential bias ( $+0.5 \text{ V}$ ) across  $E_2$ . (b, c) Plots representing the release (top) and capture kinetics (bottom) observed in each of the three cases depicted in (a). Dotted lines in (c) indicate signal onset; extracted using tangents to the linear segments of the curves. For each group,  $n = 3$  independent devices were tested per sample, each incubated with 500 nM of N-PEDV at a sample volume of 10  $\mu\text{L}$ . The data are presented as mean  $\pm$  standard deviation with visual guide-lines depicting the overall trend in each scenario.

### Clinical Detection

Given the literature evidence supporting the presence of sufficient viral loads in the oral fluid samples for up to 35 days post-infection as measured by reverse transcription PCR (RT-PCR), we expected viral detection in saliva to be feasible using our assay.<sup>695</sup> We next assessed the capability of the DEE-sensors for detecting PEDV in clinical swine saliva samples. We analyzed 12 anonymized, clinically-sourced

swine oral fluid samples (Figure 7.6), six of which were established as PEDv-positive and 6 of which were determined to be PEDv-negative by RT-PCR (Figure S7.6). Following lysis and dilution, the porcine saliva samples were analyzed using DEE-Chips for 60 minutes (Figure 7.6a).

PEDv-positive samples exhibited a significant peak attenuation (Fold-change range: 0.24 - 0.57) on  $E_1$  while a comparably mildly decrease (Fold-change range: 0.71 - 0.95) was observed in the PEDv-negative samples (Figure 7.6b). In comparison, a high 4- to 21.8-fold change in current was induced by the PEDv-positive samples at  $E_2$  while a <2.2 fold-change in current was induced by the PEDv-negative samples (Figure 7.6c). It is important to note, however, that the DEE-Chip was unable to identify the presence of PEDv in positive sample 4. In addition, small variations in the magnitude of fold-change were observed with the different samples, which is likely due to the differences in the composition of the individual saliva samples. Despite these variations, the electrochemical assay retains its performance over a range of statistically significant cycle threshold ( $C_t$ ) values derived from PCR (i.e.,  $C_t$  of 28.9 – 28.6 for positive samples 1 – 3 and  $C_t$  of 33.2 – 33.1 for positive samples 5 – 6). It should be noted that the false-negative sample 4 had the largest  $C_t$  value (33.9) amongst the samples and as such the lowest viral load. There are two hypotheses for the rationale behind the false-negative result generated using sample 4: (1) an insufficient viral load and (2) the presence of salivary inhibitory factors that prevent bio-recognition by the aptamer on  $E_1$ . We tested these two hypotheses by re-analyzing the false-negative sample and manually spiking it with PEDv at a concentration of 500 nM (Figure S7.7). The fold-changes elicited were then compared against an unspiked false-negative analogue and a PEDv negative sample which served as a negative control. Of these, only the PEDv spiked samples exhibited a significant fold-change attenuation (0.47-fold) on  $E_1$  and a large gain in fold-change (18.8-fold) while a comparably mild decrease ( $\geq 0.84$ -fold) and negligible increase ( $< 1.1$ -fold) was observed in the unspiked samples (Figure 7.6b). The ability of the DEE-sensor to detect the spiked sample rules out salivary inhibitory factors, pointing to the insufficient viral load as the reason for the negative response (consistent with the high  $C_t$  value of sample 4).

Receiver Operator Characteristics (ROC) curves constructed from the data from the DEE-Chip (Figure 7.6b, c) were subsequently used to assess the clinical performance characteristics of this assay (Figure S7.8). The ROC depicted here was extracted using the ‘Analyse-It’ software for Microsoft Excel (Analyse-it, Leeds UK) to determine the decision threshold to maximize the sensitivity and specificity of the assay, as identified in our previous work.<sup>697–699</sup> An overall accuracy, or area under the curve (AUC), of 0.975 (CI, 0.936 – to 1.014) with an optimum sensitivity of 83.3% (true-positive cases detected) was obtained at a decision threshold of 0.66 (fold change) and a corresponding specificity of 100% (no false-positive cases detected) at  $E_1$ ; a corresponding AUC of 0.877 (CI, 0.741 – to 1.012), sensitivity of 83.3% at a threshold of 2.17 (fold change) and specificity of 100% (no false-positive cases detected) was obtained using  $E_2$  data. Inspection of the clinical performance metrics (sensitivity, specificity and AUC) reveals that the DEE-Chip performance falls well within the standard threshold of a reliable diagnostic test (AUC > 0.8, 700 sensitivity  $\geq 80\%$ <sup>31</sup> and specificity  $\geq 90\%$ <sup>31</sup>), thereby indicating the potential of this assay for future clinical use.

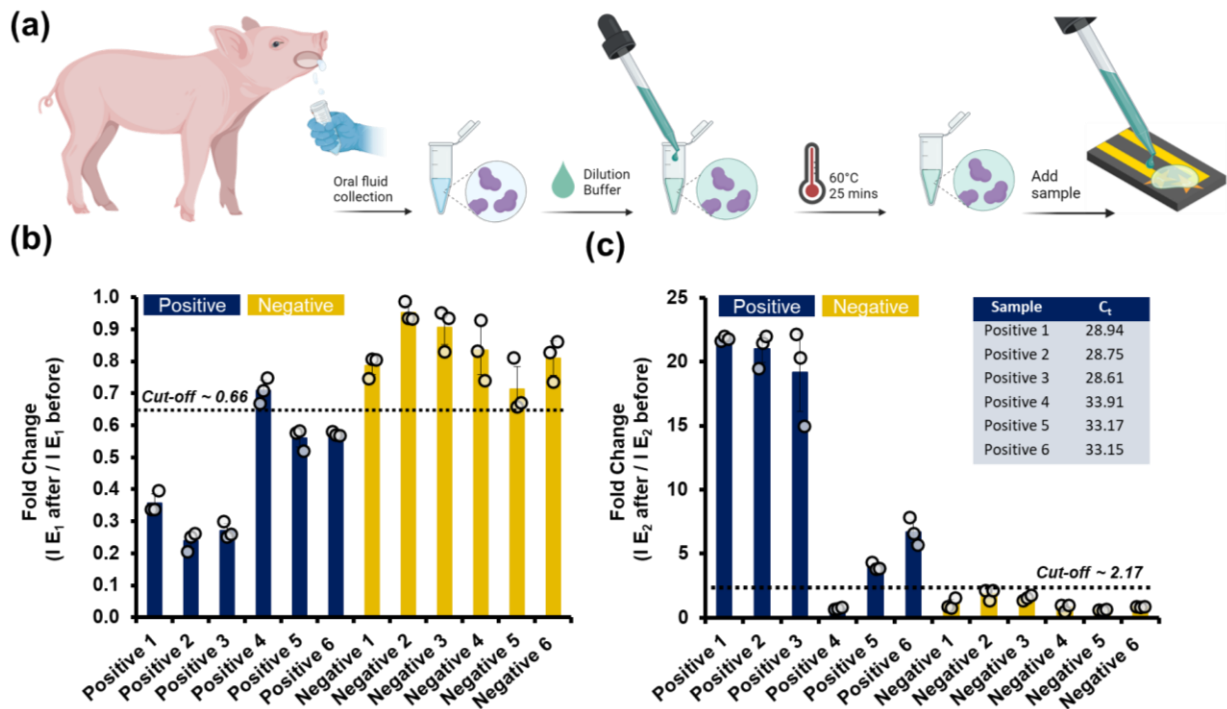


Figure 7.6 (a) Illustration of the diagnostic workflow from sample collection to sensor operation. Following sample dilution and heating, the collected porcine saliva sample is added to the DEE-Chip, incubated for 60 mins at room temperature and scanned using a lightweight benchtop potentiostat (Palmsens). Jitter-plots depicting fold-changes measured on (b)  $E_1$  and (c)  $E_2$  for six clinically-obtained positive (navy) and 6 negative (yellow) porcine saliva samples. Dotted lines indicate the cut-off threshold of the assay as extracted using the ‘Analyse-it’ toolkit in excel. The bars represent the mean of the fold-change extracted from square wave voltammograms on  $E_1$  and  $E_2$  for a given sample. The error bars represent the standard deviation from the mean obtained using three ( $n=3$ ) separate devices per sample. All square wave voltammograms were obtained using 25 mM phosphate buffer solution containing 25 mM NaCl (25/25 buffer) as the supporting electrolyte against a silver / silver chloride (Ag/AgCl) electrode and a platinum (Pt) counter electrode in a potential range of 0 to -0.6 V and a scan rate of 0.1 V sec<sup>-1</sup>. In addition,  $E_2$  electrodes were biased using a bias potential of +0.5V to reduce the detection window to 60 min.

### 7.5 Conclusion

Considering recurrent surges in PEDv outbreaks coupled with increasing reports of more highly communicable and infective variants of concern, the need for a simple, on-farm, saliva-based PEDv test is more critical than ever. In response, we developed a rapid, simple, and reagent-free assay for on-farm detection of PEDv. We developed a dual-electrode electrochemical (DEE) chip featuring functional e-aptamers to bridge the current diagnostic gap — the reliance on centralized laboratories — for PEDv testing. Towards this end, SELEX was first employed to select a novel high-affinity DNA aptamer ( $K_d = 2.3$  nM) that discriminately targets the highly conserved, mutation-resistant N-protein of the PEDv virus. The DEE-Chip used a unique approach for integrating the PEDv aptamer for reagent-less sensing; it included one electrode for housing the aptamer annealed with a redox DNA barcode and another electrode for capturing the DNA barcode and transducing an electrochemical signal. Using this approach, the DEE-Chip yielded a clinically relevant LOD of 1.1  $\mu\text{g mL}^{-1}$  in 10  $\mu\text{L}$  of buffer- and saliva-spiked N-PEDv samples.

To reduce the assay time of the DEE-Chip from (initially 120 minutes) for rapid on-farm testing, we focused on engineering the inter-electrode spacing of the chip and the use of a bias potential to enhance the mass transport of the DNA barcode from one electrode to another. Using the rationally-engineered DEE-Chip, we analyzed 12 clinically-derived swine saliva samples. The DEE-Chip successfully

analyzed 91.6% (and 100% of all samples for  $C_t \leq 33.17$ ) of the clinical samples (sample volume of 12  $\mu$ L) with a clinical sensitivity of 83%, specificity of 100%, and an AUC > 0.83 (extracted from an ROC plot) in 60 minutes without target amplification, target enrichment, target labelling, or the addition of readout reagents. The DEE-chip is versatile and can be integrated with other e-aptamers for detecting various bioanalytes, including other bacterial and viruses, for fulfilling the unmet need of rapid and on-farm animal disease surveillance.

## 7.6 Acknowledgement

The work is supported by the Natural Science and Engineering Research Council (NSERC) of Canada. L.S. is supported by the Canada Research Chair program. The electron microscopy was carried out at the Canadian Centre for Electron Microscopy (CCEM), a national facility supported by the NSERC and McMaster University.

## 7.7 Supplementary Information

Table S7.1 DNA oligonucleotides used in this study.

DNA library and primers used for SELEX		
Name	Size (nt)	Sequence
DNA library	79	CGCACCGTAG CAGATGAC-N <sub>40</sub> -TGGGTTATAC TGGCTGACAC T
Forward primer FP	18	CGCACCGTAG CAGATGAC
Reverse primer RP1	21	AGTGTCAGCC AGTATAACCC A
Reverse primer RP2	41	TTTTTTTTTT TTTTTTTTTT-L-AGTGTCAGCC AGTATAACCC A
Aptamers tested		
Name	Size (nt)	Sequence
PEA1	79	CGCACCGTAG CAGATGACCA TTCTGATTGC TTCCTAAGCG GGTTCCTTT TAGGGGCTTG GGTTATACTG GCTGACACT
PEA2	79	CGCACCGTAG CAGATGACCC ACGCGCCTTC TCTCTGTCTG GGTTCCTTC TAGGGTTTTG GGTTATACTG GCTGACACT
PEA3	79	CGCACCGTAG CAGATGACGG TGATAACGGG TTCCATATTA GGGTGTATCT TTCTGCTTTG GGTTATACTG GCTGACACT
PEA4	79	CGCACCGTAG CAGATGACCA CAACTTCTCA CATCCGGATT CCTACTAAG GCCTTGCTG GGTTATACTG GCTGACACT
PEA5	79	CGCACCGTAG CAGATGACGG TGTCCTGGAT TCCTTACTAA GGTTTTTAT GGTACCCTCT GGGTTATACT GGCTGACACT
PEA1-1	66	CGCACCGTAG CGATTGCTTC CTAAGCGGGT TCCCTTTTAG GGGCTTGGGT TATACTGGCT GACACT
PEA1-2	51	CGCACCGTAG CAGATGACCA TTCTGATTGC TTCGTTATAC TGGCTGACAC T
PEA1-3	54	AGCAGATGAC CATTCTGATT GCTTCCTAAG CGGGTTCCT TTTAGGGGCT TGGG
PEA1-4	41	AGCGATTGCT TCCTAAGCGG GTTCCCTTTT AGGGGCTTGG G
PEA1-5	45	AGCAGATGAC CATTCTGATT GCTTCCTAAG CGGGTTCGGC TTGGG
PEA1-6	49	AGCAGATGAC CATTCTGATT GCTTCCTAAG CCCCTTTTAG GGGCTTGGG
PEA1-7	15	CAGATGACCA TTCTG
PEA1-8	30	CCTAAGCGGG TTCCTTTTA GGGGCTTGGG
DNA oligonucleotides used for electrochemical assays		
Name	Size (nt)	Sequence
Aptamer (PEA1-3)	54	[5ThioMC6-D] - AGCAGATGAC <u>CATTCTGATT</u> GCTTCCTAAG <u>CGGGTTCCT</u> TTTAGGGGCT TGGG

Biobarcode	31	<u>CCGCTTAGGC</u> CTGTCGAGTC <u>ATGGTCATCT</u> G-[MB]
Capture probe	31	[5ThioMC6-D]-CAGATGACCA TGACTCGACA GGCCTAAGCG G

Note: Sequences are written 5'-3'. N40: 40-nucleotide random region; L: non-amplifiable linker. [5ThioMC6-D]: Thiol modifier; [MB]: methylene blue. Complementary bases between PEA1-3 and biobarcode are underlined.

Table S7.2 DNA sequences in pool 10 ranked by their percentage.<sup>[a]</sup>

Rank in pool 10	Sequences (5'→3') <sup>[a]</sup>	% in pool 10	$K_d$ (nM) <sup>[c]</sup>
1	CATTCTGATT GCTTCCTAAG CGGGTTCCT TTAGGGGCT	8.91	2.3 ± 0.2
2	CCACGCGCCT TCTCTCTGTC TGGGTTCCCT TCTAGGGTTT	2.77	3.6 ± 0.4
3	GGTGATAACG GGTTCCATAT TAGGGTGTAT CTTTCTGCTT	1.82	22.1 ± 1.6
4	CACAACTTCT CACATCCGGA TTCCTTACTA AGGCCTTGTC	1.40	3.8 ± 0.5
5	GGTGTCTGG ATTCCTTACT AAGGTTTTTA TGGTACCCTC	0.85	26.3 ± 2.5
6	TATGTGATTA CTTTCTAAGT TTAGGTTTCC TTCTAGGATT	0.78	
7	GTTTGGTTCC CTTTLAGGGT TGTTTCCTTT TTAAGTTTAT	0.75	
8	GTAACGGGTT CCATAATAGG GCGCAGGGGT TAAGTCCATC	0.67	
9	CACACGCTCA CTA CTCTTTC CGGATTCCTT TCTAAGGTTT	0.64	
10	GTCACCGGCC ACGTTTGGAT TCCTTTTAA GGCCTTTGTC	0.54	
11	GTCATCATGG GTTCCCTTGT AGGGCCTCTT TCTTCATTCT	0.53	
12	GTCACGCTGC TTGTTTTTC CGGATTCCTT TCTAAGGCTA	0.52	
13	CCACGCGCCT TCTCTCTGTC TGGGTTCCCT TCTAGGGTTC	0.51	
14	GTGTGATTAC TTTCTAAGT GAGGGTTCCT TTCTAGGGTG	0.41	
15	GGTGATAACG GGTTCCATAT TAGGGTGTAT CTTTCTGCTC	0.36	
16	AGGGGTTCCA TTATAGGGGA TGCTCATT TCGTTTCTCT	0.32	
17	GGTCACTCTG TAGGGTTTGG ATTCCTTCT AAGGGCGTTT	0.31	
18	GTCATATTGG GTTCCCTTAT AGGGTTTACT TTGGTTTTTCG	0.28	
19	GTCATGTGTT TCTTTTGGAT TCCTTTTAA GTTTTTGT	0.25	
20	CTTCACTATA CTCCCTCT TCGGATTCCT TTCTAAGGTT	0.25	
21	GTCATCAGCT CTATTGGATT CCTTCTAAG GGTTTATTC	0.23	
22	CATCTAAGTG TAAATATAAC CGGGTTCAT TCCTTAGGGT	0.22	
23	GATTGTAATG GATTCCTTTT TAAGGTTTGG GTACCCTTAT	0.22	
24	GGCATTGCTT GTTCTTGGGT TCCCTCTTAG GGCTCCTTAC	0.22	
25	CTTACCCCA CCCTTCTGG ATTCCTTTT AAGGCTCTCA	0.21	
26	GTTATCTCTT ATTTCCGGG TTCCCTCTTA GGCCTTCTCC	0.21	
27	TCACGTCTTC ATTTGGGTT CCTATTAGGG GGTTACTCTC	0.21	
28	CCCATTCGGA TTCCTTCTA AGGCTTTTAC CTCATTAGTC	0.20	
29	TACGGTTGAC ACGGATTCCT TCCTAAGGTT TTGCTACGAT	0.19	
30	GTCGAATGTT GGATTCCTT CTAAGGCTAT TTTTTACTC	0.19	
31	TACACTCCC ACCTTCTTT CGGGTTCCT TCTAGGGCTA	0.18	
32	GTCTTCTGT TTTTGGATT CCTTCTAAG GCTTTCATGT	0.18	
33	GTCTGCTCC CTCCGGATTC CTTTCTAAG GTTTATATT	0.17	
34	GTCATCCCTA CTTTTCGTT TGGGTTCCCT TGTAGGGTTC	0.17	
35	GATTCCCTC TCGTTTAA TC CCGGGTTC ATTCTAGGGG	0.17	
36	GTTCCTCCTG CTCTCCGCAT CCCC GGTTTCCTTCTAGGG	0.16	
37	GTCCCTCCG CTCATGATTC CTTTCTAAG CCCTTTTTTC	0.16	
38	ACCGCTTCC TCCGGATTCC TTTTAAAGGC CCTTTTCTTT	0.16	
39	CGATTACTTT ATAAGTCCGT GGGTTCCTA CTAGGGGTAT	0.16	
40	GGCCAGTTTT GTTTGGGATT CCTTGTTAAG GCTTTGTCAG	0.16	
41	GGGATTGGGT TCCCTCCTAG GGCTTTGTTG CTTTCTCTCT	0.15	
42	GTTTGGTTCC CTTTLAGGGT TGTTTCCTTT TTAAGTTTAC	0.15	
43	TATGTGATTA CTTTCTAAGT TTAGGTTTCC TTCTAGGATC	0.15	
44	GTCATATTGG GGTTCCCTTC TAGGGCTACT TCTCGCCCT	0.15	
45	GTTATCTTCT CCATGGGATT CCTTCTAAG GCTTTTGTTC	0.15	
46	CGGATTCCT TCTAAGGCCT TATTCTTTT TTCACCTATT	0.15	

47	GGGTTGCCTT CTAGGGCTCA TCTATTTGGG TTCCCTCCTA	0.14	
48	GACGGGTTCC CTCCTAGGGC TTTTACCTT GGGTACCCCC	0.14	
49	GTCATATTAT TTGGATTCTT TTCTAAGGCC CTTTTATCGT	0.14	
50	CACCCCTTC GCGTTATTTT TGGATTCTT TTTAAGGTTA	0.14	

[a]: Each sequence also contains primer regions of CGCACCGTAGCAGATGAC and TGGGTTATACTGGCTGACACT at the 5' end and 3' end, respectively.

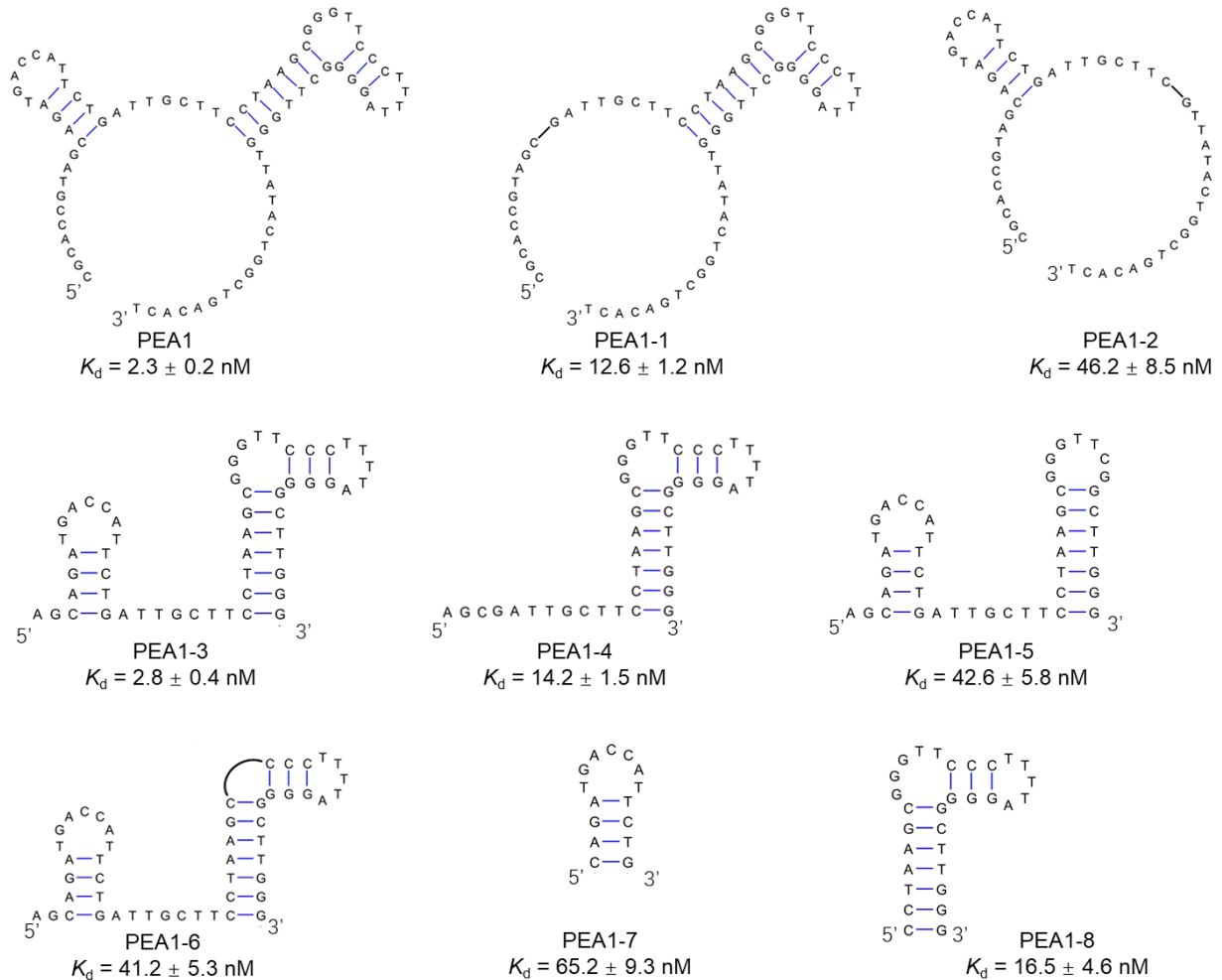


Figure S7.1. Secondary structures and affinities ( $K_d$ ) of full-length aptamer PEA1 and truncated derivatives (PEA1-1 to PEA1-8).

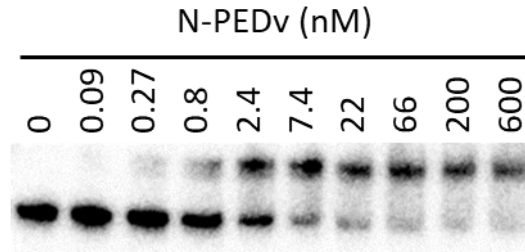


Figure S7.2 EMSA result of aptamer PEA1-3 binding with N-PEDv protein.

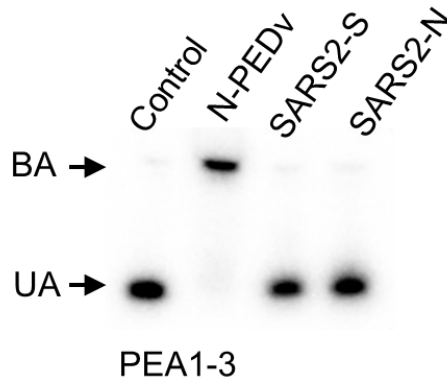


Figure S7.3 Selectivity tests of PEA1-3 binding the target N-PEDv in comparison with Spike (S) and N protein of SARS-CoV-2. 10 nM proteins were used in the tests.

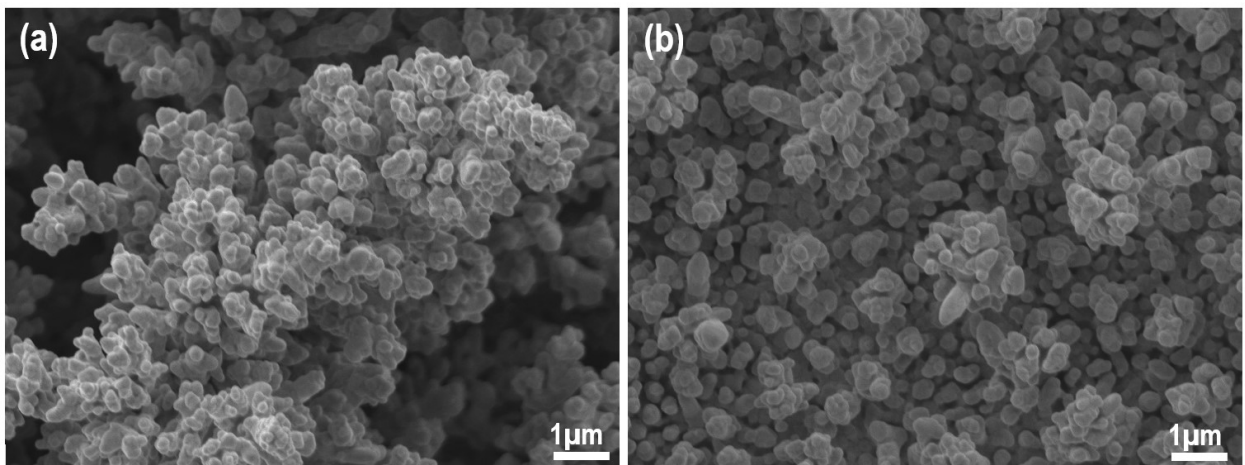


Figure S7.4 SEM micrographs of the two sensing electrodes (a) E<sub>1</sub> and (b) E<sub>2</sub>

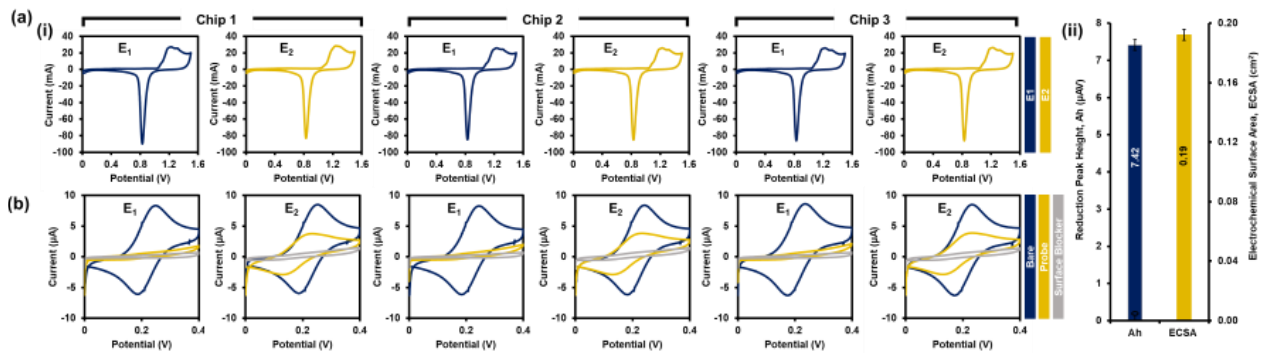


Figure S7.5 DEE-chip Validation using three independent chips comprising of E1 and E2 electrodes. (a) (i) Cyclic voltammetry (CV) scans of bare gold electrodes in sulphuric acid post acid cleaning to assess reproducibility and surface area of each E1 and E2 pair on the three chips. (ii) Extracted reduction peak heights (Ah) and the associated electrochemical surface areas calculated using these peak heights for E1 and E2. (b) CV graphs of E1 and E2 electrodes, before (bare) and after probe deposition and post surface blocking agent deposition (PEG-6000) extracted from three independent chips. Characteristic redox curve for Au in 0.5 M H<sub>2</sub>SO<sub>4</sub> produced from reversible cycling from 0 – 1.6 V against Ag/AgCl at a scan rate of 0.1 V/s

Here we see similar surface area measurements depicted for a triplicate of nanostructured DEE-sensors E<sub>1</sub> and E<sub>2</sub> following electrochemical cleaning (Figure S1a). Similarities in shape of the CV curves following probe and surface blocker deposition qualitatively indicate reproducible biofunctionalization (Figure S1b). Differences in CV profiles of E<sub>1</sub> and E<sub>2</sub> post biofunctionalization with probe are attributed to the differences in size between the e-aptamer complex and the capture probe. Here, a greater decrease in CV is exhibited in the case of the larger e-aptamer due to increased steric hinderance while a relatively smaller decrease is seen in the case of the shorter single-stranded capture probe.

Porcine epidemic diarrhea virus PCR - NEGATIVE oral fluid samples			
Sample ID	Specimen Type	Result (Ct)	Interpretation
1	Oral Fluids	Not detected	NEGATIVE
2	Oral Fluids	Not detected	NEGATIVE
3	Oral Fluids	Not detected	NEGATIVE
4	Oral Fluids	Not detected	NEGATIVE
5	Oral Fluids	Not detected	NEGATIVE
6	Oral Fluids	Not detected	NEGATIVE

Porcine epidemic diarrhea virus PCR - POSITIVE oral fluid samples			
Sample ID	Specimen Type	Result (Ct)	Interpretation
N1	Oral Fluids	28.94	POSITIVE
N2	Oral Fluids	28.75	POSITIVE
N3	Oral Fluids	28.61	POSITIVE
F4	Oral Fluids	33.91	POSITIVE
F5	Oral Fluids	33.17	POSITIVE
F6	Oral Fluids	33.15	POSITIVE

Figure S7.6 RT-PCR testing results of the clinically acquired swine oral fluid samples. Here samples N1 – F6 pertain to samples labeled positive 1 – positive 6 (in the main manuscript) while samples 1 – 6 refer to samples labelled negative 1 – negative 6, respectively.

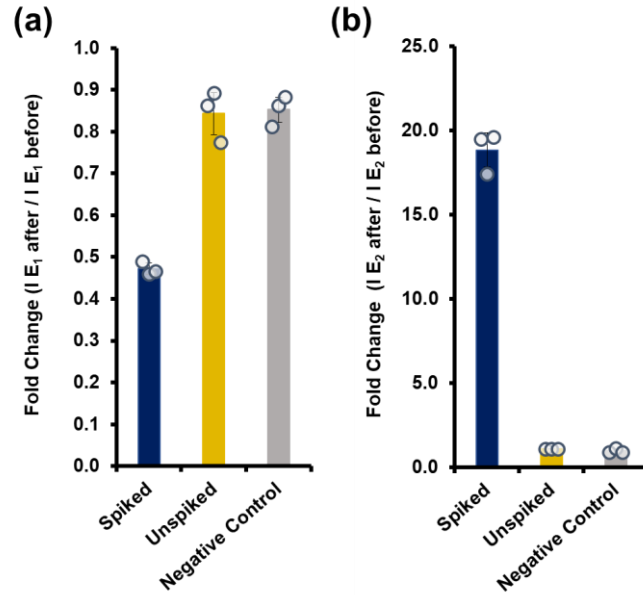


Figure S7.7 False-negative sample study. Jitter plots obtained from (a)  $E_1$  and (b)  $E_2$  incubated with 500 nM N-PEDv spiked in clinically acquired sample ‘positive 4’ (Spiked), unspiked clinically acquired sample ‘positive 4’ (Unspiked) and an unspiked clinically acquired PEDv negative sample (Negative Control). The error bars represent the standard deviation from the mean obtained using three ( $n=3$ ) separate devices per sample. All square wave voltammograms were obtained using 25 mM phosphate buffer solution containing 25 mM NaCl (25/25 buffer) as the supporting electrolyte against a silver / silver chloride (Ag/AgCl) electrode and a platinum (Pt) counter electrode in a potential range of 0 to -0.6 V and a scan rate of 0.1 V sec<sup>-1</sup>. In addition, E2 electrodes were biased using a bias potential of +0.5V to reduce the detection window to 60 minutes.

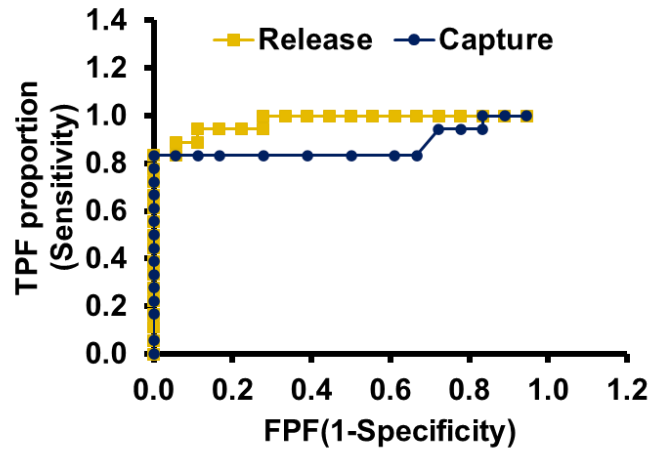


Figure S7.8 Receiver Operator Characteristics (ROC) curve for the clinical diagnosis of PEDv as obtained from the analysis of the signal fold-change on the release electrode (yellow) and the capture electrode (navy) for a set of 12 anonymized, clinically sourced swine oral fluid samples. TPF is true-positive fraction. FPF is false-positive fraction.

## Chapter 8: Conclusion

### 8.1 Thesis Summary

Considering rising incidences of disease and a growth in aging population, the need for sensitive, reliable, non-invasive molecular diagnostics with the potential for on-location testing is more critical than ever. In theory, barcode-based biorecognition systems hold the key to achieving the ultrasensitivity, reliability (minimizing false positive) and programmability necessary to advance molecular diagnostics towards the point-of-care. Thus, the overarching goal of this thesis was the development of ultrasensitive, dynamic, PEC and EC barcode-integrated biorecognition strategies—as tools to enable POC sensing—capable of reliably detecting biomolecular targets in complex biological matrices by enhancing the analytical sensitivity, decreasing response time, and enabling reagentless signal transduction (EC).

Towards this end, we first engineered a strategy to develop robust, solution-processed, three-dimensional transducers for PEC biosensing. Here, a photoactive transducer—comprised of P25 TiO<sub>2</sub> nanoparticles (NPs) integrated within a catecholic polymeric network of chitosan (CHIT) and 3,4-dihydroxy benzaldehyde (DHB)—demonstrated biofunctionality, large baseline signal generation and repeatable and stable photocurrents under cyclic operation. This novel electrode served as the building block for all the PEC sensing strategies developed in this body of work. Solution-based fabrication was utilized to make these electrodes amenable to low cost, mass-scalable, rapid processing and industrial manufacture.

Au NPs have been widely used to modulate the PEC current of P25 TiO<sub>2</sub> photoelectrodes in sensing systems. Consequently, the next study probed the distinct interaction mechanisms between Au NPs and TiO<sub>2</sub> NPs under varied excitation regimes (397 and 540 nm) to determine the effect of Au NP density on PEC current generation. Using photoelectrodes developed in the previous work, different Au NP loadings (134, 181, 433 and 623  $\mu\text{m}^{-2}$ ) were examined at the photoelectrode surface. It was discovered that the density of Au NPs on the electrode surface could be used to control competitive loss (light absorption and scattering by Au NPs) and enhancement mechanisms (direct charge transfer between Au and TiO<sub>2</sub> NPs); thereby, enabling tunability of photocurrent response under UV illumination. Furthermore, at smaller Au NP loadings (< 181  $\mu\text{m}^{-2}$ ), high energy carriers—generated through interband excitation of Au NPs under UV illumination—significantly enhance ascorbic acid oxidation and the resulting PEC current as compared the to lower energy carriers generated through intraband transitions in the visible light regime.

A *dual-wavelength* operated strategy was subsequently demonstrated for Au labelled oligonucleotide target (1 pM) detection by exploiting the programmability of this system. In essence, this study delineates the effect of Au NPs when used in direct contact with the underlying P25 TiO<sub>2</sub> photoelectrodes. As interband transitions favour enhanced anodic current generation and offer signal-tunability—using Au NP density control—at a single excitation wavelength, UV illumination was chosen over visible light excitation to power the next iteration of PEC biosensors. To streamline PEC biosensing for a more POC-friendly format, we then explored if a similar response could be attained using DNA nano-spacers to program the signal response as opposed to Au NP density. Towards this end, ss-DNA probes of different lengths (15-mer (signal-on) and 20-mer (signal-off)) were used to modulate the probability of collision—and thus, direct electron transfer—between Au NP-labelled DNA targets and TiO<sub>2</sub> NPs on the electrode surface. These DNA signal-on and signal-off sensing channels were integrated onto a single device and operated at a single wavelength (397 nm) to create a differential *directly-labelled* DNA biosensor, which enhanced the device sensitivity and resulted in a remarkable limit of detection of 800 aM.

Despite the remarkable detection limit demonstrated by the previous strategy, direct labelling of bioanalytes is impractical in real world settings and contributes to sensitivity loss stemming from high backgrounds. In response to this, a new *single wavelength* PEC biosensing strategy featuring dynamic barcoded DNA motifs and differential signal generation—combining signals from two separate but

correlated binding events on the biosensor—was used to improve the limit-of-detection, as demonstrated by the LOD of 5 fM obtained using the differential strategy as compared to 73 fM using a single binding strategy; increase sensitivity, by greater than 3-times as compared to a single binding analogue; and enhance specificity (single-base mismatch) of PEC DNA biosensors in biological samples (urine). While the detection of spiked samples in complex matrices such as urine is not a trivial task, it however closely demonstrates—rather than represents—the detection of a biomolecular analyte from a clinically acquired sample.

As the next rational step in ushering molecular diagnostics closer to the POC, we investigated whether functional-DNA motifs, paralleled with the sensitivity and reliability of dual-signal transduction, could be used to achieve reagentless disease detection, directly in clinically sourced swine saliva samples. In response, we introduced a rapid (< 60 min), simple, non-invasive and reagent-less dual-electrode electrochemical (DEE) chip featuring a novel functional e-aptamer—aptamer sequences hybridized with a redox tagged (methylene-blue) biobarcode—for potential on-farm detection of porcine epidemic diarrhea virus (PEDv). This DEE-Chip successfully analyzed 91.6% (and 100% of all samples for  $C_t \leq 33.17$ ) of the clinical porcine saliva samples (sample volume of 12  $\mu\text{L}$ ) with a clinical sensitivity of 83% and a specificity of 100%, without target amplification, target enrichment, target labelling, or additional readout reagents. In conclusion, we have addressed the challenges presented in the ‘Motivation’ section of this thesis and have realized the rational development of ultrasensitive, dynamic, PEC and EC barcode-integrated diagnostics capable of reliably detecting biomolecular targets in complex biological matrices. These dynamic strategies integrate biorecognition and signal transduction, thus serving as tools to build POC molecular diagnostics.

## 8.2 Thesis Conclusions

- i. A facile solution-based method for developing P25-TiO<sub>2</sub>-based nanoparticles with increased light absorption and charge separation (i.e., through DHB), binding sites for attaching biorecognition probes (i.e., through aldehyde terminals), and built-in film-forming properties (i.e., through CHIT) for creating well-adhered and uniform photoactive frameworks on the photoelectrode was demonstrated. Optimized photoelectrodes augmented baseline photocurrent by a factor of 10, offered the required stability and signal magnitude to distinguish between complementary and noncomplementary DNA sequences, and demonstrated repeatable and stable photocurrents (Rsd ~ 5.40%) under cyclic operation (i.e., 10 cycles in 600 secs).
- ii. A series of Au NP loadings (134, 181, 433 and 623  $\mu\text{m}^{-2}$ ) were used to examine the surface coverage dependency of TiO<sub>2</sub> photocurrent generation mechanisms under visible (LSPR excitation; intraband carriers) and UV excitation (interband carriers). It was found that both current loss – due to reduced light absorption by TiO<sub>2</sub> – and gain – due to direct charge transfer between Au and TiO<sub>2</sub> NPs were possible under UV light. In contrast, under visible light illumination, strong light absorption and localized surface plasmon resonance of Au NPs and negligible light absorption by TiO<sub>2</sub> NPs led to signal gain with increasing Au NP surface concentrations. This study asserts that when gold is in direct contact with TiO<sub>2</sub>, there exists an optimal Au loading that can be exploited to program signal gain or signal attenuation by either varying excitation wavelength or local Au density.
- iii. Surface anchored oligonucleotides exhibit distinct dynamic mobilities (i.e., rotational, hinge) based on their conformational rigidity (single stranded (ss) versus double stranded (ds)). Exploiting this stochastic motion of anchored oligonucleotides, ss-DNA probes of different lengths (15-mer and 20-mer; individual channels) were used as nanospacers to predictively modulate direct electron transfer between Au NP-labelled DNA targets (25-mer) and TiO<sub>2</sub> NPs on the electrode surface. Furthermore, a theoretical model was put forth to predict collision probabilities incurred by the distance dependency of each channel (15-mer versus 20-mer) of the Au and TiO<sub>2</sub> NP system.
- iv. Harnessing the insight gained from the statistical model, a single wavelength (UV) and label (Au) operated differential PEC DNA biosensor was designed to predictively elicit both signal-on and signal-off responses on a single multiplexed chip. This rational differential design increased the device sensitivity by a factor of 1.5 or 3.2 compared to using only the 15-mer or

- 20-mer channels, respectively, and resulted in a remarkable limit of detection of 800 aM for DNA detection.
- v. A rationally designed PEC biosensor featuring dynamic barcoded DNA motifs and differential combinatorial signals, from two separate but correlated binding events on the device, enhanced the limit-of-detection—i.e., 5 fM using the differential strategy as compared to 73fM using a single binding strategy; sensitivity—i.e., greater than 3-times as compared to a single binding analogue; and specificity (single-base mismatch) of PEC DNA detection in biological samples (urine).
  - vi. A reagentless, label-free, dual-electrode electrochemical (DEE) PEDv aptasensor incorporating functional aptamers (i.e., electrochemically active biobarcode) and mass transport control strategies (i.e., reduced inter-electrode spacing and electrical field mediated transport) enabled faster kinetics and expedited assay operation (60 min). This DEE-Chip successfully analyzed 91.6% (and 100% of all samples for  $C_t \leq 33.17$ ) of the clinically sourced swine saliva with a clinical sensitivity of 83%, specificity of 100%, and an AUC > 0.83 (extracted from an ROC plot) in 60 minutes without target amplification and target enrichment; thus, fulfilling the need for a non-invasive PEDv sensor capable of potential on-farm operation.
  - vii. A series of signalling strategies—featuring dynamic barcoded DNA entities and dual-response capability—were introduced, with remarkable analytical performance in both buffer and complex non-invasive biological matrices (i.e., urine, saliva).

### **8.3 Contributions to the Field**

#### Engineering P25-TiO<sub>2</sub> with enhanced optical and film-forming properties for PEC biosensing

It is essential for photoelectrodes to demonstrate large baseline PEC currents to compensate for the signal loss induced by biofunctionalization, to demonstrate repeatable and stable photocurrents under cyclic scanning in liquid environments and enable facile functionalization for coupling with biorecognition elements. Chapter 3 delineates the rational design of the first one-pot, solution-based method of fabricating DHB-CHIT functionalized P25-TiO<sub>2</sub> photoactive electrodes to simultaneously increase the base current output, improve film-forming properties, enhance photonic absorption over the UV and visible wavelengths, enable facile biofunctionalization through aldehyde bearing terminals, offer the required stability and signal magnitude to distinguish between complementary and noncomplementary DNA sequences, and demonstrate repeatable and stable photocurrents under cyclic operation. In addition, the one-pot fabrication of high-performance, stable photoactive electrodes demonstrated here is important as the solution-based fabrication process presents a low-cost technique, to generate highly specialized materials using extremely simple techniques, making it suitable for low-resource settings and amenable to synthesis on an industrial scale. While the photoelectrodes developed using this method have been validated in PEC biosensing, the engineered P25-TiO<sub>2</sub> may also find its use in large-area photoactive coatings for energy harvesting, coatings for antibacterial applications and in photoelectrochemical and photochemical systems for water remediation. Furthermore, as catechol molecules demonstrate ultra strong adhesion to inorganic particles and surfaces<sup>673</sup>, this one-pot method of generating photoactive coatings may also be used to integrate other metal oxide species or a mixture of metal oxide species within the organic framework aside from P25-TiO<sub>2</sub>.

#### Examination of surface coverage density dependency in Au/TiO<sub>2</sub> systems

Understanding the different mechanisms responsible for photocurrent modulation at different frequencies is important for building optimized photoelectrochemical systems. Chapter 4 demonstrated the first examination of Au NP density on PEC current generation under two different light excitation modes using a single material system (Au/TiO<sub>2</sub>). Using a single materials system, a 540 nm excitation mode was used to probe the localized surface plasmon resonance (LSPR) of Au NPs, while an illumination wavelength of 397 nm probed the interband excitation of Au NPs in conjunction with the bandgap excitation of TiO<sub>2</sub> NPs. Based on the understanding gained, it was demonstrated that competitive photocurrent signal loss and enhancement mechanisms and their extent can be controlled by simply tuning the density of Au NPs on the electrode surface. Building on this, light-based toggling between interband (UV excitation) dominated and intraband (visible excitation) dominated regimes to drive ascorbic acid oxidation was demonstrated and the photocurrent generation efficiencies of these

two types of hot carriers was compared. Furthermore, this body of work proved that PEC sensing systems fuelled by interband carriers are more suited for applications harnessing the oxidation of reactant species to generate signal responses. By systematically studying and understanding that at certain Au NP density regimes, UV excitation yields signal-off responses while 540 nm excitation yields signal-on responses in the same system, a novel proof-of-concept DNA detection strategy was designed on the principle that a single material system (Au/TiO<sub>2</sub>) could be used to evoke both signal-off and signal-on responses on the same electrode, by simply tuning the excitation wavelength. This study, thus, allows photoelectrochemical systems to be tailored for programmable signal-off, signal-on, or ratiometric signalling by combining the former sensing modes to enhance the limit-of-detection.

#### Examination of spatial dependency in Au/TiO<sub>2</sub> systems

Surface anchored oligonucleotides exhibit distinct dynamic mobilities (i.e., rotational, hinge) based on their conformational rigidity (single stranded (ss) versus double stranded (ds)). Chapter 5 demonstrated the first use of ss-DNA probes of different lengths (15-mer and 20-mer; individual channels) as nanopacers to predictively modulate direct electron transfer between Au NP-labelled DNA targets (25-mer) and TiO<sub>2</sub> NPs on the photoelectrode surface using a single excitation wavelength. In this novel design, a larger portion of DNA nanopacers remain single-stranded following target binding (25-mer) on the 15-mer channel as compared to the 20-mer channel. As double-stranded DNA (dsDNA) is significantly more rigid than ss-DNA having the same number of nucleotides, a smaller average separation between the Au NP and TiO<sub>2</sub> surface (i.e., more collisional probability between Au and TiO<sub>2</sub> NP) is anticipated for the 15-mer channel as compared to the 20-mer channel; thus, yielding signal-on responses for the 15-mer channel and signal-off responses on the 20-mer channel. To further explain our experimental design, a theoretical model was put forth to predict collision probabilities incurred by the distance dependency of each channel (15-mer versus 20-mer) of the Au/TiO<sub>2</sub> NP system. The model further corroborated our experimental results. This study is critical as while spatial control of signal response using surface anchored oligonucleotides have been previously demonstrated using FRET, this has not been demonstrated in the context of Au/TiO<sub>2</sub> systems separated by biological spacers using PEC. Predictive tunability, evolved through the understanding of spatial dependency, using precisely separated Au/TiO<sub>2</sub> architectures unlocks the possibility for a whole new range of diagnostics operating on the principle of distance tailored programmable signal-off, signal-on, or ratiometric signalling. Additionally, the new understandings achieved here are expected to reach beyond the biosensing community with potential smart-switching applications in bio-circuits for molecular computing (logic gates)<sup>674</sup> using a new class of materials, DNA data storage using PEC (currently demonstrated using EC arrays<sup>675,676</sup>), for programmable environmental remediation, energy harvesting and in the construction of molecular motors<sup>677,678</sup> (using asymmetry, dimer architectures and oxidation of ascorbic acid as fuels).

#### Engineering spatially resolved predictive dual-signal biosensing in Au/TiO<sub>2</sub> systems

For PEC biosensors to be translated beyond laboratory settings, it is highly desirable for high sensitivity and specificity to be paralleled with facile operation and instrumentation. Biosensors featuring dual-signalling assays are particularly attractive, given their ability to reduce environmental contributions (i.e., interference and experimental variations), enhance detection accuracy at trace analyte concentrations, and improve analysis reliability. As such, the knowledge gained through the examination of spatial dependency in Au/TiO<sub>2</sub> was harnessed to design the first instance of a differential PEC biosensor featuring predictive dual-signal modulation (i.e., by exploiting 15-mer and 20-mer DNA spacers), using *a single* photoactive species (Au; label) and *single* excitation wavelength, to elicit both signal-on and signal-off responses on spatially resolved (adjacent) individual electrodes integrated on a single multiplexed chip. This differential design increased the PEC device sensitivity by a factor of 1.5 or 3.2 as compared to the 15-mer (signal-on sensor) or 20-mer channels (signal-off sensor), respectively, and resulted in a remarkable limit of detection of 800 aM for directly-labelled DNA detection in buffer. Given its performance and reliance on robust materials, we expect this dynamic differential PEC readout strategy to also be applicable to a wide range of electrochemical biosensing architectures where enzymes and redox species are currently used as labels. Furthermore, the changes in carrier dynamics (lifetime, flat-band modulation) with the modulation of spacer length and stability of the hybridized constructs were also examined and reported; thus, advancing the existing scientific repository for

designing PEC processes capitalizing on the degree of separation between metallic nanoparticles and semiconductive species in physically linked Au/TiO<sub>2</sub> systems. In addition to biosensing, chapter 5 effectively delineates the development of a novel tool to study the characteristics of dynamic DNA motifs—including persistence length effects and motional dynamics based on the ratio of ss-DNA to ds-DNA in DNA architectures—typically conducted previously using optical and electrochemical techniques. The new understandings achieved here are envisioned to reach beyond the biological sensing and synthetic biology community, generating wide interest within the photoelectrochemistry community. It is anticipated that the knowledge generated here could find applications in new smart switching materials for molecular computing, environmental remediation (of water and pathogens), futuristic data storage solutions and energy harvesting.

#### Single-electrode molecular diagnostic using predictive dual-signal modulation in Au/TiO<sub>2</sub> systems

Although it has been previously shown that dual signaling is possible using PEC readout, the handful of previously reported assays require multiple labels that are activated under different potentials or wavelengths adding to the assay complexity. In direct response, chapter 6 describes the *first* development of a novel Au/TiO<sub>2</sub> PEC biosensor featuring dynamic barcoded DNA motifs (signal-amplification) and combinatorial signal generation—from two separate but correlated binding events on the device—to enable dual-signal, *single-electrode, single-wavelength* operated differential DNA detection in both buffer and urine without target amplification, direct target labelling, or target enrichment. This differential strategy exhibited an enhanced limit-of-detection—i.e., 5 fM using the differential strategy as compared to 73 fM using a single binding strategy—and improved sensitivity—i.e., greater than 3-times as compared to a single binding analogue—of PEC DNA detection in biological samples (urine). Furthermore, this differential PEC biosensor also demonstrated superior DNA detection specificity (single-base mismatch) as compared to its non-differential counterparts. The strategy further stands apart from other sandwich designs by demonstrating a reverse signal-to-concentration effect, where the largest signals are obtained at the lowest concentrations. This allows high signal-to-noise ratios to be obtained at low concentrations often needed for trace clinical analysis, a feature that is not possible with traditional sandwich assays. Highly sensitive detection in spiked urine samples further highlights the potential use of this PEC sensing strategy for detection and monitoring of health biomarkers (such as nucleic acids) in non-invasive bio-fluids. Moreover, as metal tags are far more stable than redox species, the described Au-bearing biobarcode strategy overcomes limitations posed by traditional structure switching molecular probes featuring redox tags, i.e., the difficulty of identifying redox species that are stable and robust under complex biological or environmental conditions with varying oxygen levels, temperature, and pH. This advantage makes the Au/TiO<sub>2</sub> system devised in this study more suitable for building stable and programmable POC systems, potentially capable of in-vitro, in-situ and in-vivo signalling in environmentally diverse matrices (water, food matrices, biofluids, etc.). While sequential target association is used to build the current detection format, in the future, this design may be extended to real life analysis wherein DNA machines (DNAzymes, CRISPR-Cas systems, and strand displacement-based systems) can generate AuNP-tagged DNA in response to target analyte (nucleic acids, proteins, macromolecules and cells), as is currently done with fluorescent signal generation (DNA machines to generate a redox or fluorescent tag).

#### Non-invasive, dual-electrode, dual-signalling, EC aptasensor for PEDv detection in swine saliva

While aptamer-based reagent-less sensing has been previously demonstrated for bioanalytes using EC readout<sup>166,175,672</sup>, these assays often result in large background signals, even prior to target capture, due to the direct integration of redox labels on structure-switching aptamers anchored to the electrode surface. Alternatively, while aptamers relying on the displacement of a labelled single-stranded DNA strand for signal transduction offer more precise thermodynamic control by tuning the length and complementarity of the displacement strand,<sup>175,181,183–185</sup> such assays typically operate in a signal-off configuration<sup>184,185</sup> or carry a large background current in the few reported signal-on designs,<sup>183,186</sup> both prone to introducing errors in heterogeneous clinical samples that generate varying backgrounds. The biosensing strategy developed in chapter 7 overcomes these limitations by creating a reagent-free, signal-on, low background, dual-signalling sensor for detecting PEDv. This dual-electrode electrochemical (DEE) aptasensor is designed to house aptamers bound to a DNA barcode onto one

electrode and detect the released barcode on an adjacent electrode. The separation of the analyte capture and signal reporting on two different electrodes enables signal-on sensing, featuring large signal magnitude changes with almost no redox background in saliva. Mass transport enhancement strategies, such as reduction of inter-electrode spacing and electrical field mediated transport were effectively harnessed to overcome slow kinetics, enabling the dual-electrode sensor to discriminate between healthy and diseased samples from 12 clinically derived porcine oral fluids in 60 minutes without necessitating target labelling, amplification, or enrichment techniques; thus, fulfilling the need for a non-invasive PEDv sensor capable of potential on-farm operation. Furthermore, while this design has been demonstrated using N-PEDv aptamers to facilitate detection, the ease of thiol-based anchoring of bio-recognition elements onto Au electrodes makes it easy to interchange the aptamer sequence with other pathogen or bioanalyte specific aptamers. In essence, this study details the rational design of a universal aptamer-based platform, constructed to generate DNA barcodes from DNA machines (such as aptamers) for dual-signal, near-zero background detection. This platform may also be extended to PEC detection by swapping the redox-tagged biobarcode with a Au NP tagged biobarcode and replacing the Au electrodes with TiO<sub>2</sub> photoelectrodes.

### **8.5 Future Work**

This section discusses recommendations to extend the current scope of work, and theoretical ideas to solve critical challenges posed by the discoveries presented in this thesis.

#### *Eliminating variations from fabrication and biofunctionalization*

This study utilizes solution-based processing to make electrode fabrication amenable to low-cost processing. Current margins of error arising from benchtop, user-based deposition during biofunctionalized photoelectrode fabrication may be potentially minimized using automated controls and bioprinting to enable greater precision. Furthermore, in addition to implementing automated fabrication, it is critical to investigate effects of humidity during the solution-based deposition of photoactive species and the biorecognition moieties. Solution-based processing is often subject to edge effects (i.e., coffee ring effects)—where drop edges are pinned to the substrate, while radial outward capillary flow from the centre of the drop brings suspended particles to the edge, concentrating it as evaporation proceeds—during deposition, with changes in humidity contributing and viscosity to variability.<sup>679</sup> Gradients in surface tension, known as Marangoni effects<sup>680</sup>, enabled by auto-production<sup>681</sup> or exogenous addition<sup>682</sup> of surfactants, humidity cycling<sup>683</sup>, or temperature control<sup>684</sup> may be utilized to counteract such effects.

The use of strategies to minimize edge effects remain critical as variations in the number of photoactive species may result in fluctuations in baseline photocurrent while changes in the number of anchored biorecognition molecules may yield higher variability in the number of captured bio-analytes and, thus, affect the magnitude of signal readout. In this thesis, elevated deposition temperatures during photoelectrode fabrication<sup>684</sup>, signal reporting reliant on percentage changes against the baseline signal and differential signalling are used to combat such effects. However, it is the author's belief that studies optimizing, comparing and modelling the effects of humidity, temperature and the use of surfactants, alongside the implementation of automated controls are critical to reduce variability and further extend the limits of detection and device sensitivity.

#### *Enhancing analytical performance of PEC biosensing by tuning metal nanoparticle morphology*

In metal/metal oxide systems such as Au/TiO<sub>2</sub>, the generation of hot electrons is a surface scattering process, one largely influenced by the inhomogeneity of electromagnetic fields inside the plasmonic nanostructure.<sup>685</sup> Consequently, hot electron generation in such systems is significantly dependent on the shape<sup>686,687</sup> and size<sup>688,689</sup> of the metal nanocrystal. Generally, small metal nanoparticles demonstrate superior hot electron generation compared to large particles, while nanostars and nanocubes outperform nanorods and nanospheres in the generation of hot carriers.<sup>689,690</sup> Furthermore, plasmonic hot spots are believed to amplify hot electron generation, implying that dimers and meta-structures (decorated/textured surfaces) may be instrumental in enhancing the efficiency of hot electron generation. Based on these studies, decreasing the size of Au NPs (12 nm) used in this thesis and tuning

the shape of Au NPs—to structures presenting enhanced electric field effects (plasmonic hot spots) such as cubes, stars, urchins and/or pyramids—may improve hot electron generation, the resultant photocurrent and the detection limits of PEC biosensing. Furthermore, as the current size of Au NPs (12 nm) is large in comparison to the size of oligonucleotide sequences used in this work, decreasing the NP size may also improve assay kinetics (large size increases diffusion time) and enhance hybridization kinetics (steric effects decrease hybridization efficiency due to obstructed access). Given the potential benefits of tuning metal NP morphology, it is critical to construct rational studies correlating morphological changes to assay kinetics and performance.

#### *PEC detection of macromolecules (proteins, cells, large genomic sequences)*

A significant challenge presented by the Au/TiO<sub>2</sub> affinity-based signalling demonstrated in this thesis is the spatial dependency—i.e., Au NPs need to directly contact underlying TiO<sub>2</sub> NPs with statistically high probabilities to switch the system into a signal-on regime. While this architecture is suited for the detection of small molecule targets (i.e., microRNA) and shorter nucleic acid sequences, challenges arise when the current PEC design is applied to large biomolecular targets (i.e., proteins, enzymes, cells and genomic/chromosomal DNA). These targets bring with them, steric hindrance based signal loss, interference in signal response as target size supersedes that of the Au DNA barcode and weight induced non-specific signals as Au labels are forced to contact the underlying TiO<sub>2</sub> post hybridization.

In response to this, dual-electrode TiO<sub>2</sub> PEC biosensors comprising of a similar architecture to that demonstrated using the Au/MB system in chapter 7 (a barcode release channel and a barcode capture channel) may help subvert this limitation. Barcodes, hairpins, toe-hold mediated strand displacement constructs and other dynamic DNA motifs terminated with plasmonic metal labels such as Au may be utilized in conjunction with semiconductors such as TiO<sub>2</sub> to induce signal changes that can be directly or indirectly correlated bio-analyte concentration. These dynamic DNA constructs may overcome steric hindrance-based baseline loss, typically incurred with the use of antibody-antigen biorecognition elements, whilst simultaneously offering better stability and selectivity compared to these classes of bioreceptors.<sup>61,79</sup> Furthermore, in contrast to TiO<sub>2</sub> photoelectrodes biofunctionalized with highly flexible and mobile ss-DNA probes, DNA tetrahedron structures functionalized with dual ss-DNA probes may ensure the rigidity of DNA motifs, required to support large target binding, while simultaneously enabling the flexibility required by the Au NPs to directly contact the underlying TiO<sub>2</sub>. These tetrahedron structures offer more precise control of the spatial separation between the metal label and TiO<sub>2</sub> NP.

To enhance sensitivity of detection while ensuring single electrode operation, DNA motifs (i.e., DNazymes, aptamers) immobilized on magnetic or polymeric beads suspended in a reaction solution, in conjunction with magnetic field aided mixing, may be utilized to release multiple Au tagged barcodes following large molecule capture. As each bead has the capability to immobilize biorecognition elements superseding that of a planar surface, the effective binding affinity—and by extension the detection capability—for the bead will be higher than that of surface immobilized detection; thus, permitting efficient capture in 3-D of trace biomolecular targets.<sup>691</sup> Subsequently, the supernatant of this solution—comprised of Au-tagged barcodes—obtained following on-chip magnetic aided separation may be introduced onto a TiO<sub>2</sub> PEC biosensor to correlate barcode binding to target concentration. The extension of the current PEC design in the detection of large bio-molecules is thus, critical to furthering the versatility of the Au/TiO<sub>2</sub> platform developed in this thesis.

#### *Modelling competitive binding and target displacement to optimize response*

This work demonstrates an experimental approach to minimizing competitive performance losses incurred in the sandwich-like strategy—demonstrated using dynamic DNA motifs (Chapter 6)—by controlling hybridization time and measuring competitive hybridization losses using signal deviations as compared against the best-case scenarios. However, in contrast to this experimental approach, a mathematical model based on dual binding of surface immobilized nucleic acids, one that considers local nucleic acid concentration (with respect to available probe sites), salt concentration, temperature, binding affinities (which will need to be experimentally ascertained) and reversibility of binding, such

as that demonstrated in functional nucleic acid switches<sup>692</sup>, would be beneficial to understanding limitations and thresholds of this design.

#### Large scale clinical study of PEDv detection

The current study demonstrated in chapter 7 is a small-scale pre-clinical study (12 samples). To truly ascertain the accuracy and reproducibility of the PEDv DEE-Chip for clinical testing beyond a pilot-scale, it is critical to validate the device with significantly larger sample sizes (>500)<sup>693</sup>, ideally obtained from geographically diverse locations to minimize sampling bias. Geographically diverse data is critical as it challenges the detection capability of the biosensor (detects N-PEDv protein), in a manner independent of the disease strain and the resultant nucleocapsid protein mutations.

#### Multiplexed PEC and EC detection

Biomarkers such as microRNA (miRNA) hold great promise for disease detection (i.e., endometriosis, cancer, HIV and heart disease) owing to their abundance in biofluids such as urine and saliva; thus, enabling relatively non-invasive sample collection. In contrast to typical biomarkers (pathogenic proteins), the detection and quantification of a single miRNA sequence cannot be used as a hallmark of disease presence and progression; fluctuations in expression levels of multiple miRNAs—which are simultaneously altered during disease onset and progression—must be quantified and monitored. Furthermore, in contrast to singleplex detection, multiplexed POC assays that parallelly test for a panel of biomarkers/pathogens, can be used to distinguish between multiple diseases that present with similar symptoms. This parallelization further reduces the potential for false negative outcomes.

Diagnostics presenting multiplexed capability are thus, the inevitable next rational step of biosensor design. EC multiplexed detection may be enabled by chip and/or bead-based strategies incorporating multiple redox labels, or distinct positions of a single type of redox label immobilized on dynamic nucleic acid motifs (i.e., barcodes, hairpins, toe-hold mediated strand displacement constructs, etc.) to program variable signal responses for each individual target. Similarly, multiplexed PEC detection may be enabled by replacing redox labels with optical labels (i.e., dyes, semiconductive quantum dots, and plasmonic labels) for each individual target. Furthermore, metastructures, multiwavelength operation and bias-control may further the versatility of multiplexed detection. However, the incorporation of multiple signal reporters comes at the cost of increased complexity of signal actuation and calibration algorithms needed to address the large variety of signal baselines present prior to detection.

#### Combating non-specific binding in PEC

In the PEC systems highlighted in this thesis, signal generation is simultaneously reliant on contact between the Au NPs and TiO<sub>2</sub> NPs, the excitation of the underlying TiO<sub>2</sub> NPs, and adequate access of the electrolyte species to the photoelectrode surface. As such, non-specific binding at this PEC biosensor surface not only sterically hinders contact between the photoactive elements and limits electrolytic access to the photoelectrode, but also physically screens the excitation of the underlying TiO<sub>2</sub>. While the former may be experienced in similar EC analogues reliant on redox-tagged biobarcode for detection, the latter is notably absent as EC systems do not typically require optical excitation. As such, complex matrices presenting a higher probability of non-specific binding may be far more detrimental to PEC systems as compared to their EC counterparts. The existing passive antifouling strategies (chemical/electrostatic repulsion, physical spacing)<sup>694</sup> employed in EC may not adequately address the needs of a similar PEC system, inevitably resulting in baseline losses in complex matrices. Thus, there is a critical need to develop novel antifouling strategies combining photoactive actuation (to combat baseline losses), conductivity (to enable electron transfer between the metal and semiconductive particles), and physical spacing (to enable electrolytic access and biorecognition kinetics). Photoactive tetrahedrons and three-dimensional spacers featuring photoactive and conductive NPs and conductive polymers may present avenues to jointly realize these goals.

#### Addressing biosensor portability

It is of utmost importance to streamline assay operation (i.e., decrease auxiliary equipment) and minimize the reliance of the presented biosensor design on centralized power sources. The integration of EC and PEC biosensors with commercially available battery-operated, handheld analyzers capable

of amperometric, conductimetric and/or potentiometric analysis (i.e., Palmsens Emstat, smart phone technology, etc.) offers an avenue to realize portable, on-field analysis in remote and resource challenged locations. In addition, in-situ chemiluminescent<sup>695-697</sup> powered diagnostics present alternative elegant pathways to address the reliance of the current Au/TiO<sub>2</sub> design on external illumination sources.

### **8.6 Final Remarks**

The primary goal of this thesis is the development of ultrasensitive, dynamic, PEC and EC barcode-integrated biorecognition strategies—as tools to architect translatable POC molecular diagnostics—capable of reliably detecting biomolecular targets in complex biological matrices. Towards this end, interaction mechanisms between plasmonic NPs (Au) and semiconductive NPs (TiO<sub>2</sub>) were systematically investigated to develop programmable dual-signalling PEC strategies using DNA motifs. Previously unattainable predictive dual-signal modulation in PEC biosensing (in urine) using a single photoactive species (Au), single illumination regime (UV) and operated at a low bias-voltage (0 V) on a single chip, was demonstrated. Furthermore, this programmable feature was instrumental to the generation of a novel differential signaling strategy that enhanced sensitivity and signal-to-noise ratio. Dynamic DNA motifs bearing biobarcode (e-aptamers) were subsequently harnessed to realize successful, non-invasive, saliva-based detection of PEDv using a reagentless, label-free, dual-electrode electrochemical (DEE) aptasensor.

## References

1. United Nations Department of Economic and Social Affairs. *Population Division I World Population Prospects: The 2017 Revision, Key Findings and Advance Tables*. (2017).
2. Teresa, M. *et al.* Global, regional, and national comparative risk assessment of 79 behavioural, environmental and occupational, and metabolic risks or clusters of risks, 1990–2015: a systematic analysis for the Global Burden of Disease Study 2015. *The Lancet* **388**, 1659–1724 (2016).
3. World Health Organization. *Global Health Estimates 2020: Deaths by Cause, Age, Sex, by Country and by Region, 2000-2019*. . (2020).
4. Bhalla, N., Pan, Y., Yang, Z. & Payam, A. F. Opportunities and Challenges for Biosensors and Nanoscale Analytical Tools for Pandemics: COVID-19. *ACS Nano* **14**, 7783–7807 (2020).
5. Jones, K. E. *et al.* Global trends in emerging infectious diseases. *Nature* **451**, 990–993 (2008).
6. Hawkes, N. Cancer survival data emphasise importance of early diagnosis. *BMJ* **l408** (2019) doi:10.1136/bmj.l408.
7. Siegel, R. L., Miller, K. D. & Jemal, A. Cancer statistics, 2020. *CA: A Cancer Journal for Clinicians* **70**, 7–30 (2020).
8. Canadian Cancer Statistics Advisory Committee, Canadian Cancer Society, Statistics Canada & Public Health Agency of Canada. *Canadian Cancer Statistics 2021*. cancer.ca/Canadian-Cancer-Statistics-2021-EN (2021).
9. Tuttle, K. R. *et al.* Clinical Characteristics of and Risk Factors for Chronic Kidney Disease Among Adults and Children. *JAMA Network Open* **2**, e1918169 (2019).
10. Drawz, P. E. & Rosenberg, M. E. Slowing progression of chronic kidney disease. *Kidney International Supplements* **3**, 372–376 (2013).
11. Aletaha, D. & Smolen, J. S. Diagnosis and Management of Rheumatoid Arthritis. *JAMA* **320**, 1360 (2018).
12. Schneider, M. & Krüger, K. Rheumatoid Arthritis. *Deutsches Ärzteblatt international* (2013) doi:10.3238/arztebl.2013.0477.
13. Kabir, M. A., Zilouchian, H., Caputi, M. & Asghar, W. Advances in HIV diagnosis and monitoring. *Critical Reviews in Biotechnology* **40**, 623–638 (2020).
14. Wouters, O. J., O’Donoghue, D. J., Ritchie, J., Kanavos, P. G. & Narva, A. S. Early chronic kidney disease: diagnosis, management and models of care. *Nature Reviews Nephrology* **11**, 491–502 (2015).
15. Kumar, S. *et al.* Aspects of Point-of-Care Diagnostics for Personalized Health Wellness. *International Journal of Nanomedicine* **Volume 16**, 383–402 (2021).
16. Matthews, Q., da Silva, S. J. R., Norouzi, M., Pena, L. J. & Pardee, K. Adaptive, diverse and decentralized diagnostics are key to the future of outbreak response. *BMC Biology* **18**, 153 (2020).
17. Yager, P., Domingo, G. J. & Gerdes, J. Point-of-Care Diagnostics for Global Health. *Annual Review of Biomedical Engineering* **10**, 107–144 (2008).

18. Samb, B. *et al.* Prevention and management of chronic disease: a litmus test for health-systems strengthening in low-income and middle-income countries. *The Lancet* **376**, 1785–1797 (2010).
19. Metkar, S. K. & Girigoswami, K. Diagnostic biosensors in medicine – A review. *Biocatalysis and Agricultural Biotechnology* **17**, 271–283 (2019).
20. George Kerry, R. *et al.* A comprehensive review on the applications of nano-biosensor-based approaches for non-communicable and communicable disease detection. *Biomaterials Science* **9**, 3576–3602 (2021).
21. Qin, J., Wang, W., Gao, L. & Yao, S. Emerging Biosensing and Transducing Techniques for Potential Applications in Point-of-Care Diagnostics. *Chemical Science* (2022) doi:10.1039/D1SC06269G.
22. Kumar, S. *et al.* Aspects of Point-of-Care Diagnostics for Personalized Health Wellness. *International Journal of Nanomedicine* **Volume 16**, 383–402 (2021).
23. Grand View Research. *Biosensors Market Size, Share & Trends Analysis Report By Application (Medical, Agriculture, Environment) By Technology (Thermal, Electrochemical, Optical), By End-use, By Region, And Segment Forecasts, 2021 - 2028.* (2021).
24. Urdea, M. *et al.* Requirements for high impact diagnostics in the developing world. *Nature* **444**, 73–79 (2006).
25. Land, K. J., Boeras, D. I., Chen, X.-S., Ramsay, A. R. & Peeling, R. W. REASSURED diagnostics to inform disease control strategies, strengthen health systems and improve patient outcomes. *Nature Microbiology* **4**, 46–54 (2019).
26. Peeling, R. W., Holmes, K. K., Mabey, D. & Ronald, A. Rapid tests for sexually transmitted infections (STIs): the way forward. *Sexually Transmitted Infections* **82**, v1–v6 (2006).
27. Manocha, A. & Bhargava, S. Emerging challenges in point-of-care testing. *Current Medicine Research and Practice* **9**, 227–230 (2019).
28. Hosseini, A. *et al.* Roadmap to the Bioanalytical Testing of COVID-19: From Sample Collection to Disease Surveillance. *ACS Sensors* **5**, 3328–3345 (2020).
29. Ratanghayra, N. What Led to Reagent Shortages for Coronavirus Testing in the US? *Clinical Lab Manager* (2020).
30. Wiencek, J. & Nichols, J. Issues in the practical implementation of POCT: overcoming challenges. *Expert Review of Molecular Diagnostics* **16**, 415–422 (2016).
31. World Health Organization (WHO). Antigen-detection in the diagnosis of SARS-CoV-2 infection. in (WHO/2019-nCoV/Antigen\_Detection/2021.1, 2020).
32. Noh, J. Y. *et al.* Pipetting-based immunoassay for point-of-care testing: Application for detection of the influenza A virus. *Scientific Reports* **9**, 16661 (2019).
33. Koczula, K. M. & Gallotta, A. Lateral flow assays. *Essays in Biochemistry* **60**, 111–120 (2016).
34. Rabold, E. & Waggoner, J. Rapid Diagnostic Tests for Infectious Diseases. in *CDC Yellow Book 2020: Health Information for International Travel is published* (Centers for Disease Control and Prevention, 2020).
35. Dinnes, J. *et al.* Rapid, point-of-care antigen and molecular-based tests for diagnosis of SARS-CoV-2 infection. *Cochrane Database of Systematic Reviews* **2021**, (2021).

36. Corman, V. M. *et al.* Comparison of seven commercial SARS-CoV-2 rapid point-of-care antigen tests: a single-centre laboratory evaluation study. *The Lancet Microbe* **2**, e311–e319 (2021).
37. Möckel, M. *et al.* SARS-CoV-2 antigen rapid immunoassay for diagnosis of COVID-19 in the emergency department. *Biomarkers* **26**, 213–220 (2021).
38. Kelley, S. O. What Are Clinically Relevant Levels of Cellular and Biomolecular Analytes? *ACS Sensors* **2**, 193–197 (2017).
39. Bellassai, N., D'Agata, R., Jungbluth, V. & Spoto, G. Surface Plasmon Resonance for Biomarker Detection: Advances in Non-invasive Cancer Diagnosis. *Frontiers in Chemistry* **7**, (2019).
40. Cowling, T. & Dolcine, B. *Point-of-care testing*. (2017).
41. Aslan, B., Stemp, J., Yip, P. & Gun-Munro, J. Method Precision and Frequent Causes of Errors Observed in Point-of-Care Glucose Testing. *American Journal of Clinical Pathology* **142**, 857–863 (2014).
42. Sung, W.-H., Tsao, Y.-T., Shen, C.-J., Tsai, C.-Y. & Cheng, C.-M. Small-volume detection: platform developments for clinically-relevant applications. *Journal of Nanobiotechnology* **19**, 114 (2021).
43. Shrivastava, S., Trung, T. Q. & Lee, N.-E. Recent progress, challenges, and prospects of fully integrated mobile and wearable point-of-care testing systems for self-testing. *Chemical Society Reviews* **49**, 1812–1866 (2020).
44. van Norman, G. A. Drugs and Devices. *JACC: Basic to Translational Science* **1**, 399–412 (2016).
45. Genzen, J. R. Regulation of Laboratory-Developed Tests. *American Journal of Clinical Pathology* **152**, 122–131 (2019).
46. Nuzzo, J. *et al.* *Diagnosing Infection at the Point of Care*. (2013).
47. Morales, M. A. & Halpern, J. M. Guide to Selecting a Biorecognition Element for Biosensors. *Bioconjugate Chemistry* **29**, 3231–3239 (2018).
48. Sezgintürk, M. K. Introduction to commercial biosensors. in *Commercial Biosensors and Their Applications* 1–28 (Elsevier, 2020). doi:10.1016/B978-0-12-818592-6.00001-3.
49. Morales, M. A. & Halpern, J. M. Guide to Selecting a Biorecognition Element for Biosensors. *Bioconjugate Chemistry* **29**, 3231–3239 (2018).
50. Baryeh, K., Takalkar, S., Lund, M. & Liu, G. Introduction to medical biosensors for point of care applications. in *Medical Biosensors for Point of Care (POC) Applications* 3–25 (Elsevier, 2017). doi:10.1016/B978-0-08-100072-4.00001-0.
51. Cahn, T. M. Construction of Biosensors. in *Biosensors Volume 1 of Sensor Physics and Technology Series* vol. 1 (Springer Science & Business Media, 2007).
52. Zhong, Y. Electronic nose for food sensory evaluation. in *Evaluation Technologies for Food Quality* 7–22 (Elsevier, 2019). doi:10.1016/B978-0-12-814217-2.00002-0.
53. Rogers, K. R. Principles of Affinity-Based Biosensors. *Molecular Biotechnology* **14**, 109–130 (2000).

54. Chambers, J. P., Arulanandam, B. P., Matta, L. L., Weis, A. & Valdes, J. J. Biosensor recognition elements. *Curr Issues Mol Biol* **10**, 1–12 (2008).
55. Oue, S., Okamoto, A., Yano, T. & Kagamiyama, H. Redesigning the Substrate Specificity of an Enzyme by Cumulative Effects of the Mutations of Non-active Site Residues. *Journal of Biological Chemistry* **274**, 2344–2349 (1999).
56. Habimana, J. de D., Ji, J. & Sun, X. Minireview: Trends in Optical-Based Biosensors for Point-Of-Care Bacterial Pathogen Detection for Food Safety and Clinical Diagnostics. *Analytical Letters* **51**, 2933–2966 (2018).
57. Economou, A. *et al.* Enzyme-based Sensors. in *Advances in Food Diagnostics* 231–250 (John Wiley & Sons, Ltd, 2017). doi:10.1002/9781119105916.ch9.
58. Zhao, W.-W., Xu, J.-J. & Chen, H.-Y. Photoelectrochemical enzymatic biosensors. *Biosensors and Bioelectronics* **92**, 294–304 (2017).
59. Miller, E. & Sikes, H. D. Addressing Barriers to the Development and Adoption of Rapid Diagnostic Tests in Global Health. *Nanobiomedicine (Rij)* **2**, 6 (2015).
60. Iyer, P. v. & Ananthanarayan, L. Enzyme stability and stabilization—Aqueous and non-aqueous environment. *Process Biochemistry* **43**, 1019–1032 (2008).
61. Crivianu-Gaita, V. & Thompson, M. Aptamers, antibody scFv, and antibody Fab' fragments: An overview and comparison of three of the most versatile biosensor biorecognition elements. *Biosensors and Bioelectronics* **85**, 32–45 (2016).
62. Marinho, F. L. de O., Santos, N. L. de L., Neves, S. P. F. & Vasconcellos, L. de S. Performance evaluation of eight rapid tests to detect HIV infection: A comparative study from Brazil. *PLOS ONE* **15**, e0237438 (2020).
63. Han, M.-Y. *et al.* Evaluation of Lateral-Flow Assay for Rapid Detection of Influenza Virus. *BioMed Research International* **2020**, 1–16 (2020).
64. Moore, C. Point-of-care tests for infection control: should rapid testing be in the laboratory or at the front line? *Journal of Hospital Infection* **85**, 1–7 (2013).
65. Yin, X. *et al.* Commercial MPT64-based tests for rapid identification of Mycobacterium tuberculosis complex: A meta-analysis. *Journal of Infection* **67**, 369–377 (2013).
66. Blacksell, S. D. *et al.* The Comparative Accuracy of 8 Commercial Rapid Immunochromatographic Assays for the Diagnosis of Acute Dengue Virus Infection. *Clinical Infectious Diseases* **42**, 1127–1134 (2006).
67. Ouyang, M. *et al.* A review of biosensor technologies for blood biomarkers toward monitoring cardiovascular diseases at the point-of-care. *Biosensors and Bioelectronics* **171**, 112621 (2021).
68. Sharma, S., Byrne, H. & O'Kennedy, R. J. Antibodies and antibody-derived analytical biosensors. *Essays in Biochemistry* **60**, 9–18 (2016).
69. Kim, J., Campbell, A. S., de Ávila, B. E.-F. & Wang, J. Wearable biosensors for healthcare monitoring. *Nature Biotechnology* **37**, 389–406 (2019).
70. Apetrei, C. & Ghasemi-Varnamkhasi, M. Biosensors in Food PDO Authentication. in 279–297 (2013). doi:10.1016/B978-0-444-59562-1.00011-6.
71. Gubala, V., Harris, L. F., Ricco, A. J., Tan, M. X. & Williams, D. E. Point of Care Diagnostics: Status and Future. *Analytical Chemistry* **84**, 487–515 (2012).

72. Gooding, J. J. Electrochemical DNA Hybridization Biosensors. *Electroanalysis* **14**, 1149–1156 (2002).
73. Shen, M. *et al.* Recent advances and perspectives of nucleic acid detection for coronavirus. *Journal of Pharmaceutical Analysis* **10**, 97–101 (2020).
74. Ho, T. H., Guillon, F.-X., Bigey, P., Bedioui, F. & Lazerges, M. Analysis of the evolution of the detection limits of electrochemical nucleic acid biosensors II. *Analytical and Bioanalytical Chemistry* **409**, 4335–4352 (2017).
75. Zhang, J. Y., Bender, A. T., Boyle, D. S., Drain, P. K. & Posner, J. D. Current state of commercial point-of-care nucleic acid tests for infectious diseases. *Analyst* **146**, 2449–2462 (2021).
76. Henihan, G. *et al.* Label- and amplification-free electrochemical detection of bacterial ribosomal RNA. *Biosensors and Bioelectronics* **81**, 487–494 (2016).
77. D’Agata, R., Giuffrida, M. & Spoto, G. Peptide Nucleic Acid-Based Biosensors for Cancer Diagnosis. *Molecules* **22**, 1951 (2017).
78. Tuerk, C. & Gold, L. Systematic evolution of ligands by exponential enrichment: RNA ligands to bacteriophage T4 DNA polymerase. *Science (1979)* **249**, (1990).
79. McConnell, E. M., Cozma, I., Morrison, D. & Li, Y. Biosensors made of synthetic functional nucleic acids toward better human health. *Analytical Chemistry* vol. 92 (2020).
80. Breaker, R. R. Natural and engineered nucleic acids as tools to explore biology. *Nature* **432**, 838–845 (2004).
81. Kammer, M. N. *et al.* Quantification of opioids in urine using an aptamer-based free-solution assay. *Analytical Chemistry* **91**, (2019).
82. Swensen, J. S. *et al.* Continuous, real-time monitoring of cocaine in undiluted blood serum via a microfluidic, electrochemical aptamer-based sensor. *J Am Chem Soc* **131**, (2009).
83. Baird, G. S. Where Are All the Aptamers? *American Journal of Clinical Pathology* **134**, 529–531 (2010).
84. Maimaitiyiming, Y., Hong, D. F., Yang, C. & Naranmandura, H. Novel insights into the role of aptamers in the fight against cancer. *Journal of Cancer Research and Clinical Oncology* **145**, 797–810 (2019).
85. Narita, F. *et al.* A Review of Piezoelectric and Magnetostrictive Biosensor Materials for Detection of COVID-19 and Other Viruses. *Advanced Materials* **33**, 2005448 (2021).
86. Pradhan, A. *et al.* Biosensors as Nano-Analytical Tools for COVID-19 Detection. *Sensors* **21**, 7823 (2021).
87. Skládal, P. Piezoelectric biosensors. *TrAC Trends in Analytical Chemistry* **79**, 127–133 (2016).
88. Pohanka, M. Overview of Piezoelectric Biosensors, Immunosensors and DNA Sensors and Their Applications. *Materials* **11**, 448 (2018).
89. Saylan, Y., Erdem, Ö., Ünal, S. & Denizli, A. An Alternative Medical Diagnosis Method: Biosensors for Virus Detection. *Biosensors (Basel)* **9**, 65 (2019).
90. Tombelli, S. Piezoelectric biosensors for medical applications. in *Biosensors for Medical Applications* 41–64 (Woodhead Publishing, 2012). doi:10.1533/9780857097187.1.41.

91. Pashchenko, O., Shelby, T., Banerjee, T. & Santra, S. A Comparison of Optical, Electrochemical, Magnetic, and Colorimetric Point-of-Care Biosensors for Infectious Disease Diagnosis. *ACS Infectious Diseases* **4**, 1162–1178 (2018).
92. Xianyu, Y., Wang, Q. & Chen, Y. Magnetic particles-enabled biosensors for point-of-care testing. *TrAC Trends in Analytical Chemistry* **106**, 213–224 (2018).
93. Su, D., Wu, K., Saha, R., Peng, C. & Wang, J.-P. Advances in Magnetoresistive Biosensors. *Micromachines (Basel)* **11**, 34 (2019).
94. Reisbeck, M. *et al.* Magnetic fingerprints of rolling cells for quantitative flow cytometry in whole blood. *Scientific Reports* **6**, 32838 (2016).
95. Osterfeld, S. J. *et al.* Multiplex protein assays based on real-time magnetic nanotag sensing. *Proceedings of the National Academy of Sciences* **105**, 20637–20640 (2008).
96. Gaster, R. S. *et al.* Matrix-insensitive protein assays push the limits of biosensors in medicine. *Nature Medicine* **15**, 1327–1332 (2009).
97. Liong, M. *et al.* Magnetic barcode assay for genetic detection of pathogens. *Nature Communications* **4**, 1752 (2013).
98. Peltomaa, R., Glahn-Martínez, B., Benito-Peña, E. & Moreno-Bondi, M. Optical Biosensors for Label-Free Detection of Small Molecules. *Sensors* **18**, 4126 (2018).
99. Khansili, N., Rattu, G. & Krishna, P. M. Label-free optical biosensors for food and biological sensor applications. *Sensors and Actuators B: Chemical* **265**, 35–49 (2018).
100. Kassal, P., Horak, E., Sigurnjak, M., Steinberg, M. D. & Steinberg, I. M. Wireless and mobile optical chemical sensors and biosensors. *Reviews in Analytical Chemistry* **37**, (2018).
101. Sadeghi, P. *et al.* Lateral flow assays (LFA) as an alternative medical diagnosis method for detection of virus species: The intertwine of nanotechnology with sensing strategies. *TrAC Trends in Analytical Chemistry* **145**, 116460 (2021).
102. Mahmoudi, T., de la Guardia, M. & Baradaran, B. Lateral flow assays towards point-of-care cancer detection: A review of current progress and future trends. *TrAC Trends in Analytical Chemistry* **125**, 115842 (2020).
103. Chen, Y. *et al.* Quantitative Fluorescence Spectroscopy in Turbid Media: A Practical Solution to the Problem of Scattering and Absorption. *Analytical Chemistry* **85**, 2015–2020 (2013).
104. McGrath, M. J. & Scanaill, C. N. Sensing and Sensor Fundamentals. in *Sensor Technologies* 15–50 (Apress, 2013). doi:10.1007/978-1-4302-6014-1\_2.
105. Nguyen, V.-T., Song, S., Park, S. & Joo, C. Recent advances in high-sensitivity detection methods for paper-based lateral-flow assay. *Biosensors and Bioelectronics* **152**, 112015 (2020).
106. Naresh, Varnakavi. & Lee, N. A Review on Biosensors and Recent Development of Nanostructured Materials-Enabled Biosensors. *Sensors* **21**, 1109 (2021).
107. Eggins, B. R. Transducers I—Electrochemistry. in 51–86 (1996). doi:10.1007/978-3-663-05664-5\_4.
108. Yoo, E.-H. & Lee, S.-Y. Glucose Biosensors: An Overview of Use in Clinical Practice. *Sensors* **10**, 4558–4576 (2010).

109. Ronkainen, N. J., Halsall, H. B. & Heineman, W. R. Electrochemical biosensors. *Chemical Society Reviews* **39**, 1747 (2010).
110. Yang, A. & Yan, F. Flexible Electrochemical Biosensors for Health Monitoring. *ACS Applied Electronic Materials* **3**, 53–67 (2021).
111. Wang, J. Electrochemical biosensors: Towards point-of-care cancer diagnostics. *Biosensors and Bioelectronics* **21**, 1887–1892 (2006).
112. Ng, W. L., Short, T. G., Gunn, K. N., Fuge, G. S. & Slon, B. Accuracy and Reliability of the i-STAT Point-of-Care Device for the Determination of Haemoglobin Concentration before and after Major Blood Loss. *Anaesthesia and Intensive Care* **42**, 495–499 (2014).
113. Luukkonen, A. A. M., Lehto, T. M., Hedberg, P. S. M. & Vaskivuo, T. E. Evaluation of a hand-held blood gas analyzer for rapid determination of blood gases, electrolytes and metabolites in intensive care setting. *Clinical Chemistry and Laboratory Medicine (CCLM)* **54**, (2016).
114. Dedeoglu, A., Kaya, S. I., Bakirhan, N. K. & Ozkan, S. A. Nanotechnological approaches and materials in commercial biosensors. in *Commercial Biosensors and Their Applications* 301–353 (Elsevier, 2020). doi:10.1016/B978-0-12-818592-6.00012-8.
115. Fan, J. *et al.* Clinical Value of Combined Detection of CK-MB, MYO, cTnI and Plasma NT-proBNP in Diagnosis of Acute Myocardial Infarction. *Clinical Laboratory* **63**, (2017).
116. Chen, C. & Wang, J. Optical biosensors: an exhaustive and comprehensive review. *Analyst* **145**, 1605–1628 (2020).
117. Ronkainen-Matsuno, N. J., Thomas, J. H., Halsall, H. B. & Heineman, W. R. Electrochemical immunoassay moving into the fast lane. *TrAC Trends in Analytical Chemistry* **21**, 213–225 (2002).
118. Huang, X.-J., O'Mahony, A. M. & Compton, R. G. Microelectrode Arrays for Electrochemistry: Approaches to Fabrication. *Small* **5**, 776–788 (2009).
119. Lin, Y., Lu, F., Tu, Y. & Ren, Z. Glucose Biosensors Based on Carbon Nanotube Nanoelectrode Ensembles. *Nano Letters* **4**, 191–195 (2004).
120. Arrigan, D. W. M. Nanoelectrodes, nanoelectrode arrays and their applications. *Analyst* **129**, 1157 (2004).
121. Wei, D., Bailey, M. J. A., Andrew, P. & Ryhänen, T. Electrochemical biosensors at the nanoscale. *Lab on a Chip* **9**, 2123 (2009).
122. Heller, I. *et al.* Individual Single-Walled Carbon Nanotubes as Nanoelectrodes for Electrochemistry. *Nano Letters* **5**, 137–142 (2005).
123. Stratmann, L., Heery, B. & Coffey, B. Embedded Electrochemistry with a Miniaturized, Software-Enabled, Potentiostat System on Module. *EmStat Pico* (2019).
124. Zumbärgel, B. *Electrochemistry A workbook for 910 PSTAT mini.* <https://www.metrohm.com/en/products/electrochemistry/portable-potentiostats/> (2013).
125. Liu, J. *et al.* Development of a microchip Europium nanoparticle immunoassay for sensitive point-of-care HIV detection. *Biosensors and Bioelectronics* **61**, 177–183 (2014).
126. Dhanapala, L., Jones, A. L., Czarnecki, P. & Rusling, J. F. Sub-zptomole Detection of Biomarker Proteins Using a Microfluidic Immunoarray with Nanostructured Sensors. *Analytical Chemistry* **92**, 8021–8025 (2020).

127. Zhao, W.-W., Xu, J.-J. & Chen, H.-Y. Photoelectrochemical DNA Biosensors. *Chemical Reviews* **114**, 7421–7441 (2014).
128. Bard, A. J. Photoelectrochemistry Bard.pdf. *Science* vol. 207 139–144 (1980).
129. Peter, L. M. CHAPTER 1. Photoelectrochemistry: From Basic Principles to Photocatalysis. in *Royal Society of Chemistry* 1–28 (2016). doi:10.1039/9781782622338-00001.
130. Jiang, C., Moniz, S. J. A., Wang, A., Zhang, T. & Tang, J. Photoelectrochemical devices for solar water splitting-materials and challenges. *Chemical Society Reviews* **46**, 4645–4660 (2017).
131. Gratzel, M. Photoelectrochemical cells. *Nature; London* (2001) doi:10.1038/35104607.
132. Shu, J. & Tang, D. Recent Advances in Photoelectrochemical Sensing: From Engineered Photoactive Materials to Sensing Devices and Detection Modes. *Analytical Chemistry* **92**, 363–377 (2020).
133. Li, M. *et al.* Ultrasensitive Photoelectrochemical Biosensor Based on DNA Tetrahedron as Nanocarrier for Efficient Immobilization of CdTe QDs-Methylene Blue as Signal Probe with Near-Zero Background Noise. *Analytical Chemistry* **90**, 8211–8216 (2018).
134. Zhou, Q. & Tang, D. Recent advances in photoelectrochemical biosensors for analysis of mycotoxins in food. *TrAC Trends in Analytical Chemistry* **124**, 115814 (2020).
135. Zhang, Q. *et al.* Smartphone-based photoelectrochemical biosensing system with graphitic carbon nitride/gold nanoparticles modified electrodes for matrix metalloproteinase-2 detection. *Biosensors and Bioelectronics* **193**, 113572 (2021).
136. Hao, N., Hua, R., Zhang, K., Lu, J. & Wang, K. A Sunlight Powered Portable Photoelectrochemical Biosensor Based on a Potentiometric Resolved Ratiometric Principle. *Analytical Chemistry* **90**, 13207–13211 (2018).
137. Qiu, Z., Shu, J., Liu, J. & Tang, D. Dual-Channel Photoelectrochemical Ratiometric Aptasensor with up-Converting Nanocrystals Using Spatial-Resolved Technique on Homemade 3D Printed Device. *Analytical Chemistry* **91**, 1260–1268 (2019).
138. Vallée-Bélisle, A. & Plaxco, K. W. Structure-switching biosensors: inspired by Nature. *Current Opinion in Structural Biology* **20**, 518–526 (2010).
139. Porchetta, A. *et al.* Programmable Nucleic Acid Nanoswitches for the Rapid, Single-Step Detection of Antibodies in Bodily Fluids. *J Am Chem Soc* **140**, 947–953 (2018).
140. Klein, D. Quantification using real-time PCR technology: applications and limitations. *Trends in Molecular Medicine* **8**, 257–260 (2002).
141. Sharma, A. *et al.* Optical Biosensors for Diagnostics of Infectious Viral Disease: A Recent Update. *Diagnostics* **11**, 2083 (2021).
142. Mollarasouli, Kurbanoglu & Ozkan. The Role of Electrochemical Immunosensors in Clinical Analysis. *Biosensors (Basel)* **9**, 86 (2019).
143. Victorious, A., Saha, S., Pandey, R., Didar, T. F. & Soleymani, L. Affinity-Based Detection of Biomolecules Using Photo-Electrochemical Readout. *Frontiers in Chemistry* **7**, (2019).
144. Lubin, A. A. & Plaxco, K. W. Folding-Based Electrochemical Biosensors: The Case for Responsive Nucleic Acid Architectures. *Accounts of Chemical Research* **43**, 496–505 (2010).

145. Rashid, J. I. A. & Yusof, N. A. The strategies of DNA immobilization and hybridization detection mechanism in the construction of electrochemical DNA sensor: A review. *Sens Biosensing Res* **16**, 19–31 (2017).
146. Victorious, A., Clifford, A., Saha, S., Zhitomirsky, I. & Soleymani, L. Integrating TiO<sub>2</sub> Nanoparticles within a Catecholic Polymeric Network Enhances the Photoelectrochemical Response of Biosensors. *The Journal of Physical Chemistry C* **123**, 16186–16193 (2019).
147. Sakib, S., Pandey, R., Soleymani, L. & Zhitomirsky, I. Surface modification of TiO<sub>2</sub> for photoelectrochemical DNA biosensors. *MEDICAL DEVICES & SENSORS* **3**, (2020).
148. Saha, S., Chan, Y. & Soleymani, L. Enhancing the Photoelectrochemical Response of DNA Biosensors Using Wrinkled Interfaces. *ACS Applied Materials & Interfaces* **10**, 31178–31185 (2018).
149. Honorato Castro, A. C. *et al.* Preparation of genosensor for detection of specific DNA sequence of the hepatitis B virus. *Applied Surface Science* **314**, 273–279 (2014).
150. Zhang, X., Zhao, Y., Li, S. & Zhang, S. Photoelectrochemical biosensor for detection of adenosine triphosphate in the extracts of cancer cells. *Chemical Communications* **46**, 9173 (2010).
151. Fojta, M. *et al.* Two-Surface Strategy in Electrochemical DNA Hybridization Assays: Detection of Osmium-Labeled Target DNA at Carbon Electrodes. *Electroanalysis* **15**, 431–440 (2003).
152. Zhao, W.-W. *et al.* Exciton-Plasmon Interactions between CdS Quantum Dots and Ag Nanoparticles in Photoelectrochemical System and Its Biosensing Application. *Analytical Chemistry* **84**, 5892–5897 (2012).
153. Kokkinos, C., Prodromidis, M., Economou, A., Petrou, P. & Kakabakos, S. Quantum dot-based electrochemical DNA biosensor using a screen-printed graphite surface with embedded bismuth precursor. *Electrochemistry Communications* **60**, 47–51 (2015).
154. Tokudome, H. *et al.* Photoelectrochemical deoxyribonucleic acid sensing on a nanostructured TiO<sub>2</sub> electrode. *Applied Physics Letters* **87**, 213901 (2005).
155. Karadeniz, H. *et al.* Electrochemical sensing of silver tags labelled DNA immobilized onto disposable graphite electrodes. *Electrochemistry Communications* **9**, 2167–2173 (2007).
156. Cui, L. *et al.* Construction of a Dye-Sensitized and Gold Plasmon-Enhanced Cathodic Photoelectrochemical Biosensor for Methyltransferase Activity Assay. *Analytical Chemistry* **93**, 10310–10316 (2021).
157. Guo, J., Oshikiri, T., Ueno, K., Shi, X. & Misawa, H. Plasmon-induced photoelectrochemical biosensor for in situ real-time measurement of biotin-streptavidin binding kinetics under visible light irradiation. *Analytica Chimica Acta* **957**, 70–75 (2017).
158. Zhao, W.-W., Ma, Z.-Y., Yan, D.-Y., Xu, J.-J. & Chen, H.-Y. *In Situ* Enzymatic Ascorbic Acid Production as Electron Donor for CdS Quantum Dots Equipped TiO<sub>2</sub> Nanotubes: A General and Efficient Approach for New Photoelectrochemical Immunoassay. *Analytical Chemistry* **84**, 10518–10521 (2012).
159. Magriñá, I. *et al.* Electrochemical genosensor for the direct detection of tailed PCR amplicons incorporating ferrocene labelled dATP. *Biosensors and Bioelectronics* **134**, 76–82 (2019).
160. Zhao, W.-W., Xu, J.-J. & Chen, H.-Y. Photoelectrochemical bioanalysis: the state of the art. *Chemical Society Reviews* **44**, 729–741 (2015).

161. Drummond, T. G., Hill, M. G. & Barton, J. K. Electrochemical DNA sensors. *Nature Biotechnology* **21**, 1192–1199 (2003).
162. Giljohann, D. A. & Mirkin, C. A. Drivers of biodiagnostic development. *Nature* **462**, 461–464 (2009).
163. Dwivedi, S. *et al.* Diseases and Molecular Diagnostics: A Step Closer to Precision Medicine. *Indian Journal of Clinical Biochemistry* **32**, 374–398 (2017).
164. Cammaerts, S., Strazisar, M., de Rijk, P. & del Favero, J. Genetic variants in microRNA genes: impact on microRNA expression, function, and disease. *Frontiers in Genetics* **6**, (2015).
165. Zhang, Y. *et al.* Dynamic DNA Structures. *Small* **15**, 1900228 (2019).
166. White, R. J., Rowe, A. A. & Plaxco, K. W. Re-engineering aptamers to support reagentless, self-reporting electrochemical sensors. *Analyst* **135**, 589 (2010).
167. Li, C. *et al.* Design of DNA nanostructure-based interfacial probes for the electrochemical detection of nucleic acids directly in whole blood. *Chemical Science* **9**, 979–984 (2018).
168. Wang, L., Fang, L. & Liu, S. Responsive hairpin DNA aptamer switch to program the strand displacement reaction for the enhanced electrochemical assay of ATP. *Analyst* **140**, 5877–5880 (2015).
169. Zang, Y. *et al.* Dual-functional  $\beta$ -CD@CdS nanorod/WS2 nanosheet heterostructures coupled with strand displacement reaction-mediated photocurrent quenching for an ultrasensitive MicroRNA-21 assay. *Electrochimica Acta* **334**, 135581 (2020).
170. Wang, H. *et al.* Signal-off photoelectrochemical aptasensor for kanamycin: Strand displacement reaction combines p-n competition. *Analytica Chimica Acta* **1181**, 338927 (2021).
171. Taghdisi, S. M. *et al.* A novel electrochemical aptasensor based on nontarget-induced high accumulation of methylene blue on the surface of electrode for sensing of  $\alpha$ -synuclein oligomer. *Biosensors and Bioelectronics* **123**, 14–18 (2019).
172. Baek, S., Ahn, J. K., Won, B. Y., Park, K. S. & Park, H. G. A one-step and label-free, electrochemical DNA detection using metal ion-mediated molecular beacon probe. *Electrochemistry Communications* **100**, 64–69 (2019).
173. Xiao, Y., Lubin, A. A., Baker, B. R., Plaxco, K. W. & Heeger, A. J. Single-step electronic detection of femtomolar DNA by target-induced strand displacement in an electrode-bound duplex. *Proceedings of the National Academy of Sciences* **103**, 16677–16680 (2006).
174. Chen, Z. *et al.* Proximity recognition and polymerase-powered DNA walker for one-step and amplified electrochemical protein analysis. *Biosensors and Bioelectronics* **128**, 104–112 (2019).
175. Feagin, T. A., Maganzini, N. & Soh, H. T. Strategies for Creating Structure-Switching Aptamers. *ACS Sensors* **3**, 1611–1615 (2018).
176. Xiao, Y., Uzawa, T., White, R. J., DeMartini, D. & Plaxco, K. W. On the Signaling of Electrochemical Aptamer-Based Sensors: Collision- and Folding-Based Mechanisms. *Electroanalysis* **21**, 1267–1271 (2009).
177. Xiao, Y., Lubin, A. A., Heeger, A. J. & Plaxco, K. W. Label-Free Electronic Detection of Thrombin in Blood Serum by Using an Aptamer-Based Sensor. *Angewandte Chemie International Edition* **44**, 5456–5459 (2005).

178. Liu, D.-Y., Zhao, Y., He, X.-W. & Yin, X.-B. Electrochemical aptasensor using the tripropylamine oxidation to probe intramolecular displacement between target and complementary nucleotide for protein array. *Biosensors and Bioelectronics* **26**, 2905–2910 (2011).
179. Huang, R. *et al.* A Sensitive Aptasensor Based on a Hemin/G-Quadruplex-Assisted Signal Amplification Strategy for Electrochemical Detection of Gastric Cancer Exosomes. *Small* **15**, 1900735 (2019).
180. Xu, G. *et al.* Branched hybridization chain reaction—using highly dimensional DNA nanostructures for label-free, reagent-less, multiplexed molecular diagnostics. *Microsystems & Nanoengineering* **5**, 37 (2019).
181. Tang, Z. *et al.* Aptamer Switch Probe Based on Intramolecular Displacement. *J Am Chem Soc* **130**, 11268–11269 (2008).
182. Ilgu, M. & Nilsen-Hamilton, M. Aptamers in analytics. *Analyst* **141**, 1551–1568 (2016).
183. Xiao, Y., Piorek, B. D., Plaxco, K. W. & Heeger, A. J. A Reagentless Signal-On Architecture for Electronic, Aptamer-Based Sensors via Target-Induced Strand Displacement. *J Am Chem Soc* **127**, 17990–17991 (2005).
184. Liu, R. *et al.* Signaling-Probe Displacement Electrochemical Aptamer-based Sensor (SD-EAB) for Detection of Nanomolar Kanamycin A. *Electrochimica Acta* **182**, 516–523 (2015).
185. Feng, K. *et al.* Label-free electrochemical detection of nanomolar adenosine based on target-induced aptamer displacement. *Electrochemistry Communications* **10**, 531–535 (2008).
186. Xiao, Y., Qu, X., Plaxco, K. W. & Heeger, A. J. Label-Free Electrochemical Detection of DNA in Blood Serum via Target-Induced Resolution of an Electrode-Bound DNA Pseudoknot. *J Am Chem Soc* **129**, 11896–11897 (2007).
187. Zhang, Z., Tao, C., Yin, J., Wang, Y. & Li, Y. Enhancing the response rate of strand displacement-based electrochemical aptamer sensors using bivalent binding aptamer-cDNA probes. *Biosensors and Bioelectronics* **103**, 39–44 (2018).
188. Zang, Y., Lei, J. & Ju, H. Principles and applications of photoelectrochemical sensing strategies based on biofunctionalized nanostructures. *Biosensors and Bioelectronics* **96**, 8–16 (2017).
189. Lee, I. *et al.* A self-calibrating electrochemical aptasensing platform: Correcting external interference errors for the reliable and stable detection of avian influenza viruses. *Biosensors and Bioelectronics* **152**, 112010 (2020).
190. Yang, W. & Lai, R. Y. Integration of two different sensing modes in an electrochemical DNA sensor for approximation of target mismatch location. *Electrochemistry Communications* **13**, 989–992 (2011).
191. Hou, T., Wang, X., Liu, X., Pan, C. & Li, F. Sensitive electrochemical assay for T4 polynucleotide kinase activity based on dual-signaling amplification coupled with exonuclease reaction. *Sensors and Actuators B: Chemical* **202**, 588–593 (2014).
192. Cao, X. *et al.* A new dual-signalling electrochemical aptasensor with the integration of “signal on/off” and “labeling/label-free” strategies. *Sensors and Actuators B: Chemical* **239**, 166–171 (2017).
193. Wu, L., Zhang, X., Liu, W., Xiong, E. & Chen, J. Sensitive Electrochemical Aptasensor by Coupling “Signal-on” and “Signal-off” Strategies. *Analytical Chemistry* **85**, 8397–8402 (2013).

194. Du, Y. *et al.* Reagentless, Ratiometric Electrochemical DNA Sensors with Improved Robustness and Reproducibility. *Analytical Chemistry* **86**, 8010–8016 (2014).
195. Hao, N., Hua, R., Zhang, K., Lu, J. & Wang, K. A Sunlight Powered Portable Photoelectrochemical Biosensor Based on a Potentiometric Resolved Ratiometric Principle. *Analytical Chemistry* **90**, 13207–13211 (2018).
196. Hao, Q. *et al.* A wavelength-resolved ratiometric photoelectrochemical technique: design and sensing applications. *Chemical Science* **7**, 774–780 (2016).
197. Zheng, Y.-N. *et al.* Universal Ratiometric Photoelectrochemical Bioassay with Target-Nucleotide Transduction-Amplification and Electron-Transfer Tunneling Distance Regulation Strategies for Ultrasensitive Determination of microRNA in Cells. *Analytical Chemistry* **89**, 9445–9451 (2017).
198. Yang, H. *et al.* Donor/Acceptor-Induced Ratiometric Photoelectrochemical Paper Analytical Device with a Hollow Double-Hydrophilic-Walls Channel for microRNA Quantification. *Analytical Chemistry* **91**, 14577–14585 (2019).
199. Yang, Y., Yang, J., He, Y. & Li, Y. A dual-signal mode ratiometric photoelectrochemical sensor based on voltage-resolved strategy for glucose detection. *Sensors and Actuators B: Chemical* **330**, 129302 (2021).
200. Hua, R. *et al.* A sensitive Potentiometric resolved ratiometric Photoelectrochemical aptasensor for Escherichia coli detection fabricated with non-metallic nanomaterials. *Biosensors and Bioelectronics* **106**, 57–63 (2018).
201. Zhang, Y. *et al.* A potentiometric resolved ratiometric photoelectrochemical aptasensor. *Chemical Communications* **53**, 5810–5813 (2017).
202. Achermann, M. Exciton–Plasmon Interactions in Metal–Semiconductor Nanostructures. *The Journal of Physical Chemistry Letters* **1**, 2837–2843 (2010).
203. Zhao, W.-W. *et al.* Exciton-Plasmon Interactions between CdS Quantum Dots and Ag Nanoparticles in Photoelectrochemical System and Its Biosensing Application. *Analytical Chemistry* **84**, 5892–5897 (2012).
204. Pu, Y.-C. *et al.* Au Nanostructure-Decorated TiO<sub>2</sub> Nanowires Exhibiting Photoactivity Across Entire UV-visible Region for Photoelectrochemical Water Splitting. *Nano Letters* **13**, 3817–3823 (2013).
205. Soleymani, L. & Li, F. Mechanistic Challenges and Advantages of Biosensor Miniaturization into the Nanoscale. *ACS Sensors* **2**, 458–467 (2017).
206. Zhao, W.-W., Xu, J.-J. & Chen, H.-Y. Photoelectrochemical bioanalysis: the state of the art. *Chem. Soc. Rev.* **44**, 729–741 (2015).
207. Zhao, W.-W., Xu, J.-J. & Chen, H.-Y. Photoelectrochemical aptasensing. *TrAC Trends in Analytical Chemistry* **82**, 307–315 (2016).
208. Zhao, W.-W., Xu, J.-J. & Chen, H.-Y. Photoelectrochemical enzymatic biosensors. *Biosensors and Bioelectronics* **92**, 294–304 (2017).
209. Zhao, W.-W., Xu, J.-J. & Chen, H.-Y. Photoelectrochemical DNA Biosensors. *Chemical Reviews* **114**, 7421–7441 (2014).

210. Zhao, W.-W., Xu, J.-J. & Chen, H.-Y. Photoelectrochemical Immunoassays. *Analytical Chemistry* **90**, 615–627 (2018).
211. Zhang, Y., Luo, J., Flewitt, A. J., Cai, Z. & Zhao, X. Film bulk acoustic resonators (FBARs) as biosensors: A review. *Biosensors and Bioelectronics* **116**, 1–15 (2018).
212. Špačková, B., Wrobel, P., Bocková, M. & Homola, J. Optical Biosensors Based on Plasmonic Nanostructures: A Review. *Proceedings of the IEEE* **104**, 2380–2408 (2016).
213. DeMiguel-Ramos, M. *et al.* Gravimetric biosensor based on a 1.3GHz AlN shear-mode solidly mounted resonator. *Sensors and Actuators B: Chemical* **239**, 1282–1288 (2017).
214. Alizadeh, N. & Salimi, A. Ultrasensitive Bioaffinity Electrochemical Sensors: Advances and New Perspectives. *Electroanalysis* **30**, 2803–2840 (2018).
215. Kirste, R. *et al.* Electronic Biosensors Based on III-Nitride Semiconductors. *Annual Review of Analytical Chemistry* **8**, 149–169 (2015).
216. Yildiz, H. B., Freeman, R., Gill, R. & Willner, I. Electrochemical, Photoelectrochemical, and Piezoelectric Analysis of Tyrosinase Activity by Functionalized Nanoparticles. *Analytical Chemistry* **80**, 2811–2816 (2008).
217. Golub, E., Pelossof, G., Freeman, R., Zhang, H. & Willner, I. Electrochemical, Photoelectrochemical, and Surface Plasmon Resonance Detection of Cocaine Using Supramolecular Aptamer Complexes and Metallic or Semiconductor Nanoparticles. *Analytical Chemistry* **81**, 9291–9298 (2009).
218. Bard, A. J. *et al.* *ELECTROCHEMICAL METHODS Fundamentals and Applications. Electrochemistry. I. Faulkner, Larry R* (1980). doi:10.1016/B978-0-12-381373-2.00056-9.
219. Fan, G.-C. *et al.* Enhanced photoelectrochemical aptasensing platform based on exciton energy transfer between CdSeTe alloyed quantum dots and SiO<sub>2</sub>@Au nanocomposites. *Chemical Communications* **51**, 7023–7026 (2015).
220. Han, Z., Luo, M., Chen, L., Chen, J. & Li, C. A photoelectrochemical immunosensor for detection of  $\alpha$ -fetoprotein based on Au-ZnO flower-rod heterostructures. *Applied Surface Science* **402**, 429–435 (2017).
221. Tu, W., Wang, Z. & Dai, Z. Selective photoelectrochemical architectures for biosensing: Design, mechanism and responsibility. *TrAC Trends in Analytical Chemistry* **105**, 470–483 (2018).
222. Chen, Z. *et al.* Efficiency Definitions in the Field of PEC. in *SpringerBriefs in Energy* 7–16 (2013). doi:10.1007/978-1-4614-8298-7\_2.
223. Kolesova, E. P. *et al.* Photocatalytic Properties of Hybrid Nanostructures Based on Nanoparticles of TiO<sub>2</sub> and Semiconductor Quantum Dots. *Optics and Spectroscopy* **125**, 99–103 (2018).
224. Fu, B. & Zhang, Z. Periodical 2D Photonic-Plasmonic Au/TiO<sub>x</sub> Nanocavity Resonators for Photoelectrochemical Applications. *Small* **14**, 1703610 (2018).
225. Kolesova, E. P. *et al.* Photocatalytic Properties of Hybrid Nanostructures Based on Nanoparticles of TiO<sub>2</sub> and Semiconductor Quantum Dots. *Optics and Spectroscopy* **125**, 99–103 (2018).

226. Devadoss, A., Sudhagar, P., Terashima, C. & Nakata, K. Journal of Photochemistry and Photobiology C : Photochemistry Reviews Photoelectrochemical biosensors : New insights into promising photoelectrodes and signal amplification strategies. **24**, 43–63 (2015).
227. Zhu, Y. C. *et al.* Alkaline Phosphatase Tagged Antibodies on Gold Nanoparticles/TiO<sub>2</sub>Nanotubes Electrode: A Plasmonic Strategy for Label-Free and Amplified Photoelectrochemical Immunoassay. *Analytical Chemistry* **88**, 5626–5630 (2016).
228. Gratzel, M. Photoelectrochemical cells. *Nature; London* (2001) doi:10.1038/35104607.
229. Zhao, W. W., Xu, J. J. & Chen, H. Y. Photoelectrochemical DNA biosensors. *Chemical Reviews* **114**, 7421–7441 (2014).
230. Tian, J., Li, Y., Dong, J., Huang, M. & Lu, J. Photoelectrochemical TiO<sub>2</sub> nanotube arrays biosensor for asulam determination based on in-situ generation of quantum dots. *Biosensors and Bioelectronics* **110**, 1–7 (2018).
231. Lin, Y. *et al.* Silver Nanolabels-Assisted Ion-Exchange Reaction with CdTe Quantum Dots Mediated Exciton Trapping for Signal-On Photoelectrochemical Immunoassay of Mycotoxins. *Analytical Chemistry* **88**, 7858–7866 (2016).
232. Li, M. *et al.* Ultrasensitive Photoelectrochemical Biosensor Based on DNA Tetrahedron as Nanocarrier for Efficient Immobilization of CdTe QDs-Methylene Blue as Signal Probe with Near-Zero Background Noise. *Analytical Chemistry* **90**, 8211–8216 (2018).
233. Hao, N. *et al.* Design of a Dual Channel Self-Reference Photoelectrochemical Biosensor. *Analytical Chemistry* **89**, 10133–10136 (2017).
234. Lv, S., Zhang, K., Lin, Z. & Tang, D. Novel photoelectrochemical immunosensor for disease-related protein assisted by hemin/G-quadruplex-based DNAzyme on gold nanoparticles to enhance cathodic photocurrent on p-CuBi<sub>2</sub>O<sub>4</sub> semiconductor. *Biosensors and Bioelectronics* **96**, 317–323 (2017).
235. Gong, L. *et al.* DNAzyme-based biosensors and nanodevices. *Chemical Communications* **51**, 979–995 (2015).
236. Ge, L., Wang, W., Hou, T. & Li, F. A versatile immobilization-free photoelectrochemical biosensor for ultrasensitive detection of cancer biomarker based on enzyme-free cascaded quadratic amplification strategy. *Biosensors and Bioelectronics* **77**, 220–226 (2016).
237. Zang, Y., Lei, J., Hao, Q. & Ju, H. CdS/MoS<sub>2</sub> heterojunction-based photoelectrochemical DNA biosensor via enhanced chemiluminescence excitation. *Biosensors and Bioelectronics* **77**, 557–564 (2016).
238. Wang, M. *et al.* Photoelectrochemical biosensor for microRNA detection based on a MoS<sub>2</sub>/g-C<sub>3</sub>N<sub>4</sub>/black TiO<sub>2</sub> heterojunction with Histostar@AuNPs for signal amplification. *Biosensors and Bioelectronics* **128**, 137–143 (2019).
239. Wang, Y.-F. *et al.* Electron Extraction Dynamics in CdSe and CdSe/CdS/ZnS Quantum Dots Adsorbed with Methyl Viologen. *The Journal of Physical Chemistry C* **118**, 17240–17246 (2014).
240. Matylytsky, V. V., Dworak, L., Breus, V. V., Basché, T. & Wachtveitl, J. Ultrafast Charge Separation in Multiexcited CdSe Quantum Dots Mediated by Adsorbed Electron Acceptors. *J Am Chem Soc* **131**, 2424–2425 (2009).

241. Han, Z. *et al.* A photoelectrochemical biosensor for determination of DNA based on flower rod-like zinc oxide heterostructures. *Microchimica Acta* **184**, 2541–2549 (2017).
242. Hong, Z., Jing, L. & Shusheng, Z. Quantum dot-based photoelectric conversion for biosensing applications. *Trends in Analytical Chemistry* 67 (2015) 56–73. *Trends in Anal. Chem.* **67**, 56–73 (2015).
243. Lin, Y. *et al.* Silver Nanolabels-Assisted Ion-Exchange Reaction with CdTe Quantum Dots Mediated Exciton Trapping for Signal-On Photoelectrochemical Immunoassay of Mycotoxins. *Analytical Chemistry* **88**, 7858–7866 (2016).
244. Hao, N. *et al.* Design of a Dual Channel Self-Reference Photoelectrochemical Biosensor. *Analytical Chemistry* **89**, 10133–10136 (2017).
245. Yu, K. J., Yan, Z., Han, M. & Rogers, J. A. Inorganic semiconducting materials for flexible and stretchable electronics. *npj Flexible Electronics* **1**, 4 (2017).
246. Jiang, Y. & Tian, B. Inorganic semiconductor biointerfaces. *Nature Reviews Materials* **3**, 473–490 (2018).
247. Nelson, J. Organic photovoltaic films. *Current Opinion in Solid State and Materials Science* **6**, 87–95 (2002).
248. Tomkiewicz, M. & Woodall, J. M. Photoelectrolysis of Water with Semiconductor Materials. *J. Electrochem. Soc* **124**, 1436–1440 (1977).
249. Wang, Y. *et al.* Reversible Chemical Tuning of Charge Carriers for Enhanced Photoelectrochemical Conversion and Probing of Living Cells. *Small* **10**, 4967–4974 (2014).
250. Liu, L., Hensel, J., Fitzmorris, R. C., Li, Y. & Zhang, J. Z. Preparation and photoelectrochemical properties of CdSe/TiO<sub>2</sub> hybrid mesoporous structures. *Journal of Physical Chemistry Letters* **1**, 155–160 (2010).
251. Chen, X. & Mao, S. S. Titanium Dioxide Nanomaterials : Synthesis , Properties , Modifications , and Applications. (2007) doi:10.1021/cr0500535.
252. Dagher, R., Drogui, P. & Robert, D. Modified TiO<sub>2</sub> For Environmental Photocatalytic Applications: A Review. *Industrial & Engineering Chemistry Research* **52**, 3581–3599 (2013).
253. Du, J. *et al.* Enhanced charge separation of CuS and CdS quantum-dot-cosensitized porous TiO<sub>2</sub>-based photoanodes for photoelectrochemical water splitting. *Elsevier* (2017).
254. Liu, P. P. *et al.* TiO<sub>2</sub>–BiVO<sub>4</sub> Heterostructure to Enhance Photoelectrochemical Efficiency for Sensitive Aptasensing. *ACS Applied Materials & Interfaces* **9**, 27185–27192 (2017).
255. Komathi, S., Muthuchamy, N., Lee, K.-P. & Gopalan, A.-I. Fabrication of a novel dual mode cholesterol biosensor using titanium dioxide nanowire bridged 3D graphene nanostacks. *Biosensors and Bioelectronics* **84**, 64–71 (2016).
256. Mitchell, K., Fahrenbruch, A. L. & Bube, R. H. Photovoltaic determination of optical-absorption coefficient in CdTe. *Journal of Applied Physics* **48**, 829–830 (1977).
257. Sarkar, S., Pal, S. & Sarkar, P. Electronic structure and band gap engineering of CdTe semiconductor nanowires. *Journal of Materials Chemistry* **22**, 10716 (2012).
258. Wang, G., Yang, X., Qian, F., Zhang, J. Z. & Li, Y. Double-Sided CdS and CdSe Quantum Dot Co-Sensitized ZnO Nanowire Arrays for Photoelectrochemical Hydrogen Generation. *Nano Letters* **10**, 1088–1092 (2010).

259. Zhou, H., Liu, J. & Zhang, S. Quantum dot-based photoelectric conversion for biosensing applications. *TrAC Trends in Analytical Chemistry* **67**, 56–73 (2015).
260. Yue, Z. *et al.* Quantum-Dot-Based Photoelectrochemical Sensors for Chemical and Biological Detection. *ACS Applied Materials & Interfaces* **5**, 2800–2814 (2013).
261. Özgür, Ü. *et al.* A comprehensive review of ZnO materials and devices. *Journal of Applied Physics* **98**, 041301 (2005).
262. Tu, W., Lei, J., Wang, P. & Ju, H. Photoelectrochemistry of free-base-porphyrin-functionalized zinc oxide nanoparticles and their applications in biosensing. *Chemistry - A European Journal* **17**, 9440–9447 (2011).
263. Kang, Z. *et al.* Electronic Structure Engineering of Cu<sub>2</sub>O Film/ZnO Nanorods Array All-Oxide p-n Heterostructure for Enhanced Photoelectrochemical Property and Self-powered Biosensing Application. *Scientific Reports* **5**, 7882 (2015).
264. Zhao, K. *et al.* Self-Powered Photoelectrochemical Biosensor Based on CdS/RGO/ZnO Nanowire Array Heterostructure. *Small* **12**, 245–251 (2016).
265. Qiao, Y. *et al.* A label-free photoelectrochemical aptasensor for bisphenol A based on surface plasmon resonance of gold nanoparticle-sensitized ZnO nanopencils. *Biosensors and Bioelectronics* **86**, 315–320 (2016).
266. Liu, F. *et al.* Application of ZnO/graphene and S6 aptamers for sensitive photoelectrochemical detection of SK-BR-3 breast cancer cells based on a disposable indium tin oxide device. *Biosensors and Bioelectronics* **51**, 413–420 (2014).
267. Jiang, D., Du, X., Liu, Q., Hao, N. & Wang, K. MoS<sub>2</sub>/nitrogen doped graphene hydrogels p-n heterojunction: Efficient charge transfer property for highly sensitive and selective photoelectrochemical analysis of chloramphenicol. *Biosensors and Bioelectronics* **126**, 463–469 (2019).
268. Rim, Y. S. *et al.* Interface Engineering of Metal Oxide Semiconductors for Biosensing Applications. *Advanced Materials Interfaces* **4**, 1700020 (2017).
269. Kadian, S. *et al.* Synthesis and Application of PHT-TiO<sub>2</sub> Nanohybrid for Amperometric Glucose Detection in Human Saliva Sample. *Electroanalysis* **30**, 2793–2802 (2018).
270. Cheng, Y. *et al.* Mechanism and Optimization of pH Sensing Using SnO<sub>2</sub> Nanobelt Field Effect Transistors. *Nano Letters* **8**, 4179–4184 (2008).
271. Ikeda, A. *et al.* Photoelectrochemical sensor with porphyrin-deposited electrodes for determination of nucleotides in water. *Organic Letters* **11**, 1163–1166 (2009).
272. Da, H., Liu, H., Zheng, Y., Yuan, R. & Chai, Y. A highly sensitive VEGF165 photoelectrochemical biosensor fabricated by assembly of aptamer bridged DNA networks. *Biosensors and Bioelectronics* **101**, 213–218 (2018).
273. Shi, X. M. *et al.* Energy Transfer between Semiconducting Polymer Dots and Gold Nanoparticles in a Photoelectrochemical System: A Case Application for Cathodic Bioanalysis. *Analytical Chemistry* **90**, 4277–4281 (2018).
274. Xu, J. *et al.* Highly stretchable polymer semiconductor films through the nanoconfinement effect. *Science* **355**, 59–64 (2017).

275. Zhao, X., Chaudhry, S. T. & Mei, J. Heterocyclic Building Blocks for Organic Semiconductors. (2017) doi:10.1016/bs.aihch.2016.04.009.
276. Malliaras, G. G. Photovoltaic Devices from Organic Semiconductors. in *Encyclopedia of Materials: Science and Technology* 6981–6986 (Elsevier, 2004). doi:10.1016/b0-08-043152-6/01237-7.
277. Zhao, X., Chaudhry, S. T. & Mei, J. Heterocyclic Building Blocks for Organic Semiconductors. (2017) doi:10.1016/bs.aihch.2016.04.009.
278. Wang, A., Wong-Ng, W., Lan, Y., Wang, C. & Fu, L. Recent Advances of Graphitic Carbon Nitride-Based Structures and Applications in Catalyst, Sensing, Imaging, and LEDs. *Nano-Micro Letters* **9**, (2017).
279. Su, F. *et al.* mpg-C 3 N 4 -Catalyzed Selective Oxidation of Alcohols Using O 2 and Visible Light. *J Am Chem Soc* **132**, 16299–16301 (2010).
280. Ong, W.-J., Tan, L.-L., Ng, Y. H., Yong, S.-T. & Chai, S.-P. Graphitic Carbon Nitride (g-C<sub>3</sub>N<sub>4</sub>)-Based Photocatalysts for Artificial Photosynthesis and Environmental Remediation: Are We a Step Closer To Achieving Sustainability? *Chemical Reviews* **116**, 7159–7329 (2016).
281. Zhu, J., Xiao, P., Li, H. & Carabineiro, S. A. C. Graphitic Carbon Nitride: Synthesis, Properties, and Applications in Catalysis. *ACS Applied Materials & Interfaces* **6**, 16449–16465 (2014).
282. Wu, G. *et al.* Graphitic carbon nitride nanosheet electrode-based high-performance ionic actuator. *Nature Communications* **6**, (2015).
283. Liu, X. & Dai, L. Carbon-based metal-free catalysts. *Nature Reviews Materials* **1**, (2016).
284. Tong, Z. *et al.* Thylakoid-Inspired Multishell g-C<sub>3</sub>N<sub>4</sub>Nanocapsules with Enhanced Visible-Light Harvesting and Electron Transfer Properties for High-Efficiency Photocatalysis. *ACS Nano* **11**, 1103–1112 (2017).
285. Panneri, S. *et al.* C<sub>3</sub>N<sub>4</sub> anchored ZIF 8 composites: Photo-regenerable, high capacity sorbents as adsorptive photocatalysts for the effective removal of tetracycline from water. *Catalysis Science and Technology* **7**, 2118–2128 (2017).
286. Shi, X. M., Fan, G. C., Tang, X., Shen, Q. & Zhu, J. J. Ultrasensitive photoelectrochemical biosensor for the detection of HTLV-I DNA: A cascade signal amplification strategy integrating λ-exonuclease aided target recycling with hybridization chain reaction and enzyme catalysis. *Biosensors and Bioelectronics* **109**, 190–196 (2018).
287. Li, C. *et al.* Unique P-Co-N Surface Bonding States Constructed on g-C<sub>3</sub>N<sub>4</sub> Nanosheets for Drastically Enhanced Photocatalytic Activity of H<sub>2</sub> Evolution. *Advanced Functional Materials* **27**, 1–8 (2017).
288. Maeda, K. *et al.* Photocatalytic Activities of Graphitic Carbon Nitride Powder for Water Reduction and Oxidation under Visible Light. *The Journal of Physical Chemistry C* **113**, 4940–4947 (2009).
289. Zhang, Y. *et al.* Biopolymer-Activated Graphitic Carbon Nitride towards a Sustainable Photocathode Material. (2013) doi:10.1038/srep02163.
290. Zheng, Y., Liu, J., Liang, J., Jaroniec, M. & Qiao, S. Z. Graphitic carbon nitride materials: controllable synthesis and applications in fuel cells and photocatalysis. *Energy & Environmental Science* **5**, 6717 (2012).

291. Khan, M. S. *et al.* A novel label-free photoelectrochemical sensor based on N,S-GQDs and CdS co-sensitized hierarchical Zn<sub>2</sub>SnO<sub>4</sub> cube for detection of cardiac troponin I. *Biosensors and Bioelectronics* **106**, 14–20 (2018).
292. Wang, H. *et al.* Photoelectrochemical Immunosensor for Detection of Carcinoembryonic Antigen Based on 2D TiO<sub>2</sub> Nanosheets and Carboxylated Graphitic Carbon Nitride. *Scientific Reports* **6**, 27385 (2016).
293. Liu, Y., Yan, K. & Zhang, J. Graphitic carbon nitride sensitized with CdS quantum dots for visible-light-driven photoelectrochemical aptasensing of tetracycline. *ACS Applied Materials and Interfaces* **2015**, (2015).
294. Kesters, J. *et al.* Porphyrin-Based Bulk Heterojunction Organic Photovoltaics: The Rise of the Colors of Life. *Advanced Energy Materials* **5**, 1–20 (2015).
295. Lash, T. D. Benziporphyrins, a unique platform for exploring the aromatic characteristics of porphyrinoid systems. *Organic & Biomolecular Chemistry* **13**, 7846–7878 (2015).
296. Zang, Y., Lei, J., Ling, P. & Ju, H. Catalytic hairpin assembly-programmed porphyrin-DNA complex as photoelectrochemical initiator for DNA biosensing. *Analytical Chemistry* **87**, 5430–5436 (2015).
297. Shu, J., Qiu, Z., Zhuang, J., Xu, M. & Tang, D. In Situ Generation of Electron Donor to Assist Signal Amplification on Porphyrin-Sensitized Titanium Dioxide Nanostructures for Ultrasensitive Photoelectrochemical Immunoassay. *ACS Applied Materials and Interfaces* **7**, 23812–23818 (2015).
298. Tu, W., Lei, J., Wang, P. & Ju, H. Photoelectrochemistry of free-base-porphyrin-functionalized zinc oxide nanoparticles and their applications in biosensing. *Chemistry - A European Journal* **17**, 9440–9447 (2011).
299. Shi, X. M., Fan, G. C., Shen, Q. & Zhu, J. J. Photoelectrochemical DNA Biosensor Based on Dual-Signal Amplification Strategy Integrating Inorganic-Organic Nanocomposites Sensitization with  $\lambda$ -Exonuclease-Assisted Target Recycling. *ACS Applied Materials and Interfaces* **8**, 35091–35098 (2016).
300. Kwon, S. J., de Boer, A. L., Petri, R. & Schmidt-Dannert, C. High-level production of porphyrins in metabolically engineered *Escherichia coli*: systematic extension of a pathway assembled from overexpressed genes involved in heme biosynthesis. *Appl Environ Microbiol* **69**, 4875–83 (2003).
301. MedKoo Biosciences. Fe-TMPyP. <https://www.medkoo.com/products/15484> (2009).
302. Wang, L. *et al.* Organic Polymer Dots as Photocatalysts for Visible Light-Driven Hydrogen Generation. *Angewandte Chemie - International Edition* **55**, 12306–12310 (2016).
303. Li, Y. *et al.* Polymer Dots for Photoelectrochemical Bioanalysis. *Analytical Chemistry* **89**, 4945–4950 (2017).
304. Zhang, N. *et al.* Gold Nanoparticle Couples with Entropy-Driven Toehold-Mediated DNA Strand Displacement Reaction on Magnetic Beads: Toward Ultrasensitive Energy-Transfer-Based Photoelectrochemical Detection of miRNA-141 in Real Blood Sample. *Analytical Chemistry* **90**, 11892–11898 (2018).

305. Zhou, X., Zhang, P., Lv, F., Liu, L. & Wang, S. Photoelectrochemical Strategy for Discrimination of Microbial Pathogens Using Conjugated Polymers. *Chemistry - An Asian Journal* **13**, 3469–3473 (2018).
306. Feng, X., Liu, L., Wang, S. & Zhu, D. Water-soluble fluorescent conjugated polymers and their interactions with biomacromolecules for sensitive biosensors. *Chemical Society Reviews* **39**, 2411–2419 (2010).
307. Wu, C. & Chiu, D. T. Highly Fluorescent Semiconducting Polymer Dots for Biology and Medicine. *Angewandte Chemie International Edition* **52**, 3086–3109 (2013).
308. Yu, J., Rong, Y., Kuo, C.-T., Zhou, X.-H. & Chiu, D. T. Recent Advances in the Development of Highly Luminescent Semiconducting Polymer Dots and Nanoparticles for Biological Imaging and Medicine. *Analytical Chemistry* **89**, 42–56 (2017).
309. Wang, Q. *et al.* Semiconducting Organic–Inorganic Nanodots Heterojunctions: Platforms for General Photoelectrochemical Bioanalysis Application. *Analytical Chemistry* **90**, 3759–3765 (2018).
310. Dyer-Smith, C. & Nelson, J. Organic Solar Cells. in *Practical Handbook of Photovoltaics* 543–569 (Elsevier, 2012). doi:10.1016/B978-0-12-385934-1.00016-7.
311. Kus, M. *et al.* Synthesis of Nanoparticles. in *Handbook of Nanomaterials for Industrial Applications* 392–429 (Elsevier, 2018). doi:10.1016/B978-0-12-813351-4.00025-0.
312. Wen, G. & Ju, H. Enhanced photoelectrochemical proximity assay for highly selective protein detection in biological matrixes. *Analytical Chemistry* **88**, 8339–8345 (2016).
313. Liu, Q. *et al.* Engineering of Heterojunction-Mediated Biointerface for Photoelectrochemical Aptasensing: Case of Direct Z-Scheme CdTe-Bi<sub>2</sub>S<sub>3</sub> Heterojunction with Improved Visible-Light-Driven Photoelectrical Conversion Efficiency. *ACS Applied Materials and Interfaces* **9**, 18369–18376 (2017).
314. Chen, E. Y., Milleville, C., Zide, J. M. O., Doty, M. F. & Zhang, J. Upconversion of low-energy photons in semiconductor nanostructures for solar energy harvesting. *MRS Energy & Sustainability* **5**, E16 (2018).
315. Naik, G. V., Welch, A. J., Briggs, J. A., Solomon, M. L. & Dionne, J. A. Hot-Carrier-Mediated Photon Upconversion in Metal-Decorated Quantum Wells. *Nano Letters* **17**, 4583–4587 (2017).
316. Qiu, Z., Shu, J. & Tang, D. Near-Infrared-to-Ultraviolet Light-Mediated Photoelectrochemical Aptasensing Platform for Cancer Biomarker Based on Core-Shell NaYF<sub>4</sub>:Yb,Tm@TiO<sub>2</sub> Upconversion Microrods. *Analytical Chemistry* **90**, 1021–1028 (2018).
317. Coropceanu, V. *et al.* Charge Transport in Organic Semiconductors. *Chemical Reviews* **107**, 926–952 (2007).
318. Hao, N. *et al.* Three-dimensional nitrogen-doped graphene porous hydrogel fabricated biosensing platform with enhanced photoelectrochemical performance. *Sensors and Actuators B: Chemical* **250**, 476–483 (2017).
319. Dai, H. *et al.* Photoelectrochemical biosensor constructed using TiO<sub>2</sub> mesocrystals based multipurpose matrix for trypsin detection. *Biosensors and Bioelectronics* **92**, 687–694 (2017).
320. Long, Y.-T. *et al.* Ultrasensitive Determination of Cysteine Based on the Photocurrent of Nafion-Functionalized CdS-MV Quantum Dots on an ITO Electrode. *Small* **7**, 1624–1628 (2011).

321. Lim, J., Bokare, A. D. & Choi, W. Visible light sensitization of TiO<sub>2</sub> nanoparticles by a dietary pigment, curcumin, for environmental photochemical transformations. *RSC Advances* **7**, 32488–32495 (2017).
322. Yan, X. *et al.* A new photoelectrochemical aptasensor for prion assay based on cyclodextrin and Rhodamine B. *Sensors and Actuators, B: Chemical* **255**, 2187–2193 (2018).
323. Ma, H. *et al.* Formation of Homogeneous Epinephrine-Melanin Solutions to Fabricate Electrodes for Enhanced Photoelectrochemical Biosensing. *Langmuir* **34**, 7744–7750 (2018).
324. Yotsumoto Neto, S., Luz, R. de C. S. & Damos, F. S. Visible LED light photoelectrochemical sensor for detection of L-Dopa based on oxygen reduction on TiO<sub>2</sub> sensitized with iron phthalocyanine. *Electrochemistry Communications* **62**, 1–4 (2016).
325. Li, Z., Su, C., Wu, D. & Zhang, Z. Gold Nanoparticles Decorated Hematite Photoelectrode for Sensitive and Selective Photoelectrochemical Aptasensing of Lysozyme. *Analytical Chemistry* **90**, 961–967 (2018).
326. Wang, Y. *et al.* Photoelectrochemical apta-biosensor for zeatin detection based on graphene quantum dots improved photoactivity of graphite-like carbon nitride and streptavidin induced signal inhibition. *Sensors and Actuators B: Chemical* **257**, 237–244 (2018).
327. Lin, Y. *et al.* Silver Nanolabels-Assisted Ion-Exchange Reaction with CdTe Quantum Dots Mediated Exciton Trapping for Signal-On Photoelectrochemical Immunoassay of Mycotoxins. *Analytical Chemistry* **88**, 7858–7866 (2016).
328. Hao, N. *et al.* Design of a Dual Channel Self-Reference Photoelectrochemical Biosensor. *Analytical Chemistry* **89**, 10133–10136 (2017).
329. Zang, Y., Lei, J., Ling, P. & Ju, H. Catalytic Hairpin Assembly-Programmed Porphyrin–DNA Complex as Photoelectrochemical Initiator for DNA Biosensing. *Analytical Chemistry* **87**, 5430–5436 (2015).
330. Liu, Q. *et al.* Engineering of Heterojunction-Mediated Biointerface for Photoelectrochemical Aptasensing: Case of Direct Z-Scheme CdTe–Bi<sub>2</sub>S<sub>3</sub> Heterojunction with Improved Visible-Light-Driven Photoelectrical Conversion Efficiency. *ACS Applied Materials and Interfaces* **9**, 18369–18376 (2017).
331. Shi, X. M., Fan, G. C., Tang, X., Shen, Q. & Zhu, J. J. Ultrasensitive photoelectrochemical biosensor for the detection of HTLV-I DNA: A cascade signal amplification strategy integrating  $\lambda$ -exonuclease aided target recycling with hybridization chain reaction and enzyme catalysis. *Biosensors and Bioelectronics* **109**, 190–196 (2018).
332. Zang, Y., Lei, J. & Ju, H. Principles and applications of photoelectrochemical sensing strategies based on biofunctionalized nanostructures. *Biosensors and Bioelectronics* **96**, 8–16 (2017).
333. Liu, S. *et al.* Conjugated Polymer-Based Photoelectrochemical Cytosensor with Turn-On Enable Signal for Sensitive Cell Detection. *ACS Applied Materials and Interfaces* **10**, 6618–6623 (2018).
334. Dai, H., Zhang, S., Hong, Z. & Lin, Y. A Potentiometric Addressable Photoelectrochemical Biosensor for Sensitive Detection of Two Biomarkers. *Analytical Chemistry* **88**, 9532–9538 (2016).

335. Zhao, W.-W., Wang, J., Zhu, Y.-C., Xu, J.-J. & Chen, H.-Y. Quantum Dots: Electrochemiluminescent and Photoelectrochemical Bioanalysis. (2015) doi:10.1021/acs.analchem.5b00497.
336. Smith, A. M. & Nie, S. Semiconductor nanocrystals: structure, properties, and band gap engineering. *Acc Chem Res* **43**, 190–200 (2010).
337. Hao, N. *et al.* A universal photoelectrochemical biosensor for dual microRNA detection based on two CdTe nanocomposites. *Journal of Materials Chemistry B* **7**, 1133–1141 (2019).
338. Malekzad, H., Zangabad, P. S., Mirshekari, H., Karimi, M. & Hamblin, M. R. Noble metal nanoparticles in biosensors: recent studies and applications. *Nanotechnol Rev* **6**, 301–329 (2017).
339. Willner, I., Patolsky, F. & Wasserman, J. Photoelectrochemistry with Controlled DNA-Cross-Linked CdS Nanoparticle Arrays. *Angewandte Chemie* **113**, 1913–1916 (2001).
340. Chu, Y., Wu, R., Fan, G.-C., Deng, A.-P. & Zhu, J.-J. Enzyme-Free Photoelectrochemical Biosensor Based on the Co-Sensitization Effect Coupled with Dual Cascade Toehold-Mediated Strand Displacement Amplification for the Sensitive Detection of MicroRNA-21. *ACS Sustainable Chemistry & Engineering* **6**, 11633–11641 (2018).
341. Meng, L. *et al.* A sensitive photoelectrochemical assay of miRNA-155 based on a CdSe QDs/NPC-ZnO polyhedra photocurrent-direction switching system and target-triggered strand displacement amplification strategy. *Chemical Communications* **55**, 2182–2185 (2019).
342. Yu, S.-Y. *et al.* Liposome-Mediated in Situ Formation of AgI/Ag/BiOI Z-Scheme Heterojunction on Foamed Nickel Electrode: A Proof-of-Concept Study for Cathodic Liposomal Photoelectrochemical Bioanalysis. *Analytical Chemistry* **91**, 3800–3804 (2019).
343. Ju, Y., Hu, X., Zang, Y., Cao, R. & Xue, H. Amplified photoelectrochemical DNA biosensor based on a CdS quantum dot/WS<sub>2</sub> nanosheet heterojunction and hybridization chain reaction-mediated enzymatic hydrolysis. *Analytical Methods* **11**, 2163–2169 (2019).
344. Zhang, N. *et al.* Simultaneous Photoelectrochemical Immunoassay of Dual Cardiac Markers Using Specific Enzyme Tags: A Proof of Principle for Multiplexed Bioanalysis. *Analytical Chemistry* **88**, 1990–1994 (2016).
345. Ju, Y., Hu, X., Zang, Y., Cao, R. & Xue, H. Amplified photoelectrochemical DNA biosensor based on a CdS quantum dot/WS<sub>2</sub> nanosheet heterojunction and hybridization chain reaction-mediated enzymatic hydrolysis. *Analytical Methods* **11**, 2163–2169 (2019).
346. Zhang, N. *et al.* Simultaneous Photoelectrochemical Immunoassay of Dual Cardiac Markers Using Specific Enzyme Tags: A Proof of Principle for Multiplexed Bioanalysis. *Analytical Chemistry* **88**, 1990–1994 (2016).
347. Xu, R. *et al.* A sensitive photoelectrochemical biosensor for AFP detection based on ZnO inverse opal electrodes with signal amplification of CdS-QDs. *Biosensors and Bioelectronics* **74**, 411–417 (2015).
348. Zang, Y., Lei, J. & Ju, H. Principles and applications of photoelectrochemical sensing strategies based on biofunctionalized nanostructures. *Biosensors and Bioelectronics* **96**, 8–16 (2017).
349. Pang, X. *et al.* Photoelectrochemical Cytosensing of RAW264.7 Macrophage Cells Based on a TiO<sub>2</sub> Nanoneedles@MoO<sub>3</sub> Array. *Analytical Chemistry* **89**, 7950–7957 (2017).

350. Fu, N. *et al.* Au nanoparticles on two-dimensional MoS<sub>2</sub> nanosheets as a photoanode for efficient photoelectrochemical miRNA detection. *Analyst* **143**, 1705–1712 (2018).
351. Saha, S., Chan, Y. & Soleymani, L. Enhancing the Photoelectrochemical Response of DNA Biosensors Using Wrinkled Interfaces. *ACS Applied Materials and Interfaces* **10**, 31178–31185 (2018).
352. Saha, S., Chan, Y. & Soleymani, L. Enhancing the Photoelectrochemical Response of DNA Biosensors Using Wrinkled Interfaces. *ACS Applied Materials and Interfaces* **10**, 31178–31185 (2018).
353. Tu, W. *et al.* Dual Signal Amplification Using Gold Nanoparticles-Enhanced Zinc Selenide Nanoflakes and P19 Protein for Ultrasensitive Photoelectrochemical Biosensing of MicroRNA in Cell. *Analytical Chemistry* **88**, 10459–10465 (2016).
354. Hao, N. *et al.* Multiple signal-amplification via Ag and TiO<sub>2</sub> decorated 3D nitrogen doped graphene hydrogel for fabricating sensitive label-free photoelectrochemical thrombin aptasensor. *Biosensors and Bioelectronics* **101**, 14–20 (2018).
355. Wu, R., Fan, G. C., Jiang, L. P. & Zhu, J. J. Peptide-Based Photoelectrochemical Cytosensor Using a Hollow-TiO<sub>2</sub>/EG/ZnIn<sub>2</sub>S<sub>4</sub> Cosensitized Structure for Ultrasensitive Detection of Early Apoptotic Cells and Drug Evaluation. *ACS Applied Materials and Interfaces* **10**, 4429–4438 (2018).
356. Ge, S. *et al.* Ultrasensitive Photoelectrochemical Biosensing of Cell Surface N-Glycan Expression Based on the Enhancement of Nanogold-Assembled Mesoporous Silica Amplified by Graphene Quantum Dots and Hybridization Chain Reaction. *ACS Applied Materials and Interfaces* **9**, 6670–6678 (2017).
357. Li, J., Lin, X., Zhang, Z., Tu, W. & Dai, Z. Biosensors and Bioelectronics Red light-driven photoelectrochemical biosensing for ultrasensitive and scatheless assay of tumor cells based on hypotoxic AgInS<sub>2</sub> nanoparticles. **126**, 332–338 (2019).
358. Zhuang, J., Lai, W., Xu, M., Zhou, Q. & Tang, D. Plasmonic AuNP/g-C<sub>3</sub>N<sub>4</sub> Nanohybrid-based Photoelectrochemical Sensing Platform for Ultrasensitive Monitoring of Polynucleotide Kinase Activity Accompanying DNAzyme-Catalyzed Precipitation Amplification. *ACS Applied Materials & Interfaces* **7**, 8330–8338 (2015).
359. Zhang, K., Lv, S., Lin, Z., Li, M. & Tang, D. Bio-bar-code-based photoelectrochemical immunoassay for sensitive detection of prostate-specific antigen using rolling circle amplification and enzymatic biocatalytic precipitation. *Biosensors and Bioelectronics* **101**, 159–166 (2018).
360. Zhang, Y. *et al.* A potentiometric resolved ratiometric photoelectrochemical aptasensor. *Chemical Communications* **53**, 5810–5813 (2017).
361. Hao, N., Hua, R., Zhang, K., Lu, J. & Wang, K. A Sunlight Powered Portable Photoelectrochemical Biosensor Based on a Potentiometric Resolve Ratiometric Principle. *Analytical Chemistry* **90**, 13207–13211 (2018).
362. Hua, R. *et al.* A sensitive Potentiometric resolved ratiometric Photoelectrochemical aptasensor for Escherichia coli detection fabricated with non-metallic nanomaterials. *Biosensors and Bioelectronics* **106**, 57–63 (2018).

363. Zhu, Y.-C. *et al.* Alkaline Phosphatase Tagged Antibodies on Gold Nanoparticles/TiO<sub>2</sub> Nanotubes Electrode: A Plasmonic Strategy for Label-Free and Amplified Photoelectrochemical Immunoassay. *Analytical Chemistry* **88**, 5626–5630 (2016).
364. Ge, S. *et al.* Photoelectrochemical immunoassay based on chemiluminescence as internal excited light source. *Sensors and Actuators B: Chemical* **234**, 324–331 (2016).
365. Shu, J. *et al.* Enzymatic Oxydate-Triggered Self-Illuminated Photoelectrochemical Sensing Platform for Portable Immunoassay Using Digital Multimeter. *Analytical Chemistry* **88**, 2958–2966 (2016).
366. Wang, Y. *et al.* A chemiluminescence excited photoelectrochemistry aptamer-device equipped with a tin dioxide quantum dot/reduced graphene oxide nanocomposite modified porous Au-paper electrode. *J. Mater. Chem. B* **2**, 3462–3468 (2014).
367. He, Y., He, X., Liu, X., Gao, L. & Cui, H. Dynamically Tunable Chemiluminescence of Luminol-Functionalized Silver Nanoparticles and Its Application to Protein Sensing Arrays. (2014) doi:10.1021/ac503123q.
368. Augusto, F. A., de Souza, G. A., de Souza Júnior, S. P., Khalid, M. & Baader, W. J. Efficiency of Electron Transfer Initiated Chemiluminescence. *Photochemistry and Photobiology* **89**, 1299–1317 (2013).
369. Fereja, T. H., Hymete, A. & Gunasekaran, T. A Recent Review on Chemiluminescence Reaction, Principle and Application on Pharmaceutical Analysis. *ISRN Spectroscopy* **2013**, 1–12 (2013).
370. Shu, J. & Tang, D. Current Advances in Quantum-Dots-Based Photoelectrochemical Immunoassays. *Chemistry – An Asian Journal* **12**, 2780–2789 (2017).
371. Hartland, G. V. Optical Studies of Dynamics in Noble Metal Nanostructures. *Chemical Reviews* **111**, 3858–3887 (2011).
372. Zhao, W.-W., Wang, J., Xu, J.-J. & Chen, H.-Y. Energy transfer between CdS quantum dots and Au nanoparticles in photoelectrochemical detection. *Chemical Communications* **47**, 10990 (2011).
373. Han, D.-M., Jiang, L.-Y., Tang, W.-Y., Xu, J.-J. & Chen, H.-Y. Photoelectrochemical determination of inorganic mercury ions based on energy transfer between CdS quantum dots and Au nanoparticles. *Electrochemistry Communications* **51**, 72–75 (2015).
374. Yun, C. S. *et al.* Nanometal surface energy transfer in optical rulers, breaking the FRET barrier. *J Am Chem Soc* **127**, 3115–3119 (2005).
375. Li, J. *et al.* In situ-generated nano-gold plasmon-enhanced photoelectrochemical aptasensing based on carboxylated perylene-functionalized graphene. *Analytical Chemistry* **86**, 1306–1312 (2014).
376. Ma, Z.-Y. *et al.* Invoking Direct Exciton–Plasmon Interactions by Catalytic Ag Deposition on Au Nanoparticles: Photoelectrochemical Bioanalysis with High Efficiency. *Analytical Chemistry* **88**, 4183–4187 (2016).
377. Zhang, L. *et al.* Ag nanoclusters could efficiently quench the photoresponse of CdS quantum dots for novel energy transfer-based photoelectrochemical bioanalysis. *Biosensors and Bioelectronics* **85**, 930–934 (2016).

378. Ma, Z.-Y. *et al.* Protein Binding Bends the Gold Nanoparticle Capped DNA Sequence: Toward Novel Energy-Transfer-Based Photoelectrochemical Protein Detection. *Analytical Chemistry* **88**, 3864–3871 (2016).
379. Fan, G.-C. *et al.* Enhanced Photoelectrochemical Immunosensing Platform Based on CdSeTe@CdS:Mn Core–Shell Quantum Dots-Sensitized TiO<sub>2</sub> Amplified by CuS Nanocrystals Conjugated Signal Antibodies. *Analytical Chemistry* **88**, 3392–3399 (2016).
380. Fan, G.-C. *et al.* Enhanced photoelectrochemical aptasensing platform based on exciton energy transfer between CdSeTe alloyed quantum dots and SiO<sub>2</sub>@Au nanocomposites. *Chemical Communications* **51**, 7023–7026 (2015).
381. Fan, G.-C. *et al.* Enhanced Photoelectrochemical Immunosensing Platform Based on CdSeTe@CdS:Mn Core–Shell Quantum Dots-Sensitized TiO<sub>2</sub> Amplified by CuS Nanocrystals Conjugated Signal Antibodies. *Analytical Chemistry* **88**, 3392–3399 (2016).
382. Liu, Q. *et al.* Resonance energy transfer from CdTe quantum dots to gold nanorods using MWCNTs/rGO nanoribbons as efficient signal amplifier for fabricating visible-light-driven “on-off-on” photoelectrochemical acetamiprid aptasensor. *Sensors and Actuators B: Chemical* **235**, 647–654 (2016).
383. Shen, Q. *et al.* Highly sensitive photoelectrochemical assay for DNA methyltransferase activity and inhibitor screening by exciton energy transfer coupled with enzyme cleavage biosensing strategy. *Biosensors and Bioelectronics* **64**, 449–455 (2015).
384. Li, R. *et al.* A competitive photoelectrochemical assay for estradiol based on in situ generated CdS-enhanced TiO<sub>2</sub>. *Biosensors and Bioelectronics* **66**, 596–602 (2015).
385. Hu, T. *et al.* A Highly Sensitive Photoelectrochemical Assay with Donor-Acceptor-Type Material as Photoactive Material and Polyaniline as Signal Enhancer. *Analytical Chemistry* **90**, 6096–6101 (2018).
386. Willner, I., Patolsky, F. & Wasserman, J. Photoelectrochemistry with Controlled DNA-Cross-Linked CdS Nanoparticle Arrays. *Angewandte Chemie* **113**, 1913–1916 (2001).
387. Yan, Z., Wang, Z., Miao, Z. & Liu, Y. Dye-Sensitized and Localized Surface Plasmon Resonance Enhanced Visible-Light Photoelectrochemical Biosensors for Highly Sensitive Analysis of Protein Kinase Activity. *Analytical Chemistry* **88**, 922–929 (2016).
388. Li, R., Liu, Y., Cheng, L., Yang, C. & Zhang, J. Photoelectrochemical Aptasensing of Kanamycin Using Visible Light-Activated Carbon Nitride and Graphene Oxide Nanocomposites. *Analytical Chemistry* **86**, 9372–9375 (2014).
389. Bettazzi, F. *et al.* Ascorbic acid-sensitized Au nanorods-functionalized nanostructured TiO<sub>2</sub> transparent electrodes for photoelectrochemical genosensing. *Electrochimica Acta* **276**, 389–398 (2018).
390. Hou, T., Xu, N., Wang, W., Ge, L. & Li, F. Truly Immobilization-Free Diffusivity-Mediated Photoelectrochemical Biosensing Strategy for Facile and Highly Sensitive MicroRNA Assay. *Analytical Chemistry* **90**, 9591–9597 (2018).
391. Li, R., Yan, R., Bao, J., Tu, W. & Dai, Z. A localized surface plasmon resonance-enhanced photoelectrochemical biosensing strategy for highly sensitive and scatheless cell assay under red light excitation. *Chemical Communications* **52**, 11799–11802 (2016).

392. Zhu, Y.-C. *et al.* Alkaline Phosphatase Tagged Antibodies on Gold Nanoparticles/TiO<sub>2</sub> Nanotubes Electrode: A Plasmonic Strategy for Label-Free and Amplified Photoelectrochemical Immunoassay. *Analytical Chemistry* **88**, 5626–5630 (2016).
393. Zhang, N. *et al.* Nanochannels Photoelectrochemical Biosensor. *Analytical Chemistry* **90**, 2341–2347 (2018).
394. Fan, G.-C., Shi, X.-M., Zhang, J.-R. & Zhu, J.-J. Cathode Photoelectrochemical Immunosensing Platform Integrating Photocathode with Photoanode. *Analytical Chemistry* **88**, 10352–10356 (2016).
395. Fan, G.-C., Shi, X.-M., Zhang, J.-R. & Zhu, J.-J. Cathode Photoelectrochemical Immunosensing Platform Integrating Photocathode with Photoanode. *Analytical Chemistry* **88**, 10352–10356 (2016).
396. Ge, L., Wang, W., Hou, T. & Li, F. A versatile immobilization-free photoelectrochemical biosensor for ultrasensitive detection of cancer biomarker based on enzyme-free cascaded quadratic amplification strategy. *Biosensors and Bioelectronics* **77**, 220–226 (2016).
397. Xu, F. *et al.* An ultrasensitive energy-transfer based photoelectrochemical protein biosensor. *Chemical Communications* **52**, 3034–3037 (2016).
398. Shu, J., Qiu, Z., Lv, S., Zhang, K. & Tang, D. Plasmonic Enhancement Coupling with Defect-Engineered TiO<sub>2-x</sub>: A Mode for Sensitive Photoelectrochemical Biosensing. *Analytical Chemistry* **90**, 2425–2429 (2018).
399. Shen, S. *et al.* Titanium dioxide nanostructures for photoelectrochemical applications. *Progress in Materials Science* vol. 98 299–385 (2018).
400. Aikens, D. A. Electrochemical methods, fundamentals and applications. *Journal of Chemical Education* **60**, A25 (1983).
401. Honda, A. & Fujishima, K. Electrochemical Photolysis of Water at a Semiconductor Electrode. *Nature* **238**, 37–38 (1972).
402. Konstantinou, I. K. & Albanis, T. A. TiO<sub>2</sub>-assisted photocatalytic degradation of azo dyes in aqueous solution: Kinetic and mechanistic investigations: A review. *Applied Catalysis B: Environmental* **49**, 1–14 (2004).
403. Barakat, M. A. New trends in removing heavy metals from industrial wastewater. *Arabian Journal of Chemistry* **4**, 361–377 (2011).
404. Jardim, W. F., Moraes, S. G. & Takiyama, M. M. K. Photocatalytic degradation of aromatic chlorinated compounds using TiO<sub>2</sub>: Toxicity of intermediates. *Water Research* **31**, 1728–1732 (1997).
405. Lhomme, L., Brosillon, S. & Wolbert, D. Photocatalytic degradation of pesticides in pure water and a commercial agricultural solution on TiO<sub>2</sub> coated media. *Chemosphere* **70**, 381–386 (2008).
406. Dagher, R., Drogui, P. & Robert, D. Modified TiO<sub>2</sub> for environmental photocatalytic applications: A review. *Industrial and Engineering Chemistry Research* vol. 52 3581–3599 (2013).
407. Reddy, K. R., Hassan, M. & Gomes, V. G. Hybrid nanostructures based on titanium dioxide for enhanced photocatalysis. *Applied Catalysis A: General* **489**, 1–16 (2015).

408. Fu, G., Vary, P. S. & Lin, C.-T. Anatase TiO<sub>2</sub> Nanocomposites for Antimicrobial Coatings. *The Journal of Physical Chemistry B* **109**, 8889–8898 (2005).
409. Yan, Z., Wang, Z., Miao, Z. & Liu, Y. Dye-Sensitized and Localized Surface Plasmon Resonance Enhanced Visible-Light Photoelectrochemical Biosensors for Highly Sensitive Analysis of Protein Kinase Activity. *Analytical Chemistry* **88**, 922–929 (2016).
410. Shu, J., Qiu, Z., Lv, S., Zhang, K. & Tang, D. Plasmonic Enhancement Coupling with Defect-Engineered TiO<sub>2-x</sub>: A Mode for Sensitive Photoelectrochemical Biosensing. *Analytical Chemistry* **90**, 2425–2429 (2018).
411. Saha, S., Chan, Y. & Soleymani, L. Enhancing the Photoelectrochemical Response of DNA Biosensors Using Wrinkled Interfaces. *ACS Applied Materials and Interfaces* **10**, 31178–31185 (2018).
412. Fujishima, A., Rao, T. N. & Tryk, D. A. Titanium dioxide photocatalysis. *Journal of Photochemistry and Photobiology C: Photochemistry Reviews* **1**, 1–21 (2000).
413. Saraswat, S. K., Rodene, D. D. & Gupta, R. B. Recent advancements in semiconductor materials for photoelectrochemical water splitting for hydrogen production using visible light. *Renewable and Sustainable Energy Reviews* **89**, 228–248 (2018).
414. Joy, J., Mathew, J. & George, S. C. Nanomaterials for photoelectrochemical water splitting – review. *International Journal of Hydrogen Energy* **43**, 4804–4817 (2018).
415. Abdullah, H., Khan, M. M. R., Ong, H. R. & Yaakob, Z. Modified TiO<sub>2</sub> photocatalyst for CO<sub>2</sub> photocatalytic reduction: An overview. *Journal of CO<sub>2</sub> Utilization* **22**, 15–32 (2017).
416. Karthikeyan, K. T., Nithya, A. & Jothivenkatachalam, K. Photocatalytic and antimicrobial activities of chitosan-TiO<sub>2</sub> nanocomposite. *International Journal of Biological Macromolecules* **104**, 1762–1773 (2017).
417. Yan, K., Wang, R. & Zhang, J. A photoelectrochemical biosensor for o-aminophenol based on assembling of CdSe and DNA on TiO<sub>2</sub>film electrode. *Biosensors and Bioelectronics* **53**, 30–3074 (2014).
418. Kumar, S. G. & Rao, K. S. R. K. Comparison of modification strategies towards enhanced charge carrier separation and photocatalytic degradation activity of metal oxide semiconductors (TiO<sub>2</sub>, WO<sub>3</sub> and ZnO). *Applied Surface Science* **391**, 124–148 (2017).
419. Abdullah, H., Khan, M. M. R., Ong, H. R. & Yaakob, Z. Modified TiO<sub>2</sub> photocatalyst for CO<sub>2</sub> photocatalytic reduction: An overview. *Journal of CO<sub>2</sub> Utilization* **22**, 15–32 (2017).
420. Chemseddine, A. & Moritz, T. Nanostructuring Titania: Control over Nanocrystal Structure, Size, Shape, and Organization. *European Journal of Inorganic Chemistry* **1999**, 235–245 (1999).
421. Rajh, T. *et al.* Surface restructuring of nanoparticles: An efficient route for ligand-metal oxide crosstalk. *Journal of Physical Chemistry B* **106**, 10543–10552 (2002).
422. Lan, Y., Lu, Y. & Ren, Z. Mini review on photocatalysis of titanium dioxide nanoparticles and their solar applications. *Nano Energy* **2**, 1031–1045 (2013).
423. Park, H., Park, Y., Kim, W. & Choi, W. Surface modification of TiO<sub>2</sub> photocatalyst for environmental applications. *Journal of Photochemistry and Photobiology C: Photochemistry Reviews* vol. 15 1–20 (2013).

424. Xu, Q. *et al.* Direct Z-scheme photocatalysts: Principles, synthesis, and applications. *Materials Today* **21**, 1042–1063 (2018).
425. Reddy, K. R., Hassan, M. & Gomes, V. G. Hybrid nanostructures based on titanium dioxide for enhanced photocatalysis. *Applied Catalysis A: General* **489**, 1–16 (2015).
426. Fujishima, A., Rao, T. N. & Tryk, D. A. Titanium dioxide photocatalysis. *Journal of Photochemistry and Photobiology C: Photochemistry Reviews* **1**, 1–21 (2000).
427. Kim, E., Liu, Y., Bentley, W. E. & Payne, G. F. Redox capacitor to establish bio-device redox-connectivity. *Advanced Functional Materials* **22**, 1409–1416 (2012).
428. Pesci, F. M., Wang, G., Klug, D. R., Li, Y. & Cowan, A. J. Efficient suppression of electron-hole recombination in oxygen-deficient hydrogen-treated TiO<sub>2</sub> nanowires for photoelectrochemical water splitting. *Journal of Physical Chemistry C* **117**, 25837–25844 (2013).
429. Shankar, K. *et al.* Recent Advances in the Use of TiO<sub>2</sub> Nanotube and Nanowire Arrays for Oxidative. *J. Phys. Chem. C* **113**, 6327–6359 (2009).
430. Snaith, H. J. *et al.* Efficiency enhancements in solid-state hybrid solar cells via reduced charge recombination and increased light capture. *Nano Letters* **7**, 3372–3376 (2007).
431. Fattakhova-rohl, D., Zaleska, A. & Bein, T. Three-Dimensional Titanium Dioxide Nanomaterials. *Chemical Reviews* **114**, 9487–9558 (2014).
432. Zhang, Q.-H., Han, W.-D., Hong, Y.-J. & Yu, J.-G. Photocatalytic reduction of CO<sub>2</sub> with H<sub>2</sub>O on Pt-loaded TiO<sub>2</sub> catalyst. *Catalysis Today* **148**, 335–340 (2009).
433. Bellardita, M., Di Paola, A., Megna, B. & Palmisano, L. Determination of the crystallinity of TiO<sub>2</sub> photocatalysts. *Journal of Photochemistry and Photobiology A: Chemistry* **367**, 312–320 (2018).
434. Qian, R. *et al.* Charge carrier trapping, recombination and transfer during TiO<sub>2</sub> photocatalysis: An overview. *Catalysis Today* (2018) doi:10.1016/j.cattod.2018.10.053.
435. Ohtani, B., Prieto-Mahaney, O. O., Li, D. & Abe, R. What is Degussa (Evonic) P25? Crystalline composition analysis, reconstruction from isolated pure particles and photocatalytic activity test. *Journal of Photochemistry and Photobiology A: Chemistry* **216**, 179–182 (2010).
436. Apopei, P., Catrinescu, C., Teodosiu, C. & Royer, S. Mixed-phase TiO<sub>2</sub> photocatalysts: Crystalline phase isolation and reconstruction, characterization and photocatalytic activity in the oxidation of 4-chlorophenol from aqueous effluents. *Applied Catalysis B: Environmental* **160–161**, 374–382 (2014).
437. Li, S. *et al.* “Signal-off” photoelectrochemical DNA sensing strategy based on target dependent DNA probe conformational conversion using CdS quantum dots sensitized TiO<sub>2</sub>nanorods array as photoactive material. *Journal of Electroanalytical Chemistry* **759**, 38–45 (2015).
438. Hantusch, M., Bessergenev, V., Mateus, M. C., Knupfer, M. & Burkel, E. Electronic properties of photocatalytic improved Degussa P25 titanium dioxide powder. *Catalysis Today* **307**, 111–118 (2018).
439. Wang, X. *et al.* Enhanced Photoelectrochemical Behavior of H-TiO<sub>2</sub> Nanorods Hydrogenated by Controlled and Local Rapid Thermal Annealing. *Nanoscale Research Letters* **12**, (2017).

440. Lü, X. *et al.* Conducting Interface in Oxide Homojunction: Understanding of Superior Properties in Black TiO<sub>2</sub>. *Nano Letters* **16**, 5751–5755 (2016).
441. Yan, P. *et al.* Photoelectrochemical water splitting promoted with a disordered surface layer created by electrochemical reduction. *ACS Applied Materials and Interfaces* **7**, 3791–3796 (2015).
442. Fan, C. *et al.* Black Hydroxylated Titanium Dioxide Prepared via Ultrasonication with Enhanced Photocatalytic Activity. *Scientific Reports* **5**, 11712 (2015).
443. Li, S. *et al.* “Signal-off” photoelectrochemical DNA sensing strategy based on target dependent DNA probe conformational conversion using CdS quantum dots sensitized TiO<sub>2</sub>nanorods array as photoactive material. *Journal of Electroanalytical Chemistry* **759**, 38–45 (2015).
444. Yan, K., Wang, R. & Zhang, J. A photoelectrochemical biosensor for o-aminophenol based on assembling of CdSe and DNA on TiO<sub>2</sub>film electrode. *Biosensors and Bioelectronics* **53**, 30–3074 (2014).
445. Kumar, S. G. & Rao, K. S. R. K. Comparison of modification strategies towards enhanced charge carrier separation and photocatalytic degradation activity of metal oxide semiconductors (TiO<sub>2</sub>, WO<sub>3</sub> and ZnO). *Applied Surface Science* **391**, 124–148 (2017).
446. Fattakhova-rohl, D., Zaleska, A. & Bein, T. Three-Dimensional Titanium Dioxide Nanomaterials. *Chemical Reviews* **114**, 9487–9558 (2014).
447. Yu, J., Yu, H., Cheng, B. & Trapalis, C. Effects of calcination temperature on the microstructures and photocatalytic activity of titanate nanotubes. *Journal of Molecular Catalysis A: Chemical* **249**, 135–142 (2006).
448. Tebby, Z. *et al.* A simple route towards low-temperature processing of nanoporous thin films using UV-irradiation: Application for dye solar cells. *Journal of Photochemistry and Photobiology A: Chemistry* **205**, 70–76 (2009).
449. Lewis, L. N. *et al.* A novel UV-mediated low-temperature sintering of TiO<sub>2</sub> for dye-sensitized solar cells. *Solar Energy Materials and Solar Cells* **90**, 1041–1051 (2006).
450. Grätzel, M. & Kay, A. Low Cost Photovoltaic Modules Based on Dye Sensitized Nanocrystalline Titanium Dioxide and Carbon Powder. *Solar Energy Materials & Solar Cells* **44**, 99–117 (2006).
451. De Marco, L. *et al.* Novel preparation method of TiO<sub>2</sub>-nanorod-based photoelectrodes for dye-sensitized solar cells with improved light-harvesting efficiency. *Journal of Physical Chemistry C* **114**, 4228–4236 (2010).
452. Hagfeldt, A. *et al.* A New Method for Manufacturing Nanostructured Electrodes on Plastic Substrates. *Nano Letters* **1**, 97–100 (2001).
453. Yu, H. *et al.* High-performance TiO<sub>2</sub> photoanode with an efficient electron transport network for dye-sensitized solar cells. *Journal of Physical Chemistry C* **113**, 16277–16282 (2009).
454. Miyasaka, T., Kijitori, ã. Y., Murakami, T. N., Kimura, M. & Uegusa, S. Efficient Nonsintering Type Dye-sensitized Photocells Based on Electrophoretically Deposited Voltage. *Chemistry Letters* 1250–1251 (2002) doi:10.1246/cl.2002.1250.
455. Tahir, A. A., Peiris, T. A. N. & Wijyantha, K. G. U. Enhancement of photoelectrochemical performance of AACVD-produced TiO<sub>2</sub> electrodes by microwave irradiation while preserving the nanostructure. *Chemical Vapor Deposition* **18**, 107–111 (2012).

456. Soleymani, L. & Li, F. Mechanistic Challenges and Advantages of Biosensor Miniaturization into the Nanoscale. *ACS Sensors* **2**, 458–467 (2017).
457. Tae, E. L. *et al.* A strategy to increase the efficiency of the dye-sensitized TiO<sub>2</sub> solar cells operated by photoexcitation of dye-to-TiO<sub>2</sub> charge-transfer bands. *Journal of Physical Chemistry B* **109**, 22513–22522 (2005).
458. Ata, M. S., Liu, Y. & Zhitomirsky, I. A review of new methods of surface chemical modification, dispersion and electrophoretic deposition of metal oxide particles. *RSC Advances* **4**, 22716–22732 (2014).
459. Li, L. & Zeng, H. Marine mussel adhesion and bio-inspired wet adhesives. *Biotribology* **5**, 44–51 (2016).
460. Clifford, A., Pang, X. & Zhitomirsky, I. Biomimetically modified chitosan for electrophoretic deposition of composites. *Colloids and Surfaces A: Physicochemical and Engineering Aspects* **544**, 28–34 (2018).
461. Ryu, J. H., Hong, S. & Lee, H. Bio-inspired adhesive catechol-conjugated chitosan for biomedical applications: A mini review. *Acta Biomaterialia* vol. 27 101–115 (2015).
462. Clifford, A., Pang, X. & Zhitomirsky, I. Biomimetically modified chitosan for electrophoretic deposition of composites. *Colloids and Surfaces A: Physicochemical and Engineering Aspects* **544**, 28–34 (2018).
463. Ata, M. S., Liu, Y. & Zhitomirsky, I. A review of new methods of surface chemical modification, dispersion and electrophoretic deposition of metal oxide particles. *RSC Advances* **4**, 22716–22732 (2014).
464. Janković, I. a., Šaponjić, Z. V., Čomor, M. I. & Nedeljković, J. M. Surface Modification of Colloidal TiO<sub>2</sub> Nanoparticles with Bidentate Benzene Derivatives. *The Journal of Physical Chemistry C* **113**, 12645–12652 (2009).
465. Wang, G. L., Xu, J. J. & Chen, H. Y. Dopamine sensitized nanoporous TiO<sub>2</sub> film on electrodes: Photoelectrochemical sensing of NADH under visible irradiation. *Biosensors and Bioelectronics* **24**, 2494–2498 (2009).
466. Wang, G. L., Xu, J. J. & Chen, H. Y. Dopamine sensitized nanoporous TiO<sub>2</sub> film on electrodes: Photoelectrochemical sensing of NADH under visible irradiation. *Biosensors and Bioelectronics* **24**, 2494–2498 (2009).
467. Janković, I. a., Šaponjić, Z. V., Čomor, M. I. & Nedeljković, J. M. Surface Modification of Colloidal TiO<sub>2</sub> Nanoparticles with Bidentate Benzene Derivatives. *The Journal of Physical Chemistry C* **113**, 12645–12652 (2009).
468. Kim, E. *et al.* Biomimetic approach to confer redox activity to thin chitosan films. *Advanced Functional Materials* **20**, 2683–2694 (2010).
469. Khan, R. & Dhayal, M. Electrochemical studies of novel chitosan/TiO<sub>2</sub> bioactive electrode for biosensing application. *Electrochemistry Communications* **10**, 263–267 (2008).
470. Karthikeyan, K. T., Nithya, A. & Jothivenkatachalam, K. Photocatalytic and antimicrobial activities of chitosan-TiO<sub>2</sub> nanocomposite. *International Journal of Biological Macromolecules* **104**, 1762–1773 (2017).
471. Pan, S., Wu, S. & Kim, J. Preparation of glucosamine by hydrolysis of chitosan with commercial  $\alpha$ -amylase and glucoamylase. *Journal of Zhejiang University SCIENCE B* **12**, 931–934 (2011).

472. Socrates, G. *Infrared and Raman characteristic group frequencies. Infrared and Raman characteristic group frequencies: tables and charts* (2004). doi:10.1002/jrs.1238.
473. Socrates, G. *Infrared and Raman characteristic group frequencies. Infrared and Raman characteristic group frequencies: tables and charts* (2004). doi:10.1002/jrs.1238.
474. Khan, R. & Dhayal, M. Electrochemical studies of novel chitosan/TiO<sub>2</sub> bioactive electrode for biosensing application. *Electrochemistry Communications* **10**, 263–267 (2008).
475. Norranattrakul, P. Fabrication of chitosan/titanium dioxide composites film for the photocatalytic degradation of dye. *Journal of Metals, Materials and Minerals* **23**, 9–22 (2013).
476. Ni, M., Leung, M. K. H., Leung, D. Y. C. & Sumathy, K. A review and recent developments in photocatalytic water-splitting using TiO<sub>2</sub> for hydrogen production. *Renewable and Sustainable Energy Reviews* **11**, 401–425 (2007).
477. Fan, D. *et al.* An ultrasensitive label-free immunosensor based on CdS sensitized Fe-TiO<sub>2</sub> with high visible-light photoelectrochemical activity. *Biosensors and Bioelectronics* **74**, 843–848 (2015).
478. Janković, I. A., Šaponjić, Z. V., Džunuzović, E. S. & Nedeljković, J. M. New Hybrid Properties of TiO<sub>2</sub> Nanoparticles Surface Modified With Catecholate Type Ligands. *Nanoscale Research Letters* **5**, 81–88 (2010).
479. Plana, D. & Fermín, D. J. Photoelectrochemical activity of colloidal TiO<sub>2</sub> nanostructures assembled at polarisable liquid/liquid interfaces. *Journal of Electroanalytical Chemistry* **780**, 373–378 (2016).
480. Kenkel, J. *Analytical Chemistry for Technicians, Third Edition.* (2002). doi:10.1201/9781420056709.
481. Saha, S., Chan, Y. & Soleymani, L. Enhancing the Photoelectrochemical Response of DNA Biosensors Using Wrinkled Interfaces. *ACS Applied Materials and Interfaces* **10**, 31178–31185 (2018).
482. Yan, K., Liu, Y., Yang, Y. & Zhang, J. A Cathodic “signal-off” Photoelectrochemical Aptasensor for Ultrasensitive and Selective Detection of Oxytetracycline. *Analytical Chemistry* **87**, 12215–12220 (2015).
483. Galasso, K., Livache, T., Roget, A. & Vieil, E. Electrogravimetric detection of DNA hybridization on polypyrrole copolymer. *Journal de Chimie Physique et de Physico-Chimie Biologique* **95**, 1514–1517 (1998).
484. Xagas, A. P. *et al.* Surface modification and photosensitisation of TiO<sub>2</sub> nanocrystalline films with ascorbic acid. *Journal of Photochemistry and Photobiology A: Chemistry* **132**, 115–120 (2000).
485. Fujishima, A., Rao, T. N. & Tryk, D. A. Titanium dioxide photocatalysis. *Journal of Photochemistry and Photobiology C: Photochemistry Reviews* **1**, 1–21 (2000).
486. Ochiai, T. & Fujishima, A. Photoelectrochemical properties of TiO<sub>2</sub> photocatalyst and its applications for environmental purification. *Journal of Photochemistry and Photobiology C: Photochemistry Reviews* **13**, 247–262 (2012).
487. Lan, Y., Lu, Y. & Ren, Z. Mini review on photocatalysis of titanium dioxide nanoparticles and their solar applications. *Nano Energy* **2**, 1031–1045 (2013).

488. Ratchford, D. C., Dunkelberger, A. D., Vurgaftman, I., Owrutsky, J. C. & Pehrsson, P. E. Quantification of Efficient Plasmonic Hot-Electron Injection in Gold Nanoparticle–TiO<sub>2</sub> Films. *Nano Letters* **17**, 6047–6055 (2017).
489. Du, L., Furube, A., Hara, K., Katoh, R. & Tachiya, M. Ultrafast plasmon induced electron injection mechanism in gold–TiO<sub>2</sub> nanoparticle system. *Journal of Photochemistry and Photobiology C: Photochemistry Reviews* **15**, 21–30 (2013).
490. Ratchford, D. C., Dunkelberger, A. D., Vurgaftman, I., Owrutsky, J. C. & Pehrsson, P. E. Quantification of Efficient Plasmonic Hot-Electron Injection in Gold Nanoparticle–TiO<sub>2</sub> Films. *Nano Letters* **17**, 6047–6055 (2017).
491. Achermann, M. Exciton-plasmon interactions in metal-semiconductor nanostructures. *Journal of Physical Chemistry Letters* **1**, 2837–2843 (2010).
492. Clavero, C. Plasmon-induced hot-electron generation at nanoparticle/metal-oxide interfaces for photovoltaic and photocatalytic devices. *Nature Photonics* **8**, 95 (2014).
493. Yen, Y.-C., Chen, J.-A., Ou, S., Chen, Y.-S. & Lin, K.-J. Plasmon-Enhanced Photocurrent using Gold Nanoparticles on a Three-Dimensional TiO<sub>2</sub> Nanowire-Web Electrode. *Scientific Reports* **7**, 42524 (2017).
494. Pu, Y.-C. *et al.* Au Nanostructure-Decorated TiO<sub>2</sub> Nanowires Exhibiting Photoactivity Across Entire UV-visible Region for Photoelectrochemical Water Splitting. *Nano Letters* **13**, 3817–3823 (2013).
495. Victorious, A., Saha, S., Pandey, R., Didar, T. F. & Soleymani, L. Affinity-Based Detection of Biomolecules Using Photo-Electrochemical Readout. *Frontiers in Chemistry* **7**, 617 (2019).
496. Chandrasekharan, N. & Kamat, P. V. Improving the Photoelectrochemical Performance of Nanostructured TiO<sub>2</sub> Films by Adsorption of Gold Nanoparticles †. *The Journal of Physical Chemistry B* **104**, 10851–10857 (2002).
497. Naseri, N., Amiri, M. & Moshfegh, A. Z. Visible photoenhanced current-voltage characteristics of Au:TiO<sub>2</sub> nanocomposite thin films as photoanodes. *Journal of Physics D: Applied Physics* **43**, 105405 (2010).
498. Li, J. *et al.* Plasmon-induced photonic and energy-transfer enhancement of solar water splitting by a hematite nanorod array. *Nature Communications* **4**, 2651 (2013).
499. Rayalu, S. S. *et al.* Photocatalytic water splitting on Au/TiO<sub>2</sub> nanocomposites synthesized through various routes: Enhancement in photocatalytic activity due to SPR effect. *Applied Catalysis B: Environmental* **142–143**, 684–693 (2013).
500. Murdoch, M. *et al.* The effect of gold loading and particle size on photocatalytic hydrogen production from ethanol over Au/TiO<sub>2</sub> nanoparticles. *Nature Chemistry* **3**, 489 (2011).
501. Subramanian, V., Wolf, E. & Kamat, P. V. Semiconductor–Metal Composite Nanostructures. To What Extent Do Metal Nanoparticles Improve the Photocatalytic Activity of TiO<sub>2</sub> Films? *The Journal of Physical Chemistry B* **105**, 11439–11446 (2001).
502. Saha, S. *et al.* Differential Photoelectrochemical Biosensing Using DNA Nanospacers to Modulate Electron Transfer between Metal and Semiconductor Nanoparticles. *ACS Applied Materials & Interfaces* **12**, 36895–36905 (2020).

503. Tran, H., Pera, F., McPherson, D. S., Viorel, D. & Voinigescu, S. P. 6-k/spl Omega/ 43-Gb/s differential transimpedance-limiting amplifier with auto-zero feedback and high dynamic range. *IEEE Journal of Solid-State Circuits* **39**, 1680–1689 (2004).
504. Hao, N. *et al.* Design of a Dual Channel Self-Reference Photoelectrochemical Biosensor. *Analytical Chemistry* **89**, 10133–10136 (2017).
505. Victorious, A., Clifford, A., Saha, S., Zhitomirsky, I. & Soleymani, L. Integrating TiO<sub>2</sub> Nanoparticles within a Catecholic Polymeric Network Enhances the Photoelectrochemical Response of Biosensors. *The Journal of Physical Chemistry C* **123**, 16186–16193 (2019).
506. Sakib, S., Pandey, R., Soleymani, L. & Zhitomirsky, I. Surface modification of TiO<sub>2</sub> for photoelectrochemical DNA biosensors. *MEDICAL DEVICES & SENSORS* **3**, (2020).
507. Grabar, K. C., Freeman, R. Griffith., Hommer, M. B. & Natan, M. J. Preparation and Characterization of Au Colloid Monolayers. *Analytical Chemistry* **67**, 735–743 (1995).
508. Chandrasekharan, N. & Kamat, P. V. Improving the Photoelectrochemical Performance of Nanostructured TiO<sub>2</sub> Films by Adsorption of Gold Nanoparticles. *The Journal of Physical Chemistry B* **104**, 10851–10857 (2000).
509. Zhang, J., Song, S., Wang, L., Pan, D. & Fan, C. A gold nanoparticle-based chronocoulometric DNA sensor for amplified detection of DNA. *Nature Protocols* **2**, 2888–2895 (2007).
510. Sundararaman, R., Narang, P., Jermyn, A. S., Goddard, W. A. & Atwater, H. A. Theoretical predictions for hot-carrier generation from surface plasmon decay. *Nature Communications* **5**, 5788 (2014).
511. Moon, S. Y. *et al.* Plasmonic hot carrier-driven oxygen evolution reaction on Au nanoparticles/TiO<sub>2</sub> nanotube arrays. *Nanoscale* **10**, 22180–22188 (2018).
512. Pinchuk, A., Kreibig, U. & Hilger, A. Optical properties of metallic nanoparticles: influence of interface effects and interband transitions. *Surface Science* **557**, 269–280 (2004).
513. Pinchuk, A., Plessen, G. von & Kreibig, U. Influence of interband electronic transitions on the optical absorption in metallic nanoparticles. *Journal of Physics D: Applied Physics* **37**, 3133–3139 (2004).
514. Tan, S. *et al.* Plasmonic coupling at a metal/semiconductor interface. *Nature Photonics* **11**, 806–812 (2017).
515. Li, J. *et al.* Distinguishing surface effects of gold nanoparticles from plasmonic effect on photoelectrochemical water splitting by hematite. *Journal of Materials Research* **31**, 1608–1615 (2016).
516. Meng, F., Cushing, S. K., Li, J., Hao, S. & Wu, N. Enhancement of Solar Hydrogen Generation by Synergistic Interaction of La<sub>2</sub>Ti<sub>2</sub>O<sub>7</sub> Photocatalyst with Plasmonic Gold Nanoparticles and Reduced Graphene Oxide Nanosheets. *ACS Catalysis* **5**, 1949–1955 (2015).
517. Naphade, R. A., Tathavadekar, M., Jog, J. P., Agarkar, S. & Ogale, S. Plasmonic light harvesting of dye sensitized solar cells by Au-nanoparticle loaded TiO<sub>2</sub> nanofibers. *Journal of Materials Chemistry A* **2**, 975–984 (2014).
518. An, X., Hu, C., Liu, H. & Qu, J. Hierarchical Nanotubular Anatase/Rutile/TiO<sub>2</sub>(B) Heterophase Junction with Oxygen Vacancies for Enhanced Photocatalytic H<sub>2</sub> Production. *Langmuir* **34**, 1883–1889 (2018).

519. Minutella, E., Schulz, F. & Lange, H. Excitation-Dependence of Plasmon-Induced Hot Electrons in Gold Nanoparticles. *The Journal of Physical Chemistry Letters* **8**, 4925–4929 (2017).
520. Robotjazi, H., Bahauddin, S. M., Doiron, C. & Thomann, I. Direct Plasmon-Driven Photoelectrocatalysis. *Nano Letters* **15**, 6155–6161 (2015).
521. Gelderman, K., Lee, L. & Donne, S. W. Flat-Band Potential of a Semiconductor: Using the Mott–Schottky Equation. *Journal of Chemical Education* **84**, 685 (2007).
522. Shu, J., Qiu, Z., Lv, S., Zhang, K. & Tang, D. Plasmonic Enhancement Coupling with Defect-Engineered TiO<sub>2-x</sub>: A Mode for Sensitive Photoelectrochemical Biosensing. *Analytical Chemistry* **90**, 2425–2429 (2018).
523. Ni, M., Leung, M. K. H., Leung, D. Y. C. & Sumathy, K. A review and recent developments in photocatalytic water-splitting using TiO<sub>2</sub> for hydrogen production. *Renewable and Sustainable Energy Reviews* **11**, 401–425 (2007).
524. Schlather, A. E. *et al.* Hot Hole Photoelectrochemistry on Au@SiO<sub>2</sub>@Au Nanoparticles. *Journal of Physical Chemistry Letters* **8**, 2060–2067 (2017).
525. Subramanian, V., Wolf, E. & Kamat, P. V. Semiconductor–Metal Composite Nanostructures. To What Extent Do Metal Nanoparticles Improve the Photocatalytic Activity of TiO<sub>2</sub> Films? *The Journal of Physical Chemistry B* **105**, 11439–11446 (2001).
526. Gomes Silva, C., Juárez, R., Marino, T., Molinari, R. & García, H. Influence of Excitation Wavelength (UV or Visible Light) on the Photocatalytic Activity of Titania Containing Gold Nanoparticles for the Generation of Hydrogen or Oxygen from Water. *J Am Chem Soc* **133**, 595–602 (2011).
527. Nbelayim, P., Kawamura, G., Kian Tan, W., Muto, H. & Matsuda, A. Systematic characterization of the effect of Ag@TiO<sub>2</sub> nanoparticles on the performance of plasmonic dye-sensitized solar cells. *Scientific Reports* **7**, 15690 (2017).
528. Lim, S. P., Pandikumar, A., Lim, H. N., Ramaraj, R. & Huang, N. M. Boosting Photovoltaic Performance of Dye-Sensitized Solar Cells Using Silver Nanoparticle-Decorated N,S-Co-Doped-TiO<sub>2</sub> Photoanode. *Scientific Reports* **5**, 11922 (2015).
529. Wen, C., Ishikawa, K., Kishima, M. & Yamada, K. Effects of silver particles on the photovoltaic properties of dye-sensitized TiO<sub>2</sub> thin films. *Solar Energy Materials and Solar Cells* **61**, 339–351 (2000).
530. Zhao, J. *et al.* A Comparison of Photocatalytic Activities of Gold Nanoparticles Following Plasmonic and Interband Excitation and a Strategy for Harnessing Interband Hot Carriers for Solution Phase Photocatalysis. *ACS Central Science* **3**, 482–488 (2017).
531. Li, H. *et al.* Surface-Plasmon-Resonance-Enhanced Photoelectrochemical Water Splitting from Au-Nanoparticle-Decorated 3D TiO<sub>2</sub> Nanorod Architectures. *The Journal of Physical Chemistry C* **121**, 12071–12079 (2017).
532. Cushing, S. K. *et al.* Controlling Plasmon-Induced Resonance Energy Transfer and Hot Electron Injection Processes in Metal@TiO<sub>2</sub> Core–Shell Nanoparticles. *J. Phys. Chem. C* **119**, 16239–16244 (2015).
533. Cushing, S. K. & Wu, N. photocatalyst-SPR enhanced solar energy harvesting-Interface. *The Electrochemical Society Interface* **22**, 63–67 (2013).

534. Wu, N. Plasmonic metal–semiconductor photocatalysts and photoelectrochemical cells: a review. *Nanoscale* **10**, 2679–2696 (2018).
535. Xu, Z. *et al.* Understanding the Enhancement Mechanisms of Surface Plasmon-Mediated Photoelectrochemical Electrodes: A Case Study on Au Nanoparticle Decorated TiO<sub>2</sub> Nanotubes. *Advanced Materials Interfaces* **2**, 1500169 (2015).
536. Bettazzi, F. *et al.* Ascorbic acid-sensitized Au nanorods-functionalized nanostructured TiO<sub>2</sub> transparent electrodes for photoelectrochemical genosensing. *Electrochimica Acta* **276**, 389–398 (2018).
537. Chu, Y., Wu, R., Fan, G.-C., Deng, A.-P. & Zhu, J.-J. Enzyme-Free Photoelectrochemical Biosensor Based on the Co-Sensitization Effect Coupled with Dual Cascade Toehold-Mediated Strand Displacement Amplification for the Sensitive Detection of MicroRNA-21. *ACS Sustainable Chemistry & Engineering* **6**, 11633–11641 (2018).
538. Nootchanat, S. *et al.* Investigation of localized surface plasmon/grating-coupled surface plasmon enhanced photocurrent in TiO<sub>2</sub> thin films. *Physical Chemistry Chemical Physics* **16**, 24484–24492 (2014).
539. Hao, Q. *et al.* A wavelength-resolved ratiometric photoelectrochemical technique: design and sensing applications. *Chemical Science* **7**, 774–780 (2016).
540. Qiu, Z., Shu, J., Liu, J. & Tang, D. Dual-Channel Photoelectrochemical Ratiometric Aptasensor with up-Converting Nanocrystals Using Spatial-Resolved Technique on Homemade 3D Printed Device. *Analytical Chemistry* **91**, 1260–1268 (2019).
541. Soleymani, L. & Li, F. Mechanistic Challenges and Advantages of Biosensor Miniaturization into the Nanoscale. *ACS Sensors* **2**, 458–467 (2017).
542. Turner, A. P. F. Biosensors: sense and sensibility. *Chemical Society Reviews* **42**, 3184–3196 (2013).
543. Zhang, B. *et al.* Fe<sup>3+</sup> doped ZnO-Ag photocatalyst for photoelectrochemical sensing platform of ultrasensitive Hg<sup>2+</sup> detection using exonuclease III-assisted target recycling and DNAzyme-catalyzed amplification. *Sensors and Actuators B: Chemical* **255**, 2531–2537 (2018).
544. Zhao, W.-W., Xu, J.-J. & Chen, H.-Y. Photoelectrochemical aptasensing. *TrAC Trends in Analytical Chemistry* **82**, 307–315 (2016).
545. Zeng, X., Ma, S., Bao, J., Tu, W. & Dai, Z. Using graphene-based plasmonic nanocomposites to quench energy from quantum dots for signal-on photoelectrochemical aptasensing. *Analytical Chemistry* **85**, 11720–11724 (2013).
546. Schoukroun-Barnes, L. R. *et al.* Reagentless, Structure-Switching, Electrochemical Aptamer-Based Sensors. *Annual Review of Analytical Chemistry* **9**, 163–181 (2016).
547. Xing, H. *et al.* Multimodal Detection of a Small Molecule Target Using Stimuli-Responsive Liposome Triggered by Aptamer–Enzyme Conjugate. *Analytical Chemistry* **88**, 1506–1510 (2016).
548. Weerathunge, P., Ramanathan, R., Shukla, R., Sharma, T. K. & Bansal, V. Aptamer-Controlled Reversible Inhibition of Gold Nanozyme Activity for Pesticide Sensing. *Analytical Chemistry* **86**, 11937–11941 (2014).
549. Sergelen, K., Liedberg, B., Knoll, W. & Dostálek, J. A surface plasmon field-enhanced fluorescence reversible split aptamer biosensor. *Analyst* **142**, 2995–3001 (2017).

550. Hao, N. *et al.* Multiple signal-amplification via Ag and TiO<sub>2</sub> decorated 3D nitrogen doped graphene hydrogel for fabricating sensitive label-free photoelectrochemical thrombin aptasensor. *Biosensors and Bioelectronics* **101**, 14–20 (2018).
551. Zang, Y., Lei, J. & Ju, H. Principles and applications of photoelectrochemical sensing strategies based on biofunctionalized nanostructures. *Biosensors and Bioelectronics* **96**, 8–16 (2017).
552. Muench, F. *et al.* Nano- and microstructured silver films synthesised by halide-assisted electroless plating. *New J. Chem.* **39**, 6803--6812 (2015).
553. Lai, R. Y., Lee, S., Soh, H. T., Plaxco, K. W. & Heeger, A. J. Differential Labeling of Closely Spaced Biosensor Electrodes via Electrochemical Lithography. *Langmuir* **22**, 1932–1936 (2006).
554. Zheng, Y.-N. *et al.* Universal Ratiometric Photoelectrochemical Bioassay with Target-Nucleotide Transduction-Amplification and Electron-Transfer Tunneling Distance Regulation Strategies for Ultrasensitive Determination of microRNA in Cells. *Analytical Chemistry* **89**, 9445–9451 (2017).
555. Hua, R. *et al.* A sensitive Potentiometric resolved ratiometric Photoelectrochemical aptasensor for Escherichia coli detection fabricated with non-metallic nanomaterials. *Biosensors and Bioelectronics* **106**, 57–63 (2018).
556. Wang, Y. *et al.* A visible light photoelectrochemical sensor for tumor marker detection using tin dioxide quantum dot-graphene as labels. *Analyst* **138**, 7112–7118 (2013).
557. Wang, M. *et al.* Photoelectrochemical biosensor for microRNA detection based on a MoS<sub>2</sub>/g-C<sub>3</sub>N<sub>4</sub>/black TiO<sub>2</sub> heterojunction with Histostar@AuNPs for signal amplification. *Biosensors and Bioelectronics* **128**, 137–143 (2019).
558. Lv, S., Zhang, K., Zeng, Y. & Tang, D. Double Photosystems-Based ‘Z-Scheme’ Photoelectrochemical Sensing Mode for Ultrasensitive Detection of Disease Biomarker Accompanying Three-Dimensional DNA Walker. *Analytical Chemistry* **90**, 7086–7093 (2018).
559. Dai, H., Zhang, S., Hong, Z. & Lin, Y. A Potentiometric Addressable Photoelectrochemical Biosensor for Sensitive Detection of Two Biomarkers. *Analytical Chemistry* **88**, 9532–9538 (2016).
560. Li, J.-M., Cheng, H.-Y., Chiu, Y.-H. & Hsu, Y.-J. ZnO–Au–SnO<sub>2</sub> Z-scheme photoanodes for remarkable photoelectrochemical water splitting. *Nanoscale* **8**, 15720–15729 (2016).
561. Huang, Y.-L. *et al.* Tunable photoelectrochemical performance of Au/BiFeO<sub>3</sub> heterostructure. *Nanoscale* **8**, 15795–15801 (2016).
562. Li, J.-M. *et al.* TiO<sub>2</sub>-Au-Cu<sub>2</sub>O Photocathodes: Au-Mediated Z-Scheme Charge Transfer for Efficient Solar-Driven Photoelectrochemical Reduction. *ACS Applied Nano Materials* **1**, 6843–6853 (2018).
563. Chiu, Y.-H. *et al.* Yolk-shell nanostructures as an emerging photocatalyst paradigm for solar hydrogen generation. *Nano Energy* **62**, 289–298 (2019).
564. Chen, K.-H. *et al.* Ag-Nanoparticle-Decorated SiO<sub>2</sub> Nanospheres Exhibiting Remarkable Plasmon-Mediated Photocatalytic Properties. *The Journal of Physical Chemistry C* **116**, 19039–19045 (2012).
565. Luo, Q. *et al.* Super non-linear RRAM with ultra-low power for 3D vertical nano-crossbar arrays. *Nanoscale* **8**, 15629–15636 (2016).

566. Hao, N., Hua, R., Zhang, K., Lu, J. & Wang, K. A Sunlight Powered Portable Photoelectrochemical Biosensor Based on a Potentiometric Resolved Ratiometric Principle. *Analytical Chemistry* **90**, 13207–13211 (2018).
567. Zhang, Y. *et al.* A potentiometric resolved ratiometric photoelectrochemical aptasensor. *Chemical Communications* **53**, 5810–5813 (2017).
568. Li, Z., Su, C., Wu, D. & Zhang, Z. Gold Nanoparticles Decorated Hematite Photoelectrode for Sensitive and Selective Photoelectrochemical Aptasensing of Lysozyme. *Analytical Chemistry* **90**, 961–967 (2018).
569. Cao, C., Zhang, F., Goldys, E. M., Gao, F. & Liu, G. Advances in structure-switching aptasensing towards real time detection of cytokines. *TrAC Trends in Analytical Chemistry* **102**, 379–396 (2018).
570. Gelderman, K., Lee, L. & Donne, S. W. Flat-Band Potential of a Semiconductor: Using the Mott–Schottky Equation. *Journal of Chemical Education* **84**, 685 (2007).
571. Anne, A. & Demaille, C. Electron Transport by Molecular Motion of redox-DNA Strands: Unexpectedly Slow Rotational Dynamics of 20-mer ds-DNA Chains End-Grafted onto Surfaces via C6 Linkers. *J Am Chem Soc* **130**, 9812–9823 (2008).
572. Murphy, M. C., Rasnik, I., Cheng, W., Lohman, T. M. & Ha, T. Probing Single-Stranded DNA Conformational Flexibility Using Fluorescence Spectroscopy. *Biophysical Journal* **86**, 2530–2537 (2004).
573. Tello, A., Cao, R., Marchant, M. J. & Gomez, H. Conformational Changes of Enzymes and Aptamers Immobilized on Electrodes. *Bioconjugate Chemistry* **27**, 2581–2591 (2016).
574. Ferapontova, E. E. DNA Electrochemistry and Electrochemical Sensors for Nucleic Acids. *Annual Review of Analytical Chemistry* **11**, 197–218 (2018).
575. Saha, S., Chan, Y. & Soleymani, L. Enhancing the Photoelectrochemical Response of DNA Biosensors Using Wrinkled Interfaces. *ACS Applied Materials & Interfaces* **10**, 31178–31185 (2018).
576. Rivetti, C., Walker, C. & Bustamante, C. Polymer chain statistics and conformational analysis of DNA molecules with bends or sections of different flexibility. *Journal of Molecular Biology* **280**, 41–59 (1998).
577. Anne, A. & Demaille, C. Dynamics of Electron Transport by Elastic Bending of Short DNA Duplexes. Experimental Study and Quantitative Modeling of the Cyclic Voltammetric Behavior of 3'-Ferrocenyl DNA End-Grafted on Gold. *J Am Chem Soc* **128**, 542–557 (2006).
578. Rant, U. *et al.* Dissimilar Kinetic Behavior of Electrically Manipulated Single- and Double-Stranded DNA Tethered to a Gold Surface. *Biophysical Journal* **90**, 3666–3671 (2006).
579. Naphade, R. A., Tathavadekar, M., Jog, J. P., Agarkar, S. & Ogale, S. Plasmonic light harvesting of dye sensitized solar cells by Au-nanoparticle loaded TiO<sub>2</sub> nanofibers. *Journal of Materials Chemistry A* **2**, 975–984 (2014).
580. White, T. P. & Catchpole, K. R. Plasmon-enhanced internal photoemission for photovoltaics: Theoretical efficiency limits. *Applied Physics Letters* **101**, 073905 (2012).
581. Liu, Z., Hou, W., Pavaskar, P., Aykol, M. & Cronin, S. B. Plasmon resonant enhancement of photocatalytic water splitting under visible illumination. *Nano Letters* **11**, 1111–1116 (2011).

582. Hou, W. & Cronin, S. B. A Review of Surface Plasmon Resonance Enhanced Photocatalysis. *Advanced Functional Materials* **23**, 1612–1619 (2013).
583. Cushing, S. K. *et al.* Photocatalytic Activity Enhanced by Plasmonic Resonant Energy Transfer from Metal to Semiconductor. *J Am Chem Soc* **134**, 15033–15041 (2012).
584. Cushing, S. K. & Wu, N. Progress and Perspectives of Plasmon-Enhanced Solar Energy Conversion. *The Journal of Physical Chemistry Letters* **7**, 666–675 (2016).
585. Wu, N. Plasmonic metal–semiconductor photocatalysts and photoelectrochemical cells: a review. *Nanoscale* **10**, 2679–2696 (2018).
586. Cushing, S. K. & Wu, N. Progress and Perspectives of Plasmon-Enhanced Solar Energy Conversion. *The Journal of Physical Chemistry Letters* **7**, 666–675 (2016).
587. Cushing, S. K. *et al.* Controlling Plasmon-Induced Resonance Energy Transfer and Hot Electron Injection Processes in Metal@TiO<sub>2</sub> Core–Shell Nanoparticles. *J. Phys. Chem. C* **119**, 16239–16244 (2015).
588. Li, J. *et al.* Solar Hydrogen Generation by a CdS–Au–TiO<sub>2</sub> Sandwich Nanorod Array Enhanced with Au Nanoparticle as Electron Relay and Plasmonic Photosensitizer. *J Am Chem Soc* **136**, 8438–8449 (2014).
589. Naphade, R. A., Tathavadekar, M., Jog, J. P., Agarkar, S. & Ogale, S. Plasmonic light harvesting of dye sensitized solar cells by Au-nanoparticle loaded TiO<sub>2</sub> nanofibers. *Journal of Materials Chemistry A* **2**, 975–984 (2014).
590. Li, Z., Su, C., Wu, D. & Zhang, Z. Gold Nanoparticles Decorated Hematite Photoelectrode for Sensitive and Selective Photoelectrochemical Aptasensing of Lysozyme. *Analytical Chemistry* **90**, 961–967 (2018).
591. Choi, H., Chen, W. T. & Kamat, P. V. Know thy nano neighbor. Plasmonic versus electron charging effects of metal nanoparticles in dye-sensitized solar cells. *ACS Nano* **6**, 4418–4427 (2012).
592. Li, J.-M. *et al.* TiO<sub>2</sub>–Au–Cu<sub>2</sub>O Photocathodes: Au-Mediated Z-Scheme Charge Transfer for Efficient Solar-Driven Photoelectrochemical Reduction. *ACS Applied Nano Materials* **1**, 6843–6853 (2018).
593. Li, J.-M., Cheng, H.-Y., Chiu, Y.-H. & Hsu, Y.-J. ZnO–Au–SnO<sub>2</sub> Z-scheme photoanodes for remarkable photoelectrochemical water splitting. *Nanoscale* **8**, 15720–15729 (2016).
594. Hartland, G. V, Besteiro, L. V, Johns, P. & Govorov, A. O. What’s so Hot about Electrons in Metal Nanoparticles? *ACS Energy Letters* **2**, 1641–1653 (2017).
595. Govorov, A. O., Zhang, H. & Gun’ko, Y. K. Theory of Photoinjection of Hot Plasmonic Carriers from Metal Nanostructures into Semiconductors and Surface Molecules. *The Journal of Physical Chemistry C* **117**, 16616–16631 (2013).
596. Besteiro, L. V., Kong, X. T., Wang, Z., Hartland, G. & Govorov, A. O. Understanding Hot-Electron Generation and Plasmon Relaxation in Metal Nanocrystals: Quantum and Classical Mechanisms. *ACS Photonics* **4**, 2759–2781 (2017).
597. Hartland, G. V, Besteiro, L. V, Johns, P. & Govorov, A. O. What’s so Hot about Electrons in Metal Nanoparticles? *ACS Energy Letters* **2**, 1641–1653 (2017).

598. Pinchuk, A., Plessen, G. von & Kreibig, U. Influence of interband electronic transitions on the optical absorption in metallic nanoparticles. *Journal of Physics D: Applied Physics* **37**, 3133–3139 (2004).
599. Zhang, J. *et al.* Efficient base-free direct oxidation of glucose to gluconic acid over TiO<sub>2</sub> - supported gold clusters. *Nanoscale* **11**, 1326–1334 (2018).
600. Asapu, R. *et al.* Plasmonic Near-Field Localization of Silver Core–Shell Nanoparticle Assemblies via Wet Chemistry Nanogap Engineering. *ACS Applied Materials & Interfaces* **9**, 41577–41585 (2017).
601. Tian, Y. & Tatsuma, T. Mechanisms and Applications of Plasmon-Induced Charge Separation at TiO<sub>2</sub> Films Loaded with Gold Nanoparticles. *J Am Chem Soc* **127**, 7632–7637 (2005).
602. Cushing, S. K. & Wu, N. Plasmon-enhanced solar energy harvesting. *The Electrochemical Society Interface* **22**, 63–67 (2013).
603. Hühn, J. *et al.* Selected Standard Protocols for the Synthesis, Phase Transfer, and Characterization of Inorganic Colloidal Nanoparticles. *Chemistry of Materials* **29**, 399–461 (2017).
604. Lin, P. *et al.* A novel protein binding strategy for energy-transfer-based photoelectrochemical detection of enzymatic activity of botulinum neurotoxin A. *Electrochemistry Communications* **97**, 114–118 (2018).
605. Zhong, X., Lv, J., Xue, S., Yuan, R. & Chai, Y. An Electrochemical Assay Based on Acid-Induced Dissolution of Nanoparticles to Trigger Enzyme-Free Cleavage for Target Detection. *Journal of The Electrochemical Society* **165**, B223–B226 (2018).
606. Wei, H., Wang, Y., Zhang, H., Zhao, H. & Jiang, W. Au nanoparticles fluorescence switch-mediated target recycling amplification strategy for sensitive nucleic acid detection. *RSC Advances* **6**, 10650–10654 (2016).
607. Wen, G., Dong, W., Liu, B., Li, Z. & Fan, L. A novel nonenzymatic cascade amplification for ultrasensitive photoelectrochemical DNA sensing based on target driven to initiate cyclic assembly of hairpins. *Biosensors and Bioelectronics* **117**, 91–96 (2018).
608. Lee, J. H., Wang, Z., Liu, J. & Lu, Y. Highly Sensitive and Selective Colorimetric Sensors for Uranyl (UO<sub>2</sub><sup>2+</sup>): Development and Comparison of Labeled and Label-Free DNAzyme-Gold Nanoparticle Systems. *J Am Chem Soc* **130**, 14217–14226 (2008).
609. Sundah, N. R. *et al.* Barcoded DNA nanostructures for the multiplexed profiling of subcellular protein distribution. *Nature Biomedical Engineering* **3**, 684–694 (2019).
610. Wang, B., Cao, J.-T. & Liu, Y.-M. Recent progress of heterostructure-based photoelectrodes in photoelectrochemical biosensing: a mini review. *Analyst* **145**, 1121–1128 (2020).
611. Zhang, N. *et al.* Quantum-dots-based photoelectrochemical bioanalysis highlighted with recent examples. *Biosensors and Bioelectronics* **94**, 207–218 (2017).
612. Qiu, Z. & Tang, D. Nanostructure-based photoelectrochemical sensing platforms for biomedical applications. *Journal of Materials Chemistry B* **8**, 2541–2561 (2020).
613. Shen, X. *et al.* Photoelectrochemical and electrochemical ratiometric aptasensing: A case study of streptomycin. *Electrochemistry Communications* **110**, 106637 (2020).

614. Zhao, W.-W., Xu, J.-J. & Chen, H.-Y. Photoelectrochemical enzymatic biosensors. *Biosensors and Bioelectronics* **92**, 294–304 (2017).
615. Zhao, W.-W., Xu, J.-J. & Chen, H.-Y. Photoelectrochemical bioanalysis: the state of the art. *Chem. Soc. Rev.* **44**, 729–741 (2015).
616. Shen, Q. *et al.* Highly sensitive photoelectrochemical assay for DNA methyltransferase activity and inhibitor screening by exciton energy transfer coupled with enzyme cleavage biosensing strategy. *Biosensors and Bioelectronics* **64**, 449–455 (2015).
617. Da, P. *et al.* Surface Plasmon Resonance Enhanced Real-Time Photoelectrochemical Protein Sensing by Gold Nanoparticle-Decorated TiO<sub>2</sub> Nanowires. *Analytical Chemistry* **86**, 6633–6639 (2014).
618. Guo, L. *et al.* Periodically Patterned Au-TiO<sub>2</sub> Heterostructures for Photoelectrochemical Sensor. *ACS Sensors* **2**, 621–625 (2017).
619. Shu, J. & Tang, D. Recent Advances in Photoelectrochemical Sensing: From Engineered Photoactive Materials to Sensing Devices and Detection Modes. *Analytical Chemistry* **92**, 363–377 (2020).
620. Liu, X.-P. *et al.* Enhanced photoelectrochemical DNA sensor based on TiO<sub>2</sub>/Au hybrid structure. *Biosensors and Bioelectronics* **116**, 23–29 (2018).
621. Zhao, M., Fan, G. C., Chen, J. J., Shi, J. J. & Zhu, J. J. Highly Sensitive and Selective Photoelectrochemical Biosensor for Hg<sup>2+</sup> Detection Based on Dual Signal Amplification by Exciton Energy Transfer Coupled with Sensitization Effect. *Analytical Chemistry* **87**, 12340–12347 (2015).
622. Yan, Z., Wang, Z., Miao, Z. & Liu, Y. Dye-Sensitized and Localized Surface Plasmon Resonance Enhanced Visible-Light Photoelectrochemical Biosensors for Highly Sensitive Analysis of Protein Kinase Activity. *Analytical Chemistry* **88**, 922–929 (2016).
623. Liu, X.-P. *et al.* Enhanced photoelectrochemical DNA sensor based on TiO<sub>2</sub>/Au hybrid structure. *Biosensors and Bioelectronics* **116**, 23–29 (2018).
624. Huang, Y.-L. *et al.* Tunable photoelectrochemical performance of Au/BiFeO<sub>3</sub> heterostructure. *Nanoscale* **8**, 15795–15801 (2016).
625. Steel, A. B., Herne, T. M. & Tarlov, M. J. Electrochemical Quantitation of DNA Immobilized on Gold. *Analytical Chemistry* **70**, 4670–4677 (1998).
626. Reynaldo, L. P., Vologodskii, A. V, Neri, B. P. & Lyamichev, V. I. The kinetics of oligonucleotide replacements. *Journal of Molecular Biology* **297**, 511–520 (2000).
627. Baker, B. A. & Milam, V. T. Hybridization kinetics between immobilized double-stranded DNA probes and targets containing embedded recognition segments. *Nucleic Acids Research* **39**, e99–e99 (2011).
628. Traeger, J. C. & Schwartz, D. K. Surface-Mediated DNA Hybridization: Effects of DNA Conformation, Surface Chemistry, and Electrostatics. *Langmuir* **33**, 12651–12659 (2017).
629. Schwarzenbach, H., Hoon, D. S. B. & Pantel, K. Cell-free nucleic acids as biomarkers in cancer patients. *Nature Reviews Cancer* **11**, 426–437 (2011).
630. Hayes, J., Peruzzi, P. P. & Lawler, S. MicroRNAs in cancer: biomarkers, functions and therapy. *Trends in Molecular Medicine* **20**, 460–469 (2014).

631. Zhou, S. *et al.* miRNAs in cardiovascular diseases: potential biomarkers, therapeutic targets and challenges. *Acta Pharmacologica Sinica* **39**, 1073–1084 (2018).
632. Tribolet, L. *et al.* MicroRNA Biomarkers for Infectious Diseases: From Basic Research to Biosensing. *Frontiers in Microbiology* vol. 11 1197 (2020).
633. Barman, T., Hussain, A. A., Sharma, B. & Pal, A. R. Plasmonic hot hole generation by interband transition in gold-polyaniline. *Scientific Reports* **5**, 18276 (2015).
634. Brongersma, M. L., Halas, N. J. & Nordlander, P. Plasmon-induced hot carrier science and technology. *Nature Nanotechnology* **10**, 25 (2015).
635. Manzanares-Palenzuela, C. L., Fernandes, E. G. R., Lobo-Castañón, M. J., López-Ruiz, B. & Zucolotto, V. Impedance sensing of DNA hybridization onto nanostructured phthalocyanine-modified electrodes. *Electrochimica Acta* **221**, 86–95 (2016).
636. Tu, W. *et al.* Dual Signal Amplification Using Gold Nanoparticles-Enhanced Zinc Selenide Nanoflakes and P19 Protein for Ultrasensitive Photoelectrochemical Biosensing of MicroRNA in Cell. *Analytical Chemistry* **88**, 10459–10465 (2016).
637. Imani, R. *et al.* Band edge engineering of TiO<sub>2</sub>@DNA nanohybrids and implications for capacitive energy storage devices. *Nanoscale* **7**, 10438–10448 (2015).
638. Ateş Sönmezoğlu, Ö., Akın, S., Terzi, B., Mutlu, S. & Sönmezoğlu, S. An Effective Approach for High-Efficiency Photoelectrochemical Solar Cells by Using Bifunctional DNA Molecules Modified Photoanode. *Advanced Functional Materials* **26**, 8776–8783 (2016).
639. Lim, S. P., Pandikumar, A., Huang, N. M. & Lim, H. N. Facile synthesis of Au@TiO<sub>2</sub> nanocomposite and its application as a photoanode in dye-sensitized solar cells. *RSC Advances* **5**, 44398–44407 (2015).
640. Johansson, M. A. & Hellenäs, K.-E. Matrix effects in immunobiosensor determination of clenbuterol in urine and serum. *Analyst* **129**, 438–442 (2004).
641. Zhang, L. *et al.* Ag nanoclusters could efficiently quench the photoresponse of CdS quantum dots for novel energy transfer-based photoelectrochemical bioanalysis. *Biosensors and Bioelectronics* **85**, 930–934 (2016).
642. Jin, Y., Yao, X., Liu, Q. & Li, J. Hairpin DNA probe based electrochemical biosensor using methylene blue as hybridization indicator. *Biosensors and Bioelectronics* **22**, 1126–1130 (2007).
643. Zhao, Y., Zhou, L. & Tang, Z. Cleavage-based signal amplification of RNA. *Nature Communications* **4**, 1493 (2013).
644. Bruch, R. *et al.* Biosensors: CRISPR/Cas13a-Powered Electrochemical Microfluidic Biosensor for Nucleic Acid Amplification-Free miRNA Diagnostics (Adv. Mater. 51/2019). *Advanced Materials* **31**, 1970365 (2019).
645. Miao, P., Zhang, T., Xu, J. & Tang, Y. Electrochemical Detection of miRNA Combining T7 Exonuclease-Assisted Cascade Signal Amplification and DNA-Templated Copper Nanoparticles. *Analytical Chemistry* **90**, 11154–11160 (2018).
646. Cui, J., Li, F. & Shi, Z.-L. Origin and evolution of pathogenic coronaviruses. *Nature Reviews Microbiology* **17**, 181–192 (2019).
647. Bevins, S. N. *et al.* Spillover of Swine Coronaviruses, United States. *Emerging Infectious Diseases* **24**, 1390–1392 (2018).

648. Schulz, L. L. & Tonsor, G. T. Assessment of the economic impacts of porcine epidemic diarrhea virus in the United States. *Journal of Animal Science* **93**, 5111–5118 (2015).
649. Bang, A. & Khadakkar, S. Opinion: Biodiversity conservation during a global crisis: Consequences and the way forward. *Proceedings of the National Academy of Sciences* **117**, 29995–29999 (2020).
650. Chen, S., Zhang, L., Wang, L., Ouyang, H. & Ren, L. Viruses from poultry and livestock pose continuous threats to human beings. *Proceedings of the National Academy of Sciences* **118**, e2022344118 (2021).
651. Vidic, J., Manzano, M., Chang, C.-M. & Jaffrezic-Renault, N. Advanced biosensors for detection of pathogens related to livestock and poultry. *Veterinary Research* **48**, 1–22 (2017).
652. Cullinane, A. & Garvey, M. A review of diagnostic tests recommended by the World Organisation for Animal Health Manual of Diagnostic Tests and Vaccines for Terrestrial Animals. *Revue Scientifique et Technique de l'OIE* **40**, 75–89 (2021).
653. Neethirajan, S., Tuteja, S. K., Huang, S.-T. & Kelton, D. Recent advancement in biosensors technology for animal and livestock health management. *Biosensors and Bioelectronics* **98**, 398–407 (2017).
654. Kang, A. *et al.* Sputum Processing Method for Lateral Flow Immunochromatographic Assays to Detect Coronaviruses. *Immune Network* **21**, (2021).
655. Zou, S. *et al.* Development of an accurate lateral flow immunoassay for PEDV detection in swine fecal samples with a filter pad design. *Animal Diseases* **1**, 1–12 (2021).
656. Xiao, W. *et al.* A simple and compact smartphone-based device for the quantitative readout of colloidal gold lateral flow immunoassay strips. *Sensors and Actuators B: Chemical* **266**, 63–70 (2018).
657. Fan, B. *et al.* Development of a Novel Double Antibody Sandwich Quantitative Enzyme-Linked Immunosorbent Assay for Detection of Porcine Epidemic Diarrhea Virus Antigen. *Frontiers in Veterinary Science* **7**, 868 (2020).
658. Poonsuk, K., Cheng, T.-Y., Ji, J., Zimmerman, J. & Giménez-Lirola, L. Detection of porcine epidemic diarrhea virus (PEDV) IgG and IgA in muscle tissue exudate (“meat juice”) specimens. *Porcine Health Management* **4**, 1–5 (2018).
659. Díaz, I. *et al.* Assessment of three commercial ELISAs for the detection of antibodies against Porcine epidemic diarrhea virus at different stages of the immune response. *Veterinary Immunology and Immunopathology* **234**, 110206 (2021).
660. Li, Y. *et al.* Development of an indirect ELISA based on a truncated S protein of the porcine epidemic diarrhea virus. *Canadian Journal of Microbiology* **61**, 811–817 (2015).
661. Okda, F. *et al.* Development of an indirect ELISA, blocking ELISA, fluorescent microsphere immunoassay and fluorescent focus neutralization assay for serologic evaluation of exposure to North American strains of Porcine Epidemic Diarrhea Virus. *BMC Veterinary Research* **11**, 180 (2015).
662. Oh, J. S. *et al.* Comparison of an enzyme-linked immunosorbent assay with serum neutralization test for serodiagnosis of porcine epidemic diarrhea virus infection. *Journal of Veterinary Science* **6**, 349 (2005).

663. Lin, H. *et al.* Development and application of an indirect ELISA for the detection of antibodies to porcine epidemic diarrhea virus based on a recombinant spike protein. *BMC Veterinary Research* **14**, 243 (2018).
664. Ma, Z. *et al.* A novel biotinylated nanobody-based blocking ELISA for the rapid and sensitive clinical detection of porcine epidemic diarrhea virus. *Journal of Nanobiotechnology* **17**, 96 (2019).
665. Hsu, W.-T. *et al.* PEDV Infection Generates Conformation-Specific Antibodies That Can Be Effectively Detected by a Cell-Based ELISA. *Viruses* **13**, 303 (2021).
666. Ren, X., Suo, S. & Jang, Y.-S. Development of a porcine epidemic diarrhea virus M protein-based ELISA for virus detection. *Biotechnology Letters* **33**, 215–220 (2011).
667. Gerber, P. F. *et al.* Detection of antibodies against porcine epidemic diarrhea virus in serum and colostrum by indirect ELISA. *The Veterinary Journal* **202**, 33–36 (2014).
668. Ma, J. *et al.* Versatile Electrochemiluminescence Assays for PEDV Antibody Based on Rolling Circle Amplification and Ru-DNA Nanotags. *Analytical Chemistry* **90**, 7415–7421 (2018).
669. Ma, J. *et al.* Novel Porphyrin Zr Metal–Organic Framework (PCN-224)-Based Ultrastable Electrochemiluminescence System for PEDV Sensing. *Analytical Chemistry* **93**, 2090–2096 (2021).
670. Li, X. *et al.* An impedimetric immunosensor for determination of porcine epidemic diarrhea virus based on the nanocomposite consisting of molybdenum disulfide/reduced graphene oxide decorated with gold nanoparticles. *Microchimica Acta* **187**, 217 (2020).
671. Song, D. & Park, B. Porcine epidemic diarrhoea virus: a comprehensive review of molecular epidemiology, diagnosis, and vaccines. *Virus Genes* **44**, 167–175 (2012).
672. Schoukroun-Barnes, L. R. *et al.* Reagentless, Structure-Switching, Electrochemical Aptamer-Based Sensors. *Annual Review of Analytical Chemistry* **9**, 163–181 (2016).
673. Deejai, N., Roshorm, Y. M. & Kubera, A. Antiviral Compounds Against Nucleocapsid Protein of Porcine Epidemic Diarrhea Virus. *Animal Biotechnology* **28**, 120–130 (2017).
674. Liu, M. *et al.* In Vitro Selection of a DNA Aptamer Targeting Degraded Protein Fragments for Biosensing. *Angewandte Chemie International Edition* **59**, 7706–7710 (2020).
675. Gysbers, R., Tram, K., Gu, J. & Li, Y. Evolution of an Enzyme from a Noncatalytic Nucleic Acid Sequence. *Scientific Reports* **5**, 1–8 (2015).
676. Li, J. *et al.* Diverse high-affinity DNA aptamers for wild-type and B.1.1.7 SARS-CoV-2 spike proteins from a pre-structured DNA library. *Nucleic Acids Research* **49**, 7267–7279 (2021).
677. Liwnaree, B., Narkpuk, J., Sungsuwan, S., Jongkaewwattana, A. & Jaru-Ampornpan, P. Growth enhancement of porcine epidemic diarrhea virus (PEDV) in Vero E6 cells expressing PEDV nucleocapsid protein. *PLOS ONE* **14**, e0212632 (2019).
678. Deng, F. *et al.* Identification and Comparison of Receptor Binding Characteristics of the Spike Protein of Two Porcine Epidemic Diarrhea Virus Strains. *Viruses* 2016, Vol. 8, Page 55 **8**, 55 (2016).
679. Gysbers, R., Tram, K., Gu, J. & Li, Y. Evolution of an enzyme from a noncatalytic nucleic acid sequence. *Scientific Reports* **5**, (2015).

680. Chang, D. *et al.* Functional Nucleic Acids for Pathogenic Bacteria Detection. *Accounts of Chemical Research* **54**, (2021).
681. Elbadawi, M., Ong, J. J., Pollard, T. D., Gaisford, S. & Basit, A. W. Additive Manufacturable Materials for Electrochemical Biosensor Electrodes. *Advanced Functional Materials* **31**, 2006407 (2021).
682. Russo Krauss, I. *et al.* High-resolution structures of two complexes between thrombin and thrombin-binding aptamer shed light on the role of cations in the aptamer inhibitory activity. *Nucleic Acids Research* **40**, (2012).
683. Bard, A. J., Denuault, G., Lee, C., Mandler, D. & Wipf, D. O. Scanning electrochemical microscopy - a new technique for the characterization and modification of surfaces. *Accounts of Chemical Research* **23**, 257–263 (1990).
684. Traynor, S. M., Wang, G. A., Pandey, R., Li, F. & Soleymani, L. Dynamic Bio-Barcode Assay Enables Electrochemical Detection of a Cancer Biomarker in Undiluted Human Plasma: A Sample-In-Answer-Out Approach. *Angewandte Chemie International Edition* **59**, (2020).
685. Kang, J., Yeom, G., Ha, S.-J. & Kim, M.-G. Development of a DNA aptamer selection method based on the heterogeneous sandwich form and its application in a colorimetric assay for influenza A virus detection. *New Journal of Chemistry* **43**, 6883–6889 (2019).
686. Chen, Z., Wu, Q., Chen, J., Ni, X. & Dai, J. A DNA Aptamer Based Method for Detection of SARS-CoV-2 Nucleocapsid Protein. *Virol Sin* **35**, 351–354 (2020).
687. Wang, R. *et al.* Selection and characterization of DNA aptamers for use in detection of avian influenza virus H5N1. *Journal of Virological Methods* **189**, 362–369 (2013).
688. Percze, K. *et al.* Aptamers for respiratory syncytial virus detection. *Scientific Reports* **7**, 1–11 (2017).
689. Zou, X., Wu, J., Gu, J., Shen, L. & Mao, L. Application of Aptamers in Virus Detection and Antiviral Therapy. *Frontiers in Microbiology* **10**, 1462 (2019).
690. Dolai, S. & Tabib-Azar, M. Whole virus detection using aptamers and paper-based sensor potentiometry. *Medical Devices & Sensors* **3**, e10112 (2020).
691. Kelley, S. O., Barton, J. K., Jackson, N. M. & Hill, M. G. Electrochemistry of Methylene Blue Bound to a DNA-Modified Electrode. *Bioconjugate Chemistry* **8**, 31–37 (1997).
692. Ngamchuea, K., Batchelor-McAuley, C. & Compton, R. G. Understanding electroanalytical measurements in authentic human saliva leading to the detection of salivary uric acid. *Sensors and Actuators B: Chemical* **262**, 404–410 (2018).
693. Baker, K. L. *et al.* Evaluation of an accelerated hydrogen peroxide disinfectant to inactivate porcine epidemic diarrhea virus in swine feces on aluminum surfaces under freezing conditions. *BMC Veterinary Research* **13**, 1–11 (2017).
694. Thomas, J. T. *et al.* Effect of Porcine Epidemic Diarrhea Virus Infectious Doses on Infection Outcomes in Naïve Conventional Neonatal and Weaned Pigs. *PLOS ONE* **10**, (2015).
695. Bjustrom-Kraft, J. *et al.* Porcine epidemic diarrhea virus (PEDV) detection and antibody response in commercial growing pigs. *BMC Veterinary Research* **12**, 1–8 (2016).
696. Werner, A. Predicting translational diffusion of evolutionary conserved RNA structures by the nucleotide number. *Nucleic Acids Research* **39**, e17–e17 (2011).

697. Analyse-it Ltd. Diagnostic performance. in *Analyse-it for Microsoft Excel* 197–208 (Analyse-it, 2020).
698. Zweig, M. H. & Campbell, G. Receiver-operating characteristic (ROC) plots: a fundamental evaluation tool in clinical medicine. *Clinical Chemistry* **39**, 561–577 (1993).
699. Zhang, Z. *et al.* High-Affinity Dimeric Aptamers Enable the Rapid Electrochemical Detection of Wild-Type and B.1.1.7 SARS-CoV-2 in Unprocessed Saliva. *Angewandte Chemie International Edition* **60**, 24266–24274 (2021).
700. Mandrekar, J. N. Receiver Operating Characteristic Curve in Diagnostic Test Assessment. *Journal of Thoracic Oncology* **5**, 1315–1316 (2010).
701. Ata, M. S., Liu, Y. & Zhitomirsky, I. A review of new methods of surface chemical modification, dispersion and electrophoretic deposition of metal oxide particles. *RSC Advances* **4**, 22716 (2014).
702. Harroun, S. G. *et al.* Programmable DNA switches and their applications. *Nanoscale* **10**, 4607–4641 (2018).
703. Nguyen, B. H. *et al.* Scaling DNA data storage with nanoscale electrode wells. *Science Advances* **7**, (2021).
704. Takahashi, C. N., Nguyen, B. H., Strauss, K. & Ceze, L. Demonstration of End-to-End Automation of DNA Data Storage. *Scientific Reports* **9**, 4998 (2019).
705. Chen, B. *et al.* Photoelectrochemical TiO<sub>2</sub>-Au-Nanowire-Based Motor for Precise Modulation of Single-Neuron Activities. *Advanced Functional Materials* **31**, 2008667 (2021).
706. Dong, R., Zhang, Q., Gao, W., Pei, A. & Ren, B. Highly Efficient Light-Driven TiO<sub>2</sub>-Au Janus Micromotors. *ACS Nano* **10**, 839–844 (2016).
707. Yunker, P. J., Still, T., Lohr, M. A. & Yodh, A. G. Suppression of the coffee-ring effect by shape-dependent capillary interactions. *Nature* **476**, 308–311 (2011).
708. SCRIVEN, L. E. & STERNLING, C. v. The Marangoni Effects. *Nature* **187**, 186–188 (1960).
709. Sempels, W., de Dier, R., Mizuno, H., Hofkens, J. & Vermant, J. Auto-production of biosurfactants reverses the coffee ring effect in a bacterial system. *Nature Communications* **4**, 1757 (2013).
710. Seo, C., Jang, D., Chae, J. & Shin, S. Altering the coffee-ring effect by adding a surfactant-like viscous polymer solution. *Scientific Reports* **7**, 500 (2017).
711. Shen, X., Ho, C.-M. & Wong, T.-S. Minimal Size of Coffee Ring Structure. *The Journal of Physical Chemistry B* **114**, 5269–5274 (2010).
712. Li, Y., Yang, Q., Li, M. & Song, Y. Rate-dependent interface capture beyond the coffee-ring effect. *Scientific Reports* **6**, 24628 (2016).
713. Zhu, H. *et al.* Mapping Hot Electron Response of Individual Gold Nanocrystals on a TiO<sub>2</sub> Photoanode. *Nano Letters* **20**, 2423–2431 (2020).
714. Sousa-Castillo, A. *et al.* Boosting Hot Electron-Driven Photocatalysis through Anisotropic Plasmonic Nanoparticles with Hot Spots in Au-TiO<sub>2</sub> Nanoarchitectures. *The Journal of Physical Chemistry C* **120**, 11690–11699 (2016).

715. Zhang, H. & Govorov, A. O. Optical Generation of Hot Plasmonic Carriers in Metal Nanocrystals: The Effects of Shape and Field Enhancement. *The Journal of Physical Chemistry C* **118**, 7606–7614 (2014).
716. Reineck, P., Brick, D., Mulvaney, P. & Bach, U. Plasmonic Hot Electron Solar Cells: The Effect of Nanoparticle Size on Quantum Efficiency. *The Journal of Physical Chemistry Letters* **7**, 4137–4141 (2016).
717. Kim, S., Lee, S. & Yoon, S. Effect of Nanoparticle Size on Plasmon-Driven Reaction Efficiency. *ACS Applied Materials & Interfaces* **14**, 4163–4169 (2022).
718. Santiago, E. Y. *et al.* Efficiency of Hot-Electron Generation in Plasmonic Nanocrystals with Complex Shapes: Surface-Induced Scattering, Hot Spots, and Interband Transitions. *ACS Photonics* **7**, 2807–2824 (2020).
719. Briggs, K., Bouhamidi, M. Y., He, L. & Tabard-Cossa, V. Efficient Simulation of Arbitrary Multicomponent First-Order Binding Kinetics for Improved Assay Design and Molecular Assembly. *ACS Measurement Science Au* aacsmeasuresciau.1c00037 (2021) doi:10.1021/acsmearuresciau.1c00037.
720. Koussa, M. A., Halvorsen, K., Ward, A. & Wong, W. P. DNA nanoswitches: a quantitative platform for gel-based biomolecular interaction analysis. *Nature Methods* **12**, 123–126 (2015).
721. Ramirez, A. *et al.* Efficient surveillance of pig populations using oral fluids. *Preventive Veterinary Medicine* **104**, 292–300 (2012).
722. Lichtenberg, J. Y., Ling, Y. & Kim, S. Non-Specific Adsorption Reduction Methods in Biosensing. *Sensors* **19**, 2488 (2019).
723. Tu, W., Wang, W., Lei, J., Deng, S. & Ju, H. Chemiluminescence excited photoelectrochemistry using graphene–quantum dots nanocomposite for biosensing. *Chemical Communications* **48**, 6535 (2012).
724. Zhang, X., Zhao, Y., Zhou, H. & Qu, B. A new strategy for photoelectrochemical DNA biosensor using chemiluminescence reaction as light source. *Biosensors and Bioelectronics* **26**, 2737–2741 (2011).
725. Yu, Z. *et al.* Chemiluminescence-Derived Self-Powered Photoelectrochemical Immunoassay for Detecting a Low-Abundance Disease-Related Protein. *Analytical Chemistry* **93**, 13389–13397 (2021).